Republic of Iraq

Ministry of Higher Education

and Scientific Research

University of Babylon

College of Engineering

Civil Engineering Department

Structural Response of Composite Reinforced Concrete Deck-Cold Formed Steel Beam to Column Semi-Rigid Connections

A Thesis

Submitted to the College of Engineering / University of Babylon in Partial Fulfillment of the Requirements for the Degree of Doctor of Philosophy in Engineering/ Civil Engineering/ Structures

By

Mustafa Salah Shaker Mahmood

Supervised by

Prof. Dr. Haitham H. Muteb Al-Daami

2023 A.D 1444 A.H

بِسْمِ اللهِ الْرَّحْمنِ الْرَّحِيمِ

((وَيَسْأَلُونَكَ عَنِ الرُّوحِ
قُلِ الرُّوحُ مِنْ أَمْرِ رَبِّي وَمَا أُوتِيتُمْ مِنَ
الْعِلْمِ إِلَّا قَلِيلًا ﴿٨٥﴾))

صَدَقَ اللهُ الْعَظِيمُ

سورة الإسراء

Dedication

To my father and Mother

To my Wife and Brothers

To my supervisor Prof. Dr. Haitham H. Muteb Al-Daami

"To my loved ones and my heart, my nephews

(Ahmed) and (Muntather)"

With respect

ACKNOWLEDGEMENTS

In the name of Allah, the most gracious, the most merciful

Praise is to Allah, Who has granted me the syncretizing and enabled me to achieve this work.

First, I would like to express my appreciation and deepest gratitude to my supervisor **Professor Dr Haitham H. Muteb Al-Daami**, for his remarkable suggestions, encouragement and guidance throughout the research. I am really indebted to him.

A special thanks and gratitude to My dear father, dear mother and my brothers for their care, patience and encouragement throughout the research. There is no description that does justice to their efforts with me throughout my studying career. I am truly indebted to them, and from the bottom of my heart, I say thank you to them and "God protect you for me".

I am very grateful to my fiancée and my life partner; she supported me and encouraged me at every step, and no description can do justice to her outstanding efforts, so I would like to tell her from the depths of my heart, "Thanks, and God bless you."

I would like to thank my friends for supporting me spiritually and practically and helping me throughout preparing the experimental work. Special thanks go to Wissam Nadir, Mustafa Kareem and my cousin Ali Safa to whom I am so grateful.

Thanks to the College of Engineering and the Civil Engineering Department staff at the University of Babylon for their appreciable support.

Great Thanks for All

Mustafa Salah Shaker

2023

ABSTRACT

Designers have recognized the benefits of designing semi-rigid connections. It decreases beam weight, reduces beam depth, overall building height and increases energy absorption. In addition, cold-formed steel (CFS) is becoming more popular in several countries, indicating good potential for using lightweight materials as an alternative to conventional steel. However, there is still a scarcity of data on joint behavior, particularly for composite connections integrated with CFS, which gives more motivation to study this type of composite joint. A composite beam-to-column semi-rigid joint formed by a composite concrete slab and two cold-formed steel C-sections as a beam and column is investigated experimentally in this study.

Thirteen specimens with cruciform subassemblies of CFS beam-to-column joints are tested experimentally with a novel approach to different beam-to-column connection shapes and different types and degrees of the shear connector. In addition, nine pushout test specimens are prepared to investigate the shear strength, stiffness, and ductility of the bolted shear connector with a single embedded nut and CFS plate shear connectors, such as single plate, single angle, single corrugated, and double angle plate, that are used in composite joint specimens.

The experimental study is divided into three parts: the experimental test of pushout specimens; the experimental test of three trial composite joints with minimum reinforcement and 300 mm slab width and the experimental test of ten main composite joints reinforced by Ø10 @ 100 mm in both directions and 750 mm slab width with different beam-to-column connection shapes tested under monotonic and cyclic load and different types and degrees of the shear connector; and numerical study.

The results show that tested specimens with beam-to-column joints connected by angles in the main composite joint group possessed high ductile properties where the rotation capacity exceeded 30 mrad. Hence, all these specimens classify as semi-rigid joints according to Eurocode 4 (EC4) and are adequate for plastic analysis and seismic design. While a back-to-back web connection forming a box column section increase the ultimate load by 33% and decreased the rotation capacity by 76%. In contrast, the specimen with a back-to-back web connection forming a box beam section increase the ultimate load by 90% and decrease the rotation capacity by 78% compared to the

specimen with an I-section shape for the beam and column connected by angles. On the other hand, the cyclic load has little effect on the ultimate moment capacity of composite joints, but it greatly increases their rotation capacity. The suggested composite cold-formed steel beam-to-column connection shapes are effective in terms of stiffness and ultimate moment capacity.

Also, using a novel approach to the CFS angle plate shear connector showed a significant improvement in the moment and initial stiffness of the joint. The partially bolted shear connector used in this study, up to 50% of which is fully shear connected, produced acceptable results and is within the recommended limits for semi-rigid joints according to the European Code.

The analytical study is using the finite element method, which investigates the nonlinear behavior of composite joints. The analytical models are carried out using ABAQUS Standard/Explicit 2017. The results of finite element models include the deformed shape at ultimate load and the moment rotational curves.

The finite element model results show good agreement with the experimental results. The program's ability to extend the study gives more results in understanding the actual behavior of composite joints. In this thesis, a parametric analysis is performed to investigate a wide range of the main variables (top and seat angle thickness, reinforcing ratio, use of stiffener in the column web, column shape, and the number of bolts). It is concluded from the parametric study that the used angle with a thickness to width ratio equal 0.092 improves the moment capacity of a composite joint by 17.3%, and the use of stiffener in the column web improves the moment capacity by 42.65 and prevents the buckling of the column web while maintaining a semi-rigid behavior of the joint.

LIST OF CONTENTS

Subject ..... Page No.

CHAPTER THREE: EXPERIMENTAL WORK

CHAPTER FOUR: EXPERIMENTAL WORK

CHAPTER FIVE: NUMERICAL ANALYSIS BY FINITE ELEMENT

CHAPTER SIX: CONCLUSIONS AND RECOMMENDATIONS

LIST OF TABELS

LIST OF FIGURES

NOTATION

The major symbols used in the text are listed below; others are indicated with their equations where they first appear.

Symbol	Definition	Unit
$\mathbf{A_c}$	Cross-section area of concrete	mm^2
$\mathbf{A_g}$	Cross-section area of steel profile	mm^2
$\mathbf{b_c}$	Slab width	mm
$\mathbf{b_{fb}}$	Flange width of beam	mm
C/C	From center to center of dimensions	
E	Young's modulus	Mpa
Es	Modulus of elasticity	MPa
Fy	Yielding stress	MPa
Fu	Ultimate strength	MPa
$\mathbf{h_b}$	Depth of beam	mm
$\mathbf{h_c}$	Depth of column	Mm
$\mathbf{h_{lip}}$	Depth of lip	Mm
$\mathbf{I_b}$	The second moment of inertia of a beam	m^4
$\mathbf{I_c}$	The second moment of inertia of a column	m^4
$\mathbf{K_c}$	The mean value of I_c/L_c for all the columns in that story	m^3
$\mathbf{K_b}$	The mean value of I_b/L_b for all the beams at the top of that story	m^3
$\boldsymbol{K}\mathbf{sc}$	Shear connector stiffness	kN/mm
$\mathbf{L_c}$	The story height of a column	m
Mn	Flexural strength	kN.m
$\mathbf{M_{pb}}$	Plastic moment of beam	kN.m
$\mathbf{M_{c,pl,Rd}}$	The design of plastic moment resistance of the connected column	kN.m

$\mathbf{M_{b,pl,Rd}}$	The design of plastic moment resistance of the connected beam	kN.m
$\mathbf{M_{j,Rd}}$	The design moment resistance of a connection	kN.m
Mu	Ultimate bending resistance	kN.m
$\mathbf{R_{ks}}$	Secant stiffness of connections at service load	kN.m/mrad
$\mathbf{R_{ki}}$	Initial rotational stiffness of connections	kN.m/mrad
$\mathbf{t_c}$	Slab thickness	mm
$\mathbf{t_{sb}}$	Thickness of beam	mm
$\mathbf{t_{sc}}$	Thickness of column	mm
$\boldsymbol{\theta_u}$	Rotational capacity	mrad
θr	Rotational deformation angle	mrad
$\boldsymbol{\delta}$**peak**	Peak slip	mm
$\boldsymbol{\delta}$**u**	Ultimate slip	mm

ABBREVIATIONS

Abbreviations	Definition
AASHTO	American Association of State Highway and Transportation Officials
ACI	American Concrete Institute
AISC	American Institute of Steel Construction
ASTM	American Society for Testing and Materials
BS	British Standard
CDP	Concrete Damage Plasticity
CFS	Cold-Formed Steel
CNC	Computer Numerical Control
C3D8R	8 node brick elements, reduced integration
D.C. A	Degree of Composite Action
EC4	Eurocode 4
EC3	Eurocode 3
Exp.	Experimental
FEM	Finite Element Method
FEN	Finite Element Analysis
IQ. S	Iraqi Specification
LRFD	Load Resisting Factor Design
Max.	Maximum
Min.	Minimum
MPa	Mega Pascal (MN/m_2)
MPCIJ	Modular Prefabricated Composite Interior Joint
No.	Number
Num.	Numerical
N/A	Not available
SCDB	Steel Connection Data Bank
TSACW	Top-Seat Angle Connections with double Web angles
T3D2	2 nodes 3 D truss element

CHAPTER ONE

INTRODUCTION

1.1 BEAM-TO-COLUMN JOINTS

Beam-column joints are important components of moment resistance frame structures since they are subjected to more shear force than adjusted beam and column members. Where failure in steel buildings is usually caused by the failure of those joints, as shown in Figures 1.1 and 1.2. The widespread damage caused by earthquakes in Northbridge, California, and Kobe, Japan, to steel structures in 1994 and 1995, respectively, prompted researchers worldwide to develop various earthquake mitigation techniques for buildings. Previous earthquakes demonstrated that beam-column joint elements played a significant role in the collapse or partial collapse of many existing steel structures. This research focuses on evaluating existing steel building and strengthening techniques, particularly the behavior of beam-to-column connections. Extensive research, study, and testing are still required to determine which systems are more cost-effective, easier to produce and install, structurally efficient, and lighter in weight.

Because of numerous advantages, such as ease of fabrication and assembly, good seismic performance, and adequate fire resistance, beam-to-column composite bolted joints are widely used in building engineering [3–6]. A typical composite connection system is made up of universal beams that are connected to columns via a variety of connections such as endplates, seat cleat angles, assembly plates, and so on. Shear connectors

are typically used to connect a concrete slab to the top of a beam flange. Three critical parameters representing the behavior of bolted joints, initial stiffness, moment resistance, and rotational capacity, have been extensively studied in recent decades [4,7-15]. Because steel-concrete composite bolted connections are favored over steel or reinforced concrete connections, their performance has been improved by optimizing the geometrical configuration and improving the moment-rotation response [16-20].

Figure 1.1: The collapse of composite steel structure in downtown New Orleans [1].

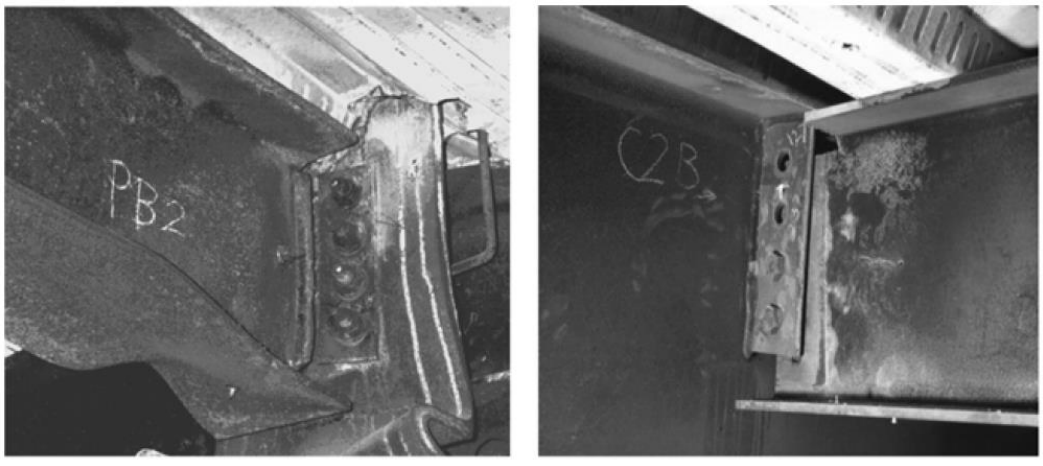

Figure 1.2: Typical failure modes of joints in the Cardington frame tests [2].

A composite steel-concrete system is one in which steel (hot-rolled, welded, or cold-formed) is combined with concrete to generate a composite

beam, composite column, composite slab, or composite connections. The composite constructions used are widely utilized worldwide; this type of structure is gaining popularity and space in Brazil. Although the usage of composite systems has traditionally been limited to hot-rolled and welded forms of steel, there is a growing trend to employ cold-formed steel in tiny structures (up to 5 floors).

1.2 COLD-FORMED STEEL

Cold-formed steel frame has been known since the 1850s1, but because of financial restrictions, decreased project timeframes, and strong demand, its popularity has surged in recent years. For example, in places like Phoenix, the luxury custom house industry has exploded in recent years, with custom builders doubling their income and active building permits up 10% since 2017. This rise has been spurred by cold-formed steel framing, which has resulted in shorter total project lengths, less waste, and lower prices. Due to these benefits, steel framing has been a go-to resource for construction and architectural professionals in various sectors [21].

Using building materials, especially for mid-rise buildings, results in more environmentally friendly materials that are easy to transport, quick to install and corrosion-resistant. The main criteria to be met include the highest strength-to-weight ratio, consistency in size and dimension, and the fact that it is a metallic material. Cold Forming Steel (CFS) is one of the most advanced and reliable alternative materials, rather than hot-rolled steel. The thickness between 1.9 and 3.2 mm contributes to the ratios of strength to weight. The yield strength is 250-450 MPa; CFS can be classified as a slim profile or slender section and generally has only one axis of symmetry. This function is prone to premature failure, local buckling and torsional buckling. As long as the CFS has economic potential and produces a better design, the use of CFS could also be more

popular and more convincing than the hot-rolled profile in composite connection. However, the use of CFS is still limited to low-risk buildings with a short span. Overall, CFS is used only as an alternative to steel profiles commonly used for masonry wall partitions, purlins and roof trusses. The connection is relatively simple and only resists the compressive and tensile forces.

The main properties of cold-formed steel are [22],[23]:

- Lightness in weight and Uniform quality.
- High strength and stiffness.
- Ease of prefabrication and mass production.
- Fast and easy erection and installation.
- More accurate detailing.
- The economy in transportation and handling.
- Recyclable material.

Some application of cold-formed steel building is in multi-story buildings, Industrial buildings, and Hospital such as Rehabilitation of Hospital in Phoenix, The Elan Westside building in Atlanta includes five stories framed in cold-formed steel (CFS) atop three stories of parking and other buildings as shown in Figures 1.3 and 1.4.

Figure 1.3: Cold-formed steel hospital in Phoenix [24].

(a) **(b)**

Figure 1.4: (a) Five stories of cold-formed steel on-3-stories-parking [25] and (b) Multi-story buildings from cold-formed steel.

1.3 SEMI-RIGID CONNECTION

It is more realistic to recognize that the composite connection behaves semi-rigidly in the design of multi-story buildings. For a long time, designers have recognized the benefits of designing semi-rigid connections. It decreases beam weight, where beam depth decreases, overall building height, and cladding cost, among other things. In comparison to pin supports, it can also improve serviceability performance due to increased stiffness; give greater robustness as a result of improved continuity between frame members; and provide good crack control in floor slabs. Despite the fact that the effect of semi-rigid composite connections on structural behavior and potential economic benefits is well recognized, all slabs currently used are either solid slabs or metal decking. There has been little research on semi-rigid composite connections with cold-formed steel sections [26].

The behavior of composite beams made of cold-formed steel differs from that of composite beams made of hot-rolled and welded steel. There have been some investigations on the structural behavior of composite

beams in the positive moment area, albeit some works discuss the region of hogging bending and the connections (beam-to-column connection or beam-to-beam). Because the continuation effect in the supports is dependent on the structural behavior of the beam-to-beam or beam-to-column connection, so the both topics are tightly coupled.

There are many types of beam-to-column connections shown in Figure 1.5, which are:

a. Single web angle.
b. Single plate.
c. Double web angle.
d. Top- and seat-angle.
e. Top- and seat-angle with double web angle.
f. Extended end-plate on the tension side only.
g. Extended end-plate on both sides.
h. Flush end-plate.
i. Header plate.

Connections are usually designed as pinned which associated with simple construction or rigid which is associated with continuous construction. However, the actual behavior falls between these two extreme cases. The use of partial strength or semi-rigid connections has been encouraged by codes and studies on the matter known as semicontinuous construction have proven that substantial savings in steel weight of the overall construction.

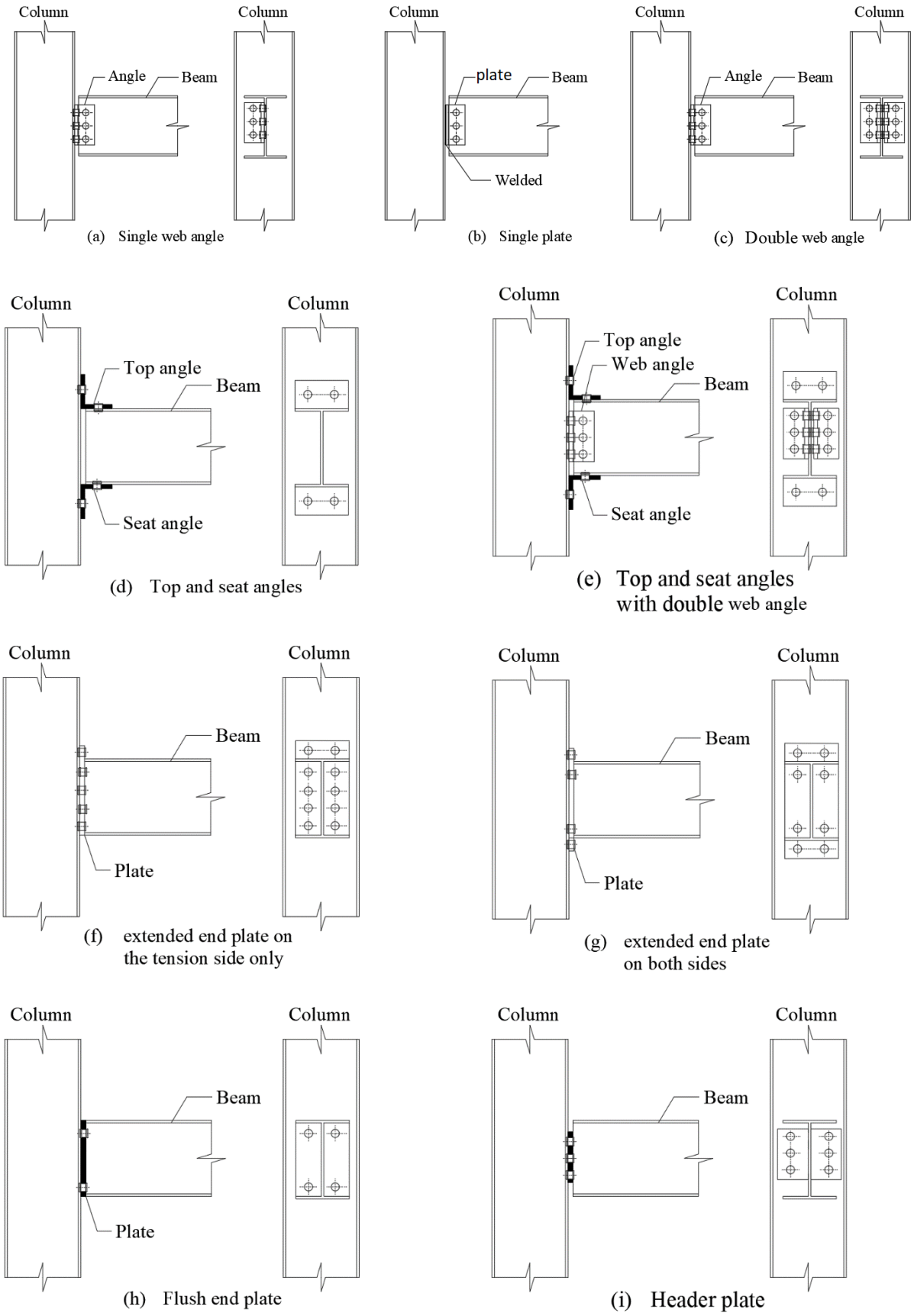

Figure 1.5: Beam-to-column connections types [27].

1.4 COMPOSITE STEEL-CONCRETE STRUCTURE

The most important and frequently encountered construction materials are steel and concrete, with applications in multi-storey commercial buildings, factories, and bridges. These materials can be used in mixed structural systems, for example, concrete cores encircled by steel tubes and in composite structures where members consist of steel and concrete act together compositely.

The use of cold-formed steel (CFS) sections has increased in popularity over the last decade, and construction professionals hypothesized the effectiveness of applying CFS sections to beams [28]. CFS is widely used in the structural elements of sustainable buildings in developed countries [29]. On the other hand, CFS sections are primarily intended to be non-composite members used for framing, roof trusses on metal buildings, and racks [30]. CFS section application is currently limited due to its thinness, which can cause buckling. Composite steel-concrete beams, on the contrary hand, are more widely used in the construction industry. They cost less and have higher strength capacities than bare steel beams [31].

Composite construction can minimize or even prevent buckling in the compressed top flange of CFS beams. This can be accomplished by using shear connectors to connect a concrete slab to a CFS beam. This raises the neutral axis of a steel beam, resulting in less compression stress at the top flange of the CFS beam. Furthermore, concrete prevents the top flange of the CFS beam from buckling, improving the composite beam's performance. As a result, a composite beam system could improve the strength and stiffness of non-composite CFS beams.

Also, for long spans, and especially where the susceptibility of steel to loss of strength from fire is not a problem, as in most bridges, steel beams

often become cheaper and better than concrete beams. It is at first customary to design the steelwork to carry the whole weight of the concrete slab and its loading. Still, by about 1950, the development of shear connectors has made it practicable to connect the slab to the beam to obtain the T-beam action that has long been used in concrete construction [32].

1.5 SHEAR CONNECTORS

For decades, a composite steel beam and concrete slab have been used in buildings and bridges. A shear connector connects all of these parts and plays an important role in a structure's seismic response. It prevents the two components from separating. It also improves longitudinal shear transmission and significantly impacts the composite beam's flexural strength. Typically, the connection is made using headed studs welded to the steel beam's top flange and embedded within the concrete deck. As a result, removing the slab entails drilling and crushing the concrete around the shear connectors, followed by breaking the slab into manageable sections [33]. Instead of traditionally headed studs, bolted shear connectors allow for easy dismantling and rapid replacement of the deteriorating deck. Bolted shear connectors make composite beam prefabrication easier, reducing onsite construction time and cost. Steel girders could be reused and recycled at the end of their service life, including utilizing bolted shear connectors in composite beams [34] in terms of environmental sustainability.

On the other hand, because the prevalent shear connector for hot-rolled steel beams, the welded-headed stud, is not convenient for cold-formed steel beams due to the thinness of CFS sections. As a result, new shear connectors must be developed for use in composite beams with CFS sections.

So, more research into new shear connectors for cold-formed steel composite structures is required. As a result, researchers began to produce and investigate various shear connectors for cold-formed steel composite parts. Hosseinpour et al. [35] experimentally studied the behavior of bolted shear connectors in the composite CFS beams, which have three variables: the thickness of the CFS section of the beam, strength, and diameter of bolted shear connectors. According to Eurocode 4 (EC4), all specimens in this study can be assumed ductile and thus suitable for partial shear connections. Pavlovi et al. [36] performed standard push-out tests on a bolted shear connector with a single embedded nut. Advanced finite element models were then used to validate the results. According to the results, bolted shear connectors with a single embedded nut achieved 95 percent of the shear resistance of headed stud shear connectors while reducing stiffness by 50 percent. Yang et al. [37] conducted ten push-out tests to investigate the effects of multi-bolt shear connector layout form, space between rows of bolts, and reinforced concrete slab strengthening measure on the behavior of multi-bolt shear connectors. The average ultimate shear strength per bolt was reduced by 11.4 % and 13.3 % for specimens with two and three rows of connectors, respectively, compared to specimens with one row of connectors. Atari et al. [38] created three push-out tests using deconstructable tensioned bolted shear connectors with varying bolt diameters. The results indicate that specimens with post-installed bolts in clearance holes behave differently than specimens with stud shear connectors in slabs cast in situ. The bolted connectors provide dependable shear connections to composite beams and connections of precast concrete slabs.

The behavior of the shear connectors is mainly relevant to the design for the relationship between the shear force transmitted and the degree of slip at the interface of the steel and concrete [39].

A shear connector between the steel and concrete surfaces prevents slip and separation between steel and concrete. In this case, the composite beam is known as (complete interaction) if no shear connecter prevents slip and separation. In this case, both steel and concrete work separately. This composite beam is known as (no or free interaction). In contrast, the composite beams between the two cases are known as partial interaction. It partially prevents slip or separation. Figure 1.6 shows no connection and full beam connection.

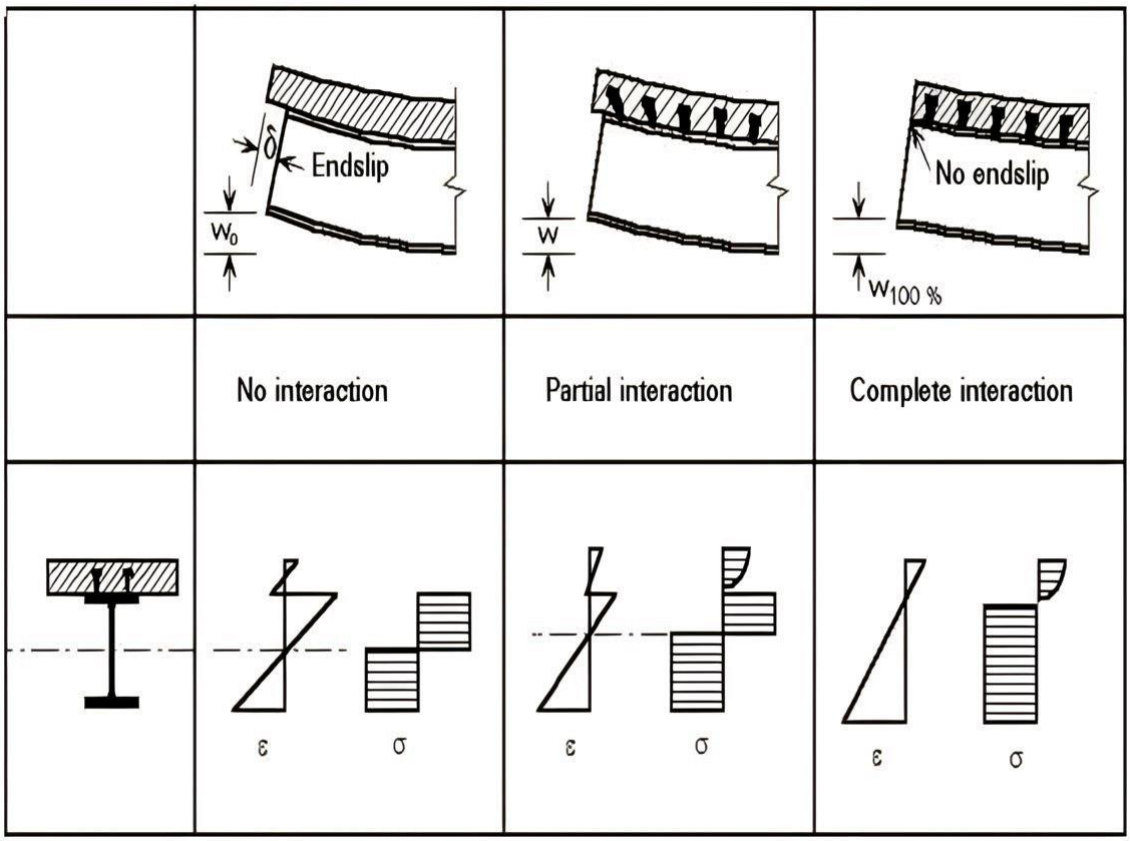

Figure 1.6: Composite Steel Beam-Concrete Slab Interaction [40].

In this study, different degrees of connection action and different shapes of the shear connector to study the effect of shear conductors on semi-rigid joints and their role in improving the performance of those joints are adopted.

1.5 RESEARCH SIGNIFICANCE

The purpose of this study is to propose and develop a experimental model regarding semi-rigid connections between composite beam and column with cold-formed steel sections that predict the moment rotation characteristics by determining three shapes of connections between beam and column and then developing these connections under static load by extending the experimental study using the Abaqus program. Also, exploiting the connection between the beam and the column in a simple and uncomplicated way to make hollow sections of the beam or column where it can be useful structurally in addition to the service benefit.

1.6 RESEARCH OBJECTIVES

The main objective of the present work is to study, experimentally and numerically, the overall behavior for limited failure modes and load carrying capacity of semi-rigid connections between composite beam-to-column with cold-formed steel sections with different shapes of connection, degree of connection, type of load, and different shapes of shear connection. The main objectives of this study can be summarized as follows:

1. Carrying out experimental tests on thirteen composite connections between cold-formed steel sections of beam and column with a different geometry. This is to study the effect of the composite sections of the beams and columns on the joints behavior.
2. Investigating the configuration effect of the composite connection between the cold-formed steel beam and column on the joint performance.
3. Studying the effect of the shear connection type and the degree of connection on the semi-rigid joint.

4. Studying the behavior of cold-formed steel sections with semi-rigid connections under cyclic load.
5. Model suggestion by the finite element method to simulate the nonlinear behavior of semi-rigid connection failure by using the ABAQUS Standard/Explicit 2017 computer program.
6. A parametric study of some variables such as using stiffener in column web at the level of seat angle, column shape, number of bolts, connection angle thickness, and reinforcing ratio. This parametric study is suggested to develop the performance of composite beam-to-column joints.

1.7 OUTLINE OF THESIS

This thesis consists of six chapters as follows:

Chapter One (Introduction) contains a general introduction to cold-formed steel sections, the composite structure of the steel to concrete, semi-rigid connection and shear connector. Then, the study's objectives are presented.

Chapter Two (Literature Review) deals with previous research and experimental and analytical studies dealing with composite and non-composite beam-to-column connections.

Chapter Three (Experimental Work) contains the experimental work, including the manufacturing cold formed steel sections (Cutting, bent and drilling processes), parts assembly, materials properties for normal concrete strength and steel, preparation of the specimens (casting procedure, fresh concrete tests and curing), hardened concrete tests and test specimens.

Chapter Four (Results and Discussion) includes results and discussion of the experimental work.

Chapter Five (Numerical Simulation) presents the finite element (FE) analysis that has been used to analyze the semi-rigid connection between

cold-formed steel beam to column section, results of the numerical analysis, and then comparing the results with the experimental work, and extending the range of the studied parameters in a parametric study (i.e., the thickness of connection angles, stiffener the column web, column shape effect, reinforcing ratio and number of connection bolts).

Chapter Six (Conclusions and Recommendations) gives several conclusions for this study and recommendations (or suggestions) for future studies.

CHAPTER TWO
LITERATURE REVIEW

2.1 INTRODUCTION

Many studies have been conducted over the last three decades using various techniques to improve the behavior of beam-column joints. The current study reviews the majority of the techniques used to improve beam-to-column joint behavior. To the authors' knowledge, no previous work is trying to provide such kind of review. Since the emphasis of this review is on the composite and non-composite joints and their classifications were presented according to many specifications, each kind of joint is reviewed with emphasis placed on the various forms of connections used and their behavior. Based on that, two types of joints are discussed in this review. The first was a non-composite joint, and the second kind of joint was a composite joint.

In this chapter, the previous studies related to the subject will be divided into four parts; the first part includes the connection types and code classification of the beam-to-column connection. In contrast, the second part includes research on the connection of the non-composite beam to the column. In contrast, the third part will include the discussion of composite joints and, finally, previous theoretical research related to the topic and modeling of these joints.

2.2 CODES CLASSIFICATION OF BEAM-TO-COLUMN JOINTS

A beam-to-column connection is typically submissive to axial force, shear force, and bending moment. Nevertheless, the connection deformation

induced by axial and shear forces is typically minor compared to the deformation caused by bending moment. As a result, for practical purposes, it needs to be considered only the influence of the moment on the rotational deformation of the connections offered in Figure 2.1. The moment-rotation curves exemplify the connection's behavior, as shown in Figure 2.2. Modelling connections as semi-rigid is more realistic because actual beam-to-column connections have some rotational stiffness that falls between the two cases of pinned and fully rigid. The assumption of ideally pinned or rigid connections greatly simplifies the design and analysis of framed structures. As a result, it is advantageous and practical to estimate whether the connections can be assumed rigid, semi-rigid, or pinned. To classify connections, the behavior of the frames at the serviceability and ultimate-limit states should be used. The primary index properties that govern the moment-rotation characteristics of connections are stiffness, strength, and rotational capacity. These properties are important factors used in classification.

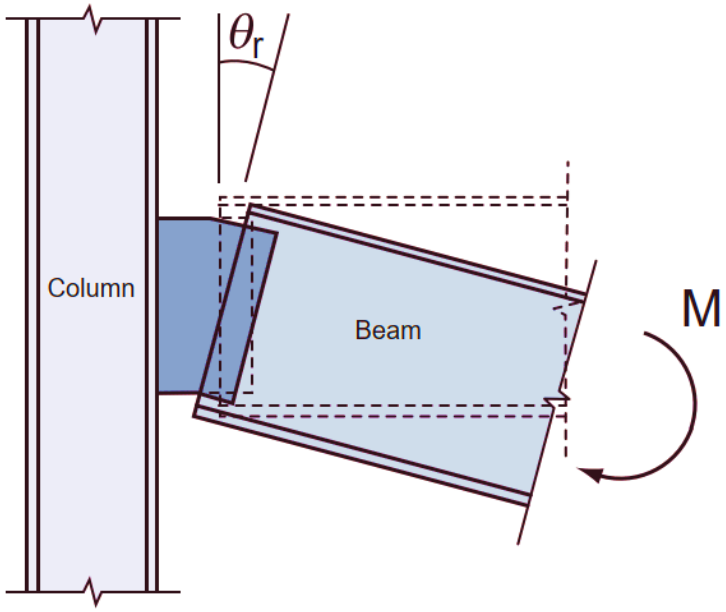

Figure 2.1: Rotational deformation of beam-column connection [41].

There are many systems to classify connections, such as Bjorhovde et al. [42], Goto et al. [43], Nethercot et al. [44], Eurocode 3 (CEN, 2005) [45], and ANSI/AISC360-06 (AISC, 2005) [46]. The current study discusses and focuses on the classification of connections by the Eurocode 3 (CEN, 2005) and AISC, 2005.

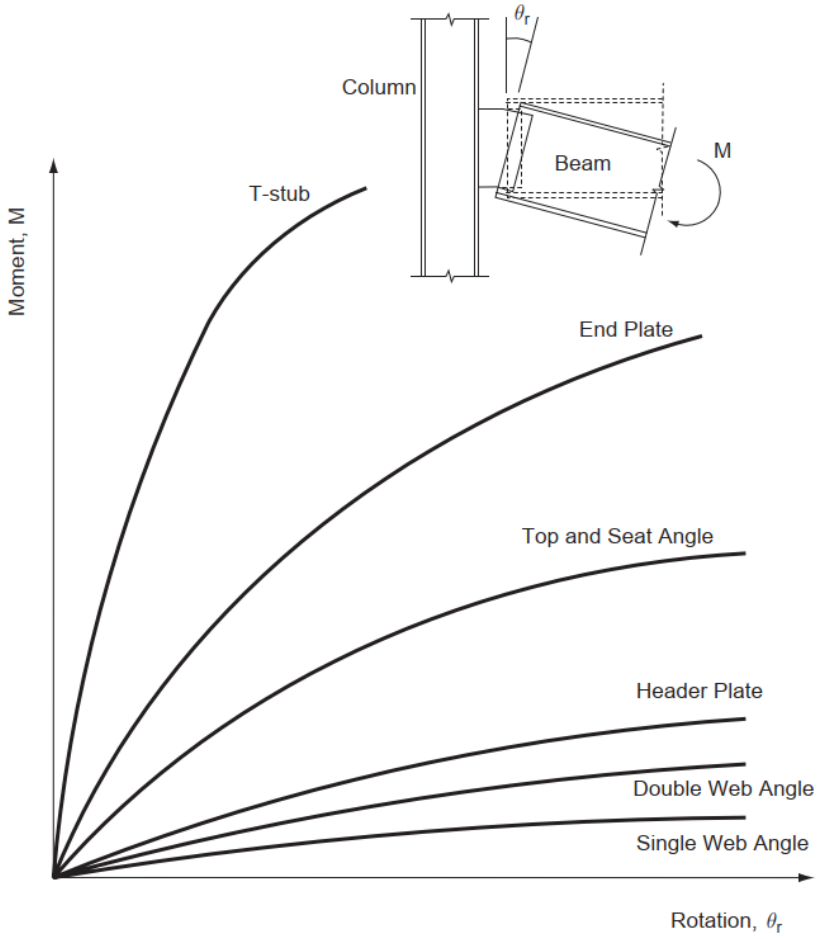

Figure 2.2: Semi-rigid connection moment-rotation curves [41].

2.2.1 Eurocode 3 Classification System (2005)

The connections in Eurocode 3 are classified based on the rotational stiffness and strength into three types of connection models simple, semicontinuous, and continuous in structural analysis. Connections are classified as rigid, semi-rigid, or nominally pinned based on their initial rotational stiffness R_{ki}, as shown in Table 2.1. The boundary among rigid and semi-rigid connections is established so that the load-carrying ability of

a semi-rigid portal frame exceeds 95% of the strength of the corresponding rigid frame. Because the effect of connection stiffness on frame strength varies depending on whether the frame is braced or unbraced, the boundaries for connection classification differ for these two types of frames. These boundaries are defined by a non-dimensional initial connection stiffness parameter kb, which is defined as $k_b = \frac{R_{ki}}{(EI_g/L_b)}$.

The ratio between the design moment resistance of the connections $M_{j,Rd}$ and the design plastic moment resistance of the connected members such as beams $M_{b,pl,Rd}$ and columns $M_{c,pl,Rd}$ determines whether a connection is a full strength, partial strength, or nominally pinned. This classification has different limits depending on whether the connections are at the top or within the height of columns. Table 2.1 summarizes the classification based on connection strength.

Table 2.1: Classification of connections according to stiffness and strength by EC3 [45].

Connection	**According to stiffness**		**According to strength**	
Rigid (full-strength)	Braced frames	$8 < K_b$	Top of column	$1 \leq \left(\frac{M_{j,Rd}}{M_{b,pl,Rd}} \text{ or } \frac{M_{j,Rd}}{M_{c,pl,Rd}}\right)$
	Un braced frames	$25 < K_b *$	Within column height	$1 \leq \left(\frac{M_{j,Rd}}{M_{b,pl,Rd}} \text{ or } \frac{M_{j,Rd}}{2M_{c,pl,Rd}}\right)$
Semi-rigid (partial strength)	Braced frames	$0.5 \leq K_b \leq 8$	Top of column	$0.25 < \left(\frac{M_{j,Rd}}{M_{b,pl,Rd}} \text{ and } \frac{M_{j,Rd}}{M_{c,pl,Rd}}\right) < 1$
	Un braced frames	$25 < K_b$**	Within column height	$0.25 < \left(\frac{M_{j,Rd}}{M_{b,pl,Rd}} \text{ and } \frac{M_{j,Rd}}{2M_{c,pl,Rd}}\right) < 1$
		$0.5 \leq K_b \leq 25$		
pinned	$K_b < 0.5$		Top of column	$\left(\frac{M_{j,Rd}}{M_{b,pl,Rd}} \text{ or } \frac{M_{j,Rd}}{M_{c,pl,Rd}}\right) \leq 0.25$
			Within column height	$\left(\frac{M_{j,Rd}}{M_{b,pl,Rd}} \text{ or } \frac{M_{j,Rd}}{2M_{c,pl,Rd}}\right) \leq 0.25$

$*\ K_b/K_c \geq 0.1$

$**\ K_b/K_c < 0.1$

2.2.2 AISC (2005) classification system

The AISC classification joint as fully restrained (FR), partially restrained (PR), and simple according to the secant stiffness R_{ks} at service load and the strength Mn, as summarized in Table 2.2. This category applies to both sway and non-sway frames. For structural analysis, simple and FR connections can be idealized as pinned and rigid. The semi-rigid connection model must estimate and include the connection flexibility in the structural analysis for structures with PR connections.

The AISC specification includes three types of framing that relate to beam-to-column connections depending on the amount of restraint developed by the connections, such as:

2.2.2.1 Fully restrained connections

Connections of type FR (fully restrained) are commonly referred to as "rigid-frame" connections, which transfer at least 90% of the moment from beam to column. They also retain a constant angle between the beam and the column during loading of the structure (i.e., zero rotation).

2.2.2.2 Partially restrained connections

The stiffness of partially restrained connections is insufficient to maintain the angle between the intersecting members. The AISC subdivided partially restrained connections into Flexible Moment Connections and Simple Shear Connections based on the available stiffness of the connection.

Semi-rigid connections are another name for flexible moment connections, which transfer 20% to 90% of the moment from beam to column. The connection is partially restrained, and there is some rotational capacity. The AISC LRFD steel construction manual recommends that the strength, stiffness, and ductility characteristics of the connections be used

in the analysis and design of steel structures using Flexible Moment Connections.

2.2.2.3 Simple framing connections

Simple framing connections (also called unrestrained connections or free-ended) transmit less than 20% of the moment between the intersecting members. Connection restraint is completely ignored in these types of connections, and the end of the beam is free to rotate. There is only shear force transfer in this type of connection from beam to column. When the authentic angle between intersecting members can change by equal to or more than 80% of what it would theoretically change if frictionless hinged connections could be used, simple framing is assumed to exist. Figure 2.3 depicts the moment-rotation characteristics of the AISC LRFD connection types.

Table 2.2: AISC classification of connections [46].

Connections		Stiffness	Strength	Ductility
Simple		$R_{ks}L_b/EI_b \leq 2$	• Satisfy shear force demand at strength-limit state • $M \leq 0.02\ M_{pb}$ at 0.02 radians	• Satisfies rotation demand at the strength-limit state or • $\theta_u = 0.03$ radians
PR		$2 < R_{ks}L_b/EI_b < 20$	• Satisfy combined shear force and moment demand at strength-limit state	• Satisfies rotation demand at the strength-limit state or • $\theta_u = 0.03$ radians
FR	With partial-strength of connected beam	$20 \leq R_{ks}L_b/EI_b$	• Satisfy combined shear force and moment demand at strength-limit state	• Satisfies rotation demand at the strength-limit state or • $\theta_u = 0.03$ radians
	With full-strength of connected beam			• No requirement

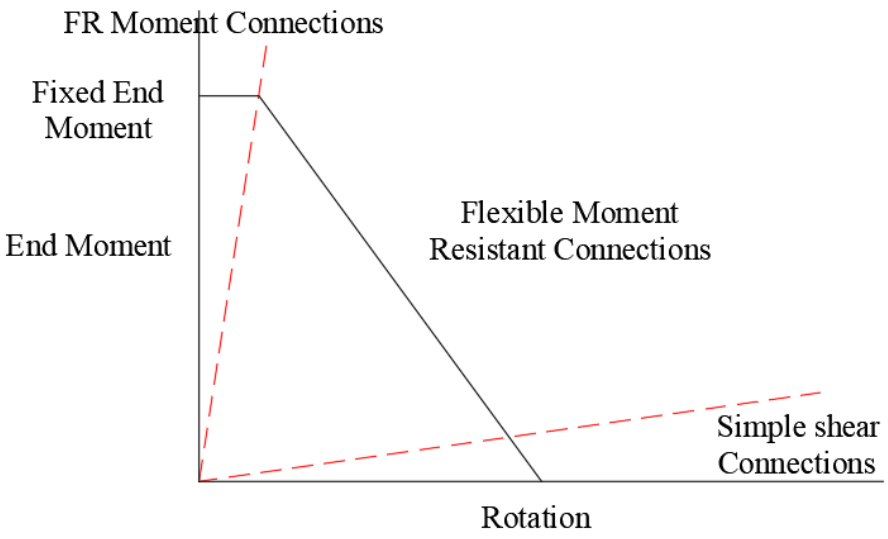

Figure 2.3: Characteristics of Moment-Rotation of AISC LRFD connection types. (Anonymous.[47]).

2.3 TYPES OF BEAM-TO-COUMN CONNECTION

Beam-to-column connections are critical in steel structures because they influence the structure's performance under load. Connections that fasten beams to columns with angles, plates, welds, and bolts act as a medium for transferring forces between members. All of these connections limit the rotation of the member ends that are connected together. Beam-to-column connections can be classified as simple, rigid, or semi-rigid depending on the extent of restraint provided (Vinnakota, 2006) [48].

2.3.1 Simple Connection

Simple connections are those that have no rotational restraint at the connections. Bending moment diagrams for a given beam supporting a uniformly distributed load are shown in Figure 2.4 for simple end connections.

Simple connections are only intended to transfer shear and normal force. Assuming no bending moment exists at the connection. The connections are flexible and pinned. The beam ends are allowed to rotate downward substantially under load. The rotation capacity should be large

enough to accommodate the rotation of the beam to which it is attached. A simple connection is depicted in Figure 2.5.

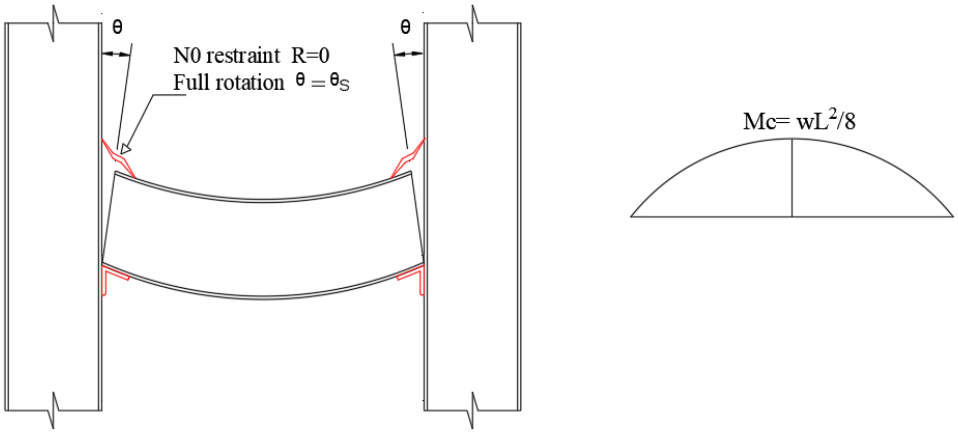

Figure 2.4: Bending moment diagrams of simple end connections for beams supporting a uniformly distributed load. (Vinnakota, 2006) [48].

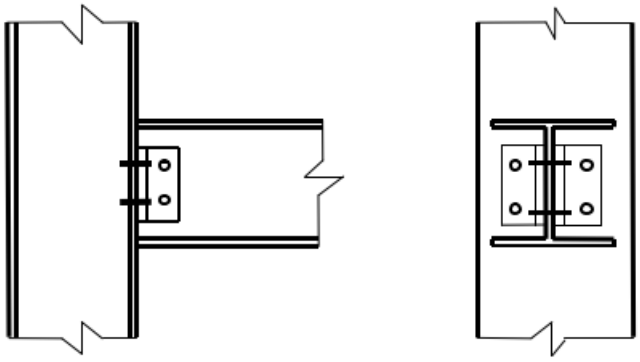

Figure 2.5: Example of a simple connection [48].

2.3.2 Rigid Connections

Rigid connections have enough rigidity to keep the original angle between intersecting members virtually unchanged under load. Figure 2.6 depicts the bending moment diagrams for rigid end connections for a beam supporting a uniformly distributed load.

Rigid connections are moment-resisting connections that can transmit both moments and end reactions to the subjected member. In theory, there is no relative rotation of the members who meet at the joint. This connection is assumed to be rigid or restrained enough to maintain the original angles between the members under load. Rigid connections have

high stiffness, and the members retain their original relationship throughout the loading history. A rigid connection is depicted in Figure 2.7.

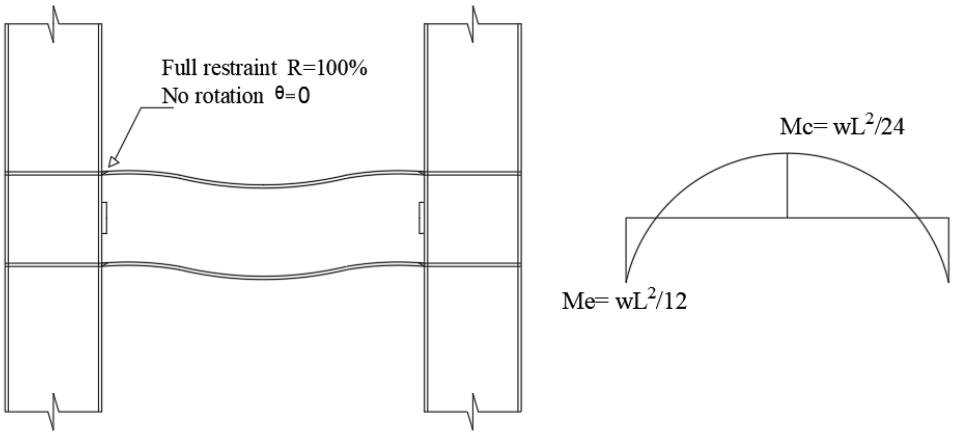

Figure 2.6: Bending moment diagrams for rigid end connections for a beam supporting a uniformly distributed load. (Vinnakota, 2006) [48].

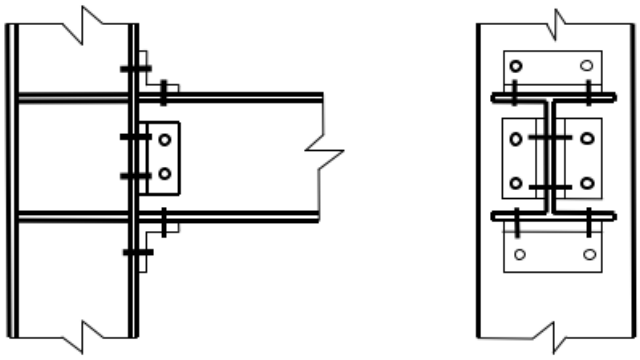

Figure 2.7: Example of rigid connection [48].

2.3.3 Semi-Rigid Connections

Semi-rigid connections have a predictable and known moment capacity that falls somewhere between the rigidity of rigid connections and the flexibility of simple shear connections. Figure 2.8 depicts the bending moment diagrams for a given beam with a uniformly distributed end connection. Semi-rigid connections are intended to withstand shear and moments with values that fall between those of simple and fully rigid connections.

Semi-rigid connections, like rigid connections, are capable of transferring moments and end reactions (shear and normal force). However, the ability of joints to transfer moments is less than that of rigid

connections. Aside from that, the member end joints can rotate, but only to a limited extent. Connection rotation has a lower value than simple connections. Figure 2.9 depicts a semi-rigid connection.

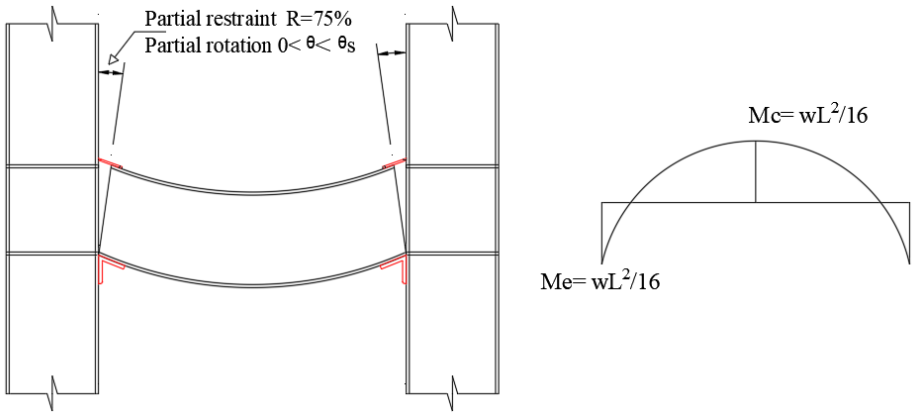

Figure 2.8: Bending moment diagrams for semi-rigid end connections for a beam supporting a uniformly distributed load. (Vinnakota, 2006) [48].

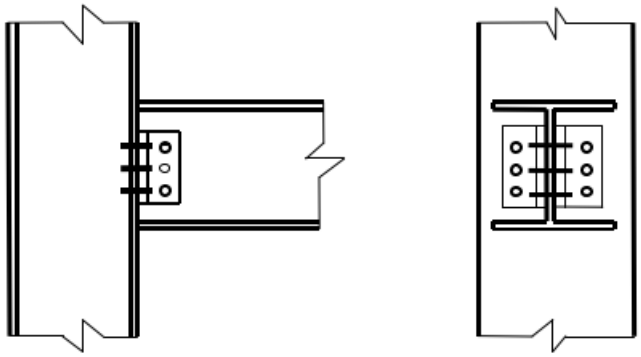

Figure 2.9: Example of semi-rigid connection [48].

2.4 STEEL BEAM-TO-COLUMN CONNECTIONS

The beam-to-column connections of steel structures are one of the significant determinants of the economy in structural steel work. So, in this section, we will conduct extensive research to obtain simple joint configurations with low manufacturing costs and ease of design.

2.4.1 Connection by angles and bolts

This type of connection is used in research to investigate the effect and behavior of beam-to-column joints. **Ghindea et al.** [49] and **Hazlan et al.** [50] studied the experimental investigation of the beam to column

connections by using angles to investigate the effect of web angle and stiffening angle in top-and-seat. The **Ghindea** [49] concluded that the configuration of web angles is less effective than stiffened top-and-seat angle cleats. The use of stiffened top-and-seat angle cleats increases the moment by 86.25%, while the increase at the moment is 64.8% when using web angle compared with a specimen that has an angle at top and seat angles and with a small difference in rotation value for all specimens. While **Hazlan et al.** [50] found the ductility is more influenced by changing the type of connection. On the other hand, the ultimate moment appears to increase as the beam's depth increases, which is expected to increase as the number of bolts in connections increases.

The shear resisting connections among cold-formed steel sections studied by **Chung** and **Lawson** [51] found both safe and structurally efficient. The rationalized use of cold-formed steel web cleats enables the formation of simple and effective connections between cold-formed steel sections, resulting in improved buildability.

Uang et al. [52] studied the beam to column connection by angles under cyclic testing, which found that the bolt's inelastic action through bearing and slippage is ductile and desirable as always occurs first, but buckling may also occur either in the beam or column. To avoid and control the local buckling in the beam and column, it appears prudent to use the w/t ratio (depth to thickness ratio for the beam and width to thickness ratio for the column) to 150 and 40, which corresponds to 6.18 $\sqrt{(E/fy)}$ and 1.58 $\sqrt{(E/fy)}$, respectively.

2.4.2 Connection by gusset plate

Wong and **Chung** [53] studied the connections between cold-formed steel sections, such as column base connections and beam-to-column joints,

experimentally by using bolted moment connections. Both exterior and interior beam-to-column connections are prepared by using a gusset plate, which has a cross-shaped for the inner joints and a T-shape for the outer joints with and without chamfers and different thicknesses. The moment resistances of these connections were found to be between 50 and 85 per cent of the connected sections' moment capacities. Based on the experimental results, it is demonstrated that bolted moment connections between cold-formed steel sections are easily achieved using the proposed connection configurations. Bolted moment connections are demonstrated to effectively transmit moment between connected sections, allowing for effective moment framing in cold-formed steel structures. Also, **Bučmys** [54] prepared a numerical model and calibrated with the experimental results of **Wong and Chung** [53] to scrutinize the influence of thickness and shape of gusset plate on all connections stiffness. The results showed that increasing the thickness of the gusset plate led to a decrease in the rotation of connection. The effect of gusset plate shape and thickness is shown in Figure 2.10 which the Chamfers shape for gusset plate shows an obvious effect on connection stiffness.

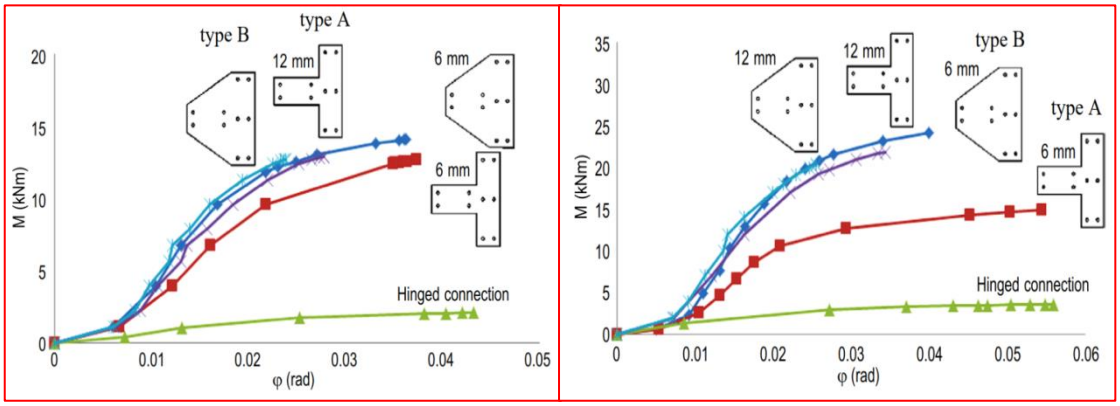

(a) C150x40x1.5 section **(b)** C150x40x2.5 section

Figure 2.10: The results of moment-rotation curves for the specimens [54].

Aminuddin et al. [55] investigated the cold-formed steel beam-to-column connections by setting up a T-joint connected by a rectangular gusset plate. The capacity of connections in this study is calculated in two ways: theoretically using Eurocode 3 BS EN 1993-1-8:2005 and experimentally using test results. The moment versus rotation of the connection developed from the experimental test results demonstrated that the connection is very ductile and can be classified as a pin connection. When the theoretical and experimental test results for moment capacity are compared, the ratio is 0.69, and the ratio for joint stiffness is 0.24. The gusset plate did not significantly stiffen the connection.

Siang et al. [56] studied the cold-formed steel beam-to-column connections connected by a gusset plate with a 6mm thickness. Three full scale isolated joints were prepared with three beam depths: 150, 200, and 250 mm. The experimental results show that the increased depth of the beam gives an increase in the moment resistance and decreases the joint rotation. The joint rotational capacities exceed 30 mrad. Rotational stiffness ranges from 511 kN.m/rad to 1671 kN.m/rad. It is indicated that the proposed connections are partial-strength connections. Also, when comparing the connections in this research with those by **Hazlan et al.** [50], as they have almost the same details for the samples, the only difference is in the type of connection between beam and column. We note that using the gusset plate gave a greater increase in the moment resistance and rotation of the joint than all other types of connection by **Hazlan et al.** [50] and for all depths of the beam.

Several studies related to the steel beam-to-column joints are summarized in Table 2.3, where they present the parameters investigated, the main results, and the main conclusion of each study.

Table 2.3: Existing non-composite steel beam-to-column plate joint tests.

Reference	Connection by	Parameters investigated	Results and observations	Conclusion
Tan, S. H. et al. [57]	Angles	- Member thickness (0.5, 0.8 and 1 mm). - Connector thickness (4.8,5.5,7.5 and 8.4 mm).	All connections tested had nonlinear behavior, and three failure modes were observed beam failure, connection failure and blend failure of beam and connection.	The stiffness increases with an increase in the thickness of the connection because of excess in the connection flexural rigidity.
El-Abidi, K. M. A., and Zacoeb [58]	Angles	location of angle connection: - Double web angles with 3-bolt. - Double web angles with 6-bolt. - Top-seat angles.	The comparisons of Mu/Mn of connections range from 37% to 78%, indicating that the connections can be classified as semi-rigid.	The specimen with top-seat angle gives the largest moment due to it has the longest moment arm.
El-Abidi, K. M. A., & Suswanto, B. [59]	Angles	Study the effect of the same parameters investigated in [58] on connection stiffness with two different yield strengths of the beam.	When reducing yield strength of beam notes, the failure mode change from buckling of angle or buckling of column flange into tension failure of bolts.	The use top-seat angle connection gives the highest stiffness from the other connections due to its high initial strength.
Huang, Y., & Young, B. [60]	Endplate	- Cross-section geometry. - Specimen length. - Loading eccentricities.	- Local buckling, flexural buckling, and both local and flexural buckling were observed as failure modes. - The test strengths were compared with other available data by various codes.	These specifications can predict the beam-column strengths of lean duplex stainless steel test specimens, and the design rules in the specifications are thought to be reliable.

Table 2.3: Continued.

Reference	Connection by	Parameters investigated	Results and observations	Conclusion
Torabian, S. et al. [61]	Endplate	- Different lengths for beams and columns. - Loading condition (combined biaxial moments and axial force).	The experimental results show that the failure modes are strongly influenced by the combined actions' stress distribution applied to the cross-section.	It was discovered that member ductility is highly related to the degree of eccentricity in the axial load, with minor-axis eccentricities producing the most ductile results overall.
Bajoria, K. M., & Talikoti, R. S. [62]	Two vertical channel sections	Study single and double cantilever beam-to-column connection.	The failure was caused by excessive axial pull opening up the column flanges during the test.	The double cantilever test was further better than the traditional single cantilever test.
Prabha, P et al. [63]	Beam end connection	- Column thickness. - Depth of the connector. - Depth of beam.	- Increased the capacity by (19-36) % for 4 and 5 lip connectors, respectively, when increasing the thickness of the column from 1.8 to 2.5 mm. - The tabs cutting into the column web caused the ultimate joint failure.	- The stiffness and strength of the beam end connector increase as the number of tabs increases. - The strength and stiffness of the joint were improved by increasing the depth of the beam and the thickness of the column.

2.5 COMPOSITE CONNECTIONS OF BEAM TO COLUMN

It has recently been demonstrated that composite beam-to-column connections are important in both economic and structural terms due to their significance to all constructions in reducing connection costs and improving connection performance.

Xiao et al. [64] described their investigation into the interaction of various steel beam-to-column details with a composite metal deck floor. The main focus is on determining the moment capacity, rotational stiffness, and rotation capacity of the connections. Twenty specimens were prepared experimentally with a wide range of variables to investigate these properties under the influence of the composite action. The test specimens were configured as "cruciform" types and "cantilever" types with four different types of steel joints: seating cleats with double web cleats, flush endplates, partial depth endplates, and tinplate.

Changes in the reinforcement ratio in the slab, metal decking, steel joint type, column web stiffening, and moment shear ratio all had an effect on the initial stiffness, moment resistance, and rotational capacity, according to the findings. The position of the partial depth endplate can also affect the strength and stiffness of the connection. The endplate should be placed at the level of the lower flange in composite beam-column connection designs.

2.5.1 Composite beam-to-column connections by using end plates

End plate connections are widely used and come in two varieties: extended end plate and flush end plate. A flush end plate connection is less rigid and has a lower moment capacity than an extended end plate connection. An extended end plate connection should be used for a rigid joint, whereas a flush end plate connection can be used for a semi-rigid joint.

Fu and Lam [65] studied experimentally the semi-rigid beam-to-column connection with composite steel beams and hollow core slab where prepared eight full scale specimens with cruciform arrangement. The main variables investigated in this study are stud spacing, spacing of first shear connector from face of column, shear connector degree, cross section area of longitudinal bar and slab thickness. From the result notice the close spacing between first stud and column face will impact the crack pattern, necessitating a high degree of longitudinal reinforcement elongation to obtain the same rotation capacity with the same joint with greater stud spacing between the column flange and the first stud. While the studs spacing for specimens with same degree of connections dose has little effect on the moment capacity and rotation capacity of connection. Two failure mode observed from the joint test: fracture of the longitudinal bar when use full shear connector due to this connection enable full mobilization of the longitudinal reinforcement or fracture of the headed studs when use partial shear connector.

According to these findings, a full shear connection should be used to allow full mobilization of the longitudinal reinforcement, whereas a partial shear connection would result in reduced moment and rotation capacity because the longitudinal bars could not be fully mobilized. It also shows that the location of the headed studs had a significant impact on the rotation capacity of the composite connections.

Loh et al. [66] studied experimentally the influence of partial shear connection in composite flush end plate joints, which prepared six specimens for this purpose, designed with different numbers of shear connections and different reinforcement ratios. The joints were created to use a new connection method that involved blind bolting (see Figure 2.11-a) steel beams to hollow columns filled with concrete. When the partial

shear connection is used, the benefits of increased ductility without sacrificing stiffness and strength are clearly highlighted. This is very useful for plastic design in both continuous and semicontinuous composite structures. As a result, the proposal to provide a partial shear connection system within the hogging moment regions should be incorporated into existing design standards.

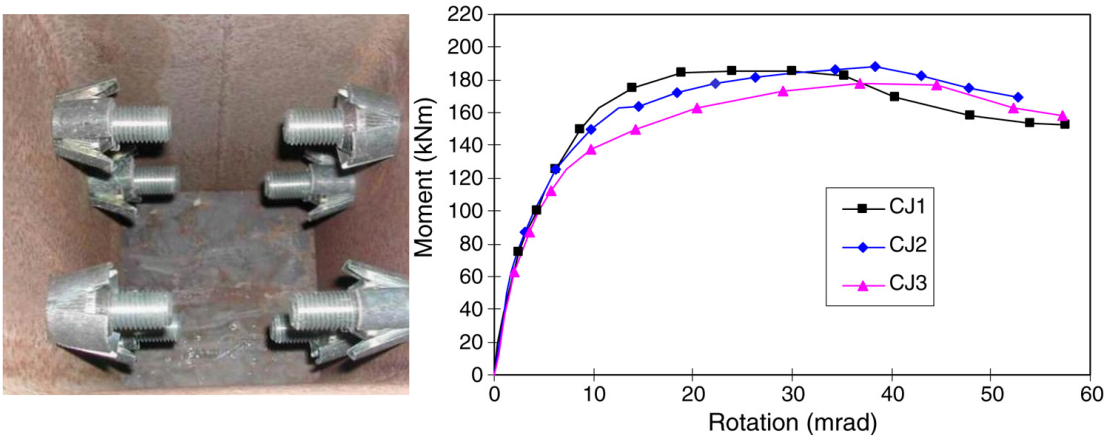

(a) **(b)**

Figure 2.11: (a) Hollo-Bolts secured to the hollow section and (b) Moment-rotation curves for specimens with different shear connection degrees [66].

The results show that as reduced the level of shear connection, attained the maximum moment at a higher rotational value. Also, Higher levels of reinforcement may allow for higher moment and rotation capacities, but only up to a certain point. According to the test results, the favourable percentage of reinforcement appears to be between 1.0 and 1.5 per cent of the effective slab area.

Using the finite element program ABAQUS, **Fu et al.** [67] studied a composite connection for eight full-scale specimens with a flush end-plate and precast hollowcore slab conducted by **Fu** [65]. Also, a parametric analysis of the impact of flange thickness was done to investigate the connection's moment resistance and rotation capacity. From the modeling

results, the bottom flange thickness of the steel beam must be enough to prevent buckling of the bottom flange to realize the high moment capacity and rotation capacity. This is because the transmission of the compression force through the connection relies on the direct bearing of the bottom flange of the beam at the ultimate limit condition. The compression side of the joint must not be the weak part to mobilize the rebars' strength. This necessitates that the steel section's bottom flange has a sufficient area and that its slenderness is sufficiently low to prevent local buckling in high plastic deformation.

Four full-scale specimens are prepared to investigate the influence of bolted shear connector type, degree of shear connection and type of precast concrete slab on the structural behavior of deconstructable composite joints. **Ataei et al.** [68] studied the composite semi-rigid joints using flush end plate steel beam and cold formed steel tubular column connected by blind bolts. The test findings reveal that these innovative composite joints have believable rotation and moment capabilities by the recommendations of EC3 and EC4 and that these types of connection can provide a higher rotation capacity, about 1.7 to 3.13 times when compared with the EC4 provisions of 30 mrad., and fracture of the joints occurs after significant rotation development. Reduced shear connections leads to a reduction in the initial capacity of a composite joint, which can increase the deflection of the composite beams under service-load conditions. Furthermore, small bolted shear connectors give small slips at different load levels.

Ataei et al. [69] presented the findings of three full-scale sustainable flush end plate semi-rigid beam-to-column connections and three push-out tests using deconstructable tensioned bolted shear connectors, which are required to demonstrate the shear connection's strength to design the joints. This novel connecting technique is designed to avoid the high-carbon

consequences of demolishing traditional steel-concrete composite frame systems. The push-out tests show that specimens with post-installed bolts in clearance holes behave very differently than members with stud shear connectors in slabs cast in situ. The bolted connectors supply a reliable and sufficient shear connection to composite beams and joints with precast concrete slabs. The test findings demonstrate that these composite joints have a believable rotation and moment capabilities within the EC3 and EC4 guidelines and that joint breakage occurs after significant rotational deformations.

Wang et al. [70] explored the structural behavior of demountable beam-to-column composite bolted joints that can be dismantled at the end of their service life. Four full-scale cruciform joints were tested experimentally and numerically to investigate the static and hysteretic behavior and structural performance, including the initial stiffness, moment capacity and rotational capacity of the demountable composite joints. The numerical models' correctness is verified using the relevant experimental results. After that, a parametric analysis is performed to see how the end-plate thickness, column width-to-thickness ratio, bolt diameter, and the number of bolts affected the moment-rotation response. When compared to specimens constructed with straight reinforcing bars, it is discovered that specimens created with bent reinforcing bars function satisfactorily and have a greater degree of hogging moment resistance. The specified joints are easily disassembled, and all steel components retain their elasticity when loaded up to 40% of their maximum capacity, similar to ordinary service load. The thickness of the end-plate, width-to-thickness ratio of the column, bolt diameter and number of bolts impose a significant effect on the performance of the bolted joints where we note that the failure mode is due to fracture of bolt washer or buckling of the end plate. This means that

the thickness of the plate and the distance between the bolts is insufficient as shown in Figure 2.12. Also found two bolt- rows in tension can improve the moment-rotation response for the joints with extended end-plates.

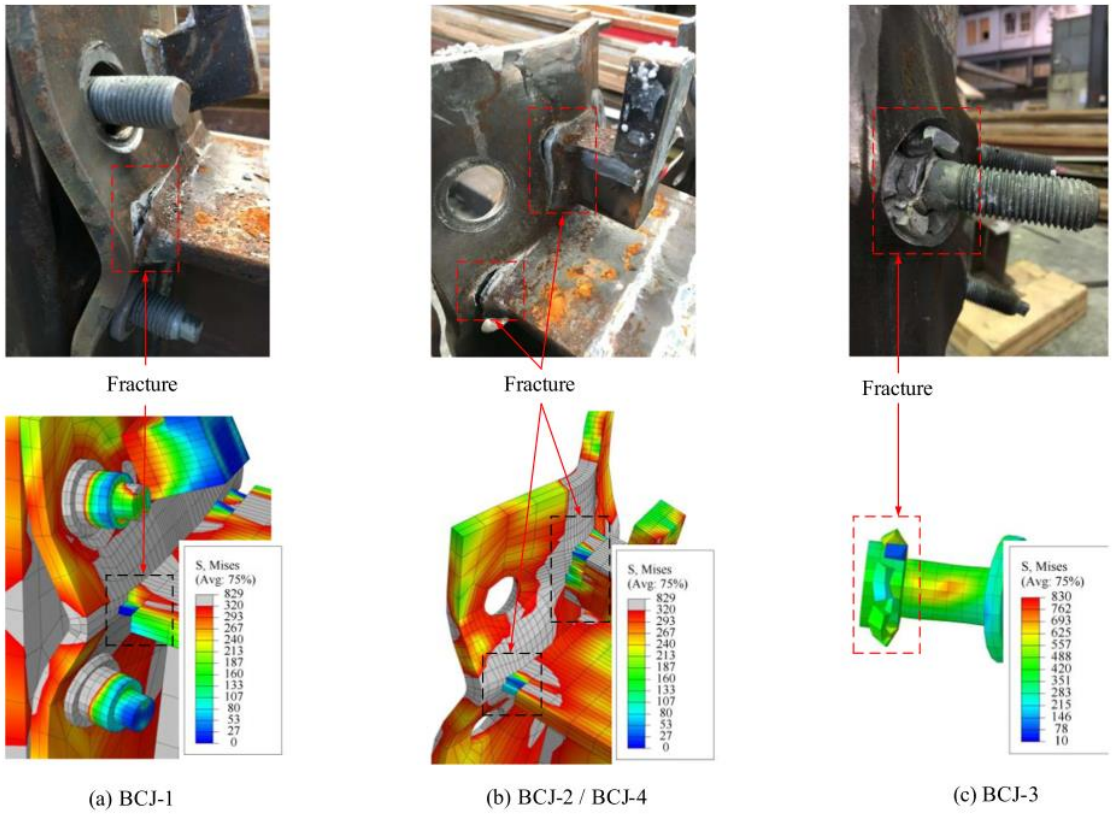

Figure 2.12: Show the failure mode of tested specimens [70].

2.5.2 Angled or gusset plate connections between composite beams and columns

Mairal and **Malite** [71] prepared two specimens to study the behaviour of the beam to column connection, using HP hot-rolled steel column and a composite double U lipped channel cold-formed steel beam, and using web and seat angles for connection in specimen one and a beam directly welded to the column in specimen two.

Model 1's moment-rotation curve showed a rapid change in stiffness following the start of the cracking process in the concrete slab, which differed from model 2's behavior. Model 1's rotation capacity was almost six times more than model 2, indicating greater ductility of this form of

connection as compared to the stiff connection (model 2). Through observation of the results of this research, the amount of rotation corresponding to the greatest moment for the first and second samples is equal to about 23 mrad. and 4 mrad., respectively, which is less than 30 mrad that is recommended by EC4 [72].

Firdaus et al. [73] examined the effect of seat angle on the composite connection consisting of a concrete slab 100 mm thick and cold-formed steel with a double lipped channel section used for beam and column, which are connected from one end by a hot-rolled steel gusset plate which has a haunched shape. Two specimens with and without seat angle are prepared for this study and used stiffener angle on the column web to reduce the weakness of the thin plate behavior in the compression zone.

Although the angle stiffener is used to reinforce the column flange, local buckling is discovered. This might be due to the rotational of the connection, which causes the beam flange to be longer in line with the angle stiffener. According to the testing results, using a seat angle as reinforcement improved the moment resistance and stiffness by up to 1.06 and 1.19, respectively.

Firdaus et al. [74] studied the behavior of the composite structure with a gusset plate connection and investigated the failure mode, strength and stiffness of this connection. This connection is made in the form of cantilever beams whose floor plates employ concrete cast with metal decking. The column and beam are made from cold-formed steel with a 2.4mm thickness and have a double-lipped channel shape. The failure modes observed in this study are torsional at the end of the beam. This is attributed to the thinness of the web. Also, at the maximum rotation of the connection, the lower part of the beam flange is pushed against the column flange.

Furthermore, due to height compression, local buckling is found at the column flange. However, no failure mode occurred on gusset plates. This failure mode indicates that the sliding bolt resistance and support affect joint resistance. Also, prepared an analytical study based on the failure mode and result of the experimental test. The analytical calculations were compared with the practical results and showed a good convergence of 1.41.

It is critical to investigate the failure mode of composite beam-column connections. The effect of joint flexibility on frame response under monotonic loading was investigated by Simoes Da Silva et al. [75], Li et al. [76], and Liew et al. [77]. Shi et al. [78], Popov and Takhirov [79], and Takhirov and Popov [80] investigated the influences on the connection moment capacity, rotational stiffness, rotation capacity, and hysteretic curves using full-scale structural steel beam-to-column end-plate moment connection experiments under earthquake loading.

Despite previous research on the development of composite connection robustness by Loh et al. [66,81] and Wang et al. [82], it is still necessary to investigate the performance characteristics of these new and innovative composite connections when subjected to severe earthquake loads. Several studies related to the composite steel beam-to-column joints are summarized in Table 2.4, where they present the parameters investigated, the main results, and the main conclusion of each study.

Table 2.4: Existing composite steel beam-to-column plate joint tests.

Reference	Connection by	Parameters investigated	Results and observations	Conclusion
Mirza, O., and Uy, B. [83]	End plate	- Three experimental specimens were tested under monolithic and cyclic loading. - Several parametric studies by Abaqus: slab depth, stud spacing, reinforcing spacing, stud distance from column face, and effect of axial loading	- The increased slab thickness will reduce concrete cracking. - The parametric study revealed that the axial load aided the beam-column connection and influenced energy dissipation. The optimal axial load value is 0.4 Pu.	- Stud spacing should be between 150 and 300 mm. If it exceeds 300 mm, it will result in stud fracture. - The stud should be placed between 200 and 350 mm from the column face. Designers must increase the amount of reinforcement around its columns if the stud is placed more than 350 mm from the column face to avoid serious cracking.
Faridmehr, I. et al. [84]	End plate	- Number and diameter of the bolt. - End-plate thickness. - Columns and beams size.	Three failure modes were observed: end-plate deformation, column flange deformation, and column web crushing. Through the test, there was no vertical slip between the column and end-plate because of the tightness of the bolts during installation.	Both experimental and analytical methods revealed that the thickness of the column flange and end-plate, among other geometric parameters of the end-plate flush beam to column connections, significantly affects the initial rotational stiffness.
Guo, L. et al. [85]	End plate	Investigate the effect: - Fracture strain and diameter of the bolt. - Welding a triangle haunch reinforced beneath the beam. - Welding an angle-steel reinforcement beneath the beam	Angle steel reinforcement is an effective method of increasing the progressive resistance of a semi-rigid composite frame. It has no effect on the distribution of forces under service load because it does not change the initial rigidity of the connection.	- The progressive resistance of a semi-rigid composite frame can be improved by increasing the diameter of the bolts or the fracture strain of the bolts. - The use of haunch reinforcement is recommended in the design of steel rigid connections to prevent progressive collapse.

Table 2.4: Continued.

Reference	Connection by	Parameters investigated	Results and observations	Conclusion
Odrobiňák, J. et al. [86]	End plate	Study the effect of reinforcement and thickness of slab on the stiffness of composite joints with different beam depths.	Increases in reinforcement ratio from 0.2 to 0.5 per cent can result in (45-51) % greater initial stiffness of the composite joint.	The initial stiffness increases gradually with increasing the depth of the beam, as well as the proportion of reinforcement.
Firdaus, M. et al. [87]	angles	studied the influence of the seat angle on the behavior of the composite connections.	It was discovered that by adding a seat angle, the behavior of these types of joints tends to transform from partial strength to full strength.	Adding seat angles to the CFS-concrete composite joints increases moment resistance and rotational stiffness (by 8% and 21%, respectively) while decreasing rotation capacity (by 17%).
Kishi, N., & Chen, W. F. [88]	angles	Study the semi-rigid steel beam-to-column connection using single and double web angles and top-and-seat angles without or with web angles.	Analytical methods determine the initial connection stiffness and ultimate moment capacity of semi-rigid connections with angles. They are two of three parameters in the power model that was chosen.	The power model is easy to implement in a second-order frame analysis and provides a realistic representation of the actual moment-rotation behavior of each connection type with angles. This advancement allows for a more effective computer-based method for type PR construction.
Kong, Z., & Kim, S. E. [89]	angles	Create more precise models to predict the moment-rotation behavior of top-seat angle connections with double web angles (TSACW).	According to the results, the equation coincides well with different test data and is more accurate than Kishi and Chen [88] and Eurocode 3' models. As a result, the proposed equations can be used in analysis and design to predict the moment-rotation behavior of TSACW.	Improved formula of the initial stiffness, ultimate moment capacity and the moment-rotation relation are proposed

Table 2.4: Continued.

Reference	Connection by	Parameters investigated	Results and observations	Conclusion
Park, H. G. et al. [90]	Bearing plate	study the seismic behavior of composite steel beam (have two depths 450 and 550mm) with U-shaped filled with concrete and RC column.	The tests revealed that the specimens had good strength, deformation, and energy dissipation capacities. The deformation capacity was greater than 4% of the inter-story drift ratio. Buckling and fracture of the steel plate in the beam were the primary failure modes of the specimens.	The composite beams exhibited good rotation capacities at the plastic hinge zones of the beam. The maximum rotations were 32.1 and 37.7 mrad for the positive moment, while for the negative moment, the maximum rotations were 41.5 and 42.3 mrad for specimens with beam depths of 450 and 550 mm, respectively.
Xu, X. et al. [91]	Double C chanels	studied the filled concrete of the beam and column under combined constant axial compression and cyclic loading with different connection details.	The specimens' primary failure mode was local buckling of the webs and fracture of the bottom flanges of the beam near the column tube.	Passing rebars through the joint core improves load carrying and energy dissipation capacities.
Chen, W. F., & Kishi, N. [92]	Different connection types	Developing and modelling a database on semi-rigid steel beam-to-column connections using different connection types.	The SCDB program is simple and effective for performing second-order nonlinear analysis on a frame with semi-rigid connections.	The moment-rotation characteristics of each connection type are made available in the SCDB program via the tabulation and plotting system, and the appropriate connection models are also provided.

2.6 MODELLING OF BEAM-TO-COLUMN JOINT BY FINITE ELEMENT METHODS

Non-linear finite element modelling is a useful tool for simulating connections. Finite element modelling could be used to investigate many variables and potential failure modes, supplementing experimental studies. Krishnamurthy [93,94] is a pioneer in 3-D modelling of connections in the history of Finite element modelling studies of steel beam to column connections, using eight-node sub-parametric bricks to reproduce the behavior of bolted end plate connections.

Bursi et al. [95] proposed a 3-D finite element model for isolated bolted end plate connections based on ABAQUS [96] solid and contact elements, and they discussed fundamental issues such as constitutive relationships, step size, number of integration points, kinematic descriptions, element types, and discretizations for endplate connection modeling. **Choi et al.** [97] refined a three-dimensional finite element model of endplate connections. Furthermore, many studies [98-104] have investigated the structural behavior of composite beam-to-column connections using the three-dimensional elastoplastic finite element method.

FU et al. [27] simulated the hollow-core precast slabs using the ABAQUS [96] program to study the semi-rigid composite connection behavior. All of the components' relationships are modelled utilizing contact elements. Nonlinear material properties and nonlinear geometric behavior are also incorporated into the model. The elastic-plastic material properties shown in Figure 2.13 are used to simulate the slab so that the moment–rotation response of the connections can be accurately simulated. Figure 2.14 shows the bolt, endplate, concrete slab, and reinforcing

modelling. All numerical results are presented and compared to experimental data, and there is a good agreement.

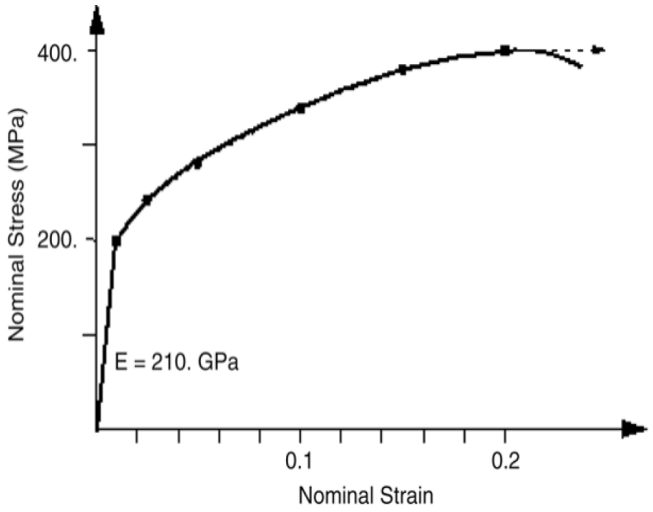

Figure 2.13: The behavior of elastic-plastic material by ABAQUS 6.4 [27].

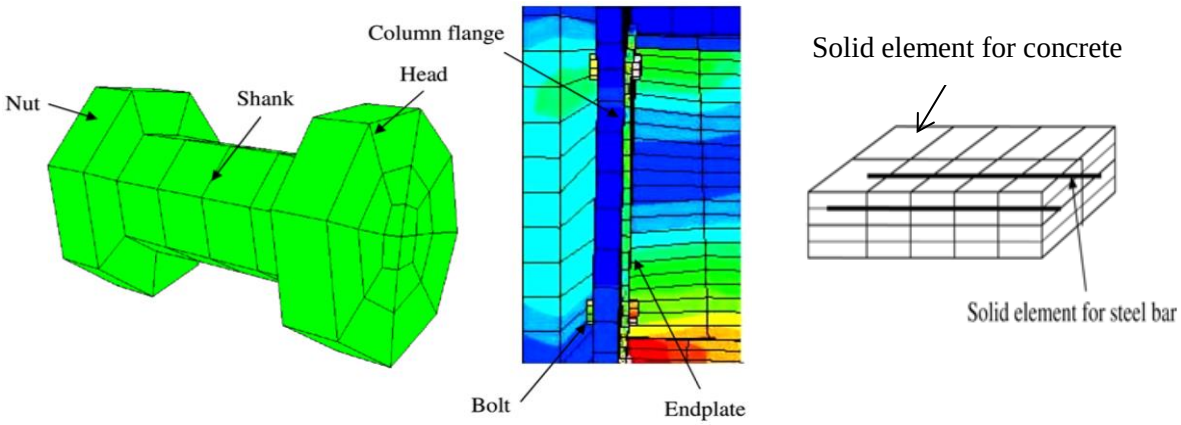

Figure 2.14: Bolted end plate connection and concrete slab models [27].

Hasan J. et al. [105] investigated experimentally and numerically the behavior of the beam-to-column connection by a top-seat and with double web angles (DWA) produced from austenitic stainless steel. A full-scale experiment was carried out as part of the study, and the results were used to develop a suitable numerical model. The numerical models developed were shown to replicate the deformation behavior of the connection components (see Figure 2.15). The experiment results show that the connection can withstand significant moments at large rotations, resulting in significant plastic deformations in various parts of the connection. It also revealed new

information about the resistance mechanism under large deformations, the onset of yielding and the propagation of plastic deformations until the end of the test. The experimental and FE studies show that stainless steel connections have significant ductility, which is important in many structural design applications. Figure 2.16 shows this connection's moment-rotation curve and compares it with the connections' characteristics according to EC3.

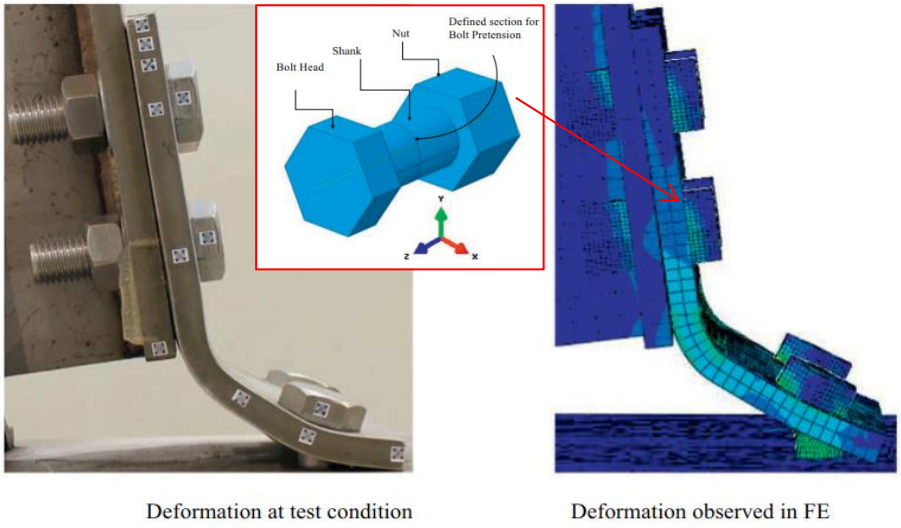

Figure 2.16: Deformation in the top angle [105].

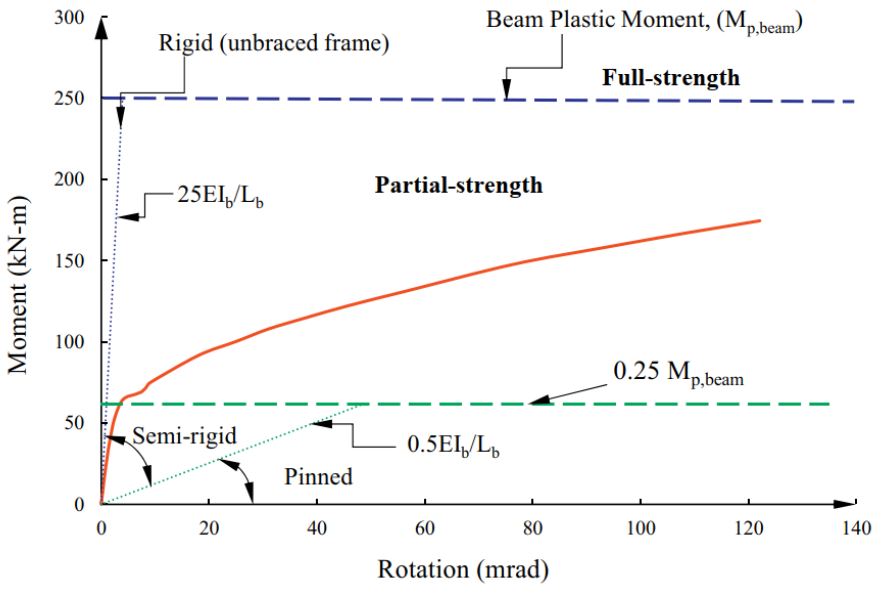

Figure 2.16: Moment-rotation curve characteristics of connections according to EC3 [105].

2.7 CONCLUDING REMARKS

This chapter presents a literature review on the beam-to-column connections and the techniques used to develop the behavior and performance of these joints. This study focuses on both composite and non-composite beam-to-column connections and their classification.

The following are some important conclusions of experimental research conducted over the last three decades.

1. The shear connector degree between concrete slab and steel beam has a large effect on the behavior of beam-to-column connections, such as moment and rotation capacity.
2. The longitudinal reinforcement should be able to develop yield with a minimum percentage of shear connection. A partial shear connection in the hogging moment region results in low moment and rotation capacity because the longitudinal bars cannot be fully mobilized.
3. The close spacing of the shear studs adjacent to the column face influences the crack pattern. It is advised to place the first stud twice the width of the column.
4. A reduced shear connection reduces the initial capacity of a composite joint, which can excess the deflection of the composite beams under the conditions of service load.
5. The ultimate moment capacities of the composite joints were approximately 2.5 times those of the non-composite joints, implying that the concrete slabs attached by bolted shear connectors significantly improved the moment capacities of the joints.
6. The thickness of the connection, such as top and seat angles, gusset plate, and end-plate, is one of the main factors that affect the behavior of the joint, as well as the moment capacity and the rotational capacity of the joint.

7. The strength and stiffness of the joint are increased by optimizing the depth of the beam and the thickness of the column.
8. The optimum percentage of reinforcement appears to be between 1.0 and 1.5 per cent of the effective slab area.
9. The design to prevent progressive collapse places a greater demand on the fracture strain of the bolt than the standard design. The progressive resistance of a semi-rigid composite frame can be improved by increasing the diameter of the bolts or the fracture strain of the bolts.

Cold-formed steel sections are still limited in steel-concrete composite structures, especially with semi-rigid joints. So far, very limited studies have included the effect of using all parts of a joint made from cold-formed steel sections, such as the CFS beam, column, and connection angles, on the composite joint behavior. So, this study focuses on using cold-formed steel beams and columns connected by simple methods such as direct connection by back-to-back webs or by top and seat angles. Due to the importance of using unconventional shear connectors for ease of installation and sustainable development, new shear connectors are also used, made of cold-formed steel, in addition to using a bolted shear connector with a single embedded nut and with different degrees of shear connection.

CHAPTER THREE

EXPERIMENTAL WORK

3.1 INTRODUCTION

The main objective of the present work is to investigate the influence of using composite cold-formed steel sections on the behavior of the semi-rigid connection between the beam and column connected by cold-formed steel top and seat angles. For this purpose, thirteen beam-to-column specimens and nine push-out specimens are prepared to be tested at the University of Babylon in the Structure laboratory. This chapter consists of three parts; the first part includes experimental work, which shows details of the specimens and the manufacture of specimens. The second part deals with material properties such as mechanical and chemical properties of the specimen's materials (cement, fine and coarse aggregate) are tested according to the Iraqi specifications (IQ. S) [106] and the American Society for Testing and Materials (ASTM) [107]. Also, many required tests are achieved to obtain some mechanical properties such as yield and ultimate strength for steel sections, bolts and reinforcing steel and compressive strength, flexural strength, stress-strain relationship and splitting tensile strength for concrete at 28-day curing wetting burlap sacks. Finally, the third part includes instrumentations used in the test and test procedure of specimens.

3.2 DESCRIPTION OF SPECIMENS

A full description of the geometry of the tested specimens and the progress of steel section manufacturing will be described in this section.

3.2.1 Geometry

In order to study the behavior of the semi-rigid connection between the composite beam and column with a cold-formed steel section, the experimental work involved testing thirteen composite steel beam-to-column joints, having different cross-section shapes of steel, different degree of shear connection and different types of shear connectors. The specimens are arranged in four groups according to cross-section shape of steel, degree of a bolted shear connector, type of shear connector and loading type.

The variables investigated in the experimental program for the beam-to-column specimens were:

1) The shape of beam-to-column connection.
2) Degree of bolt shear connection.
3) Type of shear connection.
4) Type of load (monotonic and cyclic).

In addition, nine push-out specimens are also prepared in this study to study the behavior and load-slip characteristics of the shear connectors used. So that the parameters suggested for the push-out specimens are:

1) The shape of a beam (I and box sections).
2) Shear connection type (cold-formed steel plate and bolted shear connectors).
3) The shape of a cold-formed steel plate shear connector.
4) The diameter of a bolted shear connector with a single embedded nut.

3.2.2 Manufacture of Steel Sections

Many technologies manufacture cold-formed steel sections, such as roll forming, folding, and press braking. This study used press braking technology to manufacture sections of the beams and columns. The specimen manufacturing process in this study includes several steps. First,

cut the plate used to fabricate the beam, column, and shear connector using a plate cutting machine. After that, the sections were produced on a hydraulic-press-brake machine with a lipped channel section shape with a thickness of 3 mm and a depth of 150 and 200 mm for the beam and column, respectively. Also, the plate shear connector is fabricated with an angle and corrugated shapes with a thickness of 2 mm. The second step is to represent the perforations in the flanges and webs of the CFS sections of the beam and column with a drill machine to put the bolts used for connecting the beam and column, the shear connector, and the parts.

The beam and column were connected using top and seat angles with dimensions of 75 x 75 x 130 and a thickness of 8 mm in some specimens, which were cut and perforated using a CNC machine and then produced with an L-section shape on a hydraulic-press-brake machine.

The fabrication steps above are shown in Figures 3.1 to 3.4.

Figure 3.1: Using the cutting machine to cut the plate.

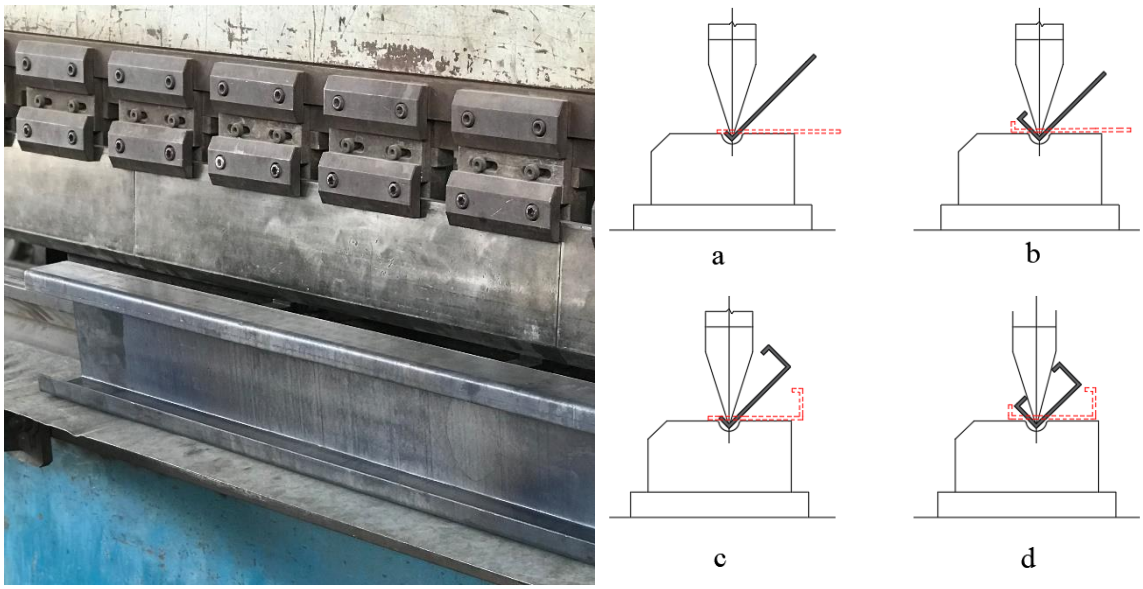

Figure 3.2: Shows how to make a lipped channel section for a beam and column using a hydraulic-press-brake machine.

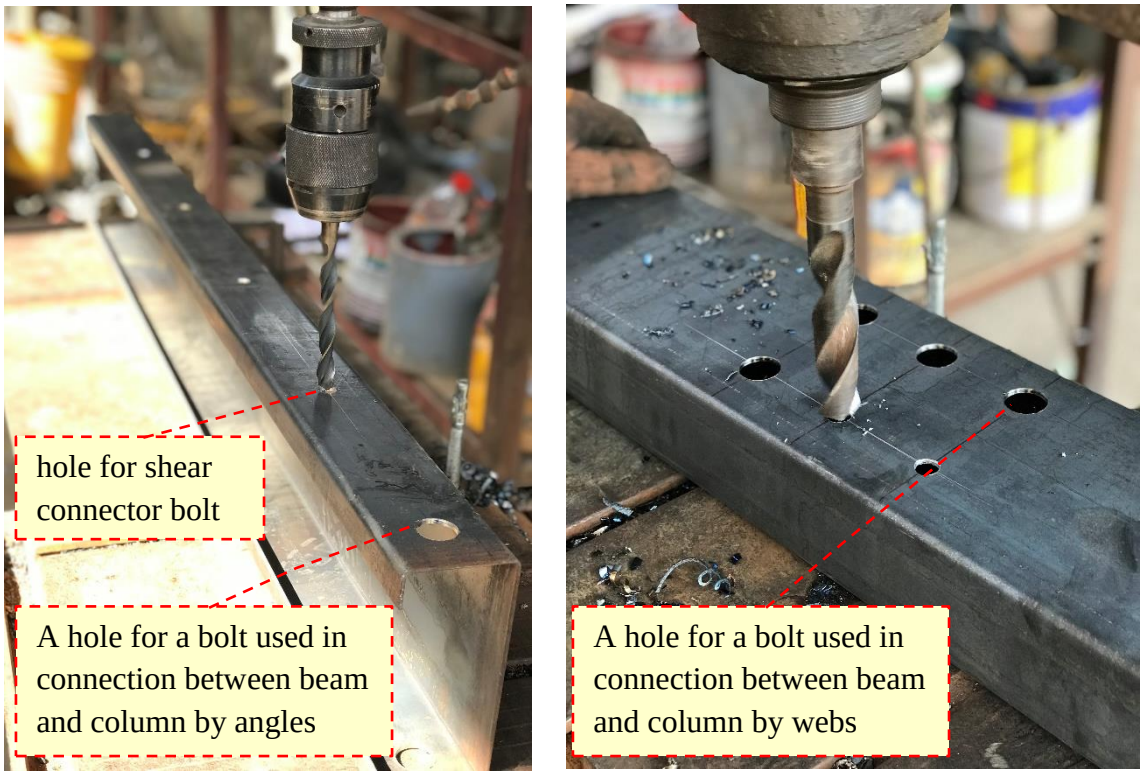

Figure 3.3: Perforation process of CFS sections by a drill machine.

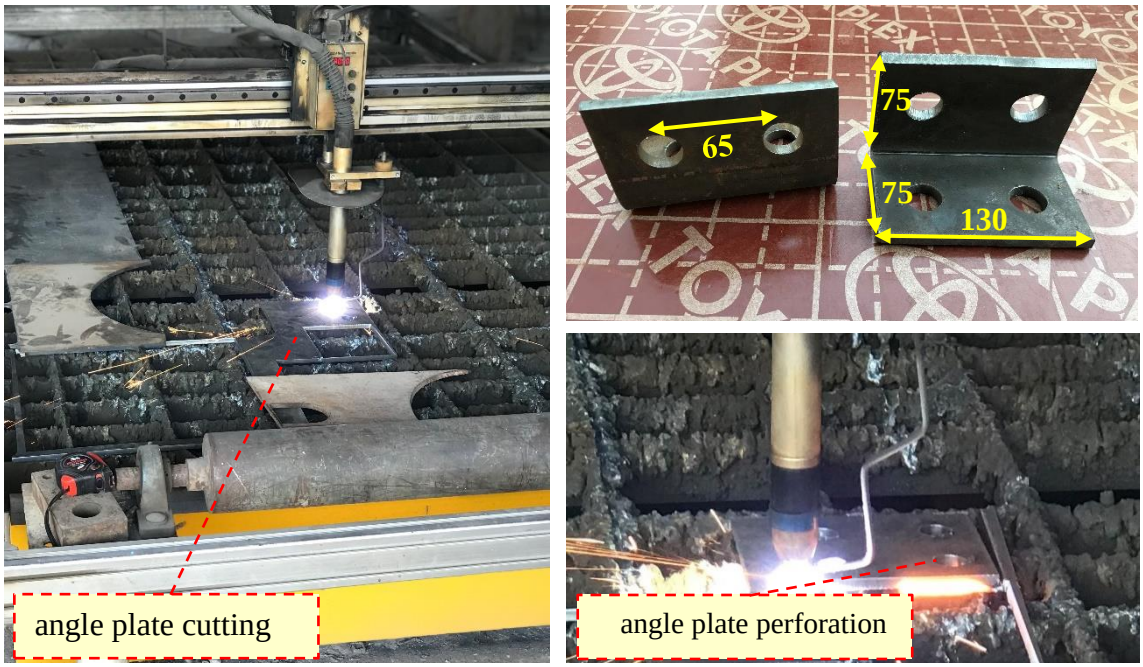

Figure 3.4: Connection plate angle fabrication steps.

After manufacturing all the parts, the assembly phase begins, which consists of the following steps:

1. Specimens connected by angles

a- Connect the two cold-formed steel C-sections placed back-to-back as a beam with a 1.1 m length by two bolts with a 10 mm diameter as shown in Figure 3.5 for specimens with a bolt shear connection and then linked the bolts/net that used a shear connector.

b- The two cold-formed steel C-sections are placed back-to-back as a beam with a 1.1 m length and a plate shear connector and connected by four bolts with a 10 mm diameter and at a 220 mm distance between them, as shown in Figure 3.6 for specimens with plate shear connection.

c- Connect the two CFS C-sections placed back-to-back as a column with a 0.6 m length and the beam collected in steps (a) or (b) from each side by top angle and seat angle using 20 mm diameter of bolts.

d- The bolts are tightened in the previous step manually. Then the angle between the beam and the column is check by a tool called locally

(orthogonal), as well as checking whether the surfaces are horizontal or vertical using the bubble level as shown in Figure 3.7.

e- Finally, the bolts are tightened using a torque screwdriver to ensure they are tightened to the same degree for all samples, as shown in Figure 3.8. A torque of 402 N.m tightened the bolt.

2. Specimens are directly connected by web

a- linked the bolts that used a shear connector on the flange of a cold-formed steel C-section beam with a 2.2 m length.

b- Connect the cold-formed steel C-section as a beam with a 2.2 m length and the cold-formed steel C-section as a column with a 0.6 m length by back-to-back web using six bolts with 20 mm diameter.

c- The same steps (d) and (e) above are used for these specimens also.

d- Use the two pieces collected in step (a) and put the beams face-to-face to form a box beam section, while when putting the columns face-to-face, they form a box column section.

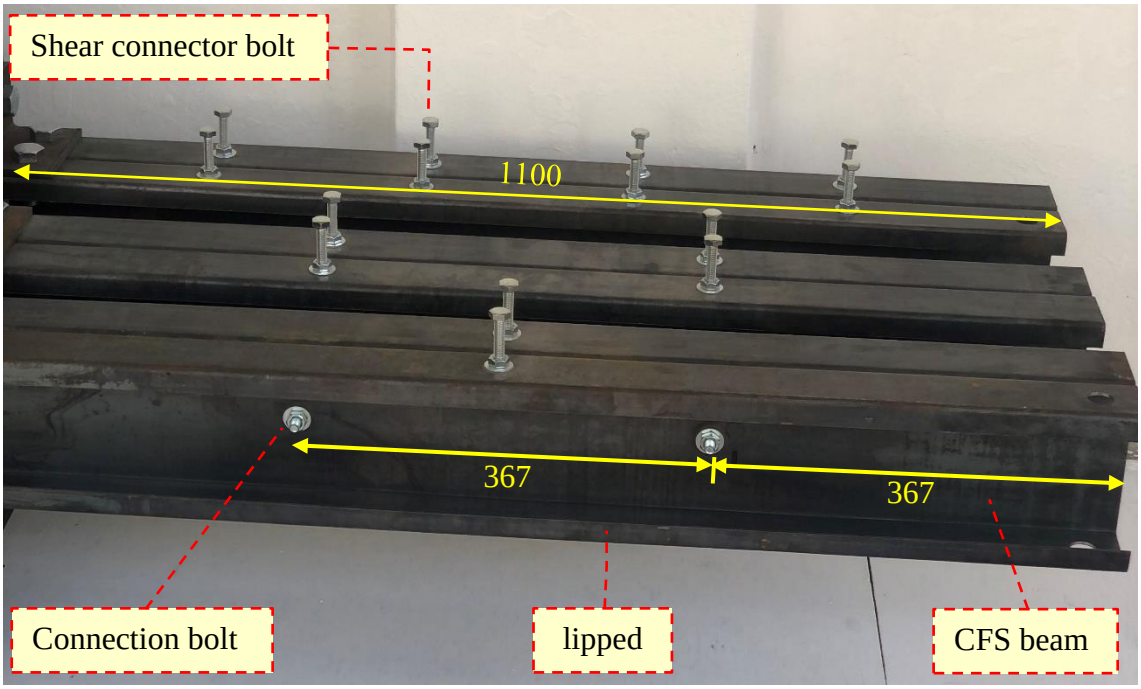

Figure 3.5: The connection between the two CFS C-sections by two connection bolts (specimens with bolt shear connector).

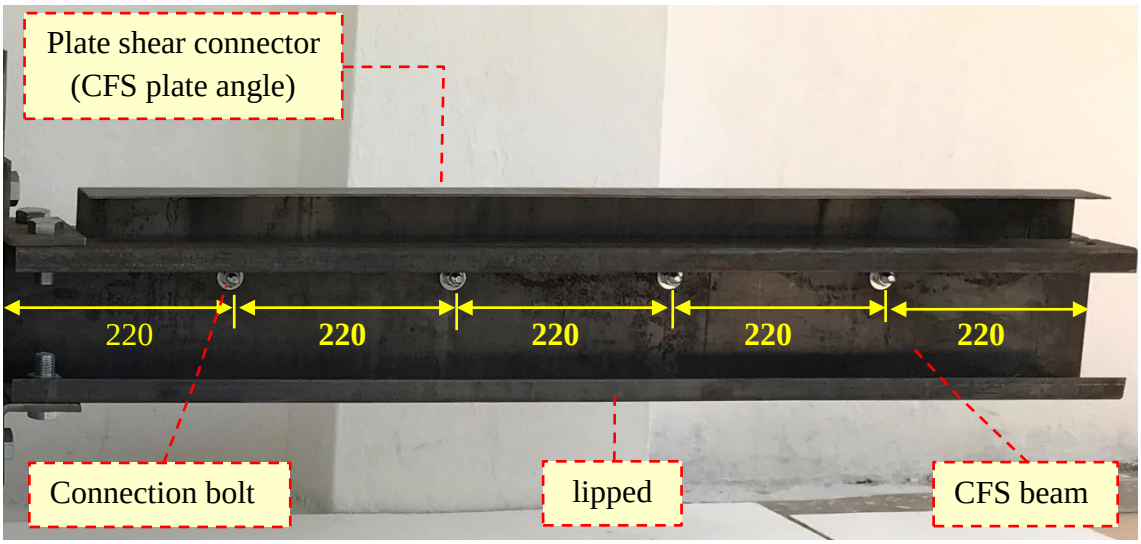

Figure 3.6: The connection between the two CFS C-sections by four connection bolts (specimens with CFS plate shear connector).

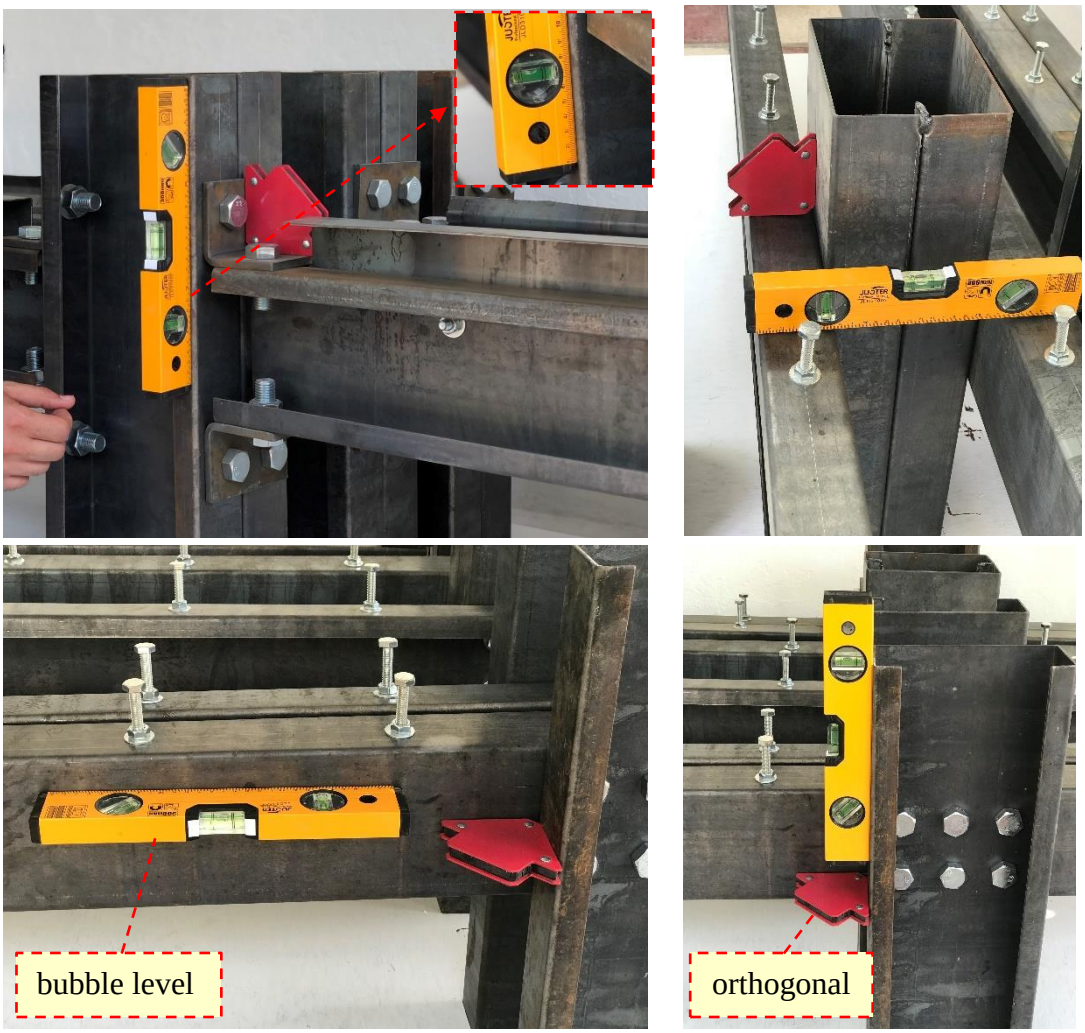

Figure 3.7: Checking the perpendicular angle and the horizontal or vertical surfaces.

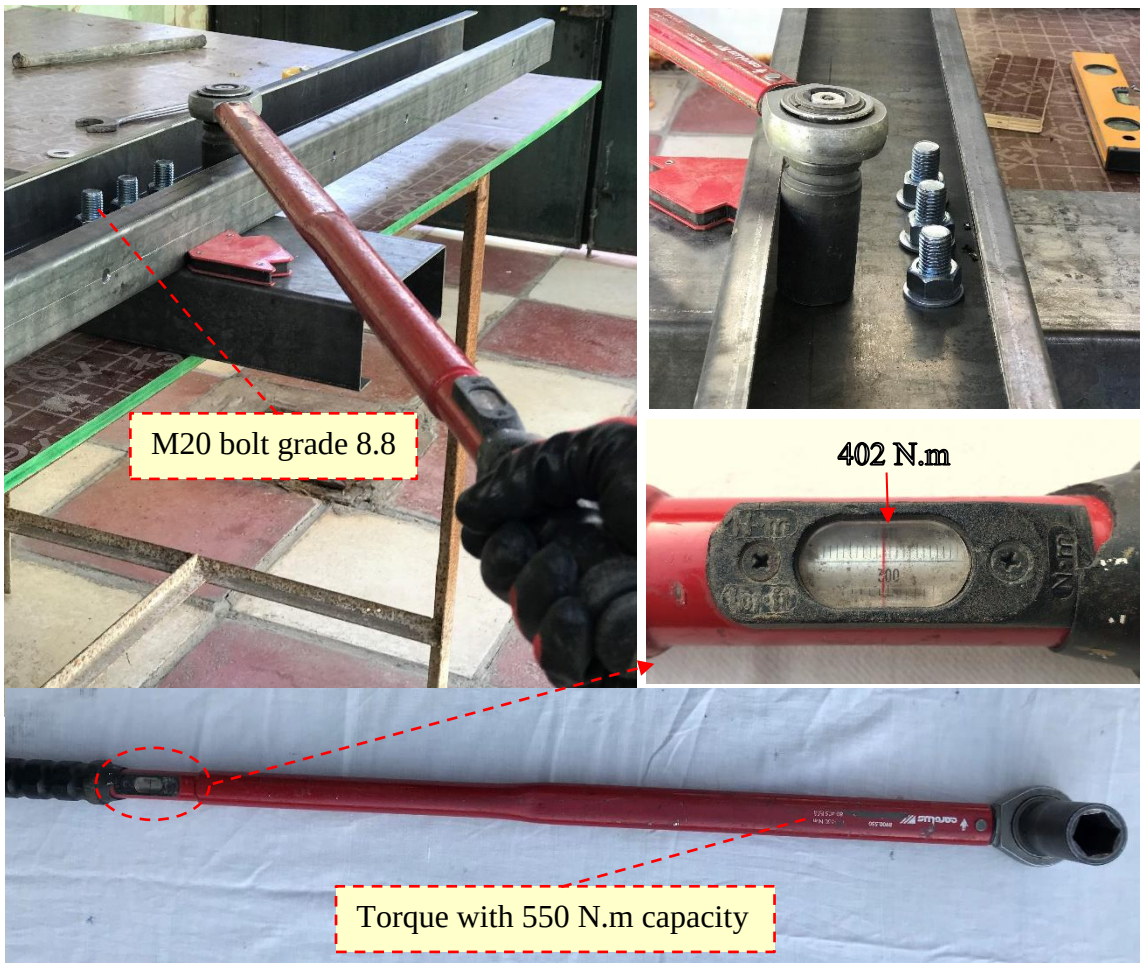

Figure 3.8: The torque screwdriver used to tighten bolts.

The joint details for each connection type and the specimens with different connection shapes are shown in Figures 3.9 and 3.10 after assembly.

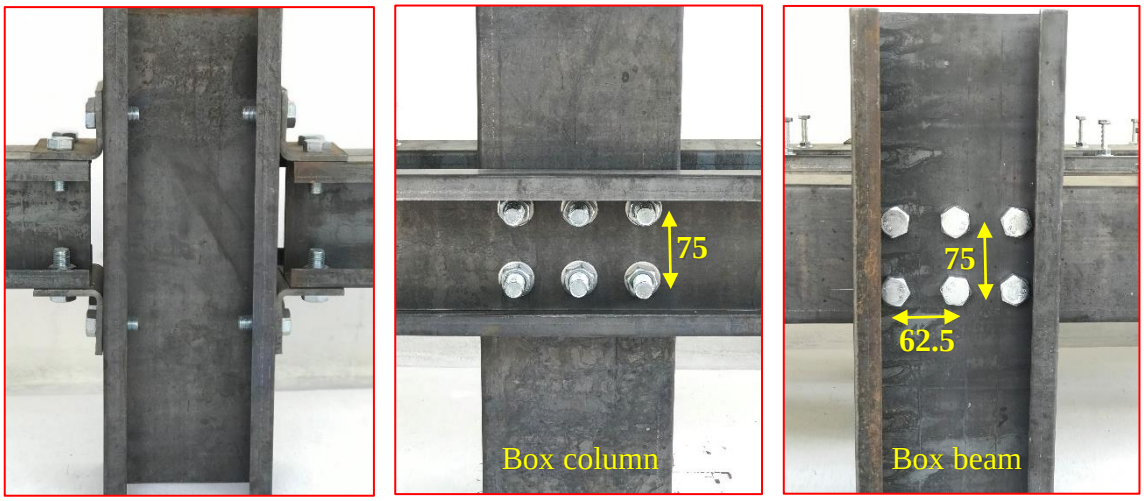

Connection by angles Connection by back-to-back web

Figure 3.9: The joint shape and details.

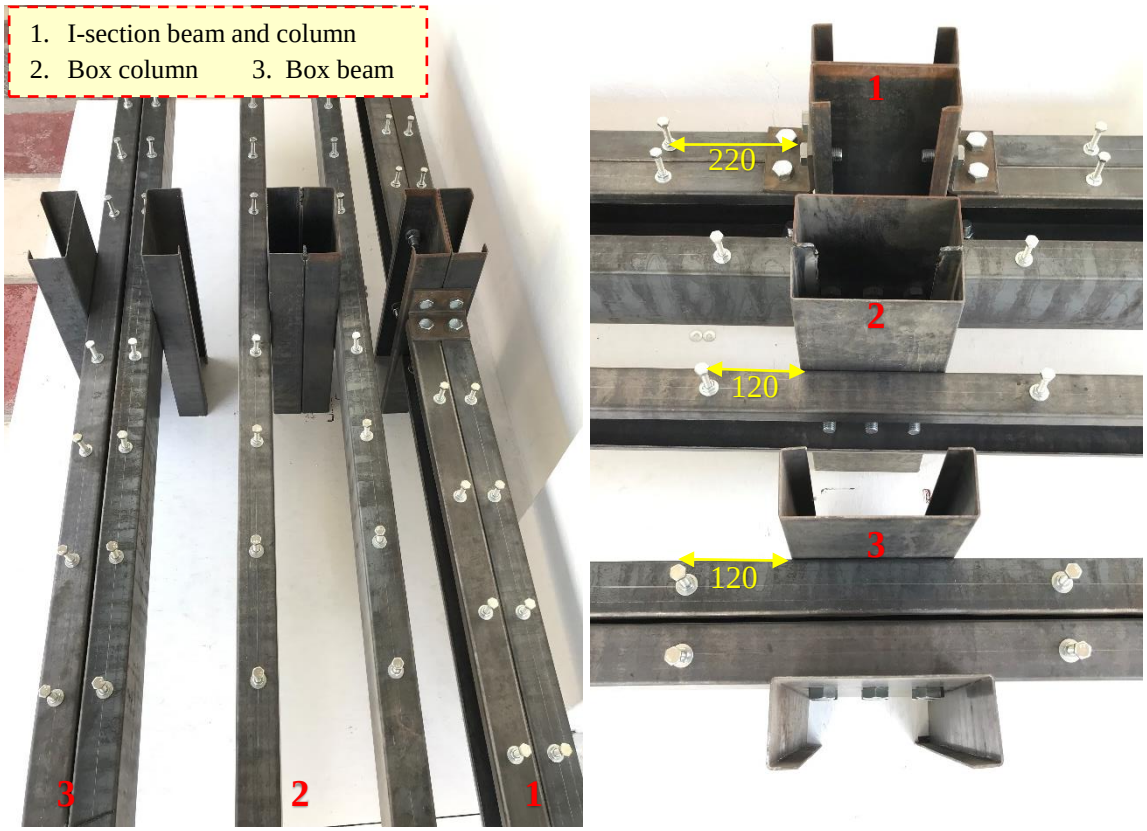

Figure 3.10: The specimens after assembly.

3.2.3 Reinforcing Steel

For trail specimens with a 300 mm slab width, the slab is reinforced with one layer of reinforcement measuring 2Ø6 mm in the long direction and Ø6mm@ 210mm in the short direction. In contrast, the specimens with a slab width of 750 mm are reinforced by Ø10 mm@ 100 mm in both directions.

The tensile test was carried out in the Material Engineering College's laboratory at the University of Babylon following ASTM A615 [108]. Table 3.1 summarizes the main findings. Figure 3.11 depicts load deformation for reinforcement bars.

The design procedure and equations used in the design are listed in Appendix A, which describes the ACI-Code provisions and requirements for bending. The reinforcement details for specimens with 300 and 750 mm slab widths are shown in Figures 3.12 and 3.13.

Table 3.1: Tensile Test results of Steel Reinforcing Bars.

Nominal diameter (mm)	Measured diameter* (mm)	Yield stress* (MPa)	Ultimate strength* (MPa)	Elongation at fracture (%)
6	5.75	560	602	3.5
10	9.8	554	647	5.8

*Each value is an average of two specimens.

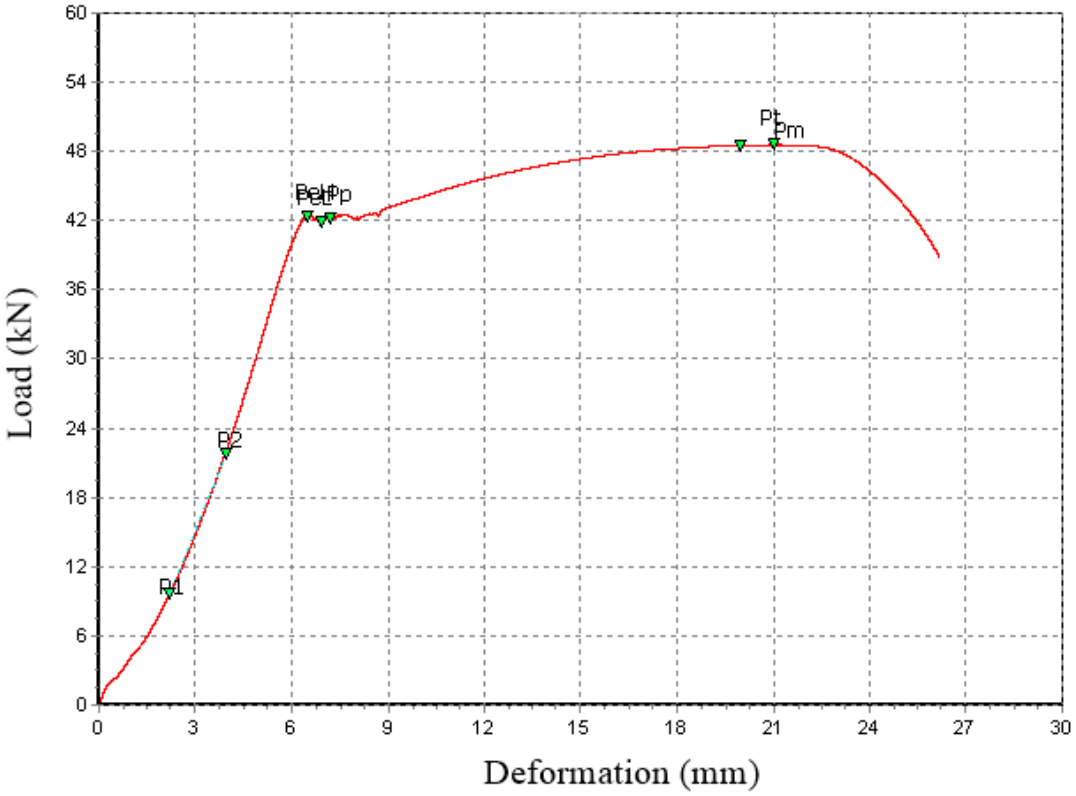

Figure 3.11: Load-Deformation Curve for Reinforcement Bars (Ø 10mm).

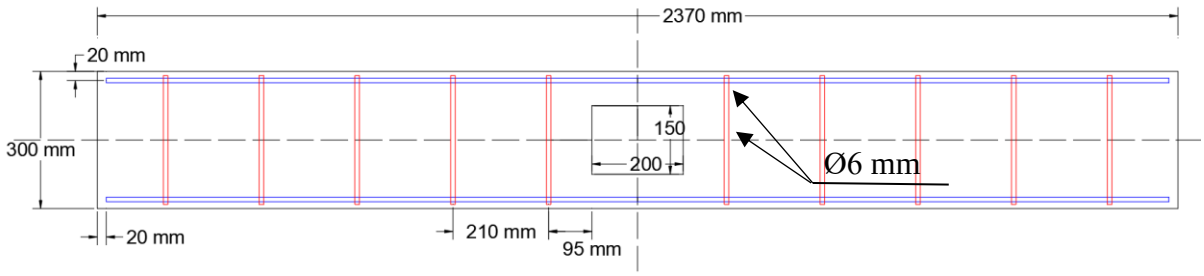

Figure 3.12: Reinforcement details for trail specimens with a 300 mm slab width.

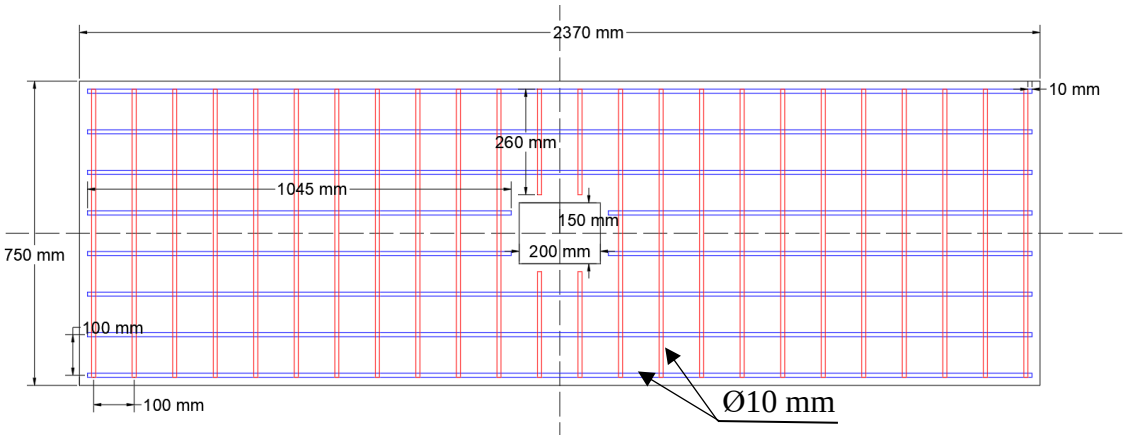

(a) Specimens with an I-section of the column and beam.

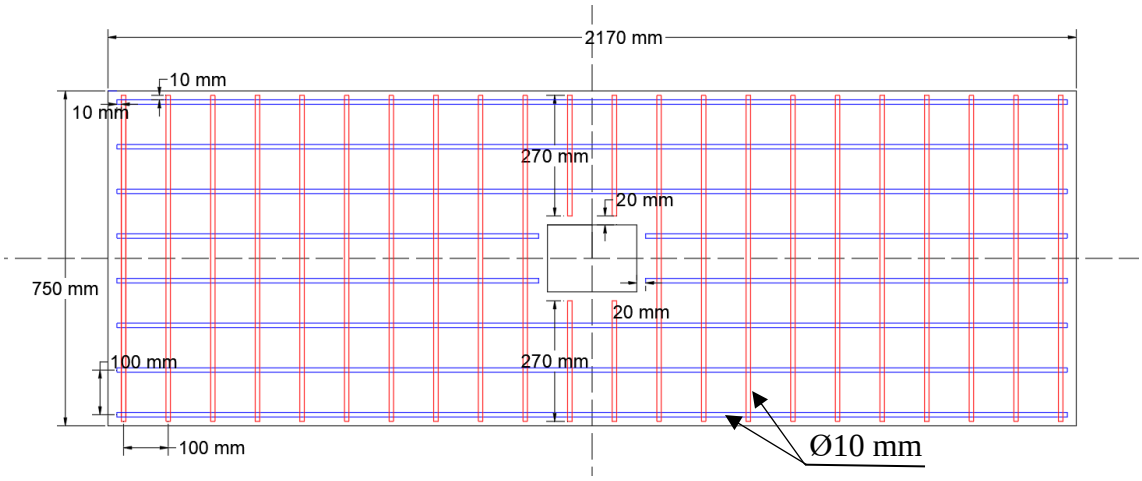

(b) Specimens with a box section of the column.

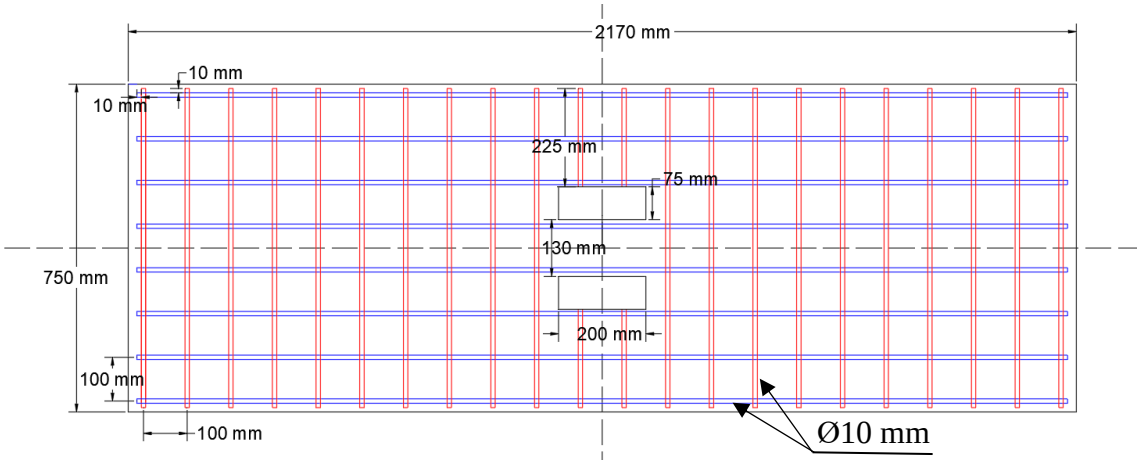

(c) Specimens with a box section of the beam.

Figure 3.13: Reinforcement Details for specimens with a 750 mm slab width.

3.2.4 Shear Connector

A shear connector connects the steel beam and the concrete slab and plays an important role in a structure's seismic response. It prevents the two components from separating. It also improves longitudinal shear transmission and significantly impacts the composite beam's flexural strength. Different types of shear connectors are used in this study, such as a bolted shear connector with a single embedded nut and threads along the entire length of the bolt and a novel approach to shear connectors manufactured from cold-formed steel sections with various shapes.

The connectors are designed to resist the flow of shear forces that are produced between the concrete slab and steel beam because of the loading of composite members, as well as they should resist the pull-out force or vertical separation of concrete from the steel beam so that the lower and upper required number of shear connectors are calculated as described in Appendix (A).

A bolted shear connector of 10 mm diameter is distributed with different degrees of shear connectors (100, 50, and 25%) over all the span with a distance (220, 367 mm) C/C between bolts for specimens with 100 and 50 % degrees of shear connector respectively. The first row of bolts is at a distance from the face of the column equals to 220, 367, and 550 mm for specimens with 100, 50, and 25 % degrees of the shear connector, respectively, as shown in Figure 3.14.

The other type of shear connector is manufactured from cold-formed steel with a 2 mm thickness and different shapes, such as angle and corrugated plate. This type of shear connector can be used to resist the shear force generated between slab and beam and increase flexural strength in composite beams simultaneously. This shear connector has a length of 1

m and a height of 45 mm, and it is attached to the web of Lipped C-channels cold-formed steel beam by four bolts with a 10 mm diameter and a distance of 220 mm C/C between bolts as illustrated in Figures 3.6 and 3.15.

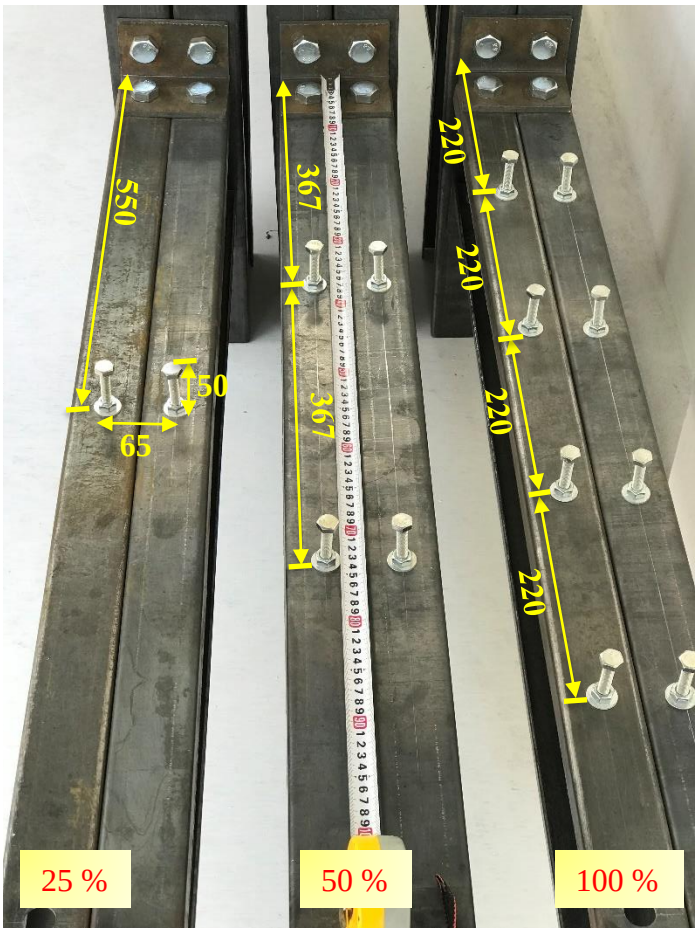

Figure 3.14: The degree of bolted shear connection and details.

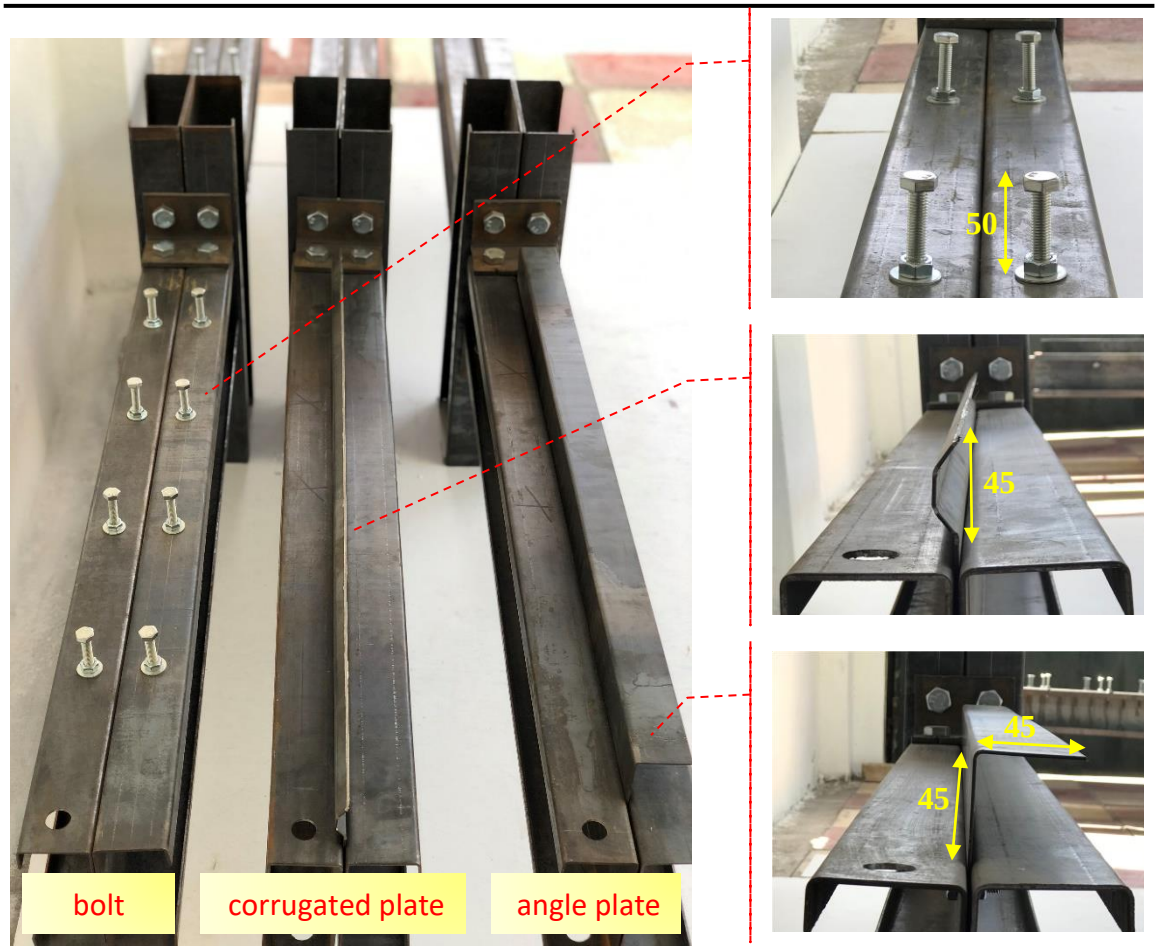

Figure 3.15: The details of shear connector types.

3.2.5 Push-out specimens

Nine push-out specimens were designed and tested following Eurocode 4 (EC4) [72] to determine the load-slip behavior, shear stiffness, and performance of cold-formed steel shear connectors such as single plate, angle plate, double angle plate, and corrugated plate, as shown in Figure 3.16 and the performance of a bolt with a single embedded nut with different bolt diameters connecting concrete slabs with the CFS beam, the description of which is listed in Table 3.2. Figure 3.17 depicts the dimensions and test details of the specimens. The push-out samples used doable channel steel beam 150 x 65 x 3 mm with two types: I and Box sections and 460 x 300 x 70 mm concrete slabs. The diameter of the reinforcement bar is 6 mm, used in both vertical and horizontal directions.

The torque arm was then used to secure four bolted shear connectors with a single nut to the steel beam in both directions .

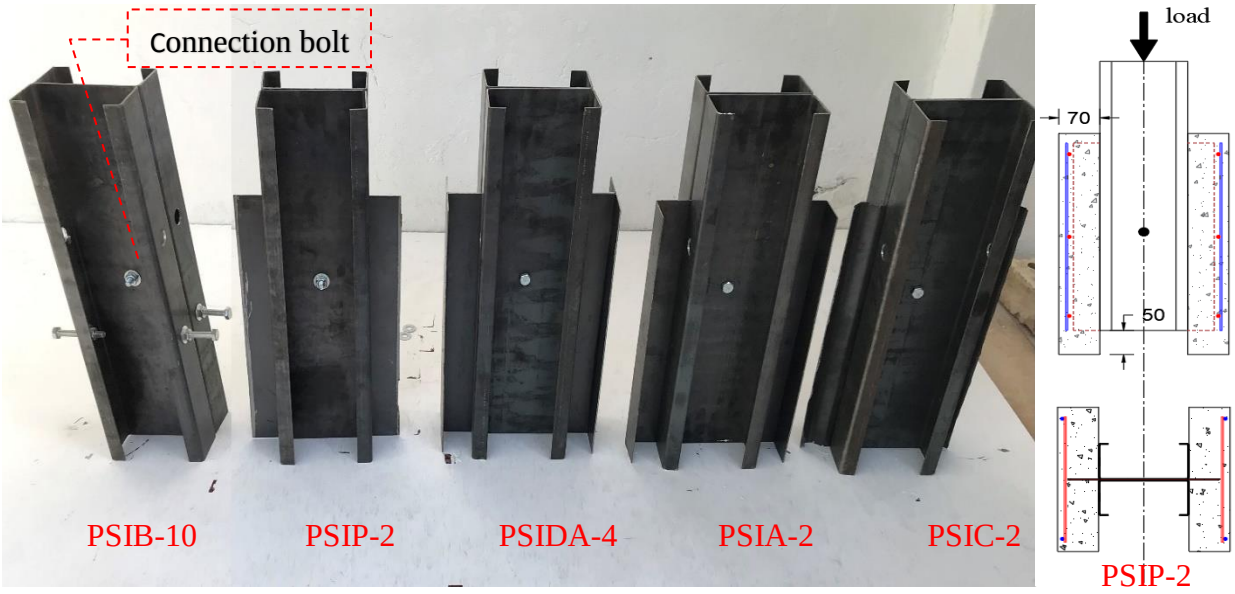

Figure 3.16: Depicts the shapes of the shear connectors.

Table 3.2: Push-out specimens' details.

specimen	Cross section type	Shear connector type	The thickness of the plate or bolt diameter (mm)	Embedded portion length (L)** (mm)
PSIB-10*	I-section	bolt	10	50
PSBB-10	Box-section	bolt	10	50
PSIB-14	I-section	bolt	14	50
PSBB-14	Box-section	bolt	14	50
PSIP-2	I-section	CFS single plate	2	45
PSIA-2	I-section	CFS angle plate	2	90
PSIDA-4	I-section	CFS double-angle plate	4	2*90
PSIC-2	I-section	CFS corrugated plate	2	45

***** Two samples of this type were prepared.

****** Embedded portion length means the length of a shear connector embedded in the concrete slab.

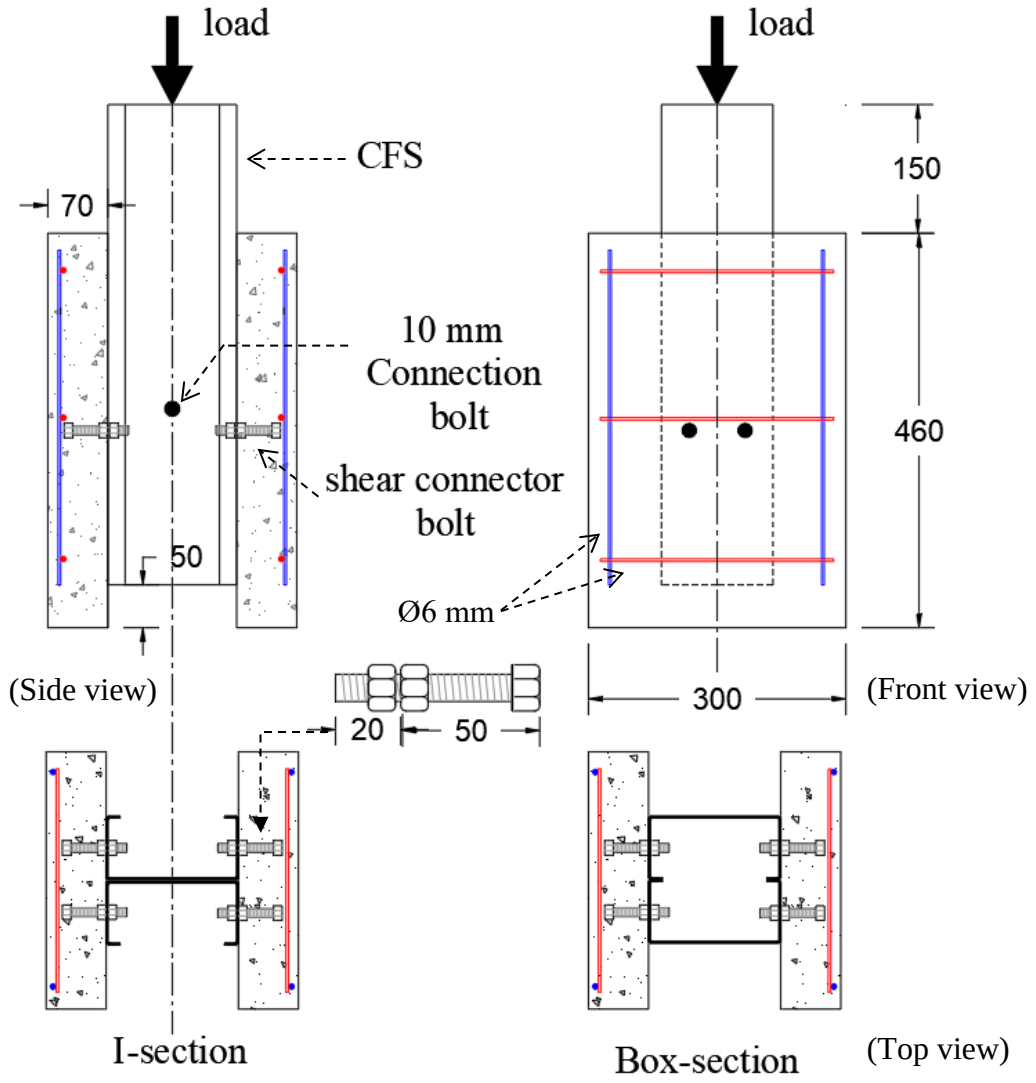

Figure 3.17: The dimensions and arrangement specifics.

The plate shear connector has a length of 390 mm and is connected with a double channel cold-formed steel beam by a bolt with a 10 mm diameter at a distance of 195 mm from the bottom of the beam. Figure 3.18 depicts the nomination system for each specimen. The specimen is denoted by the letter 'PS' followed by the cross-section type of the CFS beam (e.g., I = I-section), shape and type of shear connector (e.g., B = bolt shear connector), and the diameter of the bolted shear connector (e.g., 10 = 10 mm).

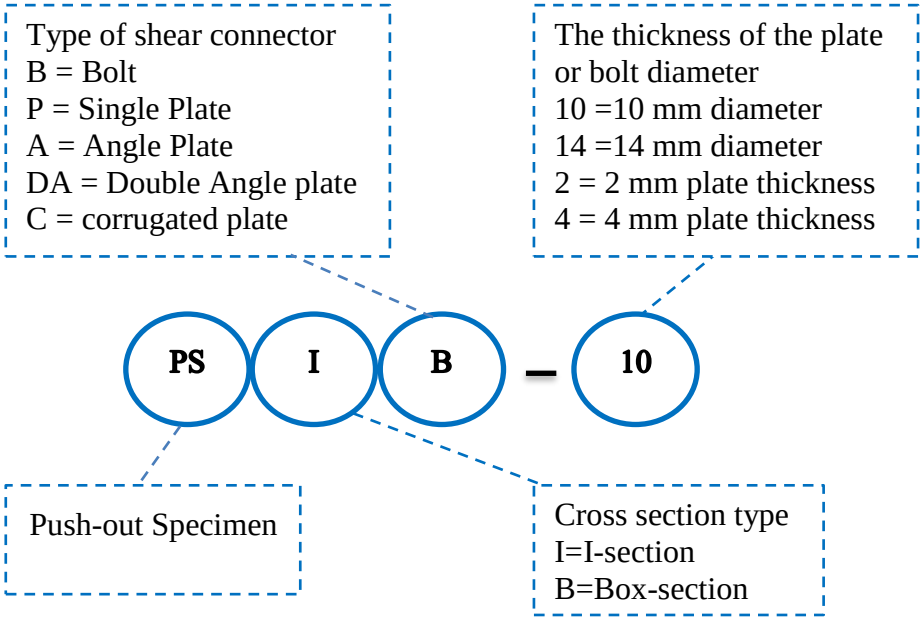

Figure 3.18: The specimen nomination system.

3.2.6 Composite Beam-to-Column Joint Specimens

Thirteen specimens with cruciform subassemblies of cold-formed steel beam-to-column joints were carried out in this study. All samples tested were identical in terms of steel beam section, column section, concrete slab thickness, top and seat angle plate connection. But different in degree and type of shear connector, the configuration of connection (shape of beam and column), concrete slab width and reinforcement, and kind of loading (monotonic and cyclic). The cold-formed steel used for the beam and column has a lipped double-channel section with a thickness of 3 mm and a depth of 150 and 200 mm, respectively. The M20 bolts grade 8.8 were used as fasteners, where they were installed using the torque screwdriver.

The tested specimens were divided into two parts. The first part is a trial case consisting of three specimens with cruciform subassemblies of cold-formed steel beam-to-column joints. They were carried out in this study with a novel approach to different shear connections: single embedded nut bolt, cold-formed angle plate, and cold-formed corrugated

plate. The beam and column were joined by an angle from top and seat only and were made from CFS with an 8 mm thickness. The concrete slab had a thickness of 70 mm and a width of 300 mm and was reinforced by a minimum of 2Ø6mm.

The second part is then prepared, consisting of ten composite joint specimens with a concrete slab thickness of 70 mm and a width of 750 mm reinforced by Ø10 @ 100 mm in both directions. The tested specimens were divided into four groups according to the type of shear connection, degree of bolt shear connection, beam-to-column connection shape, and loading type. The first group consists of three specimens with the same details as specimens in the trial case but different in slab width and reinforcement to study the effect of the cross-section area of slab to reinforcement area ratio on the behavior and rotation capacity of the joint. The other three groups, each with a single embedded nut bolt shear connector, are ready to investigate the effects of bolted shear connection degree, beam and column shape under monolithic load, and cyclic load on joint behavior. The details of the ten specimens tested are shown in Table 3.3.

Figure 3.19 depicts the nomination system for each specimen. The name of the sample begins with the letter S, indicating the shape of the beam-to-column connection (e.g., S1 = top and bottom seat cleat angle), followed by the type of shear connector (e.g., T1 = bolted shear connector), degree of bolted shear connector (e.g., D100 = degree of bolted shear connection 100%), and the loading type (e.g., M = monolithic load). For samples within the trial case, a capital letter "T" is placed before the specimen's name. Also, the reading of the specimen's designation is shown in Table 3.4. The tested specimens' details and dimensions are shown in Figures 3.20 to 3.27.

Table 3.3: Details of Tested Specimens.

Group	Sample name	Type of shear connector	Degree of bolt shear connector	Connection shape	Load type
Trial case	$TS_1T_1D_{100}M$	bolt	100	top and seat angles	monolithic
	TS_1T_2M	angle plate	-	top and seat angles	monolithic
	TS_1T_3M	corrugated plate	-	top and seat angles	monolithic
Control	$S_1T_1D_{100}M$	bolt	100	top and seat angles	monolithic
One	S_1T_2M	angle plate	-	top and seat angles	monolithic
	S_1T_3M	corrugated plate	-	top and seat angles	monolithic
Two	$S_1T_1D_{50}M$	bolt	50	top and seat angles	monolithic
	$S_1T_1D_{25}M$	bolt	25	top and seat angles	monolithic
Three	$S_2T_1D_{100}M$	bolt	100	direct webs connection	monolithic
	$S_3T_1D_{100}M$	bolt	100	direct webs connection	monolithic
Four	$S_1T_1D_{100}C$	bolt	100	top and seat angles	cyclic
	$S_2T_1D_{100}C$	bolt	100	direct web connection	cyclic
	$S_3T_1D_{100}C$	bolt	100	direct web connection	cyclic

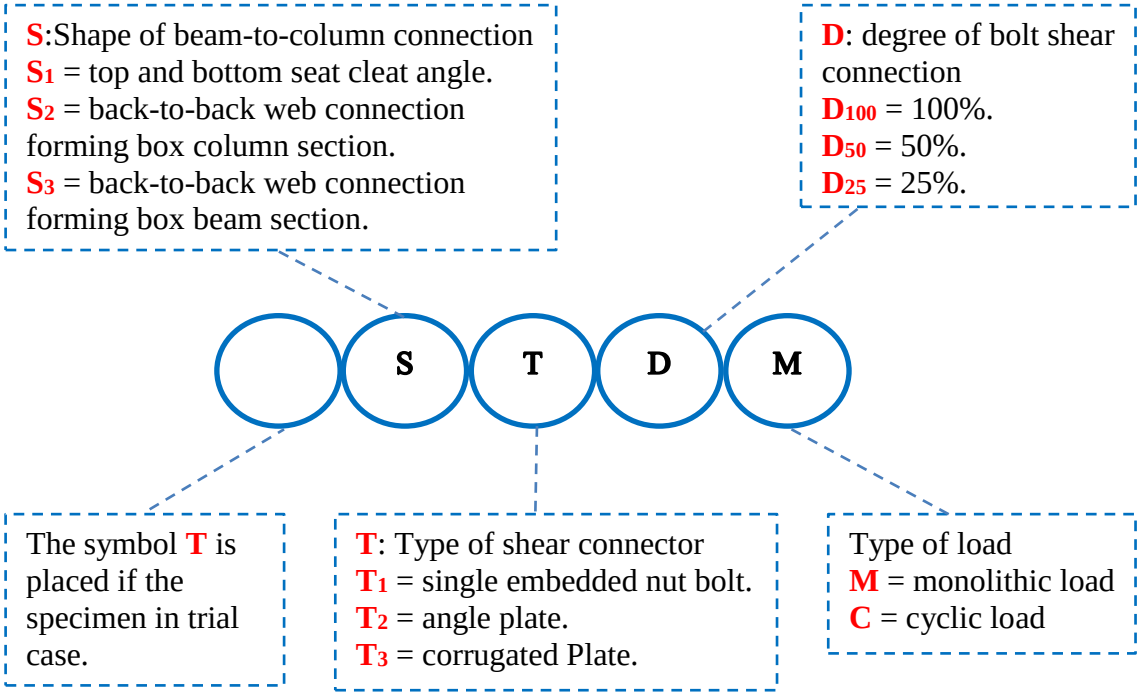

Figure 3.19: The composite joint specimen nomination system.

Table 3.4: Reading the Specimens Designation.

Specimen designation	**Reading the specimens designation**
$TS_1T_1D_{100}M$	Beam to column connection by top and bottom seat cleat angle with bolt shear connection has 100% degree of shear connection under monolithic load and with 300 mm slab thickness reinforced by a minimum of 2Ø6mm.
TS_1T_2M	Beam to column connection by top and bottom seat cleat angle with angle plate shear connection under monolithic load and with 300 mm slab thickness reinforced by a minimum of 2Ø6mm.
TS_1T_3M	Beam to column connection by top and bottom seat cleat angle with corrugated plate shear connection under monolithic load and with 300 mm slab thickness reinforced by a minimum of 2Ø6mm.
$S_1T_1D_{100}M$	Beam to column connection by top and bottom seat cleat angle with bolt shear connection has 100% degree of shear connection under monolithic load.

Table 3.4: Reading the Specimens Designation. (Continued)

Specimen designation	Reading the specimens designation
S_1T_2M	Beam to column connection by top and bottom seat cleat angle with angle plate shear connection under monolithic load.
S_1T_3M	Beam to column connection by top and bottom seat cleat angle with corrugated plate shear connection under monolithic load.
$S_1T_1D_{50}M$	Beam to column connection by top and bottom seat cleat angle with bolt shear connection have 50% degree of shear connection under monolithic load.
$S_1T_1D_{25}M$	Beam to column connection by top and bottom seat cleat angle with bolt shear connection have 25% degree of shear connection under monolithic load.
$S_2T_1D_{100}M$	Beam to column connection by back-to-back web connection forming box column section with bolt shear connection has 100% degree of shear connection under monolithic load.
$S_3T_1D_{100}M$	Beam to column connection by back-to-back web connection forming box beam section with bolt shear connection has 100% degree of shear connection under monolithic load
$S_1T_1D_{100}C$	Beam to column connection by top and bottom seat cleat angle with bolt shear connection has 100% degree of shear connection under cyclic load.
$S_2T_1D_{100}C$	Beam to column connection by back-to-back web connection forming box column section with bolt shear connection has 100% degree of shear connection under cyclic load.
$S_3T_1D_{100}C$	Beam to column connection by back-to-back web connection forming box beam section with bolt shear connection has 100% degree of shear connection under cyclic load

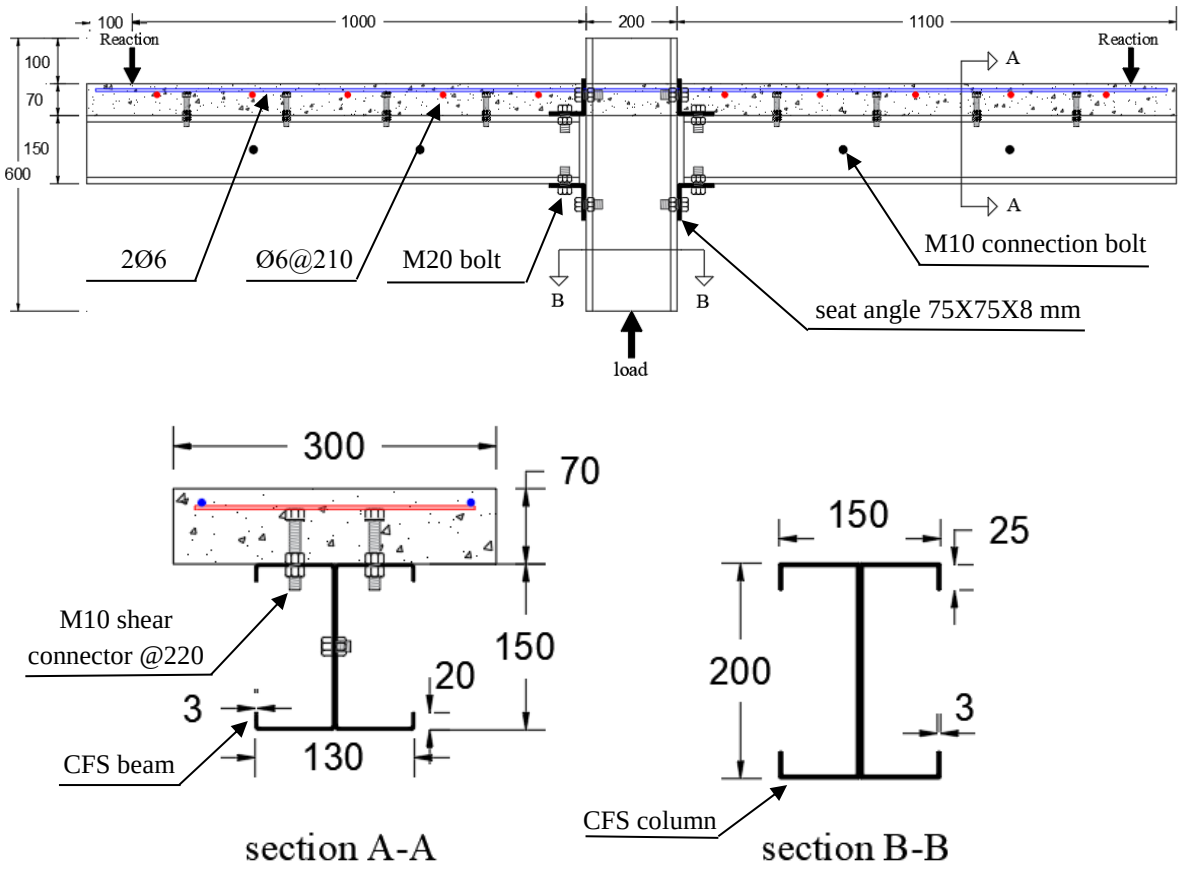

Figure 3.20: Dimensions and details of specimen $TS_1T_1D_{100}M$.

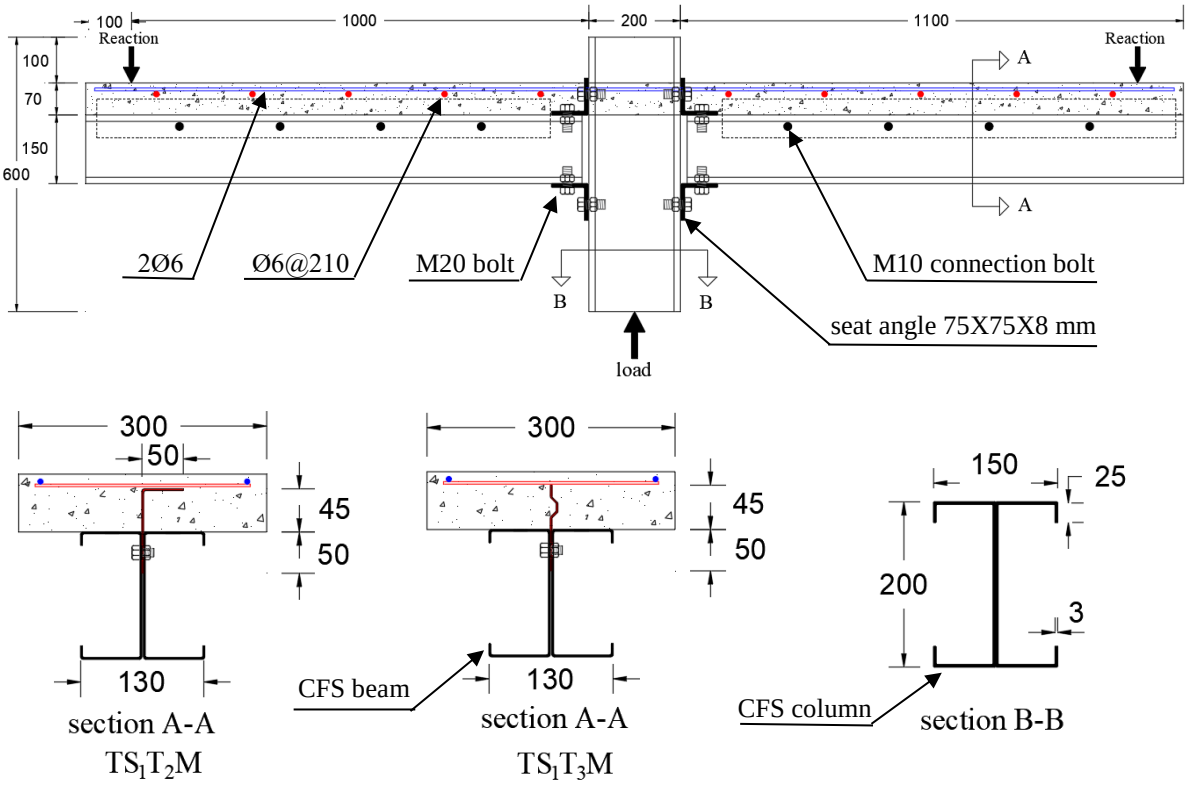

Figure 3.21: Dimensions and details of specimens TS_1T_2M and TS_1T_3M.

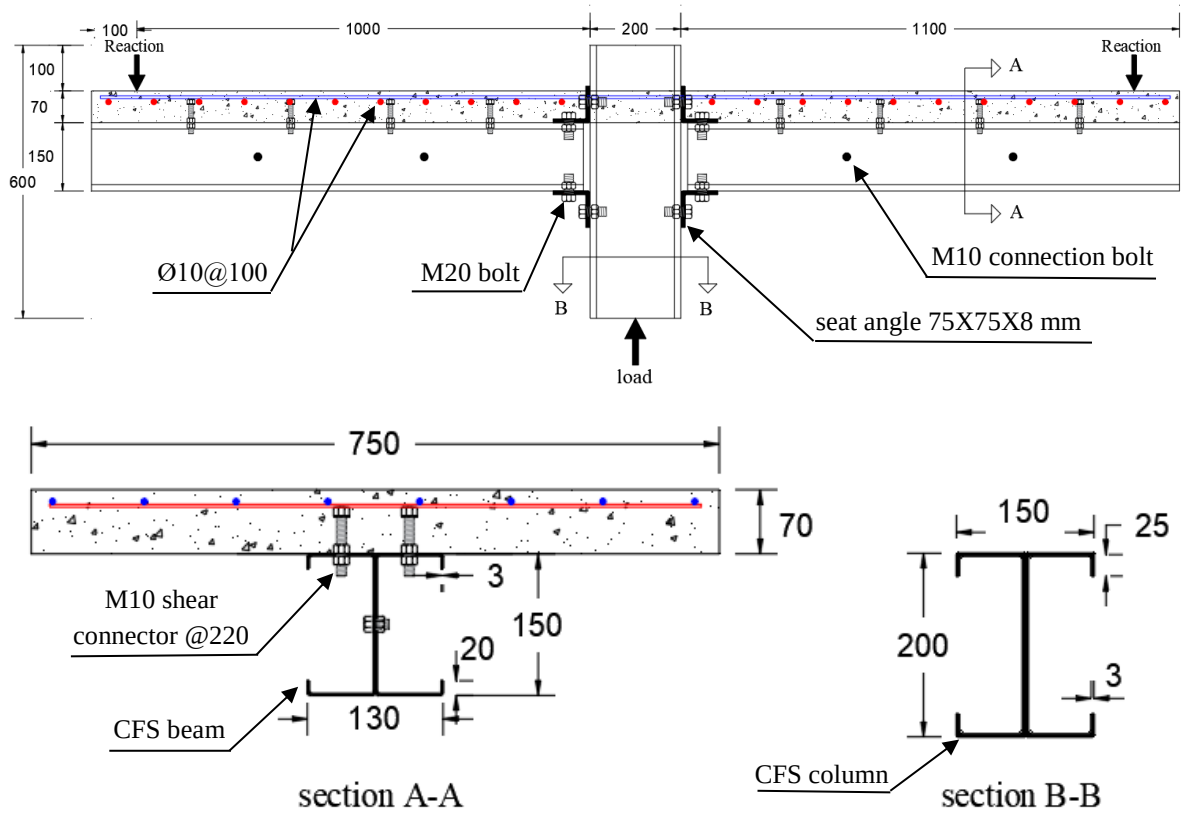

Figure 3.22: Dimensions and details of specimens $S_1T_1D_{100}M$ and $S_1T_1D_{100}C$.

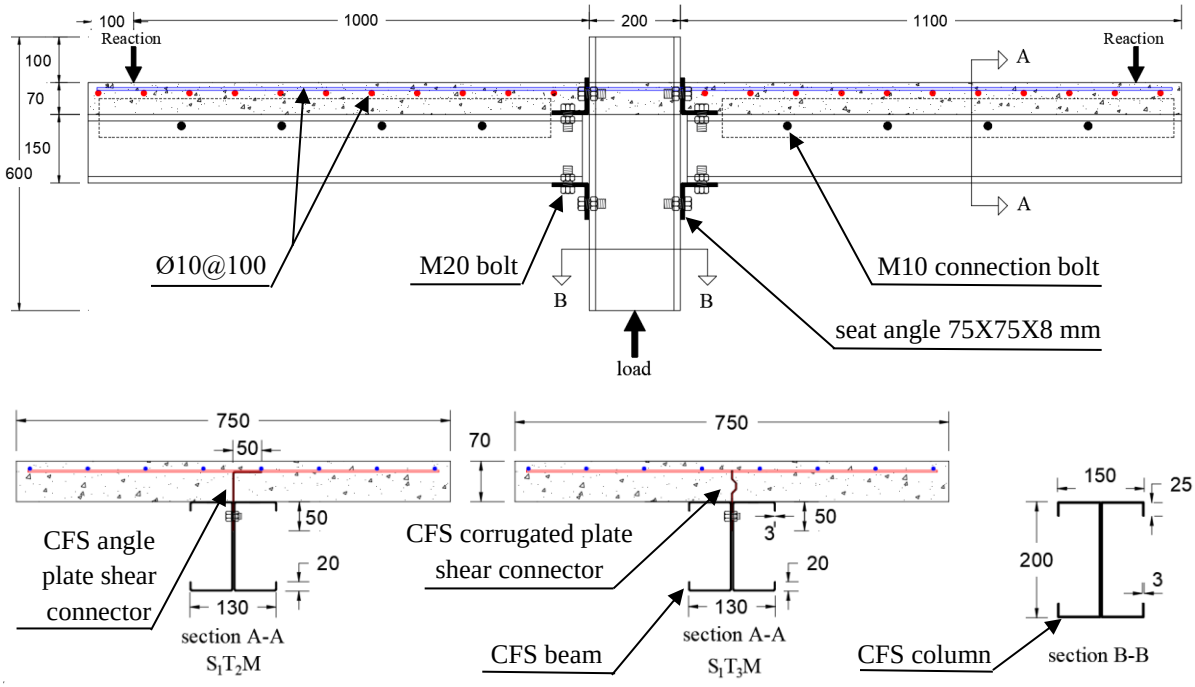

Figure 3.23: Dimensions and details of specimens S_1T_2M and S_1T_3M.

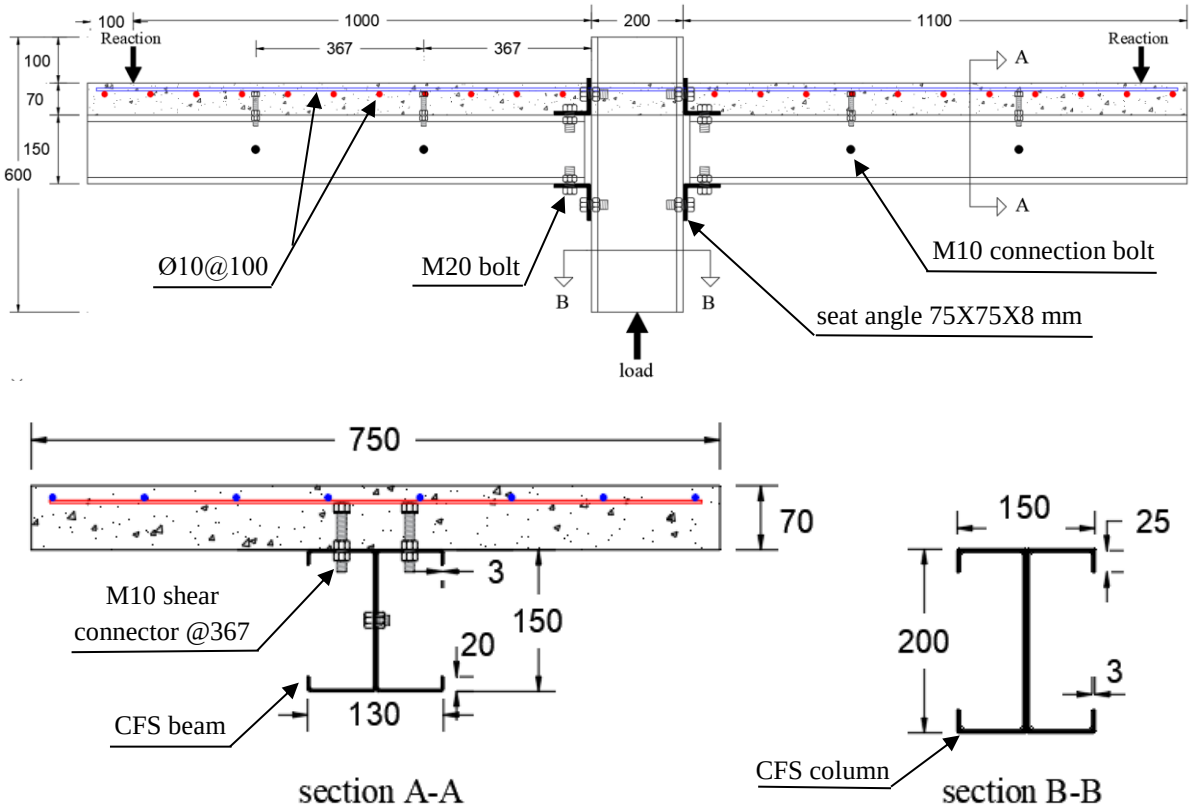

Figure 3.24: Dimensions and details of specimen $S_1T_1D_{50}M$.

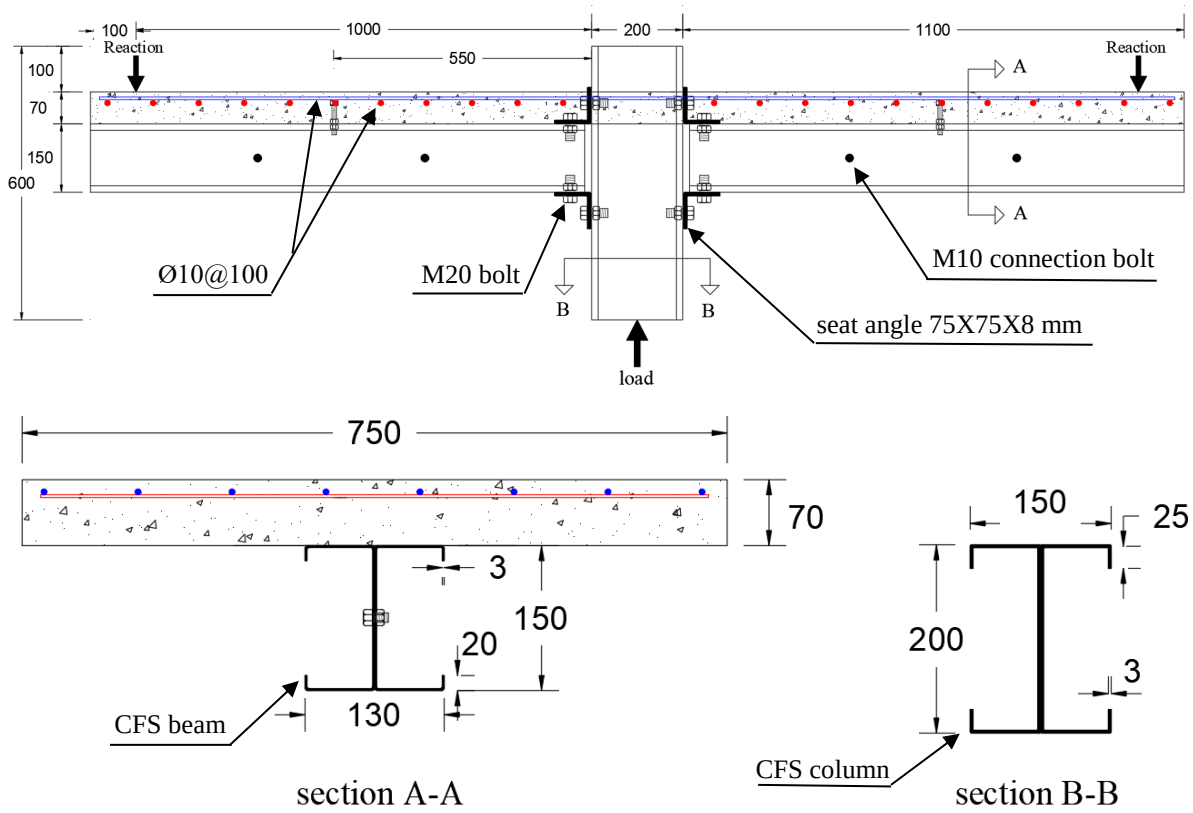

Figure 3.25: Dimensions and details of specimen $S_1T_1D_{25}M$.

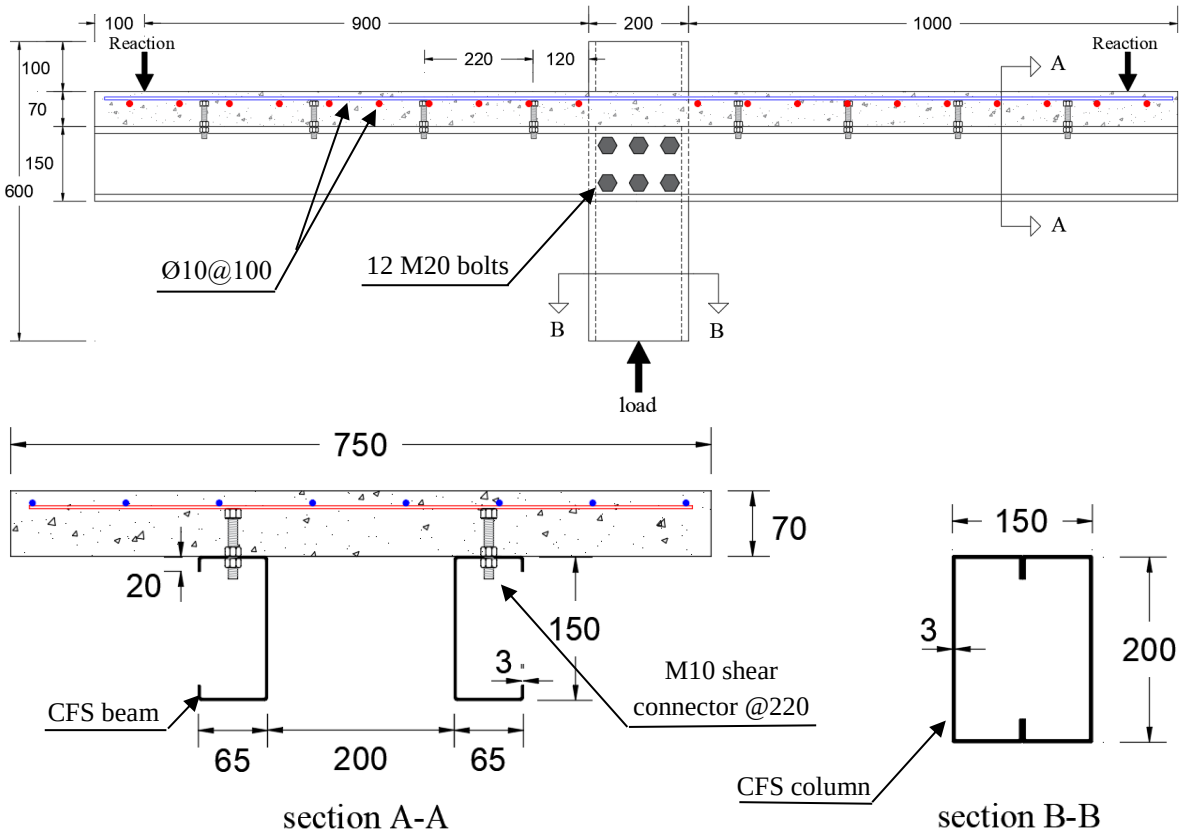

Figure 3.26: Dimensions and details of specimens $S_2T_1D_{100}M$ and $S_2T_1D_{100}C$.

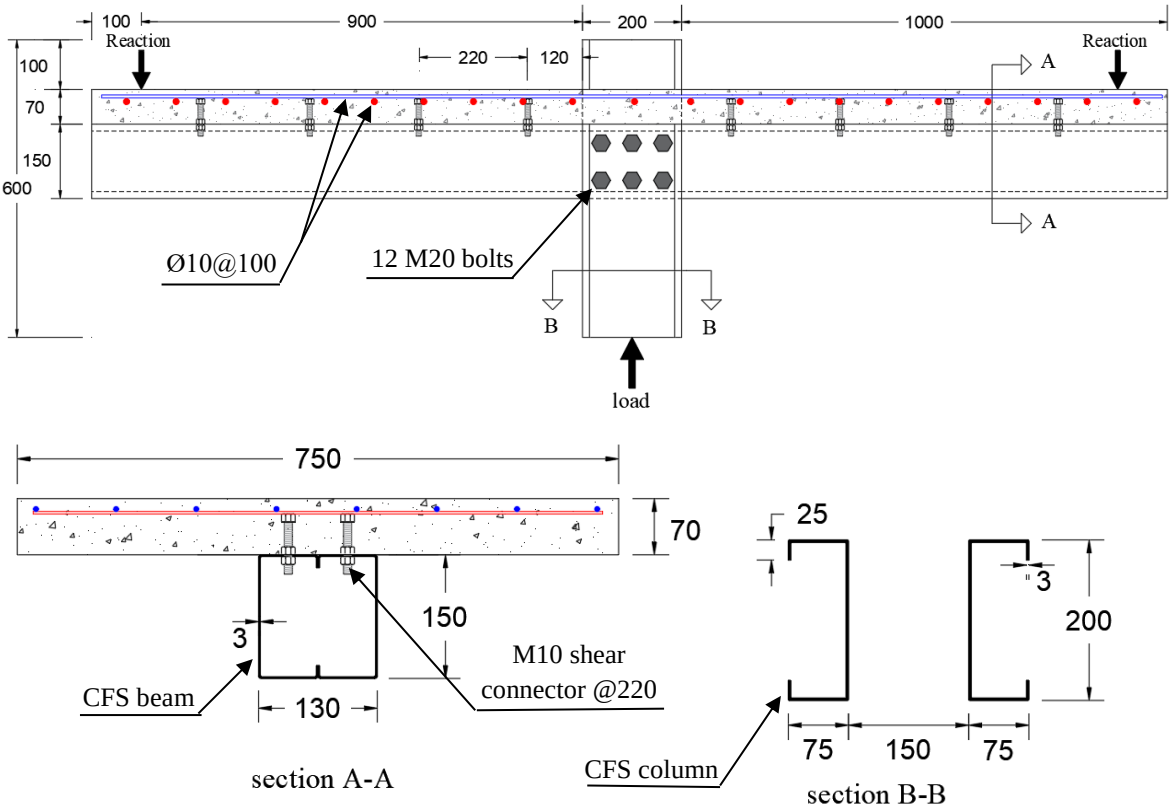

Figure 3.27: Dimensions and details of specimens $S_3T_1D_{100}M$ and $S_3T_1D_{100}C$.

3.3 MATERIAL PROPERTIES

The following subsection contains detailed descriptions of the mechanical and chemical properties of the material used in concrete and the properties of bolts and cold-formed steel sections used in this study.

3.3.1 Cement

Resistant Cement (KAR) was used in casting all tested specimens. The chemical and mechanical properties of the cement used have been tested in Construction Material and Environmental Laboratories at the University of Babylon. The mechanical and chemical properties of the used cement are given in Tables 3.5 and 3.6, respectively. These properties have been checked according to the Iraqi specification limits (IQ. S No.5/2019) [109] for resistant cement.

Table 3.5: Mechanical properties of cement.

Mechanical Properties	Test results	IQ. S No. 5/2019
Initial setting time (min)	70	≥ 45 min
Final setting time (min)	255	≤ 600 min
Fineness (m^2/kg)	303	≥ 250 m2/kg
Compressive strength, MPa		
3 days	17.39	≥ 15 MPa
7 days	27.06	≥ 23 MPa

Table 3.6: Chemical analysis of cement.

Chemical composition		% By weight.	Limits of IQ. S No.5/2019
Lime	CaO	61.25	------
Silica	SiO_2	19.78	------
Alumina	Al_2O_3	3.41	------

Table 3.6: Chemical analysis of cement. (Continued)

Chemical composition		% By weight.	Limits of IQ. S No.5/2019
Iron oxide	Fe_2O_3	4.8	------
Sulfate	SO_3	2.29	≤ 2.5 % If *C3A*< 5% ≤ 2.8 % If *C3A* > 5%
Magnesia	MgO	1.72	≤ 5%
Ratio	C_3A	0.914	≤ 3.5%
Loss on ignition	L.O. I	2.42	≤ 4%
Insoluble residue	I.R	0.85	≤ 1.5 %
Lime saturation Factor	L.S. F	0.953	(0.66–1.02) %

3.3.2 Coarse aggregate

This work used coarse aggregate with a maximum aggregate size of 19 mm. The coarse aggregate was cleaned and washed with drinkable water, then dried before use. The mechanical and chemical properties of coarse aggregate are given in Table 3.7. The sieve analysis of coarse aggregate lies within the lower and upper limits of the Iraqi specification (IQ.S No.45/2016) [106], as shown in Table 3.8.

Table 3.7: Mechanical and chemical properties of coarse aggregate.

Properties	Test results	IQ. S No. 45/2016
Specific gravity	2.66	------
Sulfate content SO3	0.03%	≤ 0.1 %
Absorption	0.6%	------
Clay content	0.2%	≤ 3%

Table 3.8: Grading of coarse aggregate.

Sieve Size (mm)	Passing %	
	Coarse aggregate	IQ. S No. 45/2016
37.5	100	100
19	100	100 - 95
9.5	43	60 - 30
5.0	3	10 - 0

3.3.3 Fine aggregate

In this work, natural sand was used as fine aggregate. The chemical and mechanical properties of sand are given in Table 3.9. The fine aggregate used has gradation that lies within the upper and lower limits of the ASTM C33/C33M specification [107] and Iraqi specification (IQ.S 45/206) zone (2) [106], as shown in Table 3.10. Fine aggregate has been tested at the University of Babylon in the Construction Material and Environmental Laboratories of the Civil Engineering Department.

Table 3.9: Chemical and mechanical properties of fine aggregate.

Properties	Test results	IQ. S No. 45/2016 zone (2)
Specific gravity	2.6	------
Fineness modulus	3.8	≤ 5 %
Sulfate content SO_3	0.22%	≤ 0.5 %
Absorption	2%	------

Table 3.10: Grading of fine aggregate.

Sieve no.	Sieve size (mm)	Passing %		
		Fine aggregate	IQ. S No. 45 Zone (2)	ASTM C 33/C 33M
3/8 in	9.5	100	100	100
NO.4	4.75	91	90 - 100	90 - 100
NO.8	2.36	83	75 - 100	80 - 100
NO.16	1.18	74.8	55 - 90	50 - 85
NO.30	0.60	57.2	35 - 59	25 - 60
NO.50	0.30	24.2	8 - 30	5 - 30
NO.100	0.15	7.2	0 - 10	0 - 10

3.3.4 Water

Potable water is used for both mixing and curing of the specimens.

3.3.5 Properties of Steel Section

In this study, two tension coupons were taken from the cold-formed steel plates used to manufacture the beams, columns, connection angles, and shear connector plates, as depicted in Figure 3.28. The tests were conducted according to the ASTM (A370-05) [110] to determine each section's ultimate strength and yielding stress. The results are shown in Table 3.11, and the coupons were tested in the Material Laboratory of Materials Engineering at Babylon University.

Table 3.11: Results of tested steel coupons.

CFS plate for section	Thickness of sample (mm)	Yield stress* (MPa)	Ultimate strength* (MPa)
Shear connector	2	161	216
beam and column	3	244	297
Connection angle	8	157	221

***** The value represents the average of two samples.

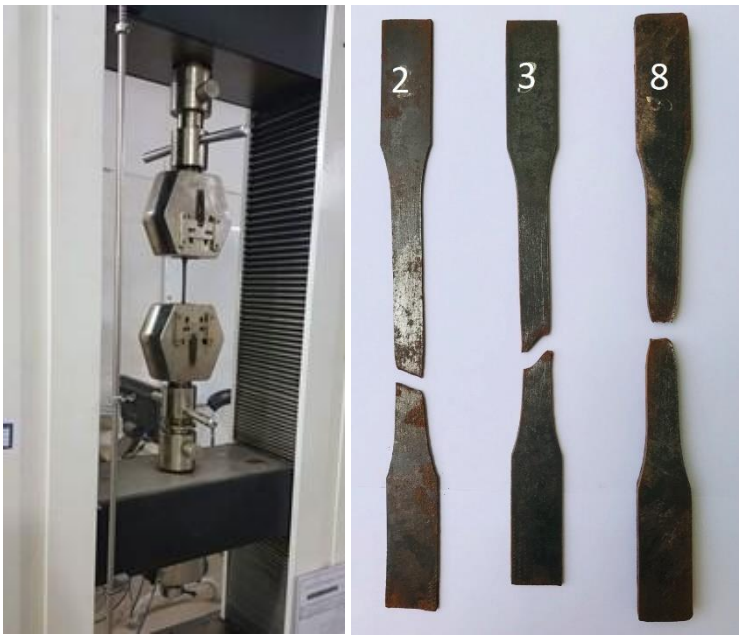

Figure 3.28: Tensile Testing Machine and Tested Coupons.

3.3.6 Properties of Bolts

Three samples of each type of bolt used in this study were tested according to ASTM (A307-14) to determine the ultimate strength and yielding stress for each bolt. The results are shown in Table 3.12, and the bolts were tested in S.I.E.R general company- engineering laboratories.

Table 3.12: Results of tested bolts.

Bolt diameter (mm)	Bolt length (mm)	Yield stress* (MPa)	Ultimate strength* (MPa)
10	70	660	783
14	70	720	807
20	50	890	973

* The value represents the average of three samples.

3.4 PREPARATION OF THE TESTED SPECIMENS

This part includes the casting and curing of all composite beam-to-column joint specimens, push-out specimens, and fresh concrete tests.

3.4.1 Casting specimens

Initially, the formwork was prepared to cast the thirteen composite beam-to-column joint specimens and nine push-out specimens. The formwork details are shown in Figure 3.29, in which the formwork is placed on flat ground, the horizontal surface's flatness is checked, and then the reinforcing steel is placed and lifted by spacers to achieve the required concrete cover. The CFS beam-to-column joint is then placed, fixed, and checked the surface's flatness in the horizontal and vertical directions, as shown in Figure 3.30.

The casting process begins, where normal strength concrete (C30 MPa) is used and prepared by the central mixer. The moulds are filled with the mixture, and the mechanical vibrator is used to expel air bubbles from the concrete mixture and obtain a homogeneous mixture without segregation. In addition, standard cubes, cylinders, and prisms are prepared to calculate the hardened concrete properties, as shown in Figure 3.31.

3.4.2 Test of Fresh Concrete

The conventional concrete slump test was carried out following (ASTM C143/C143M, 2015). A truncated cone and a tamping rod were used for the slump test. The truncated cone is 30 cm high, 20 cm in diameter from the bottom, and 10 cm across the top. It is filled with three equal layers of concrete, with each layer being stroked 25 times uniformly by a steel rod and then slowly lifted. The slump is the difference in height between the average concrete level and the top of the mould after the concrete slumping down by its weight. Figure 3.32 shows the slump test, and the slump value equals 75 mm, which ranges from (20-80) mm as recommended.

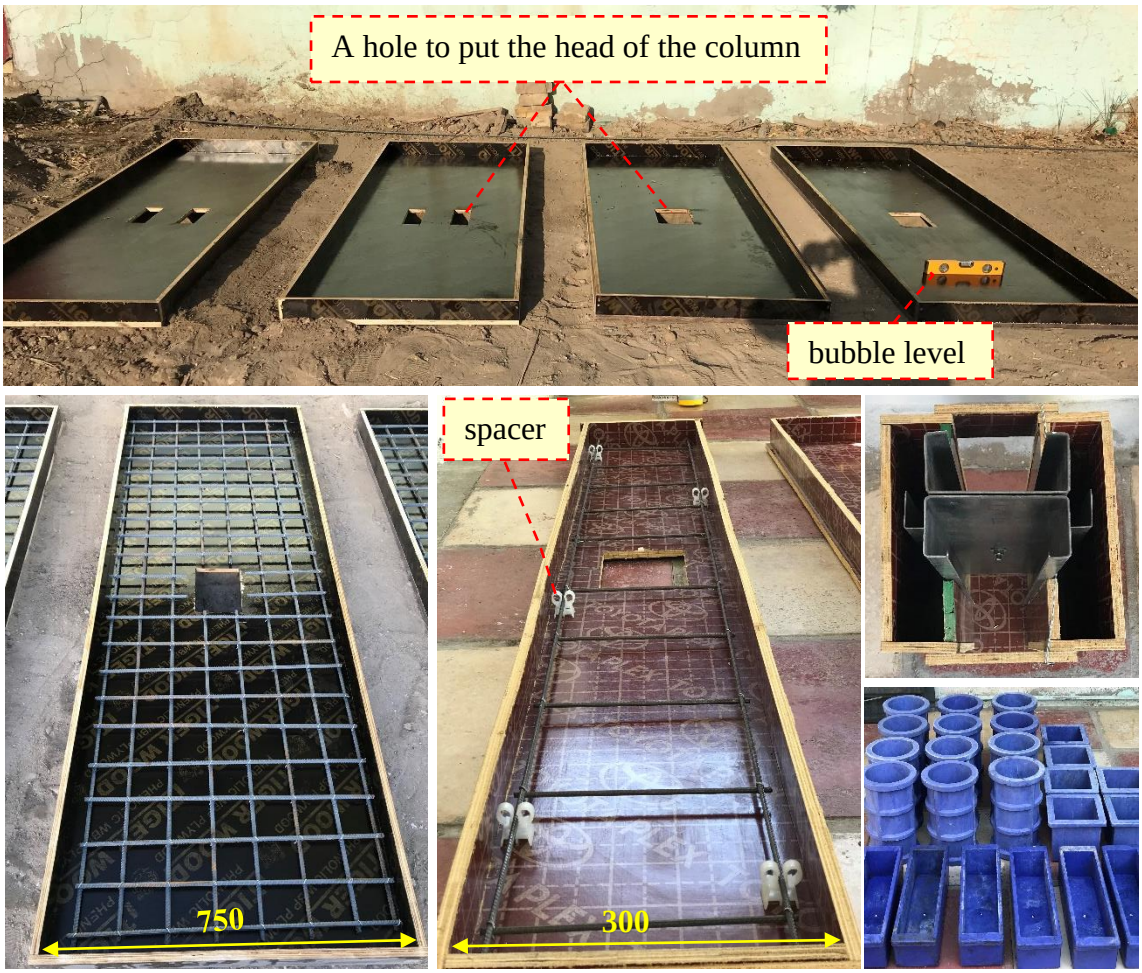

Figure 3.29: The formwork details and preparation.

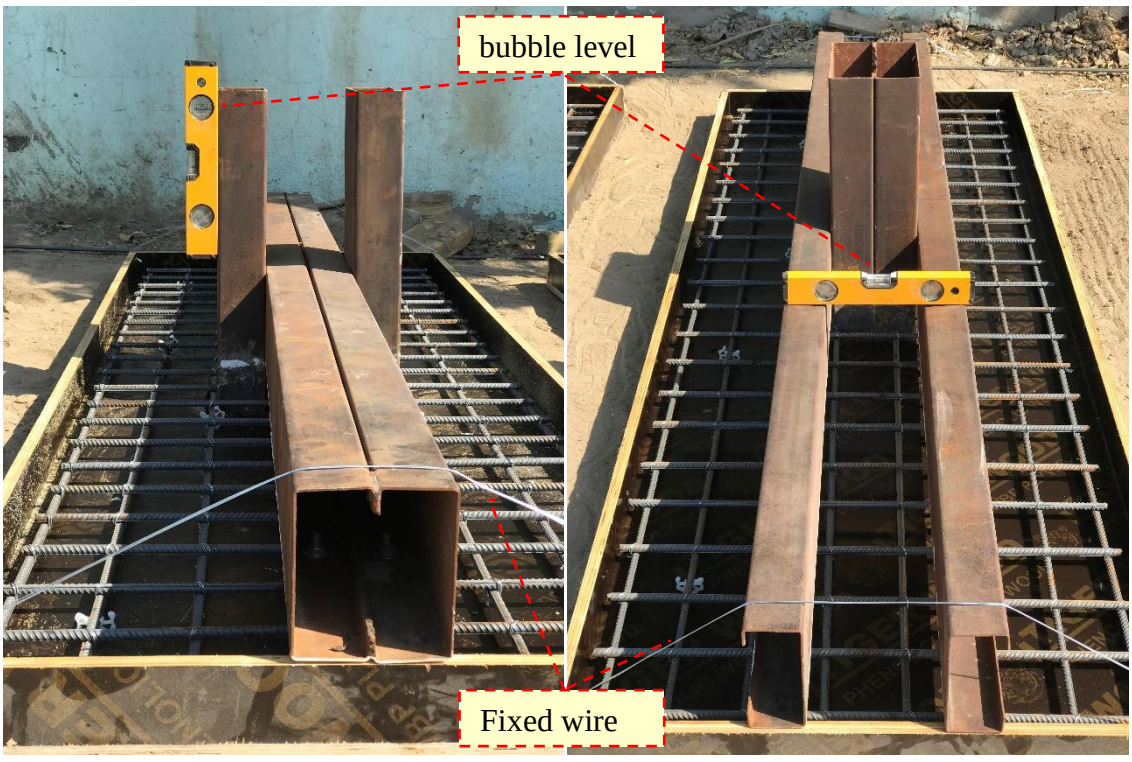

Figure 3.30: The specimens' preparation before casting.

Figure 3.31: The specimens' casting.

Figure 3.32: Slump test for fresh concrete.

3.4.3 Curing process

After the casting, the formworks were lifted after 24 hours and coated all composite beam-to-column joint specimens and push-out specimens with burlap sacks and nylon cover sheets, and they were kept wet for 28 days, as depicted in Figure 3.33. The concrete cubes, cylinders, and prism specimens are kept under the water at the same temperature during the curing duration of 28 days.

After curing and moving the weak surface layer of the steel section, a grinder machine used a steel brush to clean the steel sections.

Figure 3.33: The specimens curing process.

3.5 HARDENED CONCRETE PROPERTIES

3.5.1 Compressive Strength Test

The compressive strength test was calculated according to (ASTM C39-86) [111] and (BS.1881: Paw 116:1989) [112]. The average values of twelve cubes and three cylinders of testing specimens are listed in Table 3.13 for each casting process (trial case and the casting of main specimens). Figure 3.34 shows the compressive strength test.

Table 3.13: Average Values of Compressive Strength Test.

Test		Samples in a trial case*	Samples in main specimens**
Compressive strength (MPa)	Cube	37.22	39.19
	Cylinder	28.58	32.47

* Time of testing was after 3-month from the casting process.
** Time of testing was after 30-day from the casting process.

Figure 3.34: Compressive strength test.

3.5.2 Modulus of Rupture (Flexural Strength) Test

Prisms with dimensions of (100X100X400) mm are tested according to the (ASTM C78-2002) [113] procedure. The average values of six testing specimens are shown in Table 3.14. Figure 3.35 shows the modulus of the rupture test. The modulus of rupture is calculated from Equation (3-1).

$$f_r = \frac{P\,L}{b\,d^2} \qquad (3\text{-}1)$$

Where: P: applied load, L: length of prism between supports, b: prism width and d: prism height.

Table 3.14: Modulus of rupture values.

Test	Samples in a trial case*	Samples in main specimens**
Modulus of rupture (MPa)	3.90	4.69

* Time of testing was after 3-month from the casting process.
** Time of testing was after 30-day from the casting process.

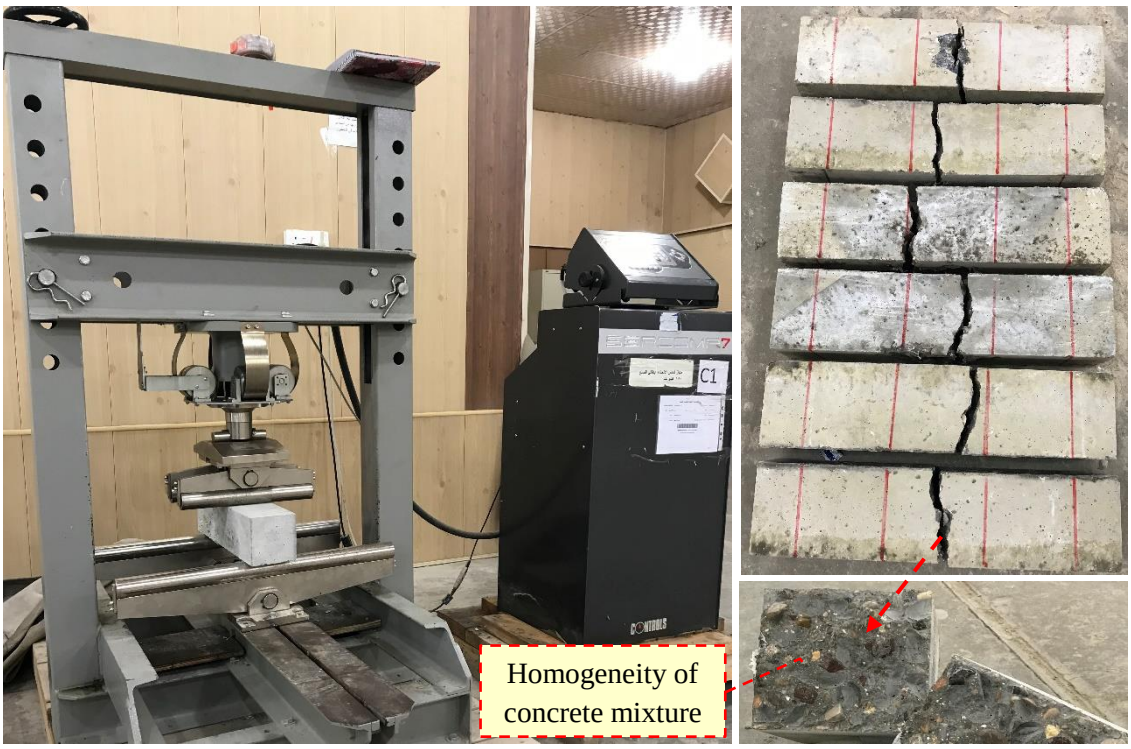

Figure 3.35: Modulus of rupture Test.

3.5.3 Splitting Tensile Strength Test

The split tensile test was computed according to the procedure in the (ASTM C496-2004) specification [106]. The average values of six testing specimens are shown in Table 3.15. Figure 3.36 shows the splitting tensile test. The splitting strength is calculated from Equation (3-2).

$$f_{sp.} = \frac{2P}{\pi\, d\, L} \qquad (3\text{-}2)$$

Where: P: applied load, L: cylinder length and d: cylinder diameter.

Table 3.15: Splitting tensile strength values.

Test	Samples in a trial case*	Samples in main specimens**
Splitting Tensile Strength (MPa)	3.08	3.58

* Time of testing was after 3-month from the casting process.
** Time of testing was after 30-day from the casting process.

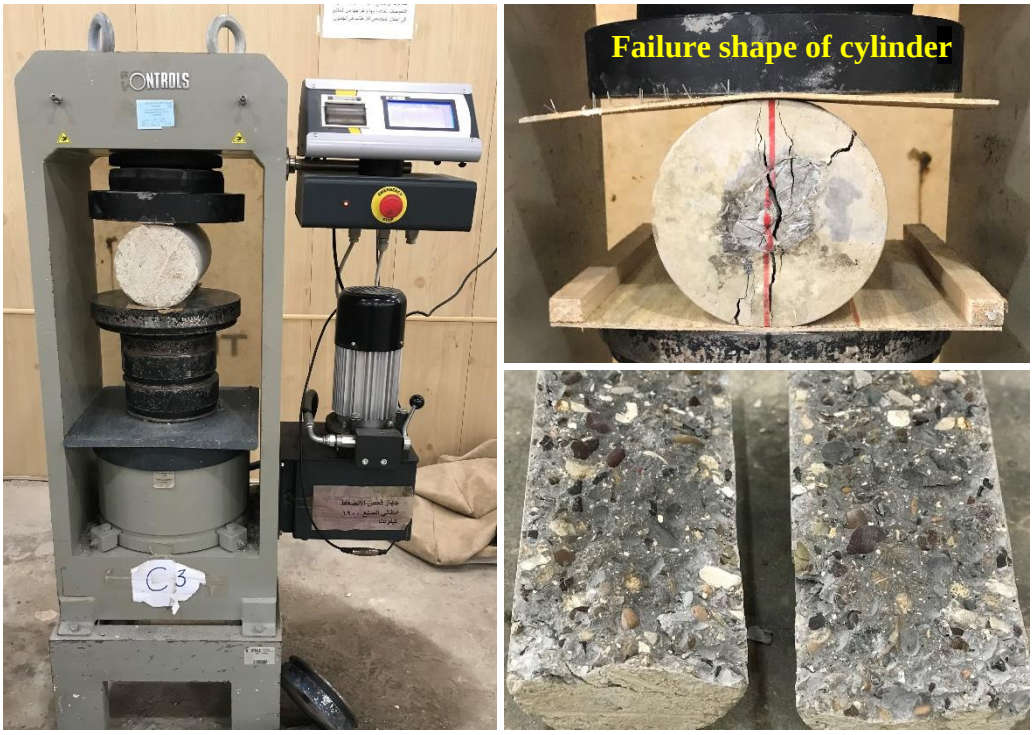

Figure 3.36: Splitting tensile test.

3.6 INSTRUMENTATION

Four linear variable displacement transducers (LVDT) were used in this study. The LVDT1 and LVDT2 are put at the bottom and top of the beam web to measure the joint's rotation. The rotation capacity of the connection was calculated by subtracting the displacement measured by LVDT1 from that measured by LVDT2 (Figure 3.37) and dividing the result by the distance between these two LVDTs. The deflection under the column and the slip between the slab and the steel beam were also measured by LVDT3 and LVDT4, respectively, as shown in Figure 3.37. Because of the symmetrical loading, it was expected that the column rotation would be negligible and thus have no effect on the rotation of the connection. During the tests, this was confirmed.

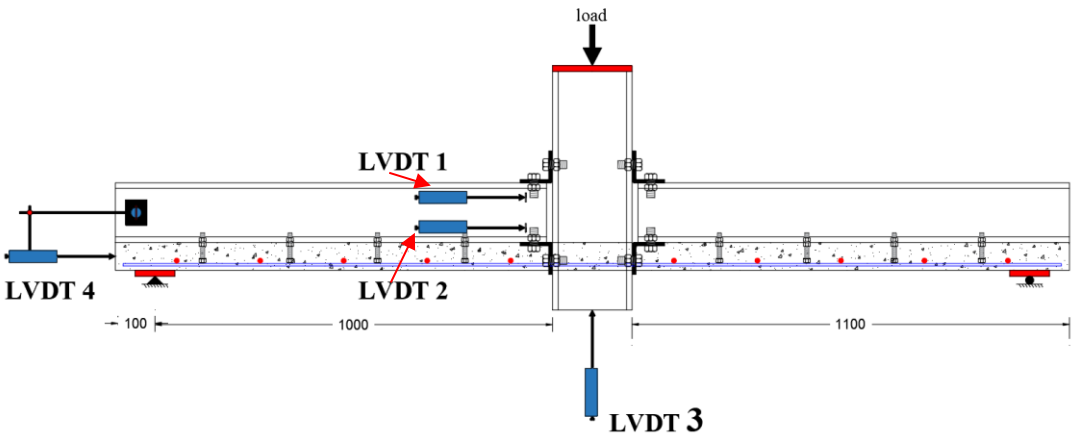

Figure 3.37: Location of LVDT used throughout the tests.

Besides the LVDT measurements, a 2D digital image correlation (DIC) measurement system was used in tests of main composite beam-to-column specimens due to its accuracy in capturing the deformation in structures, which is used to study a wide variety of material performances. It is adapted to measure and analyze surface texture, displacement, and strain on the surface of the monitoring object and obtain two-dimensional strain field data with a visual display.

For this purpose, one side of the specimen was painted white, and a stochastic dot pattern, the so-called speckle pattern, was manually dotted on with black dots on the target area afterwards to provide the surface texture necessary to run the analysis as shown in Figure 3.38. High-resolution images of 4032 x 3024 pixels were taken every 5kN loading by a 12 MP Apple iPhone 7 Plus camera and stored on the computer. The pictures were analysed using the software GOM Correlate Professional (2019). The objective of the deformation analysis in the present study is to examine the linear strain and different deformation components in the joints of the beam-to-column connections. In addition, the slip between the cold-formed steel beam and the concrete slab at various locations along the beam length must be measured.

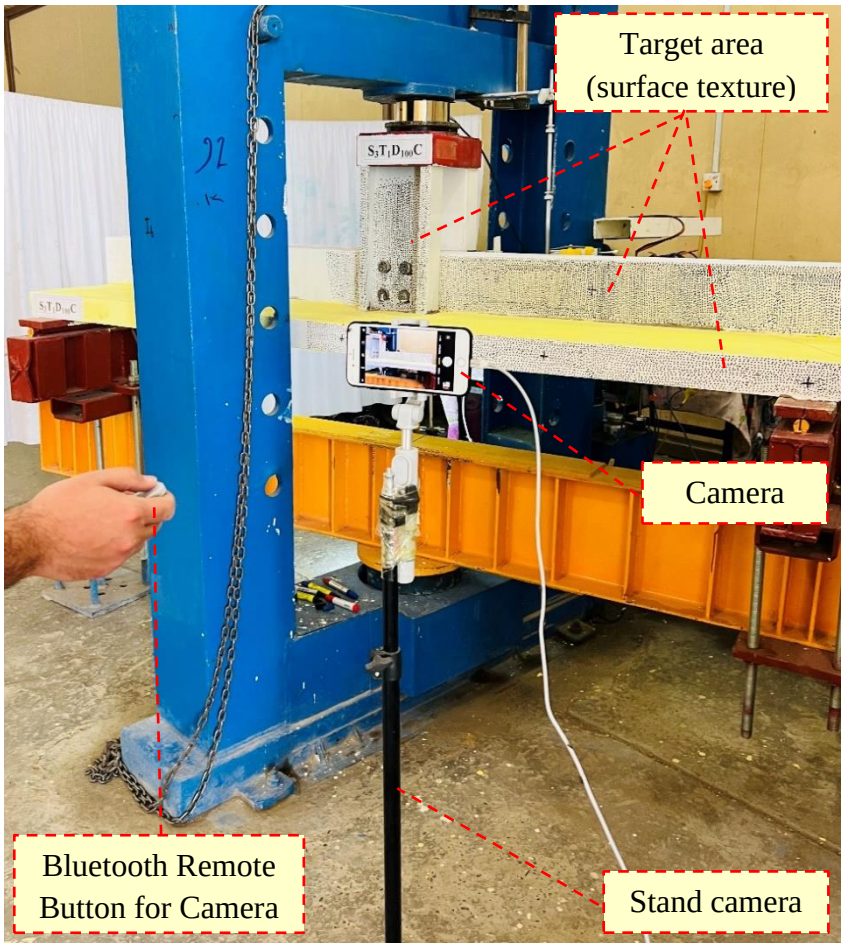

Figure 3.38: Setup of the digital image correlation technique.

3.7 TESTING CONFIGURATION AND LOADING PROCEDURE

The details of support conditions and the load application mechanism in composite joints is shown in Figure 3.39. A roller and pin system placed at an actual span length of 2.2 and 2 m for specimens connected by a top and seat angle and a directly back-to-back web connection, respectively, were used to support the specimens in the customary inverted configuration. A 15 mm thick steel plate was used at the locations of the slab and column support points to alleviate stress concentrations at these locations.

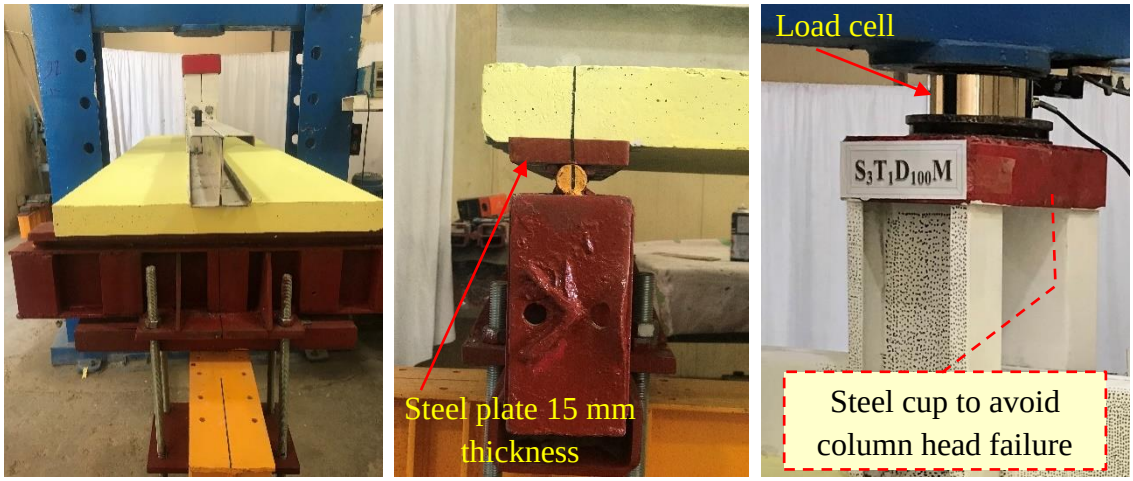

Figure 3.39: Details of supports and the load application.

Thirteen simply supported composite beam-to-column joints were tested, and the specimens installed in the test frame are shown in Figure 3.40. The total length of the beam was 1.1 m, but it was supported by supports spanning 1 m from the face of the column on each side, and the length of the column used was 0.6 m. The support rests on a roller bearing, while the hinge supports at the other end. The composite joints were reversed, with the concrete slab facing down, and the column was subjected to a vertical load. The specimens were loaded using a hydraulic jack and a load cell on the column with a capacity of 300 kN in the Structures Laboratory of the civil engineering department at the University of

Babylon. The load cell readings and LVDT perusals were registered on the data logger and saved on the computer for more analysis.

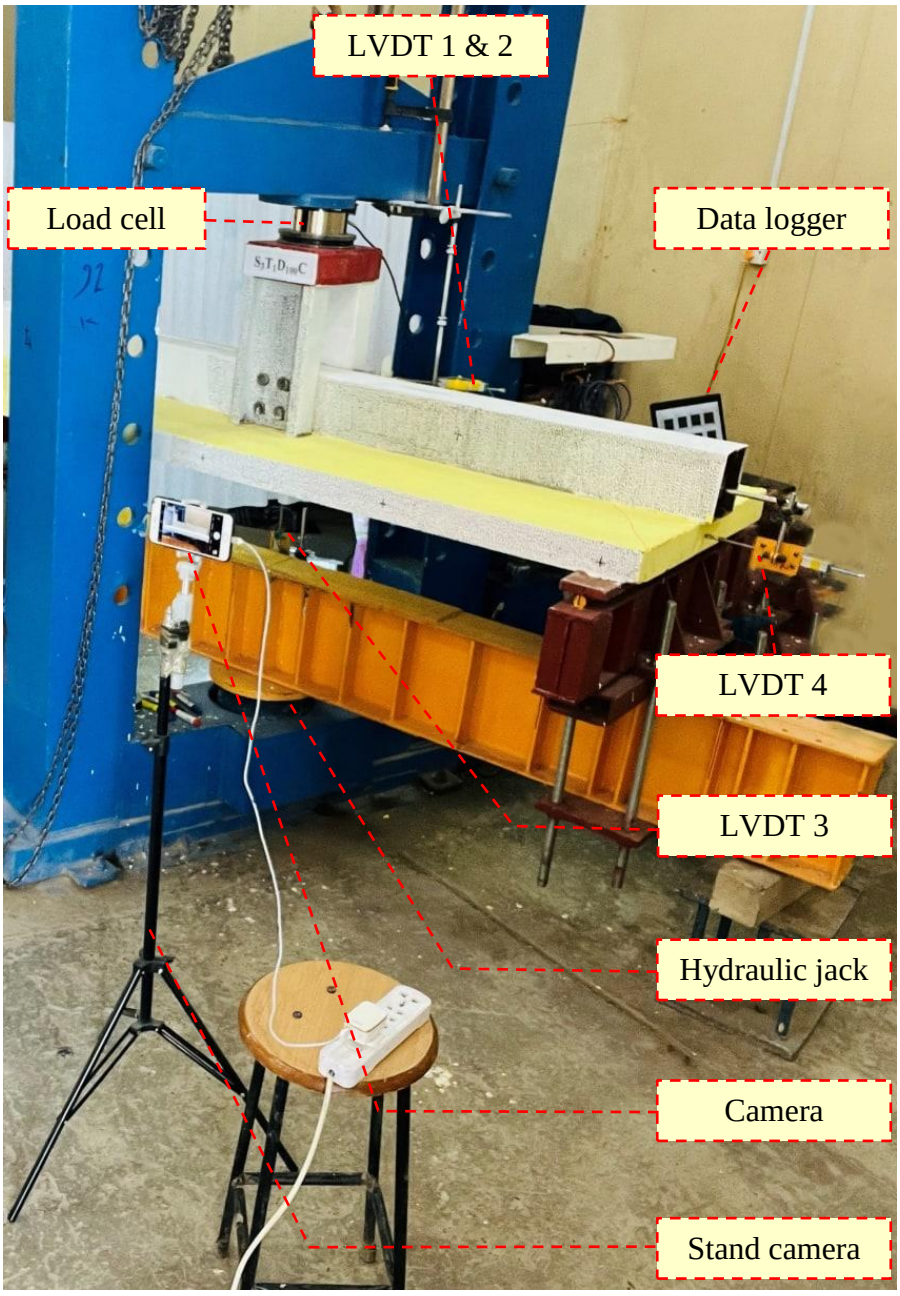

Figure 3.40: Details of Testing Machine Used for composite joint specimens.

Takemura [114] examined six cyclic loading protocol Figure 3.41-a on the behavior of identical RC bridge piers. It was found that the envelope curve of the tested specimens depending on the number of cycles, amplitude of each cycle and sequence of loading cycle. Figure 3.41-b present the envelope curves of tested specimens.

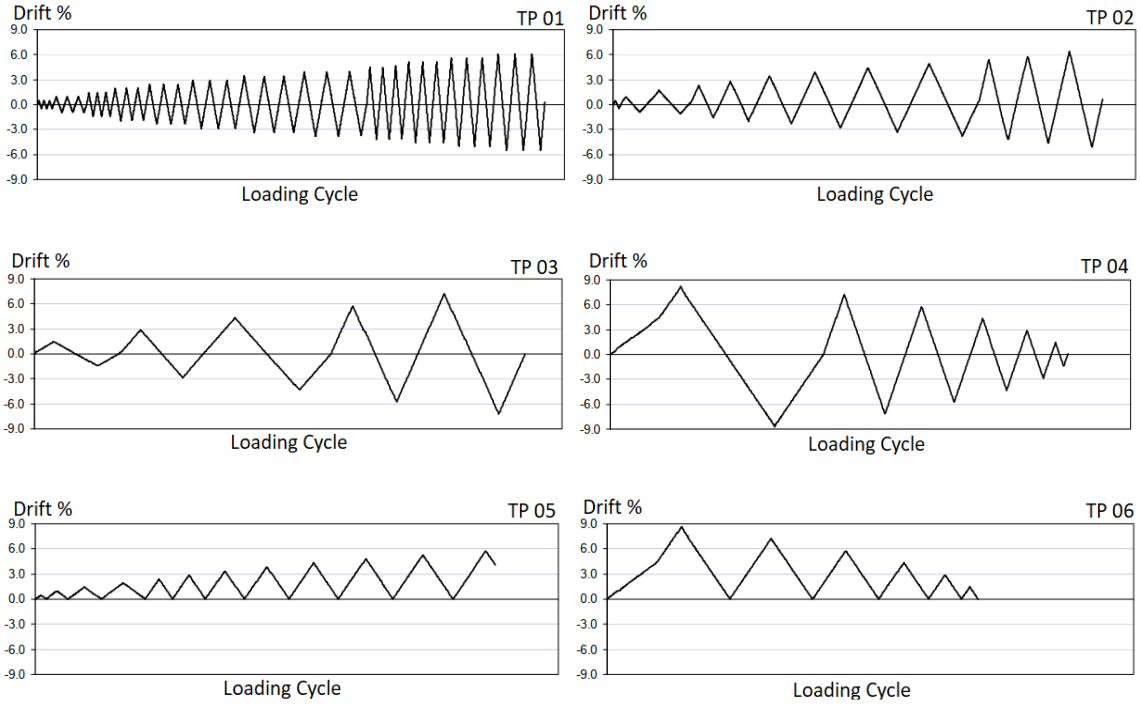

(a)

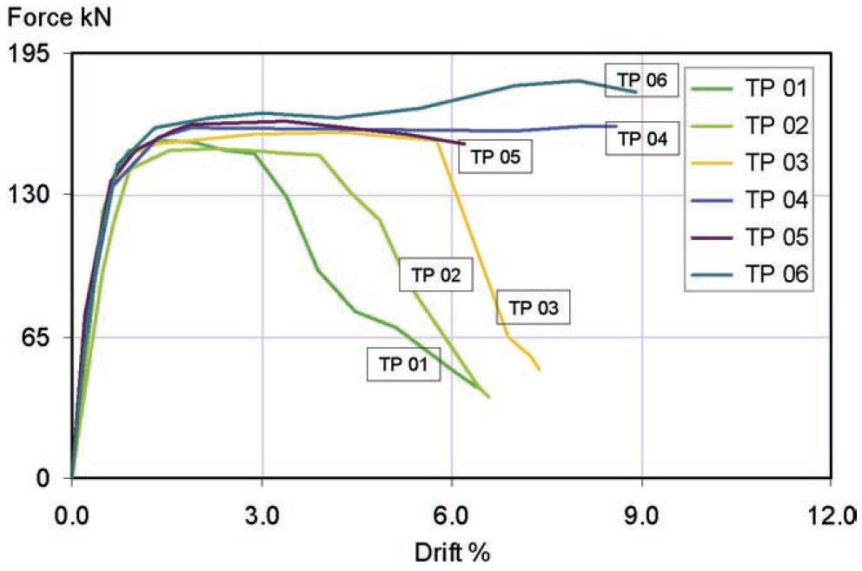

(b)

Figure 3.41: Cyclic response[114]: (a) load cycle protocols and (b) the envelope load-drift curve.

According to above discussion and available equipment, the cyclic load protocol same of TP05 as shown in Figure 3.42 was adopted in present study. So that, For specimens tested under cyclic load, the cyclic load procedure is represented by dividing the ultimate load obtained from the

specimen having the same details but under monolithic load, which was loaded by the divided of the ultimate load (Pu), i.e., 25%Pu, 50%Pu, 75%Pu, 90%Pu, and after that loaded up to failure. The control load cycled four times under each stage's ultimate load amplitude, except the 25% of Pu cycled three times. At the end of each loading stage, the phenomena of concrete cracks and the deformation of steel sections were observed. The loading test was stopped until the maximum load had decreased by 15%.

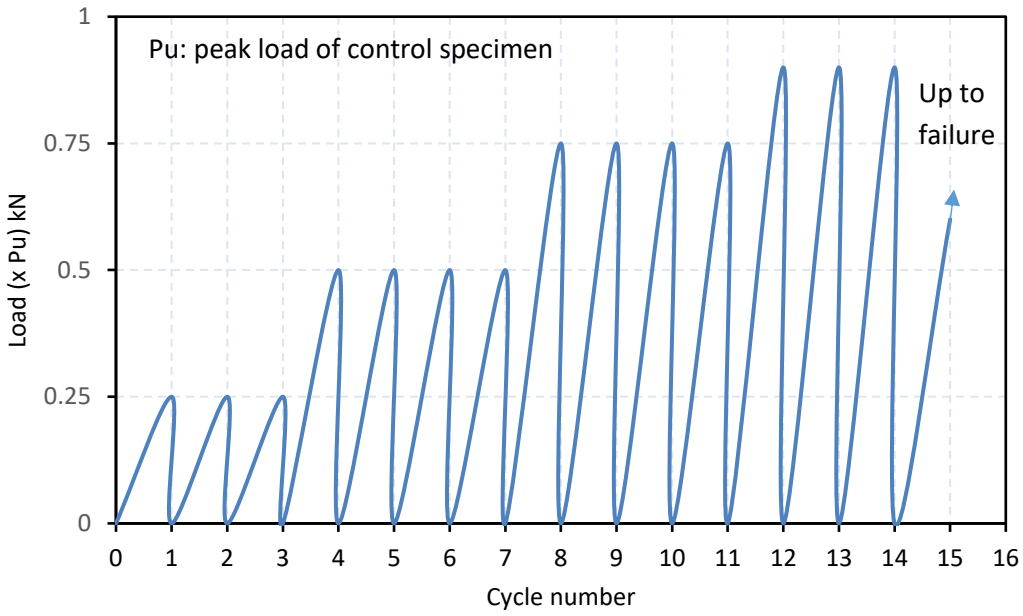

Figure 3.42: The adopted load protocol in the cyclic loading of this study.

Also, the push-out specimens were installed in the test frame, as shown in Figure 3.43, and the specimens were loaded using a hydraulic jack and a load cell on the beam with a capacity of 300 kN. The load cell readings and LVDT perusals were registered on the data logger and saved on the computer for more analysis.

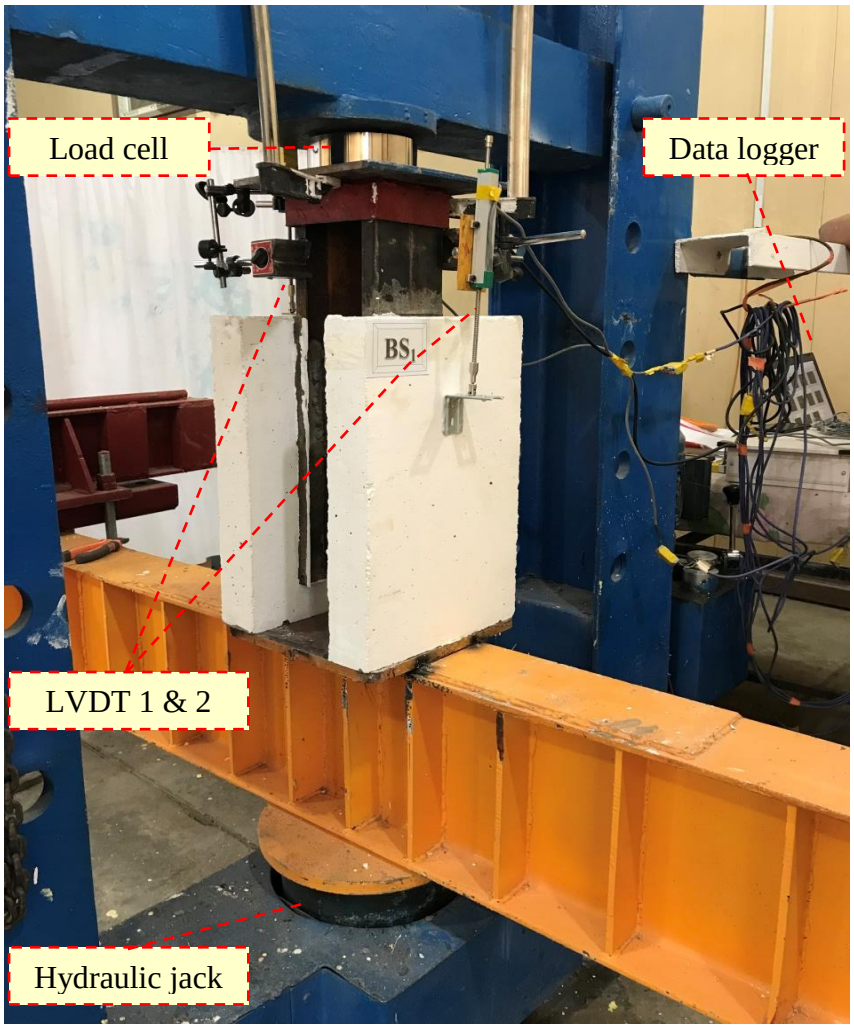

Figure 3.43: Details of testing machine used for push-out specimens.

CHAPTER FOUR
EXPERIMENTAL RESULTS AND DISCUSSION

4.1 INTRODUCTION

The study main objective is to experimentally investigate the behavior of a semi-rigid connection between the cold-formed steel beam and column under monotonic and cyclic loads.

The results of the experimental program illustrated in chapter three are presented and discussed in this chapter. The results of testing nine push-out specimens and thirteen composite joint specimens are discussed in this chapter. The experimental results were compared to each other to determine the significance of the considered experimental variables. The evaluated experimental variables test results were the ultimate moment capacity, rotational capacity, failure mode, and the load-displacement and load-slip relationships for each loading increment. Based on the estimated load-displacement relationships, ductility, stiffness, and energy absorption were calculated and compared for each variable to experimentally assess the ductility and stiffness of a semi-rigid connection. The considered experimental variables of the composite joint were the connection shape, shear connection type, degree of the shear connector and load type.

This chapter also includes the results of the digital image correlation (DIC) measurements to study the strain in different locations of the composite joint.

4.2 PUSH-OUT SPECIMENS RESULTS

The effects of variations in beam section, bolt diameter, and shear connector type on the shear resistance, slip capacity, stiffness, and ductility

of a single embedded bolted shear connector and cold-formed steel plate shear connector was assessed by carrying out experimental studies. Table 4.1 presents the details of the experimental studies' push-out specimens.

Table 4.1: Results of the tested push-out specimens.

Specimen	Load at first slip (kN)	Maximum load (kN)	Peak slip (mm)	Failure modes
PSIB-10*	50.45	109.12	3.88	Bolt fracture
PSBB-10	36.46	94.68	3.51	Bolt fracture
PSIB-14	60.41	174.91	6.85	Concrete slab cracking
PSBB-14	58.09	145.58	6.61	Concrete slab cracking
PSIP-2	18.03	64.61	0.43	Hole bearing failure for connection bolt
PSIA-2	19.03	69.05	0.90	Hole bearing failure for connection bolt
PSIDA-4	3.48	62.06	6.63	Hole bearing failure for connection bolt
PSIC-2	19.48	67.11	0.53	Hole bearing failure for connection bolt

* Each value for this specimen represents the average value of the two specimens' results.

4.2.1 Bolted shear connectors

In this part, push-out tests were performed on four specimens with different cross-section shapes and different bolt diameters to study the effect of the cross-section of the beam and bolt diameter on the behavior, stiffness, and ductility of a single embedded shear connector bolt. The results of these tests are listed in Table 4.1. The maximum load of specimens PSIB-10, PSBB-10, PSIB-14, and PSBB-14 equals 109.12, 94.68, 174.91, and 145.85 kN with congruous interface slips of 3.88, 3.51, 6.85, and 6.61 mm, respectively. The effect of the beam's cross-section and the bolt's diameter on the load-slip response of the push-out specimen tests is presented in Figure 4.1, respectively. When the interface friction was broken, the first slip appeared at about 50.45, 36.46, 60.41, and 58.09 kN for PSIB-10,

PSBB-10, PSIB-14, and PSBB-14, respectively. After that, the slip increases gradually until the failure, and when the load becomes close to collapse, a separation is observed between the CFS beam and the concrete slab.

The box section of the cold-formed steel beam caused a reduction in the ultimate load capacity by about 13% and 16.7% when compared with specimens that have an I-section CFS beam for a bolted shear connector with 10 and 14 mm diameter, respectively. This reduction in ultimate load may be due to the flange being more restricted in the box section and the stresses being equal in both directions due to the symmetry of the box section, so the bolt bears a higher shear force. In contrast, in the I-section, the shear stress is different in both directions and the small stress is transferred in the direction of the bolt. Which makes the stress concentration on the bolt in the box section greater than on the bolt in the I-section; thus, the bolt fails faster. Moreover, an improvement in the strength capacity of up to 60% and 54% was obtained by increasing the diameter of the single embedded bolt shear connector from 10 mm to 14 mm for the I-section and box-section of a cold-formed steel beam.

Figure 4.1 depicts the load-slip curve for all specimens tested. Their load-slip responses can be broadly classified into two distinct phases: a region exhibiting full shear interaction at the steel-concrete interface, where the magnitude of the slip between the slab and the CFS beam was nearly zero, indicating the near-full shear interaction provided by the friction-grip mechanism. The applied load increases significantly during the second stage, a region of partial shear interaction in which the connection exhibits a load-slip response. It must be noted that when graphing the load-slip curves, the slip value was taken as the average of two LVDTs used to record the vertical slip between the CFS beam and concrete slabs.

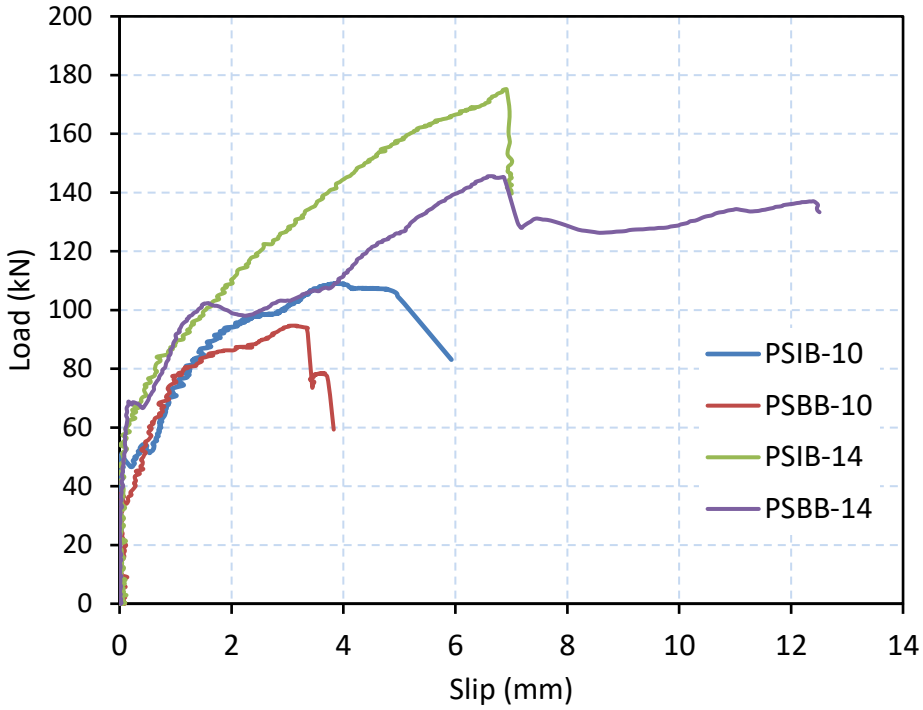

Figure 4.1: Load-slip curves of all tested push-out specimens with bolted shear connector.

4.2.1.1 Failure mode

The failure modes of specimens are listed in Table 4.1. In this part, two types of push-out specimen failure were observed: a bolt fracture, as shown in Figure 4.2, for specimens with a diameter of 10 mm of a single embedded bolted shear connector for both I and box sections of the CFS beam. Also, for these specimens, no cracking occurred on the concrete slab surface, only some crack of the concrete under the beam flange edge at a load of about 52 kN. The splitting between the concrete slab and CFS beam started appearing when the load was equal to 85 and 75 kN for specimens PSIB-10 and PSBB-10, respectively. The other type is the concrete slab failure due to some crack around the bolted shear connector region, which occurred for specimens with a bolt diameter of equal to 14 mm, without fracture of the bolted shear connector, as shown in Figure 4.3.

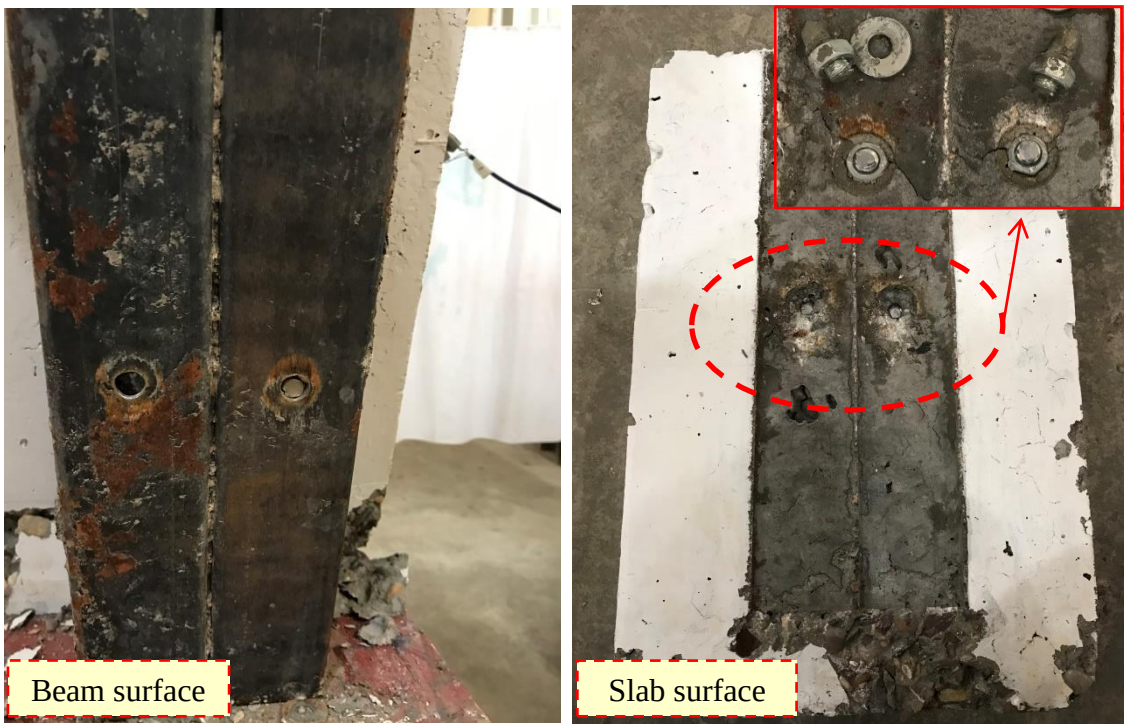

Figure 4.2: The failure mode of specimens PSIB-10 and PSBB-10.

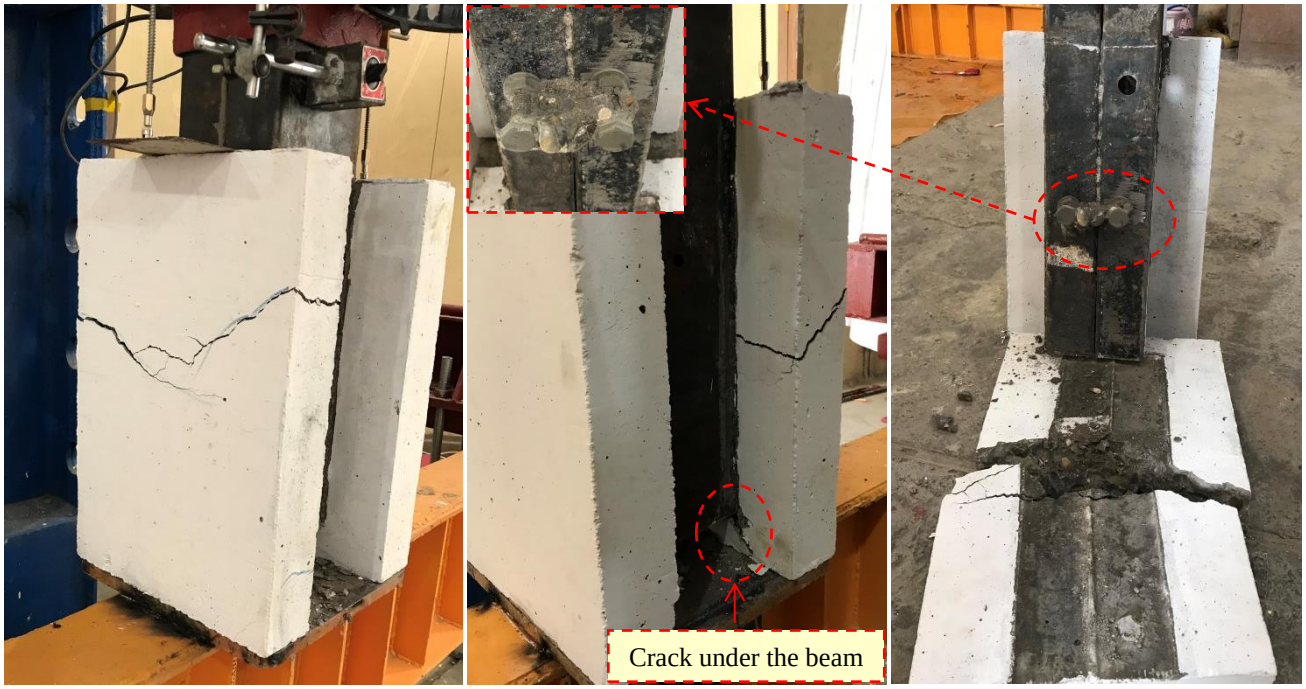

Figure 4.3: The failure mode of specimens PSIB-14 and PSBB-14.

It should be noted that the cross-section of the cold-formed steel beam does not affect the failure mode of the specimens which have the same bolted shear connector diameter. At the same time, the increase in the diameter of the bolt shear connector with a single embedded nut led to a

change in the failure mode from the fracture of the bolt for samples that contain a shear conductor with a diameter of 10 mm to the fracture of the concrete slab for samples that contain a shear conductor of 14 mm. This is due to the high shear connection bolt that leads to stress concentration in the concrete and cracking before failure occurs in the bolt.

4.2.1.2 Stiffness and ductility

As shown in Figure 4.4, there are many significant indexes, such as stiffness and ductility, for analyzing push-out results. The shear connector stiffness (Ksc) represents the secant modulus at serviceability load corresponding to 0.7Pu [36]. Furthermore, EC4 defines δu as the slip corresponding to 0.9Pu in the descending part of the load-slip curve. The ultimate slip (δu) is an important element used by EC4 to identify shear connectors in terms of ductility. According to this code, if the distinctive slip ability of the shear connector (δuk=0.9δu) is equal to or greater than 6 mm, the shear connector is considered ductile. It is worth noting that a ductile shear connector has enough deformation capacity before failing to recognize the shear connection's perfect plastic behavior. The results of the stiffness and ductility tests for bolted shear connectors are listed in Table 4.2.

The stiffness of the bolted shear connector with a single embedded nut for specimens with a 10 mm bolt diameter equals 72.24 and 88.7 kN/mm, related to specimens PSIB-10 and PSBB-10, respectively. Also, for specimens PSIB-14 and PSBB-14 with a 14 mm bolt diameter, the stiffness is 47.57 and 69.32 kN/mm, respectively. As expected, using a box section for the beam increases the shear connector's stiffness by about 23% and 46% for specimens with 10 mm and 14 mm bolt diameters, respectively.

The best ductility performance is associated with specimen PSBB-14, which has a peak slip of 6.61 mm and an ultimate slip (δu) of 7.11 mm. Figure 4.1 shows that specimen PSIB-14 ranks second in terms of ductility, with a peak of 6.85 mm and a δu of 6.97. Furthermore, comparing specimens with the same cross-section shape and various bolt diameters, it is concluded that specimens with a bolt diameter of 14 mm achieve better ductility performance than specimens with a bolt diameter of 10 mm. Furthermore, any connector with a characteristic slip (δuk=0.9δu) of 6 mm or more is a ductile connector, according to EC4. As a result, shear connectors with a 14 mm bolt diameter can be assumed to be ductile under the specific experimental setup, concrete compressive strength used, materials of the bolts and nuts, and the CFS thickness. So that they can also be used in partial simultaneous connections, according to EC4.

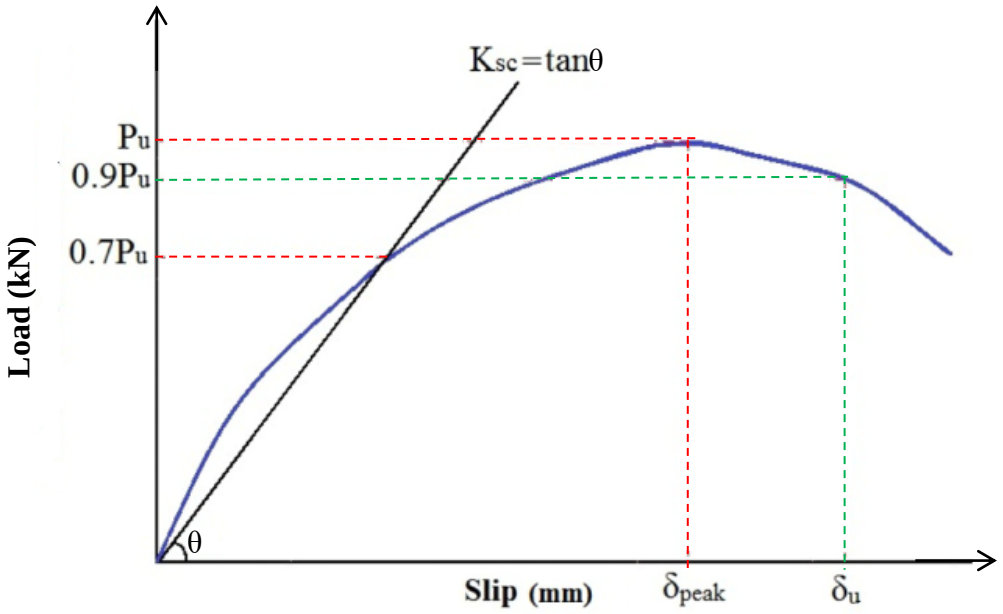

Figure 4.4: The characteristic value used to evaluate the push-out test identical to EC4 [36].

4.2.2 CFS shear connectors

The load-slip curves of the push-out specimens' tests are offered in Figure 4.5. Specimens PSIP-2, PSIA-2, PSIDA-4 and PSIC-2 are listed in Table

4.1, which reached maximum load capacities of 64.61, 69.05, 62.06 and 67.1 kN with corresponding average slips of 0.43, 0.9, 6.63 and 0.53 mm, respectively.

The specimens PSIP-2, PSIA-2 and PSIC-2 have the same behavior, noting non-ductile behavior. The specimen PSIC-2 with a corrugated cold-formed steel plate shear connector with this shape of plate shear connector was as efficient as the angle-shaped shear connector. However, the length of the conductor immersed in the concrete slab is about half less than the length of the angled shape shear connector. The specimen PSIDA-4 differed from the other specimens, which had a ductile behavior.

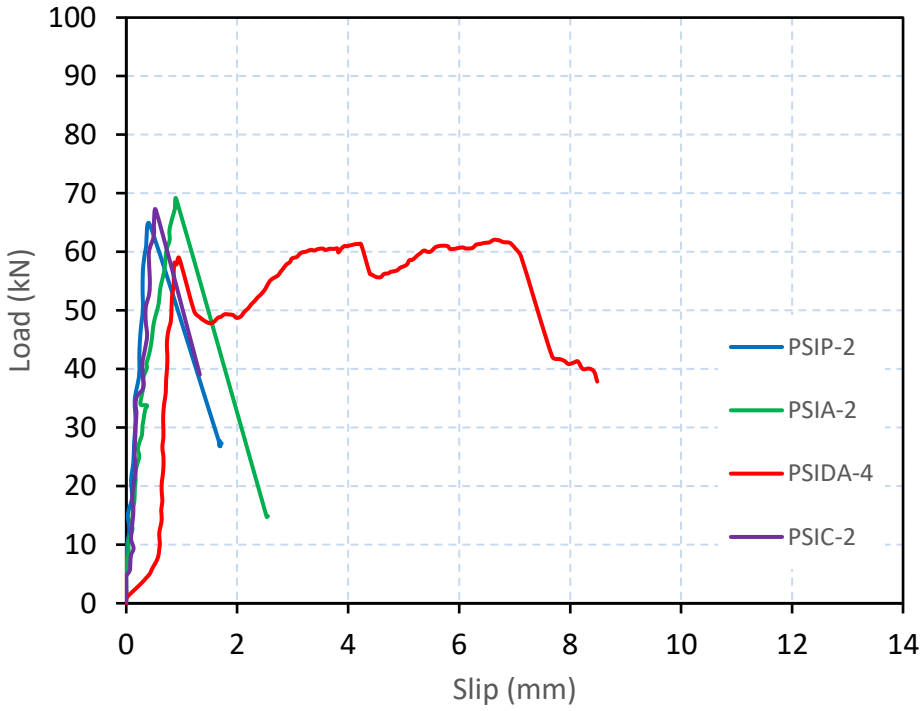

Figure 4.5: Load-slip curves of the tested push-out specimens with CFS shear connector.

4.2.2.1 Failure mode

The failure of these specimens was suddenly due to a hole-bearing failure for the connection bolt without any crack on the concrete slab surface, as

shown in Figure 4.6. The reason for this sudden failure may be attributed to the use of a single bolt to connect the CFS beam and the plate shear connector, which leads to hole expansion of the bolt connection and slippage of the plate shear connector due to the small thickness. Also, a slight separation occurred between the concrete slab and the CFS beam, which was observed during the test .

The specimen PSIDA-4 also failed due to a hole-bearing failure for the connection bolt. Still, the hole expansion of the bolt connection was small and expanded gradually, which gave a ductile behavior compared to the other samples because of the use of a double-angle shear connector (4 mm thickness of shear connector).

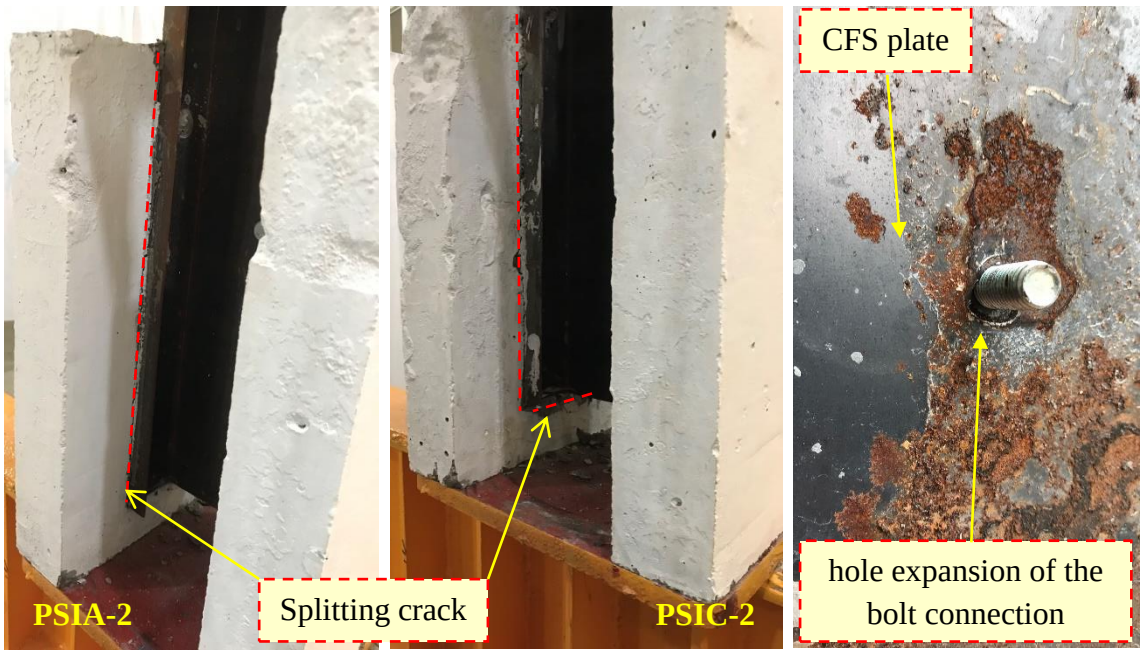

Figure 4.6: Failure modes of push-out specimens with CFS plate shear connector.

4.2.2.2 Stiffness and ductility

The shear stiffness of the connector can indicate its deformation ability, which is used to assess the performance of the composite structure behavior

in the serviceability limit state. Stiffness is calculated in the same way as used for the bolted shear connector, as shown in Figure 4.4 .

The results of the stiffness and ductility tests for CFS plate shear connectors are listed in Table 4.2. These specimens give high stiffness due to the small slip between the CFS beam and concrete slab, except for the specimen PSIDA-4, which gives low stiffness compared with other specimens that have CFS plate shear connectors. Also noted, only PSIDA-4 has a ductile behavior with a δu equal to 7.45 mm more than the required value in Eurocode 4 (6 mm).

Table 4.2: The results of stiffness from the push-out tests.

Specimen	Ultimate force (kN)	Peak slip δpeak (mm)	Ultimate slip δu (mm)	Stiffness (Ksc) (kN/mm)
PSIB-10	109.12	3.88	5.26	72.24
PSBB-10	94.68	3.51	3.39	88.70
PSIB-14	174.91	6.85	6.97	47.57
PSBB-14	145.58	6.61	7.11	69.32
PSIP-2	64.61	0.43	0.65	173.95
PSIA-2	69.05	0.90	1.11	97.65
PSIDA-4	62.06	6.63	7.45	59.51
PSIC-2	67.11	0.53	0.73	134.22

4.3 RESULTS OF COMPOSITE JOINT SPECIMENS

The main structural characteristics observed and recorded during the test of each composite beam-to-column joint specimen and at each stage of loading were used to evaluate the structural behavior of the tested composite joint specimens. A composite joint's moment-rotation relationship is a feature that defines its behavior. This curve can be used to calculate the three structural properties that characterize the global behavior

of joints: stiffness, bending resistance, and rotation capacity. These values are calculated from the test curve using the following formula:

1- Ultimate bending resistance (Mu)

The maximum resistance reached in the moment-rotation relationship corresponds to a joint ultimate bending resistance Mu. The results of the tests are shown in Table 4.3.

$$\text{Moment capacity} = \frac{\text{Maximum load (P)} * \text{length of span (L)}}{4} \qquad (4-1)$$

2- Rotation capacity

The rotation capacity of a joint is defined as the rotation at which a reinforcement bar ruptures or the test is terminated because of excessive deformation of the specimen. In case two, the rotation capacity of the associated composite joint is greater. This must be considered when evaluating joint rotation capacity. So that, the rotation at the maximum load is defined as the rotation capacity.

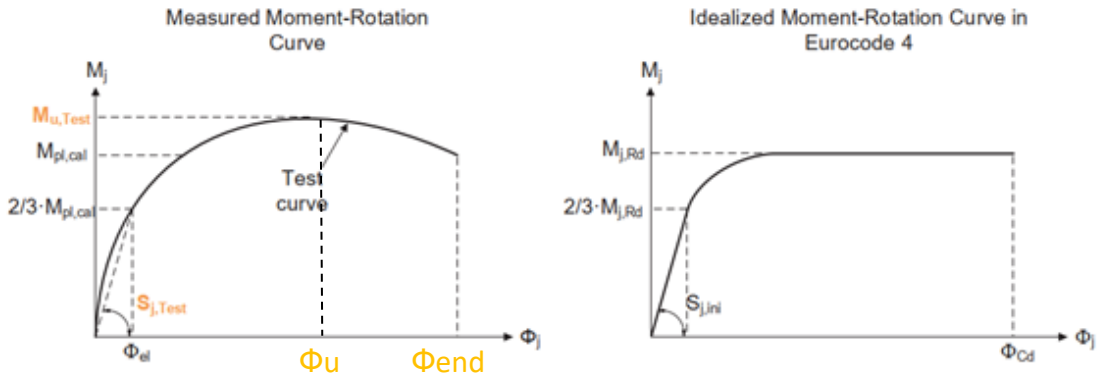

Figure 4.7: Determination of the structural properties of the joint based on the test and comparison to EC 4 [72].

The main test results of the composite joint, including the load and moment capacity, rotation of the joint, and other details, are listed in Table 4.3.

Table 4.3: Experimental results of the tested composite joints.

Group	Sample name	First crack load (kN)	Ultimate load (kN)	Ultimate deflection (mm)	Moment capacity (kN.m)	Rotation capacity (mrad)	Rotation at test end (mrad)
Trial case	$TS_1T_1D_{100}M$	5.5	26.53	20.58	14.93	13.72	14.85
	TS_1T_2M	5	29.16	27.79	15.76	17.22	19.50
	TS_1T_3M	5	29.73	30.67	16.35	21.01	25.21
Control	$S_1T_1D_{100}M$	16.2	69.81	66.22	38.28	50.04	87.40
One	S_1T_2M	10	78.50	55.65	43.18	50.16	84.02
	S_1T_3M	10	73.68	57.69	40.48	76.92	82.74
Two	$S_1T_1D_{50}M$	16	69.50	74.35	37.40	66.75	85.48
	$S_1T_1D_{25}M$	16	69.00	63.56	37.79	89.65	117.02
Three	$S_2T_1D_{100}M$	28	92.92	16.38	46.00	11.87	27.00
	$S_3T_1D_{100}M$	41.3	132.44	19.34	66.00	11.11	28.83
Four	$S_1T_1D_{100}C$	15 (C1)*	67.38	80.17	37.06	89.62	94.77
	$S_2T_1D_{100}C$	23 (C4)	91.54	18.06	45.63	23.41	33.28
	$S_3T_1D_{100}C$	30 (C3)	129.81	18.89	64.90	10.29	28.36

* (C1): represent cycle one of the loads.

3- Joint stiffness

The joint stiffness of a connection is an important parameter used in the analysis of composite frames. Also, it affects the bending moment transferred at a beam-to-column joint and the classification of the joints. In this study, the initial stiffness (Ki) and secant stiffness (Ks) were calculated to classify the connection according to EC4 and AISC 2005, respectively. The initial stiffness is defined at 2/3 of the expected plastic bending resistance of the joint $M_{pl,cal}$ (which is approximately equal to 0.85 of the ultimate moment of connection), which is calculated using the measured yield strength of materials. This definition allows us to compare the

stiffness values obtained from the tests $S_{j,Test}$ with the analytical values $S_{j,ini}$ according to EN 1994-1-1 (2004), as shown in Figure 4.7.

The secant stiffness, Ks, is calculated at service loads by dividing the moment (roughly equal to 0.85 of the ultimate moment of connection) by the corresponding rotation. If $\frac{k_s L}{EI} \geq 20$, the connection is considered fully rigid or FR connection. If $\frac{k_s L}{EI} < 2$, the connection is simple (it rotates without increasing moment). The stiffness of the connection between these two boundaries is classified as partially restrained or semi-rigid, and the connection's strength, stiffness, and ductility should be considered in the analysis. The results of the secant and initial stiffness of composite joint specimens are shown in Table 4.4.

Table 4.4: Slip and stiffness results of the tested composite joints.

Group	Sample name	Slip at ultimate load (mm)	Slip at test end (mm)	Initial stiffness (kN.m/mrad)	Secant stiffness (kN.m/mrad)
Trial case	$TS_1T_1D_{100}M$	0.05	-	1.7	1.58
	TS_1T_2M	0.07	-	2.32	1.50
	TS_1T_3M	0.12	-	0.92	0.78
Control	$S_1T_1D_{100}M$	0.60	0.66	1.54	1.23
One	S_1T_2M	0.15	0.16	2.26	1.50
	S_1T_3M	1.47	1.92	1.91	1.07
Two	$S_1T_1D_{50}M$	1.68	2.18	1.23	0.85
	$S_1T_1D_{25}M$	2.09	3.40	0.82	0.55
Three	$S_2T_1D_{100}M$	0.16	0.31	4.86	4.39
	$S_3T_1D_{100}M$	0.43	0.53	21.06	11.54
Four	$S_1T_1D_{100}C$	1.85	1.94	0.82	0.50
	$S_2T_1D_{100}C$	0.74	0.94	4.57	3.10
	$S_3T_1D_{100}C$	0.76	0.80	13.91	10.62

4.4 RESULTS OF TRIAL CASE SPECIMENS

This part presents the experimental results of the three composite CFS beam-to-column joint specimens with a 300 mm slab width and minimum reinforcement. The appraisal describes the specimens' observed behavior during the tests and their efficiency in strength and rotation. The results digest of this group is given in Table 4.3.

4.4.1 Failure mode and crack pattern

The cracks were noticed at about the edges of a column and spread diagonally from the tips of the column to the slab ends, as shown in Figure 4.8. At a load of 5.5 kN, the first crack for the three composite joints appeared at the corner of the column face. The other cracks for specimen $TS_1T_1D_{100}M$ appeared at a load of 10 kN at a distance of 23 cm from the column face (at the level of the first row of the shear connector). In contrast, for specimens TS_1T_2M and TS_1T_3M, the other cracks were noticeable 18 cm away from the column face at a load of 15 kN.

The failure shape in specimen $TS_1T_1D_{100}M$ was due to a reinforcement fracture in the region of maximum bending. After that, lateral bending occurred due to a fracture of the concrete slab, as shown in Figure 4.9. In contrast, the specimens TS_1T_2M and TS_1T_3M with cold-formed steel plate shear connectors were also governed by the failure of the slab followed by fracture of reinforcement.

There was no damage to the bolts or the column walls in any composite beam-to-column joint specimens; though a slight deformation in the angle plate was apparent at the tensile bolt row. The lower compression row's seat angle plate and bolts remained unaffected.

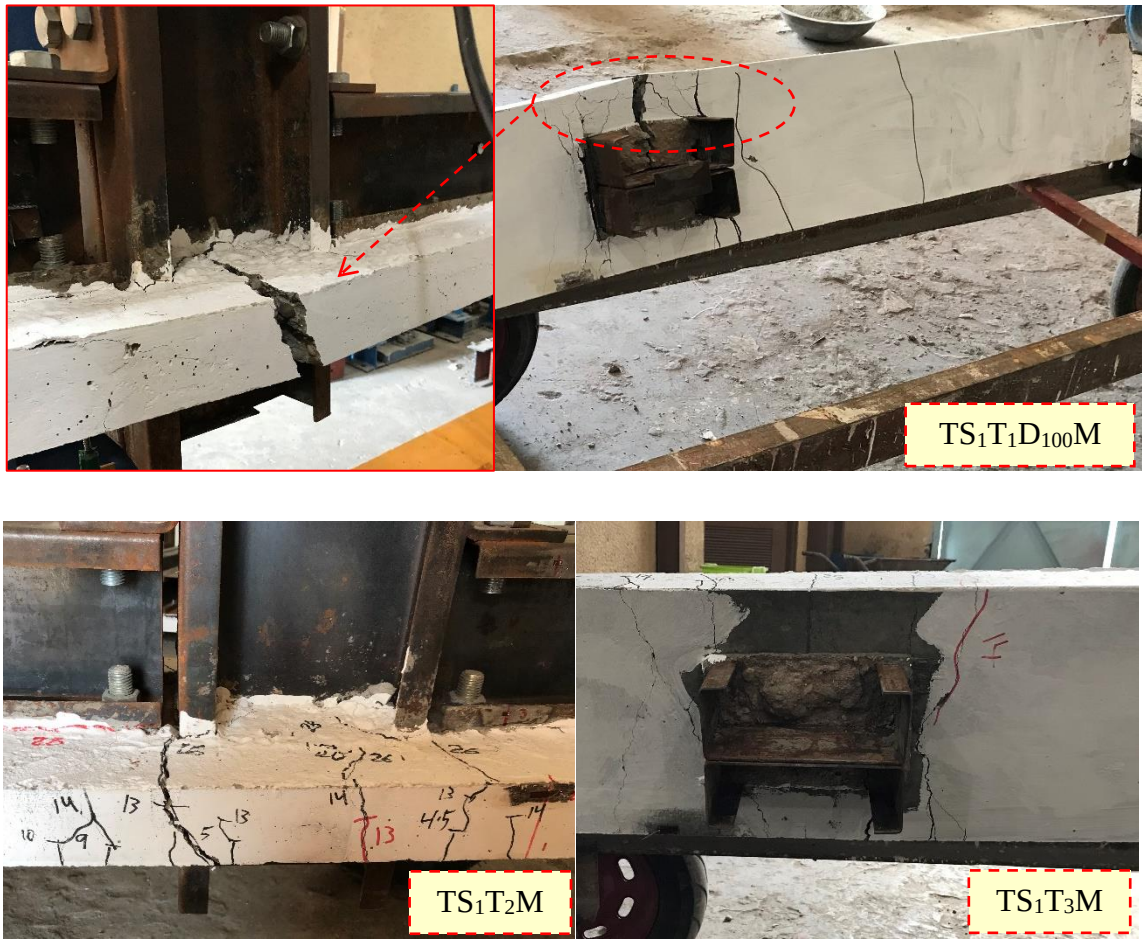

Figure 4.8: Pattern of cracks around the connection area.

Figure 4.9: Shows the lateral bending of specimen $TS_1T_1D_{100}M$.

4.4.2 Load versus deflection

The data for the load-deflection curves were acquired from the LVDT-3 and are shown in Figure 4.10. When the applied load exceeds 5 kN, the specimens begin to deform. The deflection was gradually incremented until the load reached to ultimate. This indicates that the specimen is still in elastic limit behavior and became non-linear when the final load is reached. The $TS_1T_1D_{100}M$, TS_1T_2M, and TS_1T_3M deflections at ultimate load were 20.58, 27.72, and 30.67 mm.

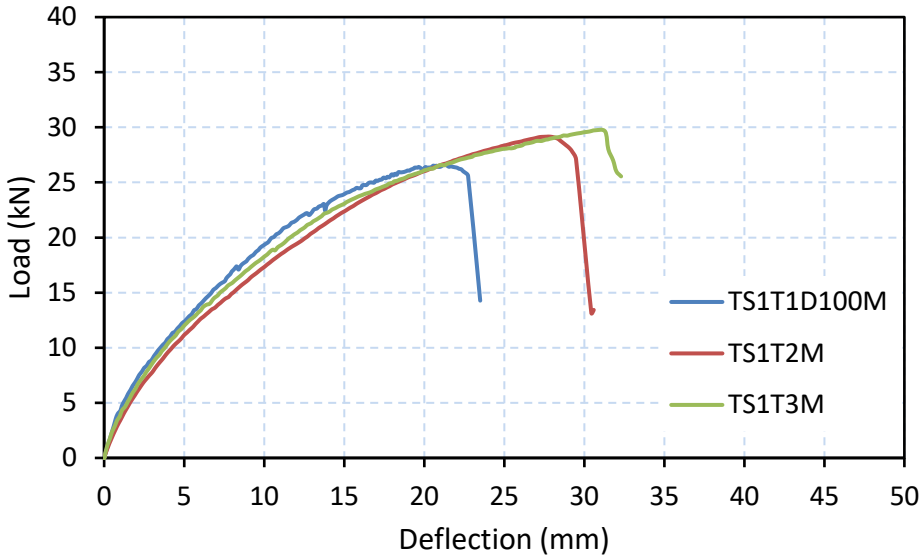

Figure 4.10: Load-deflection curves of trial case specimens.

4.4.3 Moment vs. rotation

Figure 4.11 depicts the moment-rotation curves. Due to fully tightened bolts, a high slope was observed at loads less than 5 kN. After a load of more than 5 kN, the curve declines. This occurred due to a crack taking place in the concrete slab.

When compared to the other two specimens, the specimen TS_1T_3M had a higher rotation value, which was due to the high displacement between the concrete slab and the CFS beam. When the degree of the shear

connection in the composite connections was lowered, the highest moment was achieved at a higher rotational value, according to Loh, H. Y. et al. [66].

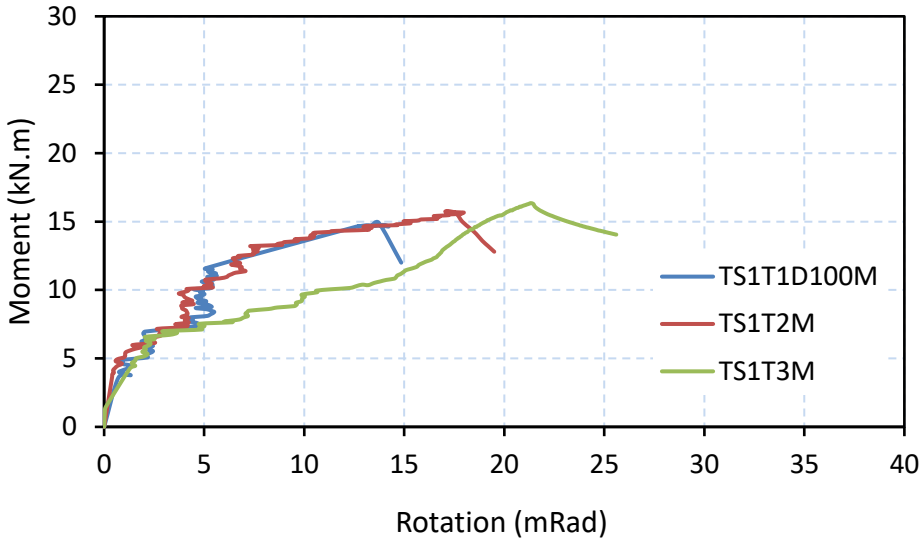

Figure 4.11: Moment-rotation curves of trial case specimens.

4.5 RESULTS OF CONTROL SPECIMEN ($S_1T_1D_{100}M$)

The specimen $S_1T_1D_{100}M$ is representative of the control specimen for the other specimens, which reached a maximum load capacity equal to 69.81 kN. The load-deflection curve for this specimen is shown in Figure 4.12 .

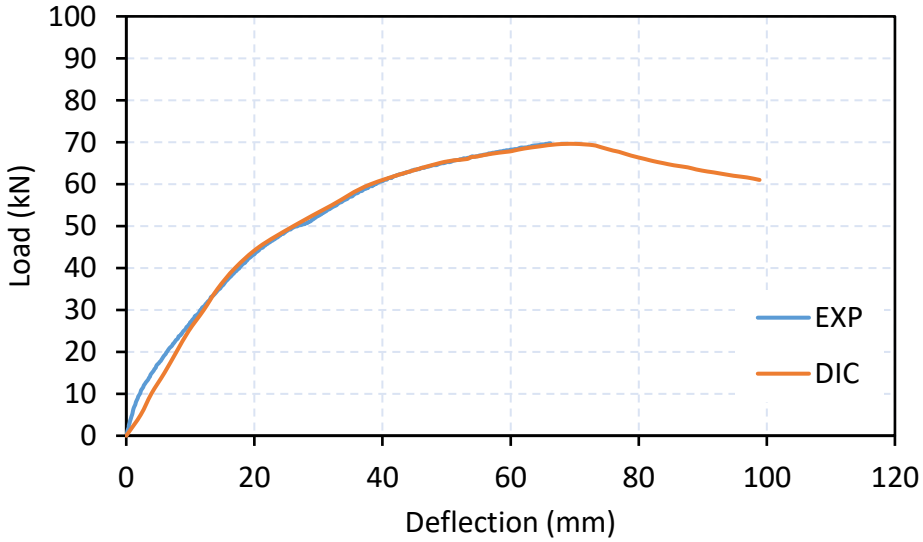

Figure 4.12: Load-deflection curve for specimen $S_1T_1D_{100}M$.

This study used the DIC technique to monitor the deformation in composite joint specimens. The load-deflection curve obtained from the DIC was compared with the experimental curve for specimen $S_1T_1D_{100}M$, gave excellent agreement, as shown in Figure 4.12, and for the other specimens also gave excellent agreement as shown in Figure 4.13.

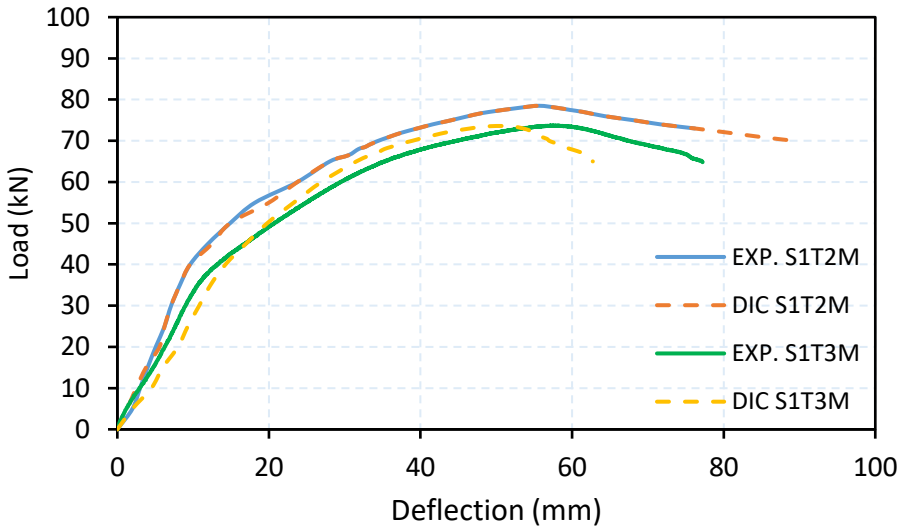

(a) Specimens S_1T_2M and S_1T_3M.

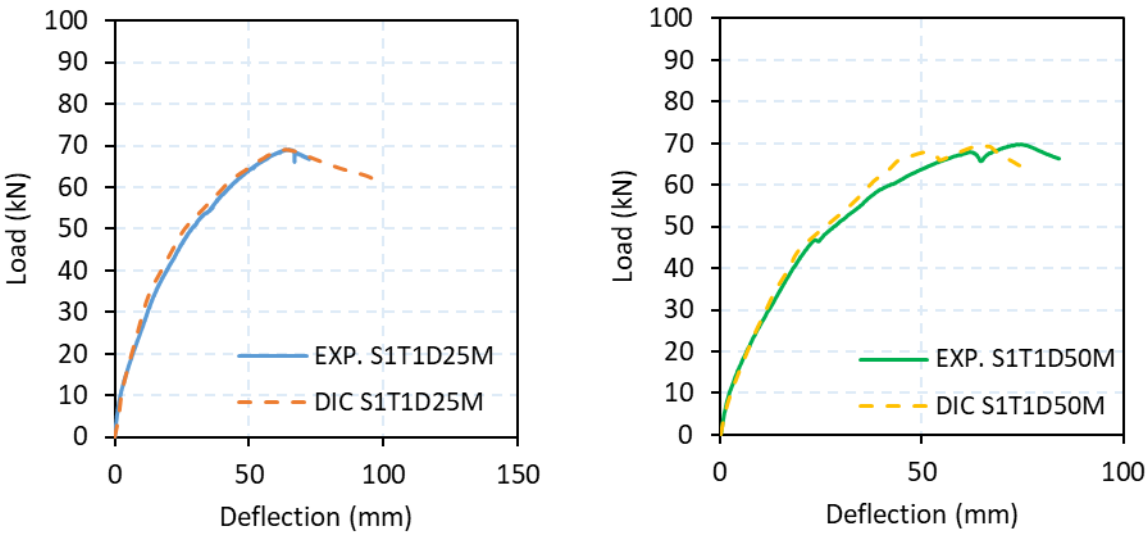

(b) Specimens $S_1T_1D_{25}M$ and $S_1T_1D_{50}M$.

Figure 4.13: load-deflection curve for: (a) specimens S_1T_2M and S_1T_3M and (b) specimens $S_2T_1D_{100}M$ and $S_3T_1D_{100}M$. (Continue)

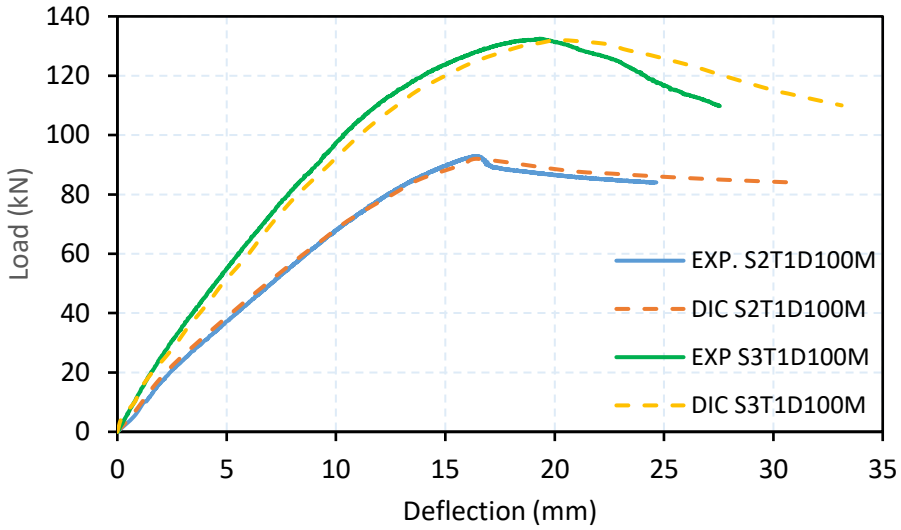

(c) Specimens $S_2T_1D_{100}M$ and $S_3T_1D_{100}M$.

Figure 4.13: Load-deflection curve for: (a) specimens S_1T_2M and S_1T_3M, (b) specimens $S_1T_1D_{25}M$ and $S_1T_1D_{50}M$ and (c) specimens $S_2T_1D_{100}M$ and $S_3T_1D_{100}M$.

4.5.1 Moment-rotation curves

The moment-rotation curve obtained from the test is shown in Figure 4.14. The ultimate moment, rotation, and initial rotational stiffness values are summarized in Tables 4.3 and 4.4. According to EC4, the minimum rotation of a beam-to-column composite joint is 30 mrad, sufficient to allow for plastic analysis and earthquake design. It can be seen that this joint possessed high ductile properties where the rotation capacity exceeded 30 mrad. Also, in terms of stiffness, the initial stiffness lies between 0.5 and 25, which means the corresponding joint should be classified as a semi-rigid connection according to EC4.

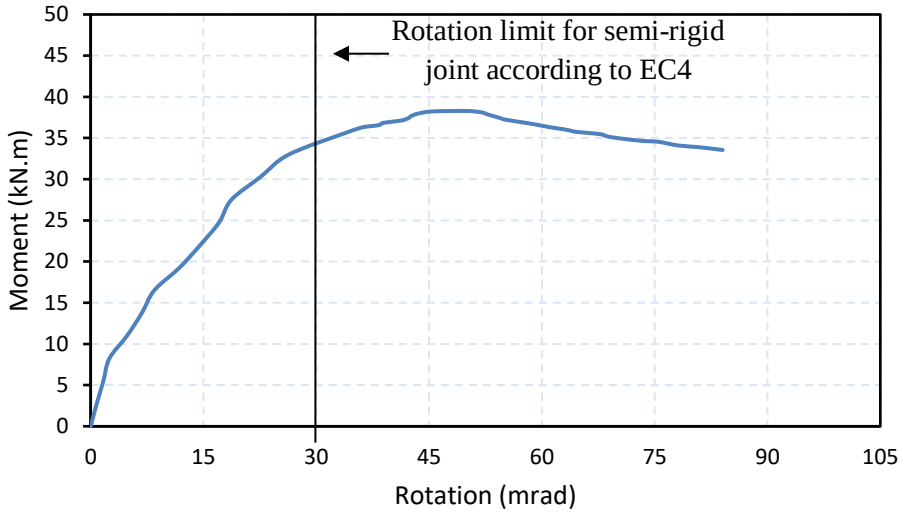

Figure 4.14: Moment-rotation curve of specimen $S_1T_1D_{100}M$.

4.5.2 Failure mode and crack pattern

The failure mode of this specimen is associated with the yielding of the connection angle and bending of the column flange at the seat angle level. Also, buckling the column's web in the compression zone, as shown in Figure 4.15, without the fracture of the longitudinal reinforcing bar. There was no failure or fracture in the connection bolt and shear connector bolt except for a slight bend in the connection bolt under the influence of tensile force at a load of 60 kN.

Figure 4.16 depicts the crack pattern of this specimen, with the first crack appearing at the column corner at a load of 16.2 kN. The cracks could be seen around the perimeter of the column region and spread diagonally from the tips of the column edges to the slab edges. These cracks formed the dominant transverse cracks across the slab width as the loading progressed. Also, at a load of 22.3 kN, a crack was observed in the transverse edge of the slab at the support under the beam and approximated at the same line as the shear connector. When the load reached 47 kN, these cracks extended longitudinally under the line of distribution of the bolted

shear connector from the support and toward the midspan of the beam, as shown in Figure 4.16.

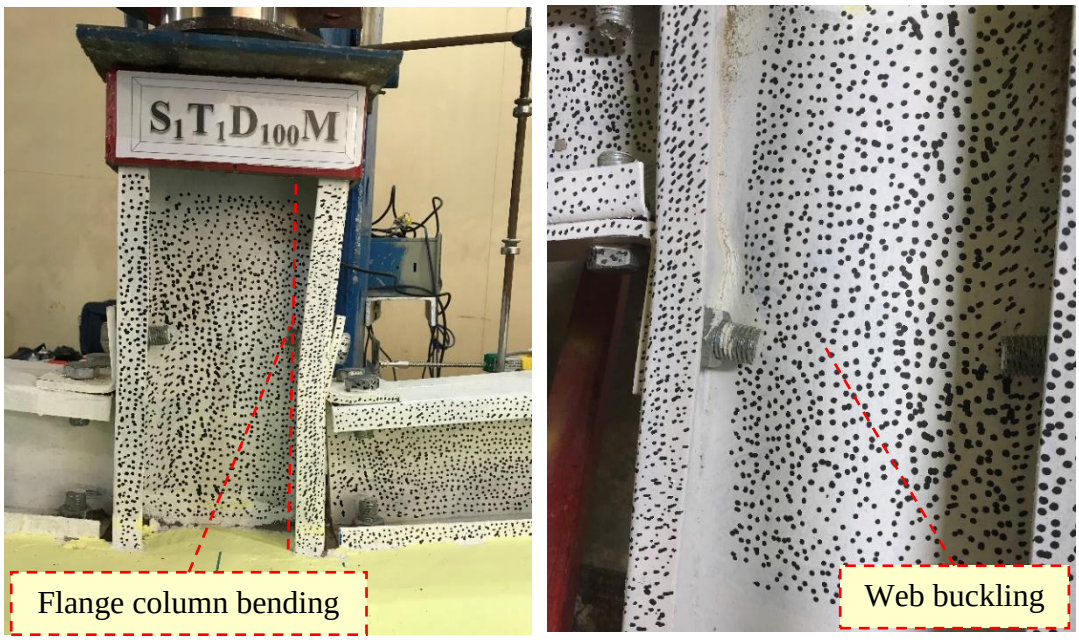

Figure 4.15: Failure mode of specimen $S_1T_1D_{100}M$.

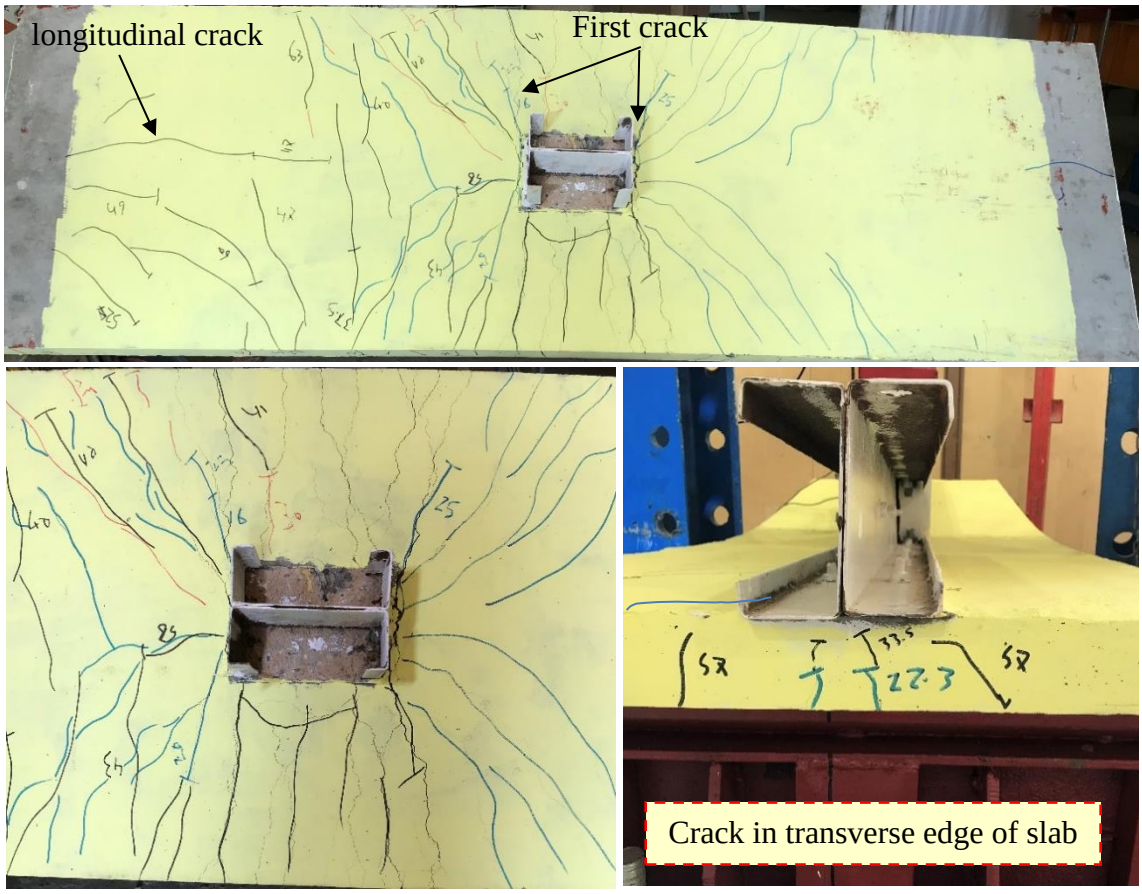

Figure 4.16: Crack pattern of specimen $S_1T_1D_{100}M$.

4.6 EFFECT OF SHEAR CONNECTION TYPES

Figure 4.17 shows the load-deflection curves of the specimens, which have different shear types. The use of a plate shear connector reduced the ultimate deflection by about 16 and 13% for specimens S_1T_2M and S_1T_3M, respectively, when compared to specimen $S_1T_1D_{100}M$. This decrease in deflection is due to the plate of the shear connector's participation in flexural resistance, in addition to its primary role in slip resistance.

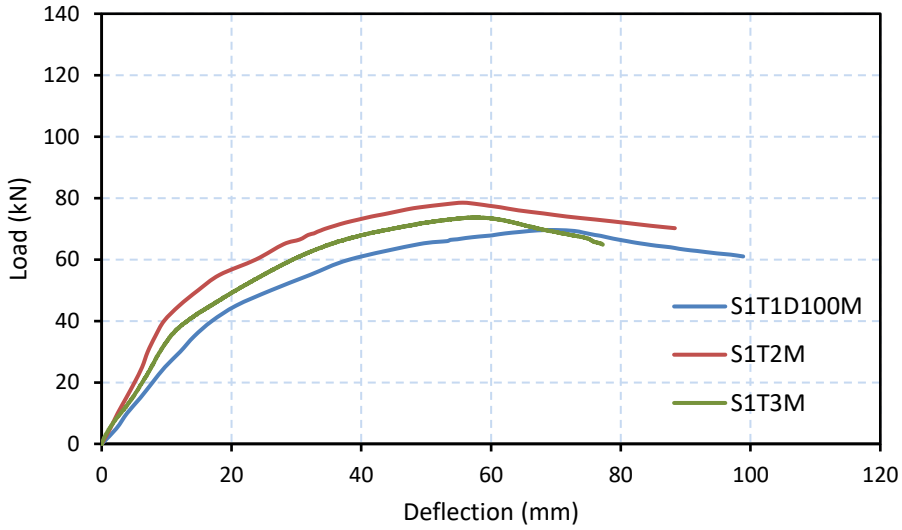

Figure 4.17: Load-deflection curves for specimens with different shear connector types.

4.6.1 Moment-rotation curves

The moment-rotation curves for specimens $S_1T_1D_{100}M$, S_1T_2M, and S_1T_3M are shown in Figure 4.18. All these specimens possessed high ductile properties where the rotation capacity exceeded 30 mrad. Hence, all these specimens were classified as semi-rigid joints according to EC4, which specifies bolted joints' classification by rotational capacity. Specimens $S_1T_1D_{100}M$ and S_1T_2M have the same rotational capacity with a slight difference in the ultimate moment. In contrast, specimen S_1T_3M has a higher rotational capacity of 54% compared with the other specimens. The increase in rotation capacity for specimen S_1T_3M is due to an increase slip

between the concrete slab and the CFS beam, which, by reducing the level of the shear connector, leads to an increase in slippage and, thus, an increase in the amplitude of joint rotation. The values of moment and rotation are also listed in Table 4.3.

In terms of stiffness, the initial stiffness is between $0.5EI_b/l_b$ and $25\ EI_b/l_b$, indicating that the corresponding joint is a semi-rigid connection according to EC3. The stiffness value for this group is shown in Figure 4.19, in which specimen S_1T_2M showed higher initial stiffness than other specimens due to the use of a CFS angle plate as a shear connector, which increases flexural resistance and thus increases stiffness.

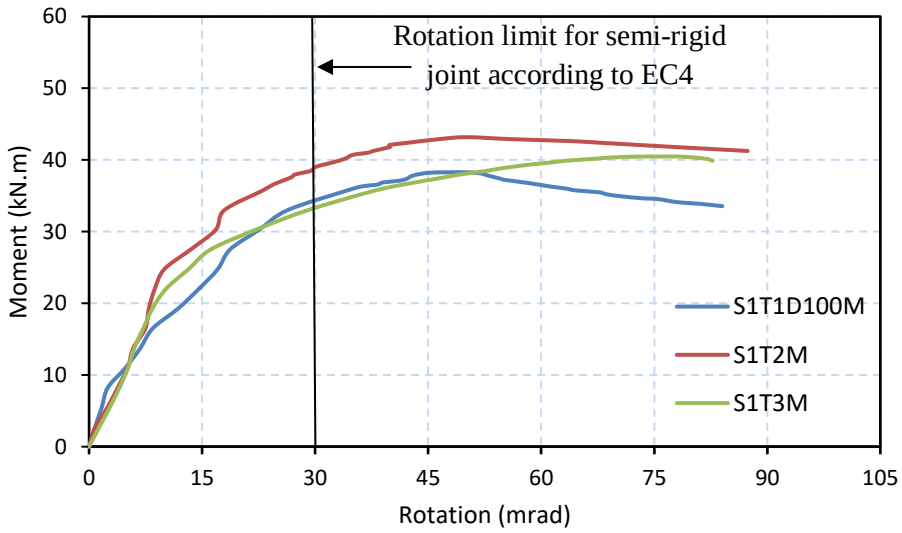

Figure 4.18: Moment-rotation curve of specimens $S_1T_1D_{100}M$, S_1T_2M, and S_1T_3M.

4.6.2 Failure mode and crack pattern

The failure modes of all tested joints in this group are shown in Figure 4.20. It is noted that the failure of all tested specimens was dominated by the significant rotation of the connection angle, which caused the bending of the column flange at the seat angle level and buckled the column's web in the compression zone. Though the significant rotation of the connection angle was observed, the vertical slip between the connection angles and the

column flange was not observed. Also, there was no fracture in the connection bolt except for a slight bend of the bolt that connected the angle with the column flange.

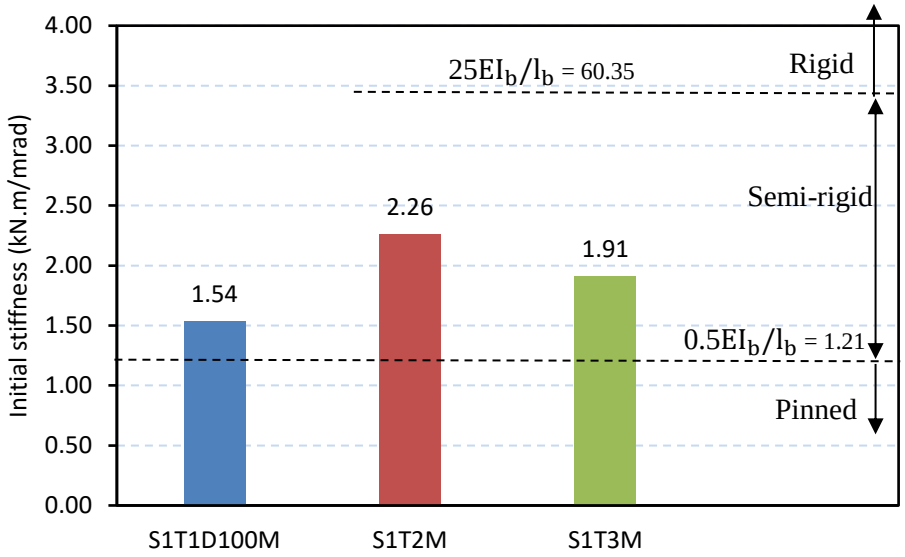

Figure 4.19: Joint stiffness value for specimens $S_1T_1D_{100}M$, S_1T_2M, and S_1T_3M.

The cracks of the tested specimens could be seen around the perimeter of the column region and spread diagonally from the tips of the column edges to the slab edges (Figure 4.21). After that, with increased loading, these cracks formed the dominant transverse cracks across the slab width. The first crack appeared at the column corner at a load of 16.2 kN for specimen $S_1T_1D_{100}M$ and 10 kN for specimens S_1T_2M and S_1T_3M. As the load increased, a new transverse crack developed along the slab width at a distance of 225 mm (the same distance as the first shear connector bolt), 100 mm, and 110 mm from the column face at a load equal to 38, 36, and 36 kN for specimens $S_1T_1D_{100}M$, S_1T_2M, and S_1T_3M, respectively. Then several transverse cracks appeared with increased loading. When the load level reached about 22 kN, the longitudinal crack appeared, whose extension was parallel to the shear connector from the support to the midspan of the beam.

The crushing crack was also observed in specimens S_1T_2M and S_1T_3M on the concrete's surface near the beam's flange parallel to the column face at 69 kN after the load dropped.

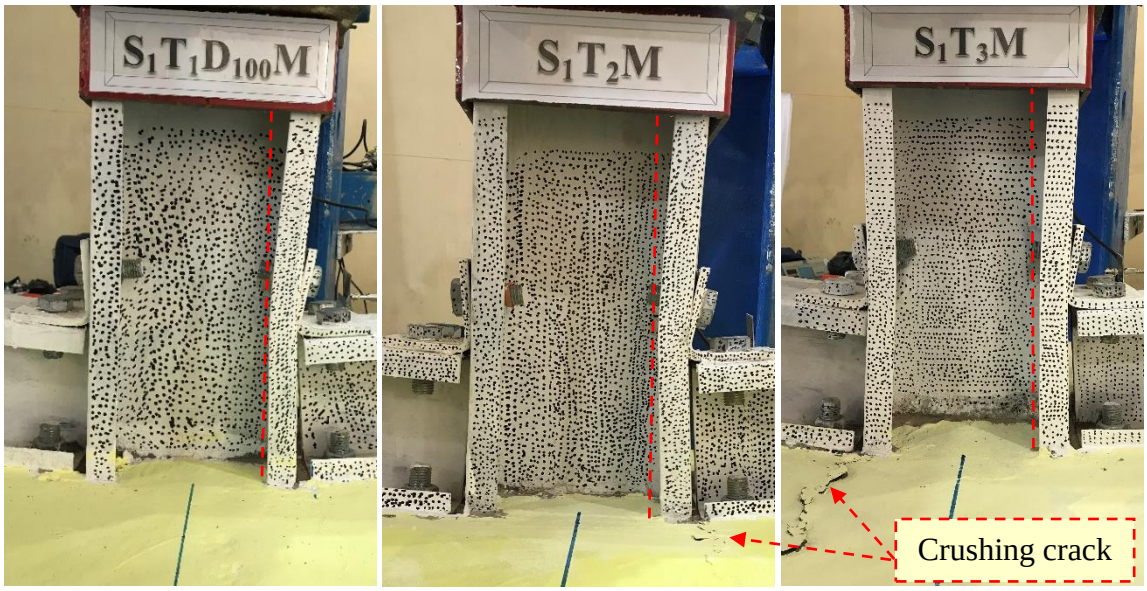

(a) Flange column bending

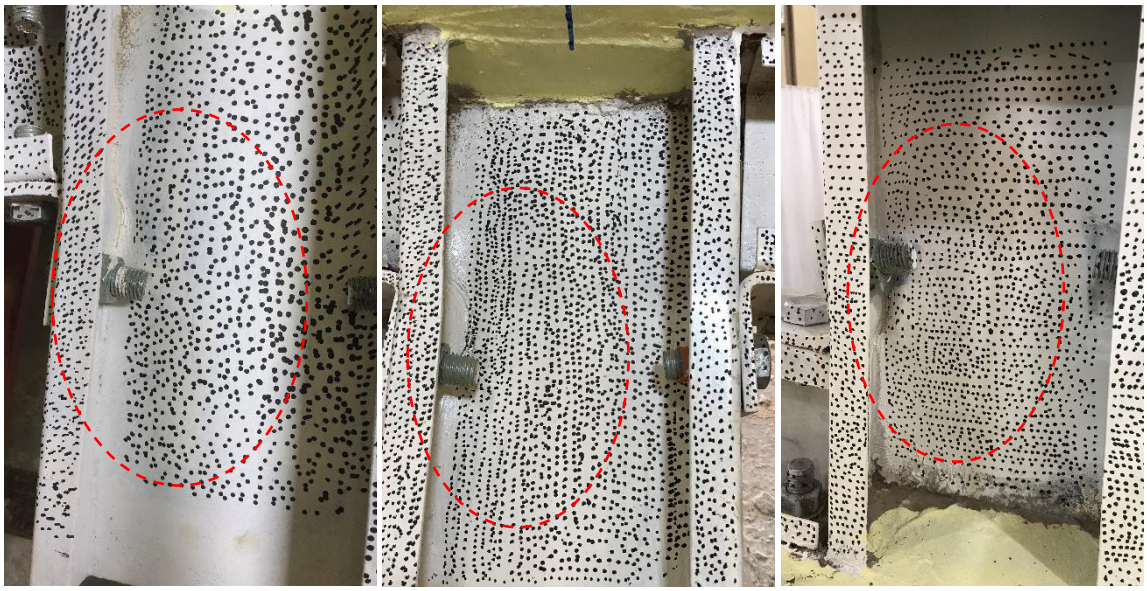

(b) Web buckling of column

Figure 4.20: Failure mode of specimens $S_1T_1D_{100}M$, S_1T_2M, and S_1T_3M.

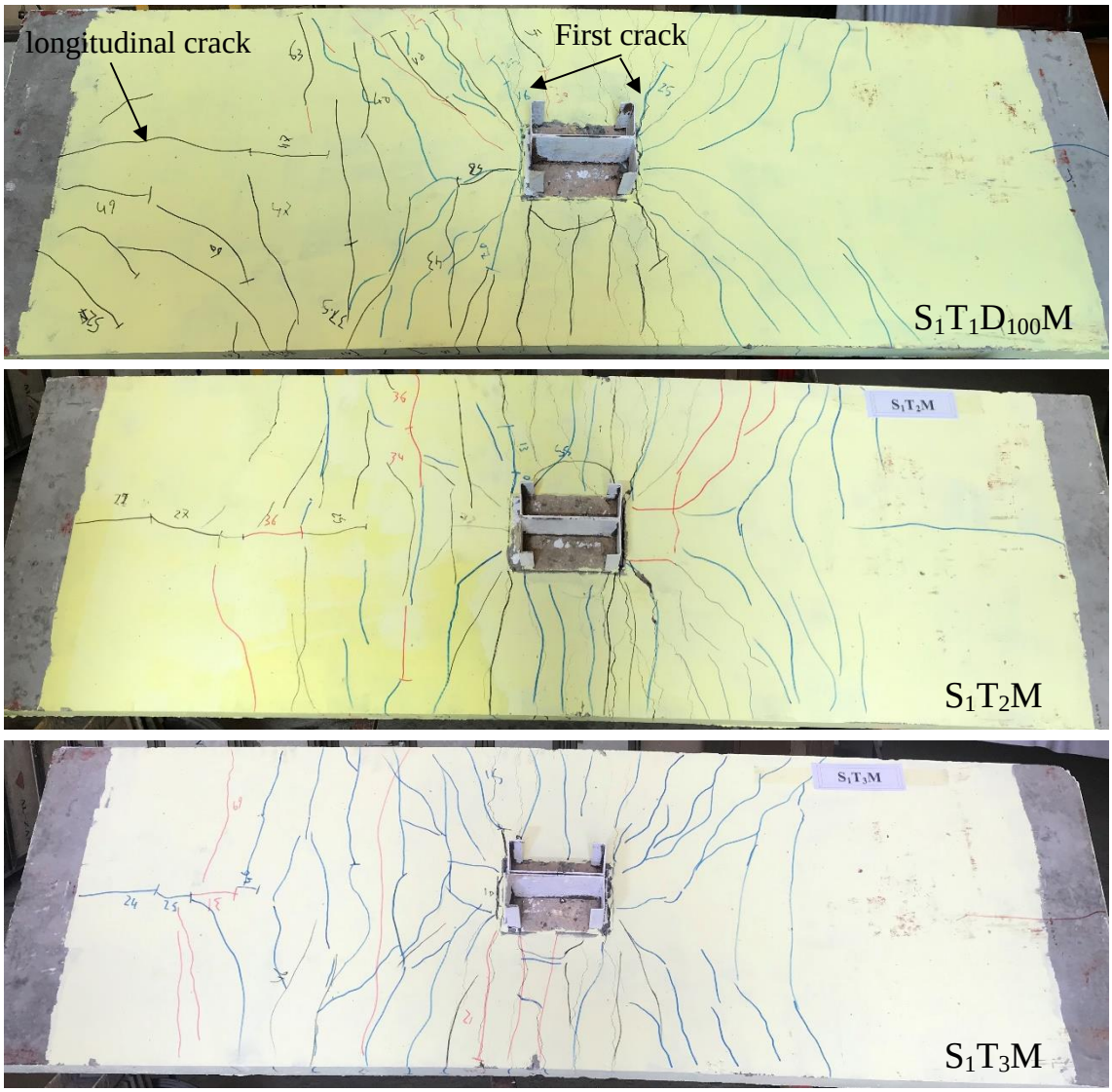

Figure 4.21: Crack pattern of specimens $S_1T_1D_{100}M$, S_1T_2M, and S_1T_3M.

4.7 EFFECT THE DEGREE OF BOLTED SHEAR CONNECTOR

The load and deflection values of specimens in this group were approximately similar, as shown in Table 4.3. This is because the capacity of these specimens depends on the angle of connection, which is similar in all specimens. All three tested specimens failed by buckling the column web and bending the column flange after a significant angle rotation.

4.7.1 Moment rotation curves

Figure 4.22 shows the moment-rotation curves for specimens $S_1T_1D_{100}M$, $S_1T_1D_{50}M$, and $S_1T_1D_{25}M$. All these specimens possessed high ductile

properties where the rotation capacity exceeded 30 mrad. It can be observed that as the bolted shear connector was reduced in the composite joints, there was no discernible difference in strength, but this was accompanied by increased rotation capacity. This corresponds to [66] reaching for a head stud connector with hot-rolled steel. The rotational capacity of specimens $S_1T_1D_{50}M$ and $S_1T_1D_{25}M$ increased by 33.4 % and 79.16%, respectively, compared with specimen $S_1T_1D_{100}M$, which has a full degree of shear connection. This indicated that the partial shear connector is a beneficial in ductility but caused a reduction in the initial rotational stiffness.

In terms of stiffness, the initial rotational stiffness decreased by reducing the level of the shear connector. The initial rotational stiffness decreased by 20% and 47% for specimens $S_1T_1D_{50}M$ and $S_1T_1D_{25}M$, respectively, compared to specimen $S_1T_1D_{100}M$, as shown in Figure 4.23. This is due to higher slip displacements for specimens with a lower degree of shear connection, which causes higher rotational capacity and thus reduces stiffness.

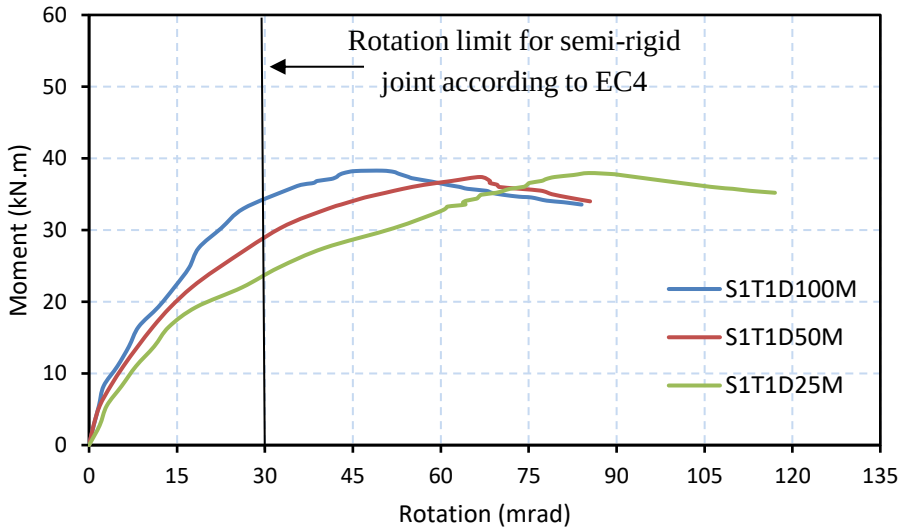

Figure 4.22: Moment-rotation curve of specimens $S_1T_1D_{100}M$, $S_1T_1D_{50}M$, and $S_1T_1D_{25}M$.

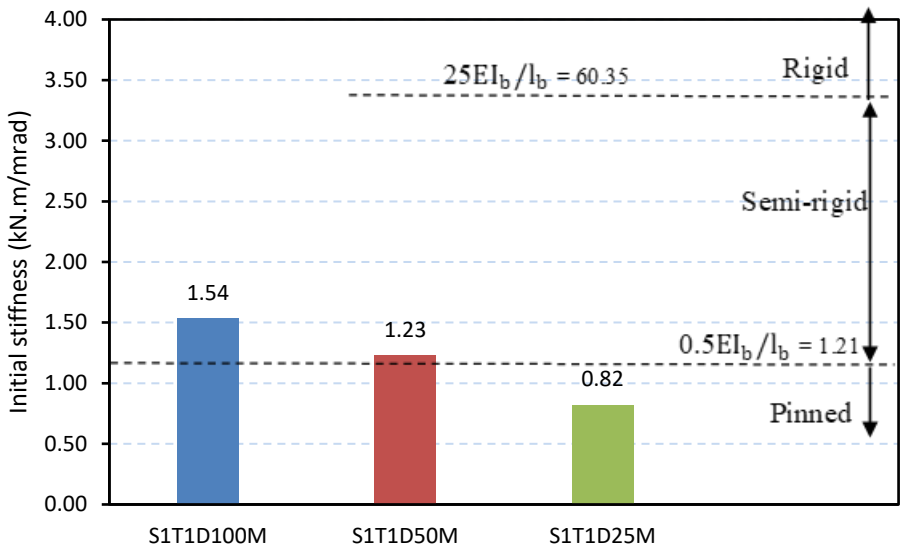

Figure 4.23: Joint stiffness value for specimens $S_1T_1D_{100}M$, $S_1T_1D_{50}M$, and $S_1T_1D_{25}M$.

4.7.2 Failure mode and crack pattern

The failure mode of specimens $S_1T_1D_{50}M$ and $S_1T_1D_{25}M$ is similar to that of specimen $S_1T_1D_{100}M$, in which the significant rotation of the connection angle caused the bending of the column flange at the seat angle level and significantly buckled the column's web in the compression zone compared with $S_1T_1D_{100}M$, as shown in Figure 4.24. It is noted that at load level 52 kN, the column flange starts buckling under the connection bolt in the compression zone, and with an increase in loading to 65 kN. This buckling has become apparent in addition to the buckling in the column web.

The first visible crack appeared at the corner of the column at a load of 16 kN for all specimens in this group. As the load increased, the first crack spread diagonally from the tips of the column edges to the slab edges. New transverse cracks developed on the slab width at load levels 28 and 22 kN for specimens $S_1T_1D_{50}M$ and $S_1T_1D_{25}M$, respectively, at a distance of 100 mm from the column face. When the load level reached 32 and 27 kN for specimens $S_1T_1D_{50}M$ and $S_1T_1D_{25}M$, the cracks developed at a distance of

230 mm from the column face along the slab width. These cracks widened and branched with increased load, and the punching perimeter crack appeared at load level 43 kN, as shown in Figure 4.25. In contrast, the longitudinal crack appeared when the load level reached about 24 and 40 kN for specimens $S_1T_1D_{50}M$ and $S_1T_1D_{25}M$, respectively, whose extension was parallel to the shear connector from the support to the midspan of the beam.

Furthermore, the separation crack between the CFS beam and concrete slab appeared clearly at the support side at load levels of 23 and 14 kN in specimens $S_1T_1D_{50}M$ and $S_1T_1D_{25}M$ with a partial shear connection, respectively, compared to specimens $S_1T_1D_{100}M$ with a full shear connection, which has a slight splitting at higher loads. As the load increased, this separation crack extended until it reached the face of the column and crushed the concrete at the column face after the load reached the ultimate.

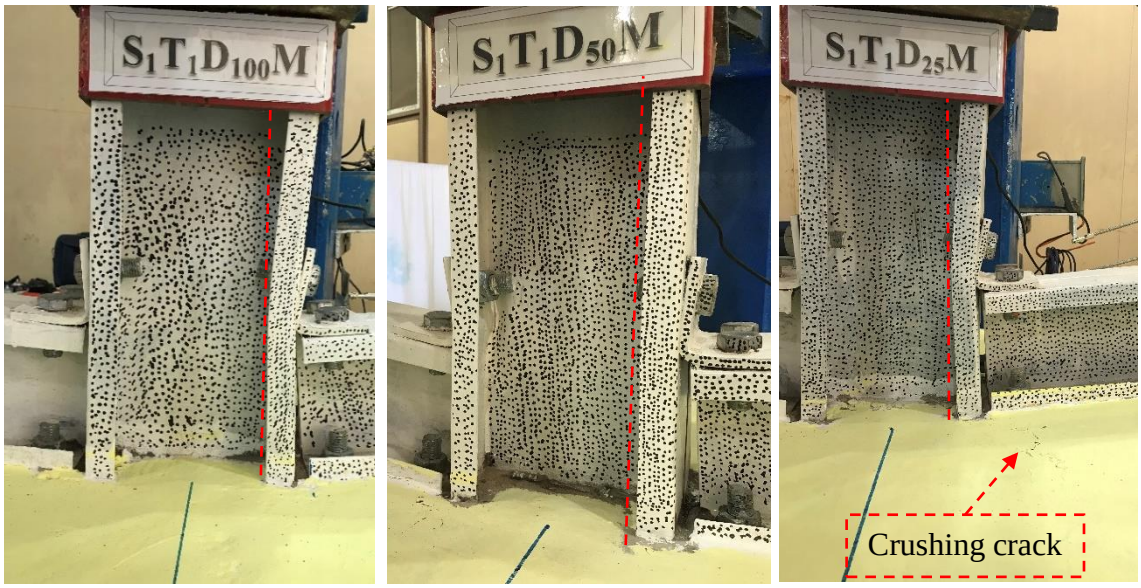

(a) Flange column bending

Figure 4.24: Failure mode of specimens $S_1T_1D_{100}M$, $S_1T_1D_{50}M$, and $S_1T_1D_{25}M$ (continue).

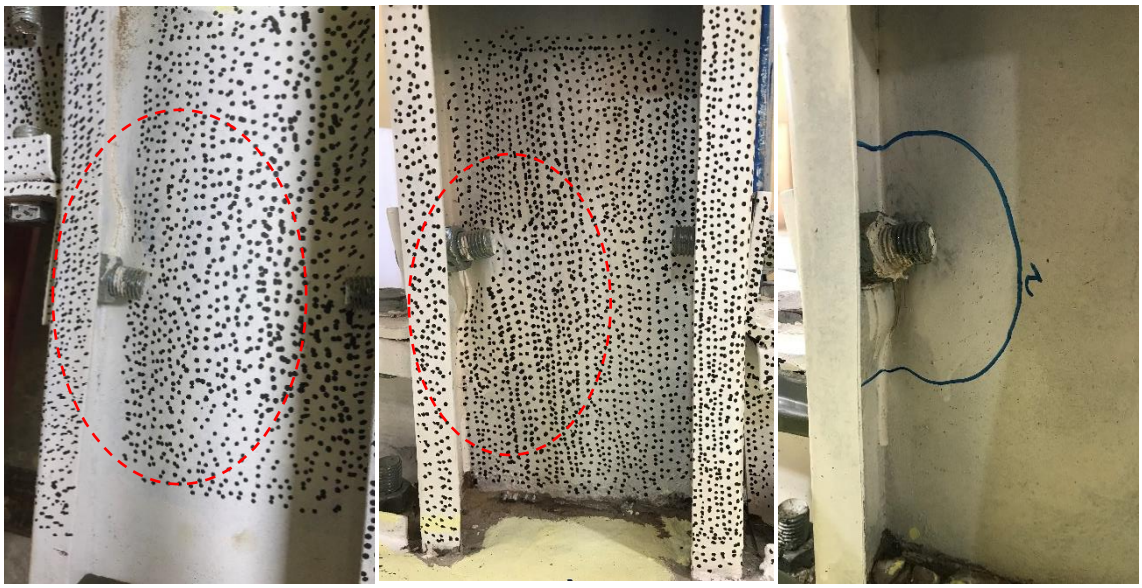

(b) Web buckling

Figure 4.24: Failure mode of specimens $S_1T_1D_{100}M$, $S_1T_1D_{50}M$, and $S_1T_1D_{25}M$.

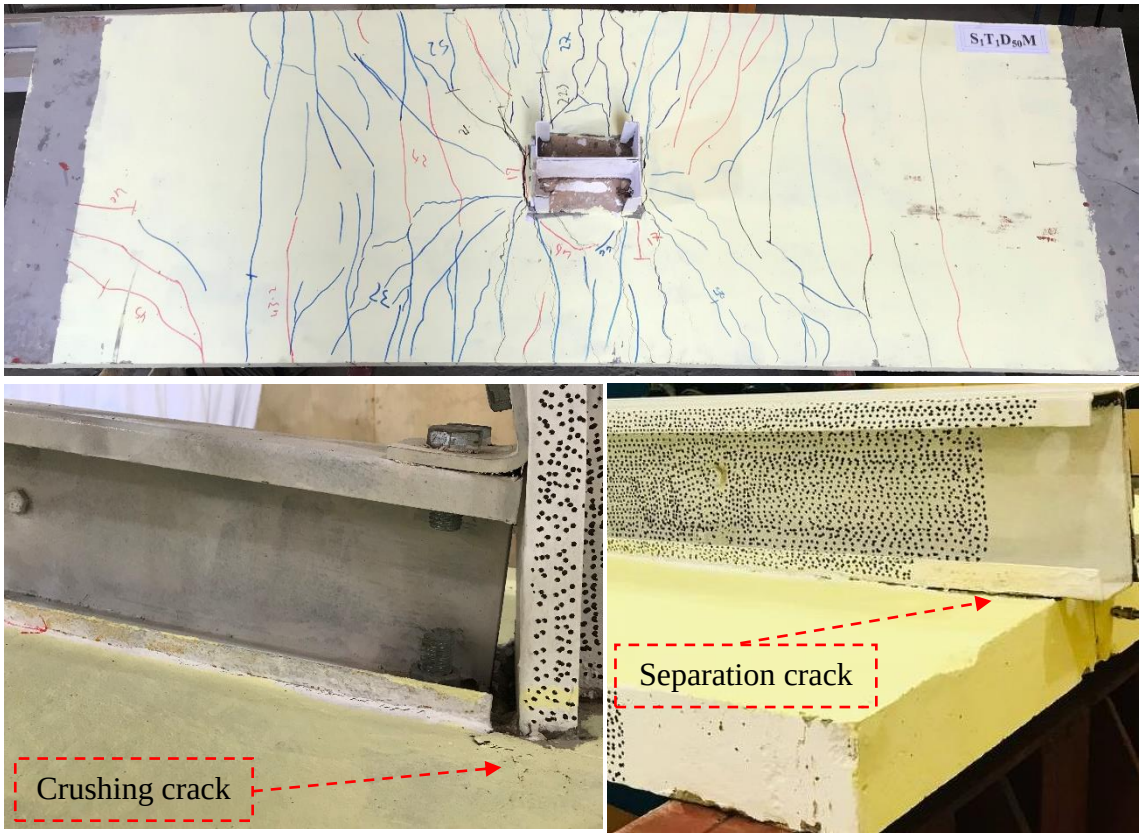

(a) $S_1T_1D_{50}M$

Figure 4.25: Crack pattern of specimens $S_1T_1D_{50}M$ and $S_1T_1D_{25}M$ (continue).

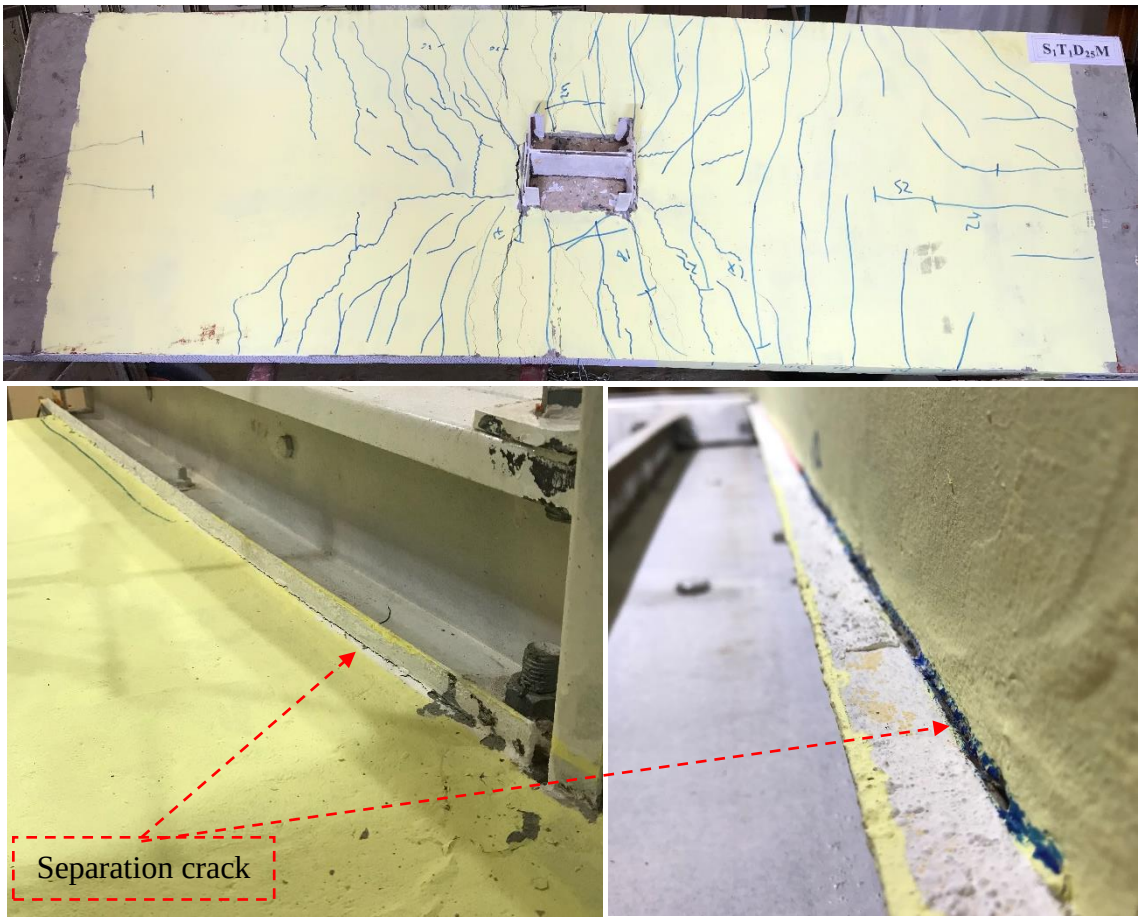

(b) $S_1T_1D_{25}M$

Figure 4.25: Crack pattern of specimens $S_1T_1D_{50}M$ and $S_1T_1D_{25}M$.

4.8 CONNECTION SHAPE EFFECT UNDER MONOLITHIC LOAD

The effect of the connection shape between the beam and column on the load-deflection response is shown in Figure 4.26, where the column and beam shapes significantly affected the joint's behavior. The specimen $S_2T_1D_{100}M$ with a box column section increased the ultimate load by 33% and decreased the deflection by 75%. In comparison, specimen $S_3T_1D_{100}M$ with a box beam section increased the ultimate load by 90% and decreased the deflection by 71%, compared with specimen $S_1T_1D_{100}M$ with an i-section shape for the beam and column. This increase in ultimate load for specimens $S_2T_1D_{100}M$ and $S_3T_1D_{100}M$ is due to a direct connection between the beam and the column, which reduces joint rotation and thus gives higher stiffness and lower deflection.

A box beam section gave higher stiffness and prevented the lateral torsional buckling of the beam. Hence, specimen $S_3T_1D_{100}M$ gave higher stiffness and capacity than specimen $S_2T_1D_{100}M$, although a direct connection was used in both specimens.

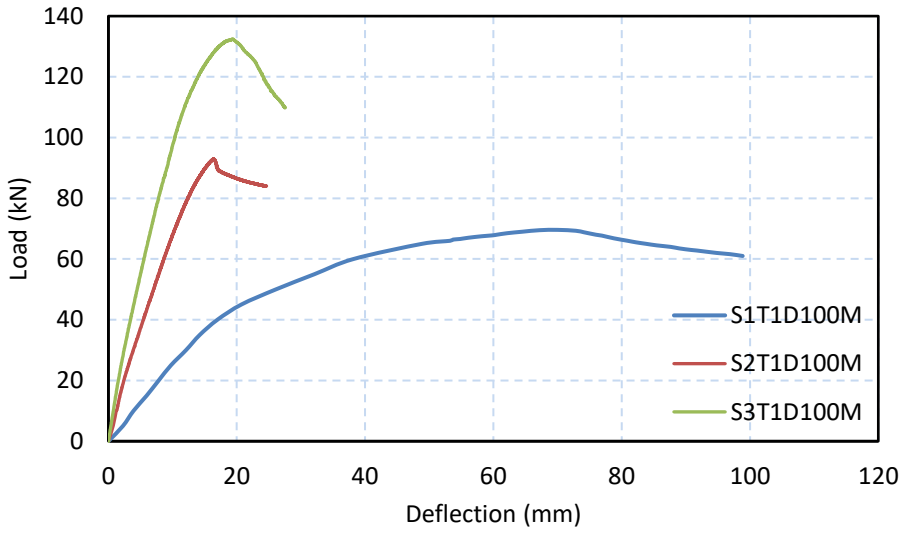

Figure 4.26: Load-deflection curves for specimens with different connection shapes.

4.8.1 Moment rotation curves

The joint rotation was reduced when the beam and column were connected back-to-back by bolts, as shown in Figure 4.27. The rotation capacity of specimens $S_2T_1D_{100}M$ and $S_3T_1D_{100}M$, which connected directly, was reduced by about 76-78% compared with specimen $S_1T_1D_{100}M$, indicating non-ductile behavior where the rotation capacity did not exceed 30 mrad. The reason for the low rotation in these specimens is the continuity of the beam, which makes the rotation of the joint minimal. In addition to the presence of six bolts on each side between the beam and column that greatly restrict the rotation of the joint. In contrast, the rotation of the joint in specimen $S_1T_1D_{100}M$ was determined by the connecting angles, resulting in a significant rotation and ductile behavior.

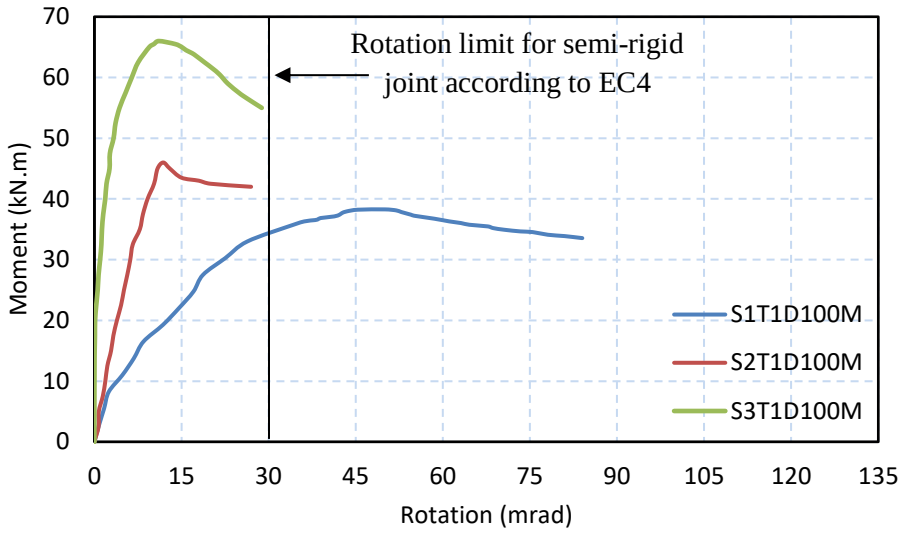

Figure 4.27: Moment-rotation curve of specimens $S_1T_1D_{100}M$, $S_2T_1D_{100}M$, and $S_3T_1D_{100}M$.

The initial rotational stiffness increased when the beam and column were directly connected. The initial rotational stiffness was 4.86 and 21.06 for specimens $S_2T_1D_{100}M$ and $S_3T_1D_{100}M$, which are very large compared to specimen $S_1T_1D_{100}M$, as shown in Figure 4.28. This is due to restricting the

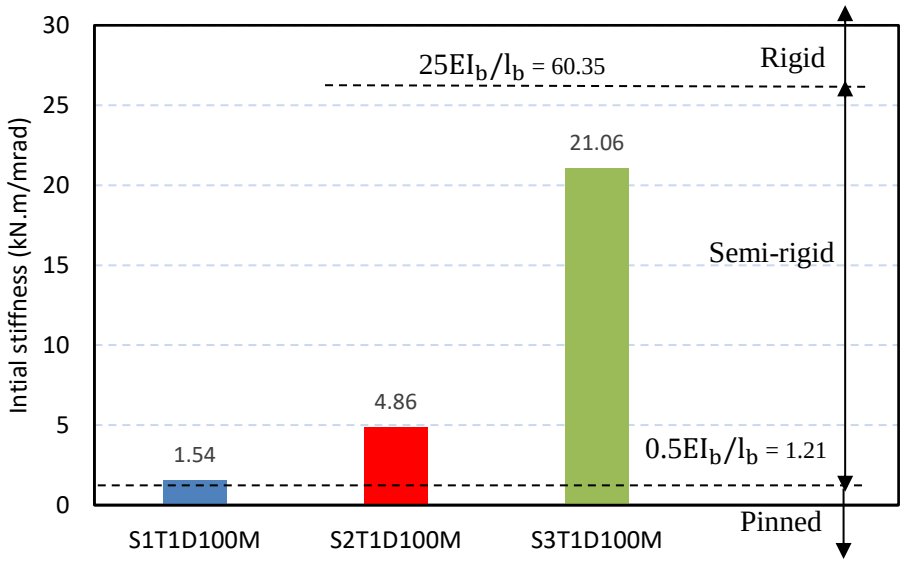

Figure 4.28: Joint stiffness value for specimens $S_1T_1D_{100}M$, $S_2T_1D_{100}M$, and $S_3T_1D_{100}M$.

joint's rotation, which becomes almost rigid, and causes a lower rotational capacity and, thus, increased stiffness. Specimen $S_3T_1D_{100}M$ has a higher

stiffness and strength than the other specimens because the beam's box shape prevented the beam's lateral torsional buckling that occurred in specimen $S_2T_1D_{100}M$ and local buckling in the column flange in specimen $S_1T_1D_{100}M$. So, the rotation of the joint was very small until it reached the high loads and local buckling occurred in the web of the beam near the column face; after that, the rotation became clear.

4.8.2 Failure mode and crack pattern

The configuration of a beam-to-column joint (beam and column shapes) greatly affects the joint strength and behavior. It is noted that the failure of specimens $S_2T_1D_{100}M$ and $S_3T_1D_{100}M$ is different from that of specimen $S_1T_1D_{100}M$. The specimen $S_2T_1D_{100}M$ failed due to lateral torsional buckling of the beam followed by local buckling in the beam web at load level 89 kN after the load dropped below ultimate. In contrast, specimen $S_3T_1D_{100}M$ failed by local buckling in the beam's web and the beam flange in the compression zone at the column face. In addition, there was no failure in the column or the connection zone between the beam and column for both specimens $S_2T_1D_{100}M$ and $S_3T_1D_{100}M$. Figure 4.29 shows the failure mode for specimens $S_2T_1D_{100}M$ and $S_3T_1D_{100}M$.

The first visible crack appeared within the column web at a load of 28 kN and at the corner of the column at a load of 41.3 kN for specimens $S_2T_1D_{100}M$ and $S_3T_1D_{100}M$, respectively, as shown in Figure 4.30. These specimens had fewer cracks around the column area than sample $S_1T_1D_{100}M$, where the cracks were concentrated in the beam's mid-span. When the load level reached 51 and 62 kN, new transverse cracks developed on the slab width at a distance of 400 and 100 mm from the column face for specimens $S_2T_1D_{100}M$ and $S_3T_1D_{100}M$, respectively. In contrast, the longitudinal crack appeared when the load level reached approximately 41 and 57 kN for specimens $S_2T_1D_{100}M$ and $S_3T_1D_{100}M$,

respectively, whose extension was parallel to the shear connector at 300 and 100 mm from the support and extended to the midspan of the beam as the load increased.

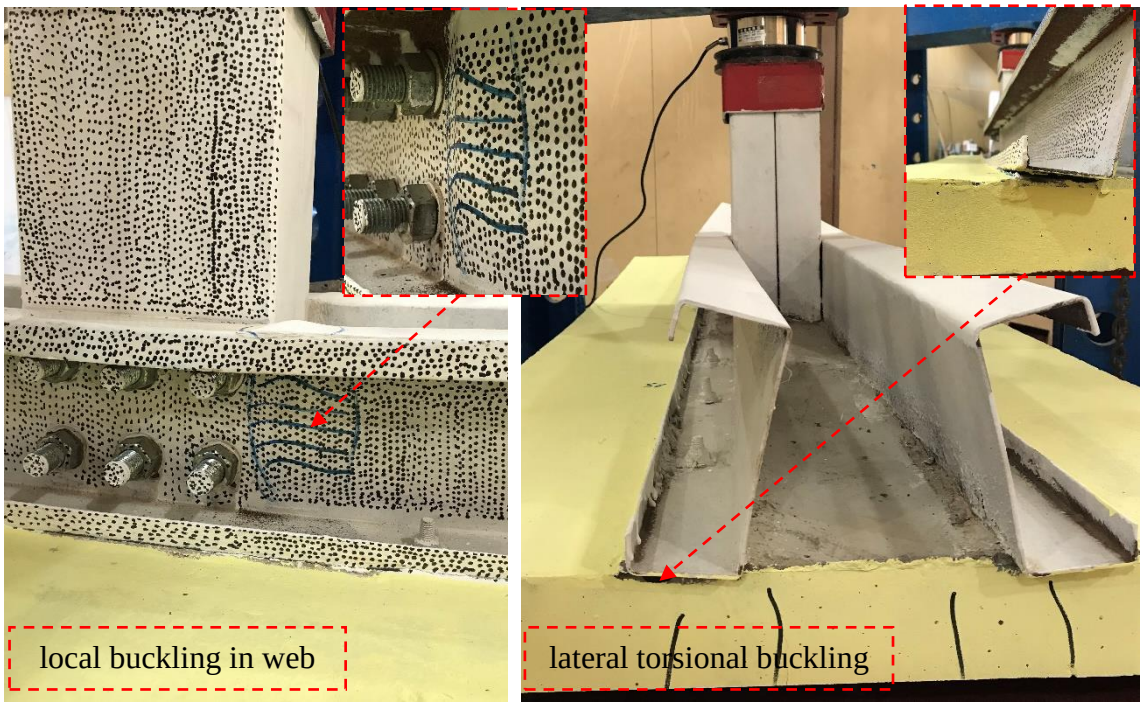

(a) $S_2T_1D_{100}M$

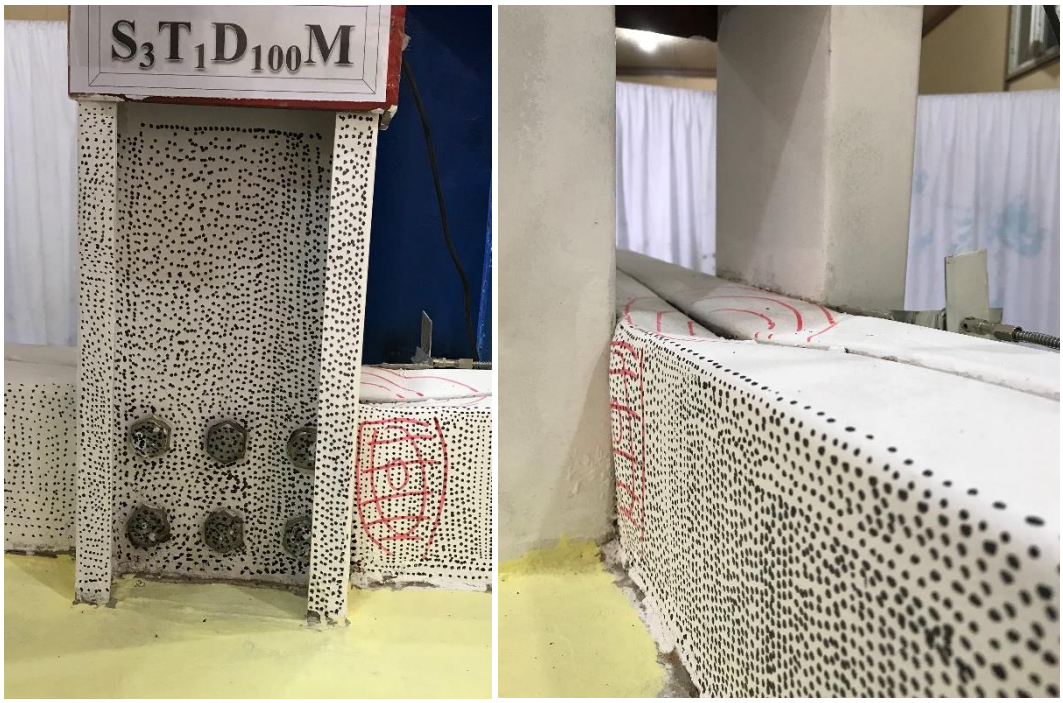

(b) $S_3T_1D_{100}M$

Figure 4.29: Failure mode of specimens $S_2T_1D_{100}M$ and $S_3T_1D_{100}M$.

Furthermore, the separation crack between the CFS beam and concrete slab appeared at the support side at load levels of 75 and 107 kN in specimens $S_2T_1D_{100}M$ and $S_3T_1D_{100}M$, respectively. As the load increased to 92 kN, the separation crack appeared clearly at the support side for specimen $S_2T_1D_{100}M$ due to lateral torsional buckling of the beam. While the shear crack appeared at the first shear connector from the support side at load levels of 107 kN for specimen $S_3T_1D_{100}M$ and extended diagonally to the edge of the slab, as shown in Figure 4.31, due to the concentration of the high shear stresses around the first shear connector bolt.

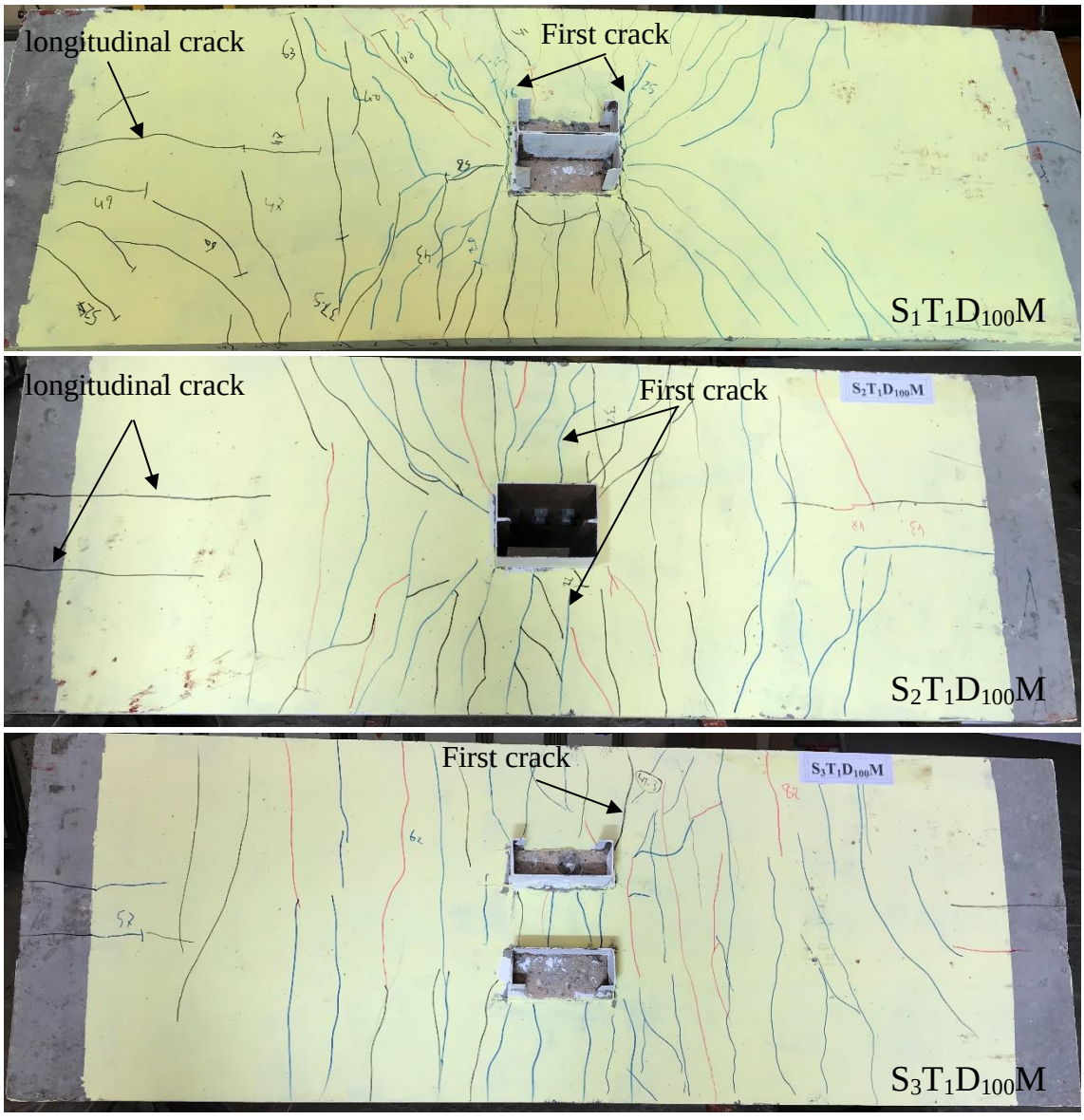

Figure 4.30: Crack pattern of specimens $S_1T_1D_{100}M$, $S_2T_1D_{100}M$, and $S_3T_1D_{100}M$.

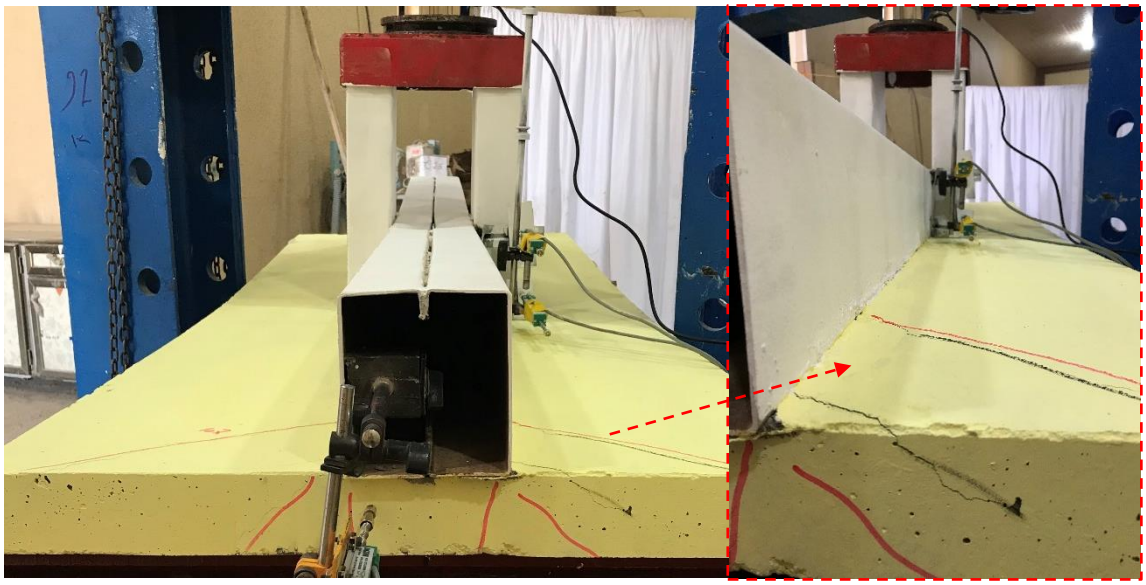

Figure 4.31: The shear crack in specimen $S_3T_1D_{100}M$.

4.9 EFFECT OF LOADING TYPE

The effect of the connection shape between the beam and column under cyclic load was studied in this group. The cyclic load was applied unidirectionally at the same rate (load and unload) as the monotonic load, in which the load was applied at a constant rate of about 0.5 kN/sec. At the last cycle, the load was applied up to the failure of the composite joints.

The comparison of the load behavior with the deflection for specimens under monotonic and cyclic loads is shown in Figures 4.32 to 4.34. It is noted that the specimens under the influence of cyclic loading showed the same behavior as the corresponding specimen under monotonic load, with a decrease in stiffness and increased deflection under the influence of cyclic loading, especially for specimen $S_1T_1D_{100}C$.

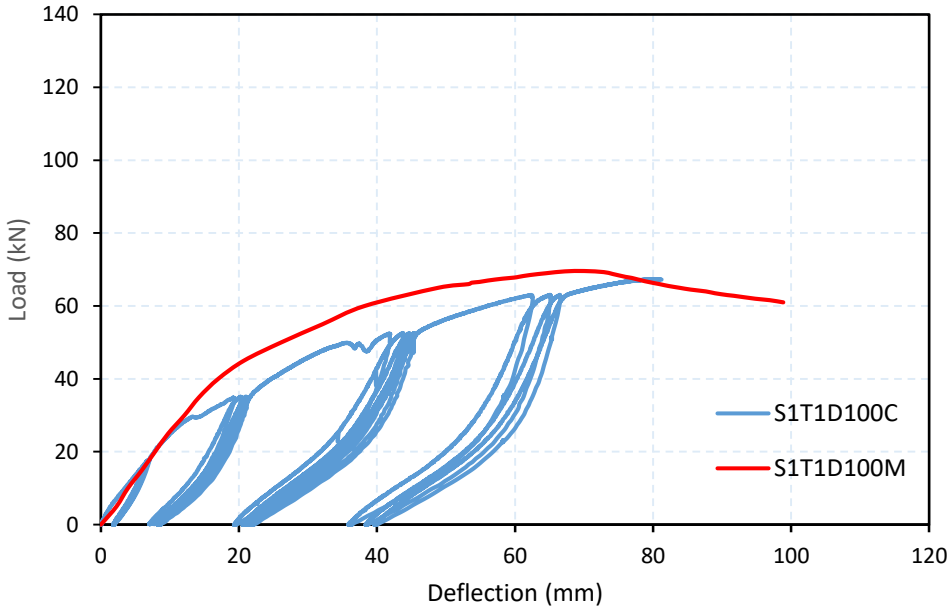

Figure 4.32: Load-deflection curves for specimens $S_1T_1D_{100}M$ and $S_1T_1D_{100}C$.

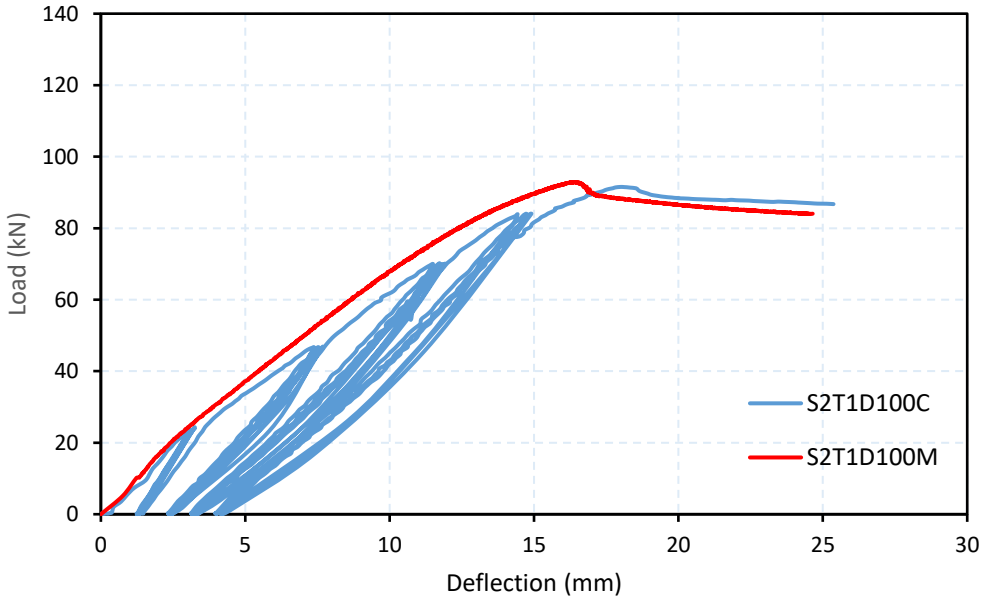

Figure 4.33: Load-deflection curves for specimens $S_2T_1D_{100}M$ and $S_2T_1D_{100}C$.

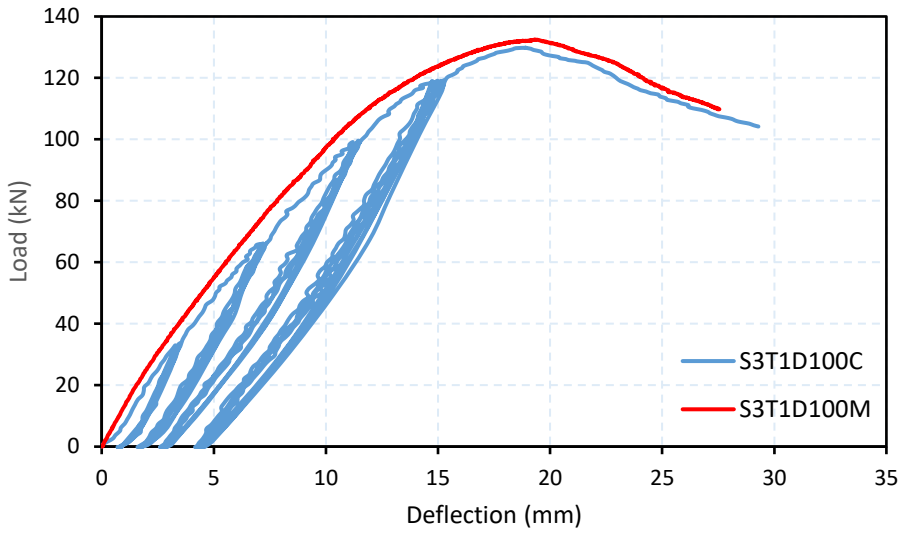

Figure 4.34: Load-deflection curves for specimens $S_3T_1D_{100}M$ and $S_3T_1D_{100}C$.

4.9.1 Moment rotation curves

Figures 4.35, 4.36, and 4.37 show the moment rotation curves for specimens with different connection shapes between beam and column tested under monotonic and cyclic load. The cyclic load slightly affects the ultimate strength of the composite joints. On the other hand, it increased the rotation capacity of joints, especially for specimens $S_1T_1D_{100}C$ and $S_2T_1D_{100}C$, which increased by 79 and 97%, respectively, compared with the corresponding specimen under monotonic load. While the specimen $S_3T_1D_{100}C$ has the same behavior and rotation as the specimen $S_3T_1D_{100}M$, due to the connection in this specimen being approximately rigid, failure occurred due to local buckling in the beam web at ultimate load so that the rotation of the connection was not affected by cyclic loading.

Also, in terms of stiffness, the initial rotational stiffness decreased due to the effect of cyclic loading, as shown in Figure 4.38. The specimen $S_1T_1D_{100}C$ appeared to have a small initial and secant stiffness compared with the other specimens in this group due to the significant rotation caused by the cyclic loading effect. The large rotation occurs as a result of fatigue of the connection angle due to the effect of cyclic loading.

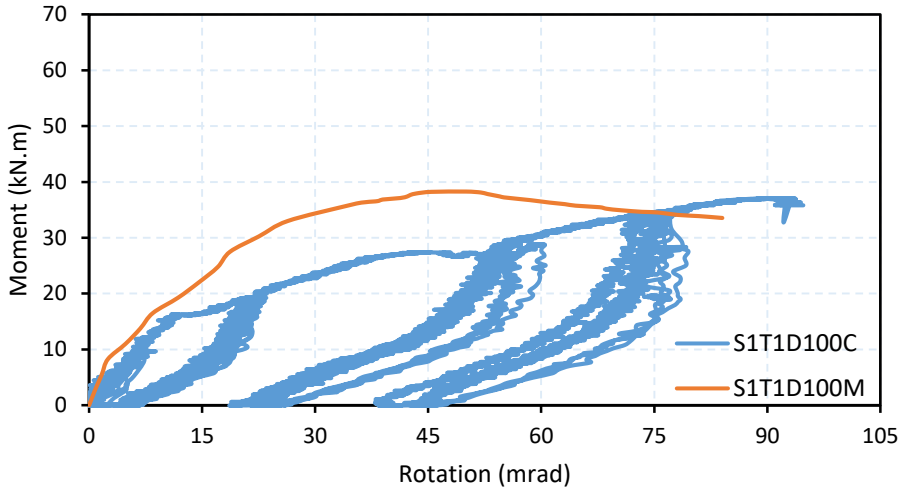

Figure 4.35: Moment-rotation curve of specimens $S_1T_1D_{100}M$ and $S_1T_1D_{100}C$.

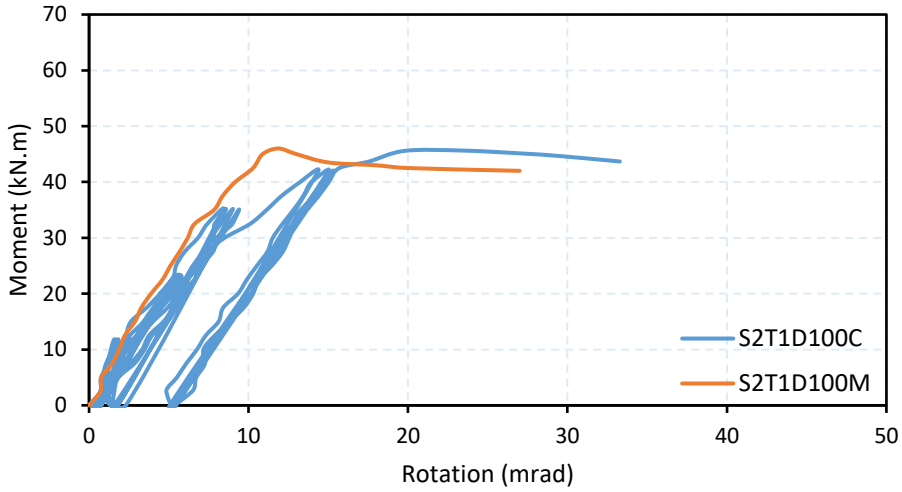

Figure 4.36: Moment-rotation curve of specimens $S_2T_1D_{100}M$ and $S_2T_1D_{100}C$.

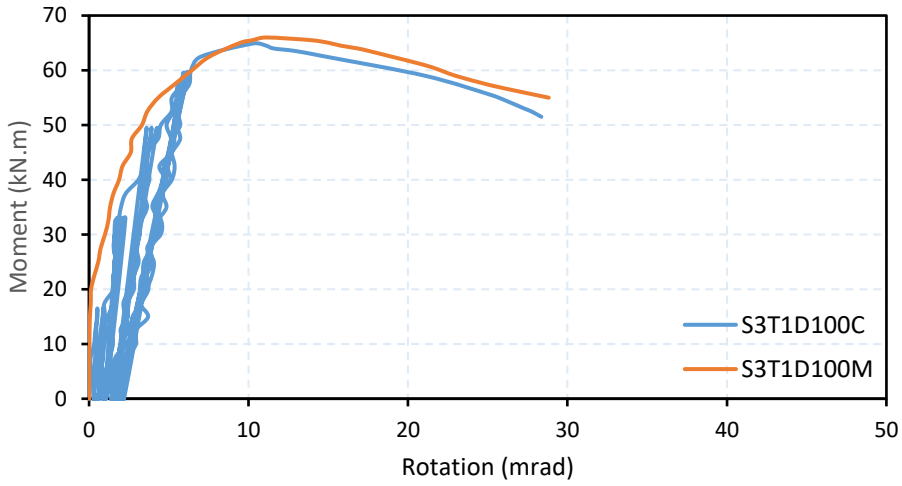

Figure 4.37: Moment-rotation curve of specimens $S_3T_1D_{100}M$ and $S_3T_1D_{100}C$.

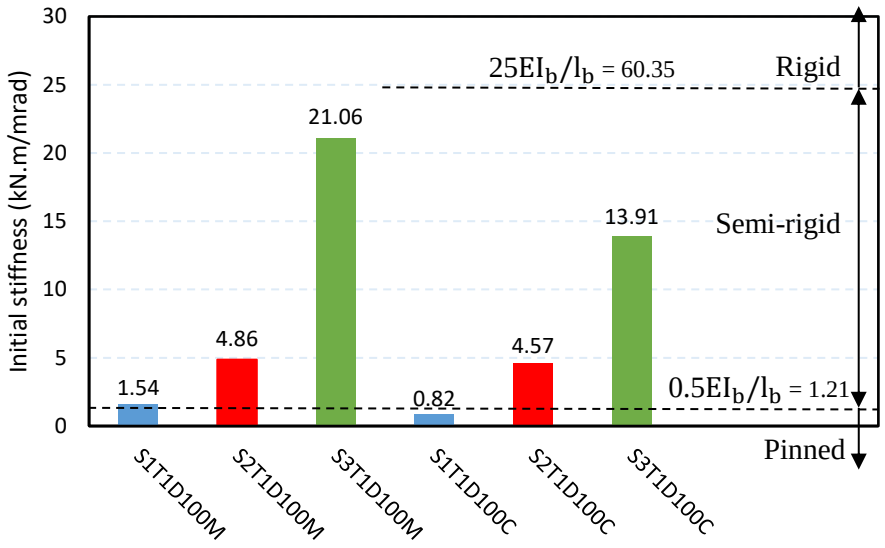

Figure 4.38: Effect of cyclic loading on the initial stiffness value.

4.9.2 Failure mode and crack pattern

Figure 4.39 shows the crack pattern for all tested specimens under cyclic load. The cyclic loading did not affect the failure of specimens, and the same failure occurred in the specimens under the monotonic and cyclic loads. Also, the crack distribution is the same as in the specimens tested under the influence of a monotonic load. Still, it is more widespread and wider, especially for the cracks in the plastic hinge region. The first visible crack for specimen $S_1T_1D_{100}C$ appeared at the column corner at a load of 15 kN. In contrast, the first visible crack for specimens $S_2T_1D_{100}C$ and $S_3T_1D_{100}C$ appeared in the same place that appeared in the similar specimen under monotonic load, but with less load, as it appeared at a load of 23 kN in the fourth cycle of the specimen $S_2T_1D_{100}C$ and 30 kN in the third cycle of the specimen $S_3T_1D_{100}C$.

The longitudinal crack appeared during cycle four of loading when the load level reached approximately 27.5, 30, and 42 kN for specimens $S_1T_1D_{100}C$, $S_2T_1D_{100}C$, and $S_3T_1D_{100}C$, respectively, and its extension was

parallel to the shear connector from the support and extended to the beam's mid-span as the load increased.

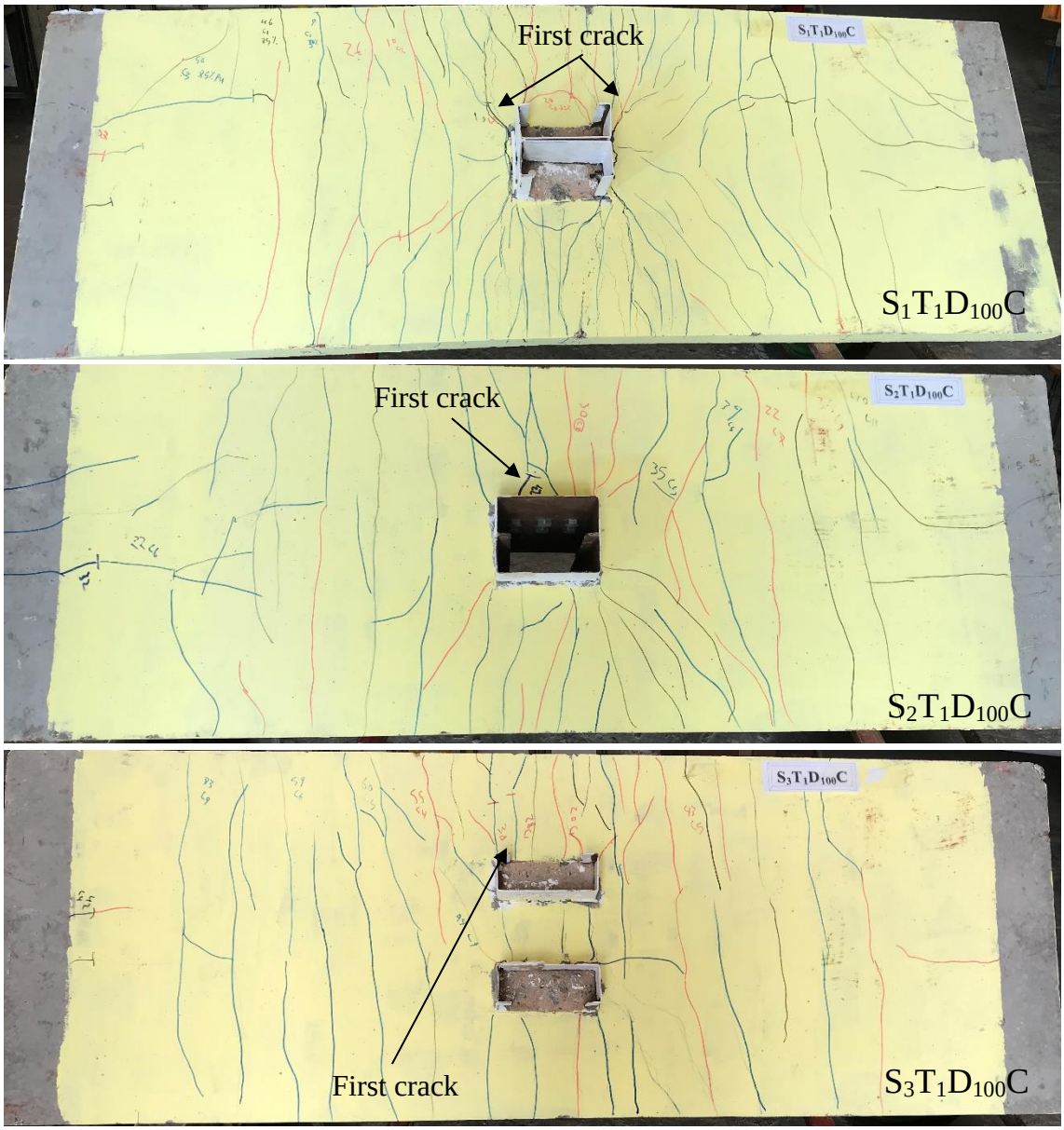

Figure 4.39: Crack pattern of specimens $S_1T_1D_{100}C$, $S_2T_1D_{100}C$, and $S_3T_1D_{100}C$.

Furthermore, the separation crack between the CFS beam and concrete slab appeared at the support side at load levels of 52 (cycle 8), 44 (cycle 6), and 85 (cycle 7) kN in specimens $S_1T_1D_{100}C$, $S_2T_1D_{100}C$, and $S_3T_1D_{100}C$, respectively. In contrast, the shear crack appeared with less load compared to monotonic load specimens at the first shear connector from the support

side with load levels of 60 (cycle 13) and 85 (cycle 7) kN for specimens $S_1T_1D_{100}C$ and $S_3T_1D_{100}C$, respectively, and extended diagonally to the slab edge, as shown in Figure 4.40.

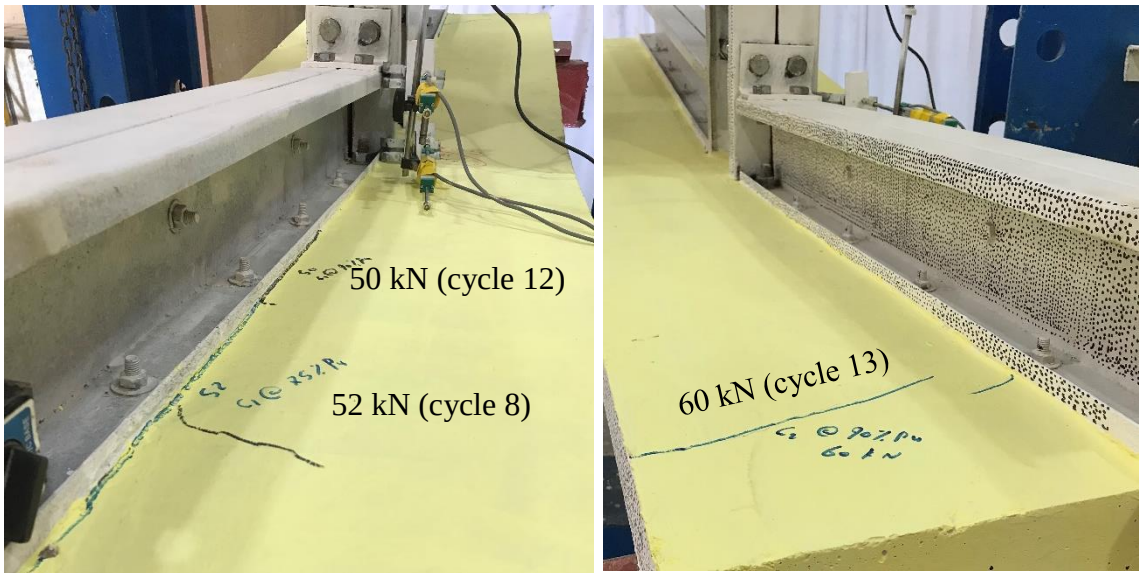

(a) $S_1T_1D_{100}C$

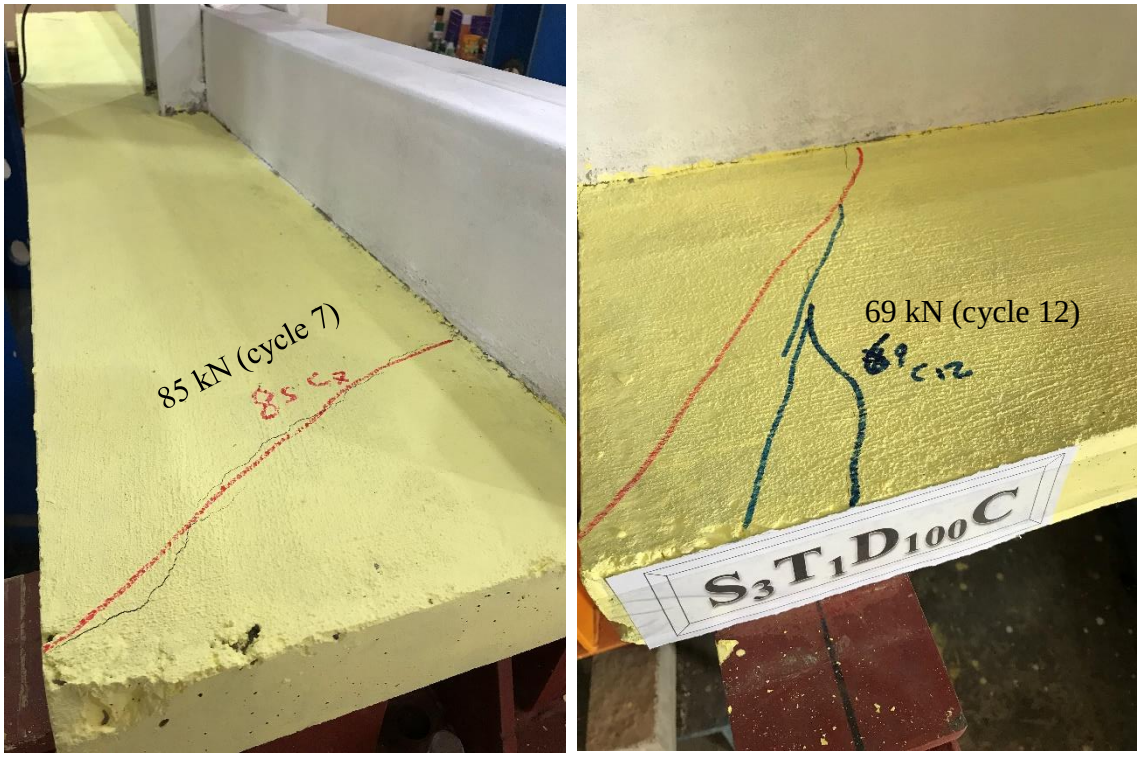

(b) $S_3T_1D_{100}C$

Figure 4.40: The shear crack in specimens $S_1T_1D_{100}C$ and $S_3T_1D_{100}C$.

4.10 STRENGTH CLASSIFICATION OF JOINT

Besides, also the EC3 and EC4 specified the classification of the bolted joints by strength. A joint can be regarded as a full-strength connection provided that its design moment resistance is greater than the design plastic moment resistance of a beam. On the contrary, if the design moment resistance is less than 25% of the design plastic moment resistance, the joint can be regarded as a pinned connection. Otherwise, the joint is classified as a partial-strength connection.

As depicted in Figure 4.41, all specimens with top and seat angle connections between the beam and column were classified as semi-rigid and partial-strength joints, except for specimen S_1T_2M, which belonged to the semi-rigid and full-strength category. On the other hand, specimens $S_2T_1D_{100}M$ and $S_3T_1D_{100}M$ exhibited a rotation capacity of less than 30 mrad and full-strength due to the beam's continuity and its fixation by six bolts on each side of the column web. This high joint stiffness resulted in a limited rotation capacity.

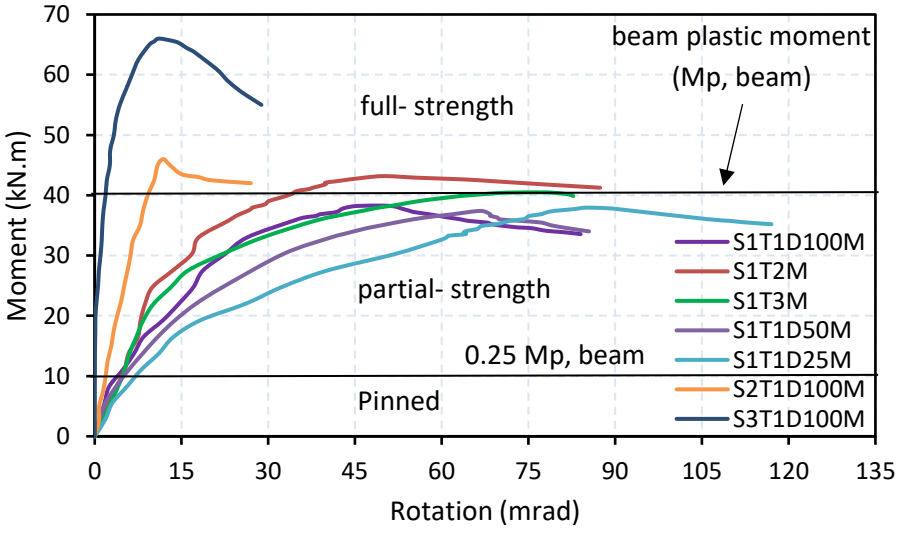

Figure 4.41: The joint classification according to strength.

4.11 LOAD-SLIP CURVES

The slip values at the ultimate load and the end of the test for all tested specimens are listed in Table 4.4. The shear connector did not fail in any of the tests. As expected, specimen $S_1T_1D_{25}M$ had the greatest slip because it has the slightest degree of shear connection. The load-slip behavior of the specimens in each group is shown in Figures 4.42 to 4.44. As demonstrated by the $S_1T_1D_{50}M$ and $S_1T_1D_{25}M$ test results, the slip value increased as the degree of shear connection decreased because of partial interactive behavior. While in the other specimens, the slip value was small due to the availability of full interactive behavior. In addition, providing a high ratio of reinforcement cause a limited extension of the reinforcement; thus, slippage between the steel beam and concrete slab is reduced. As it is known the slip between the CFS beam and the concrete slab of specimens tested under cyclic load was significantly increased compared with specimens under monotonic load due to the cyclic loading effect, as shown in Figure 4.45.

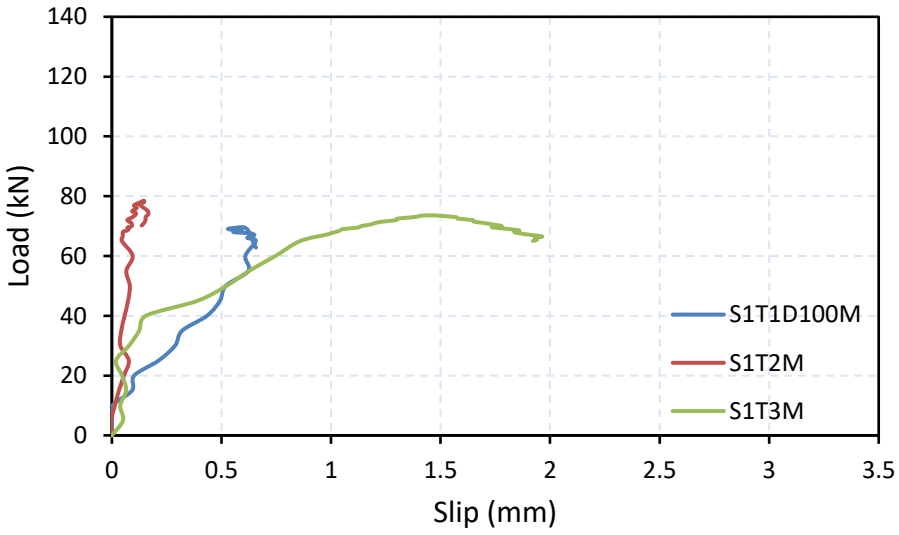

Figure 4.42: Load-slip response for specimens with different shear connector types.

Figure 4.46 shows the slip response along the beam span at various load levels for all tested specimens. Slip behavior was found to be symmetrical from the beginning of loading and increased as the load approached the maximum load. The highest slip was also observed at the beam ends, near the supports.

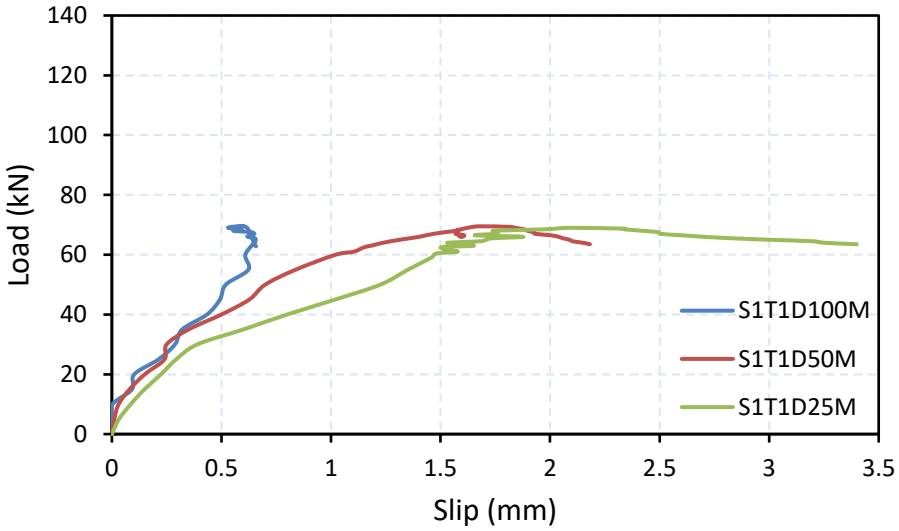

Figure 4.43: Load-slip response for specimens with different degrees of the bolted shear connector.

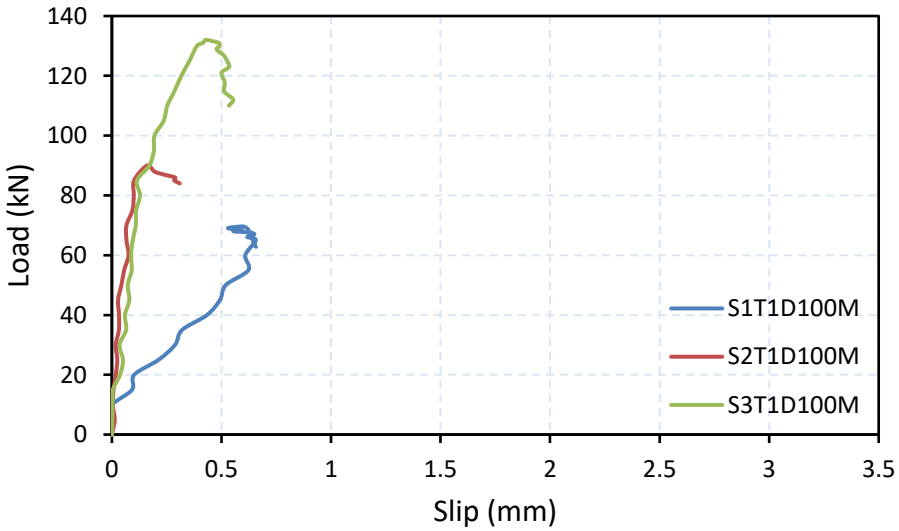

Figure 4.44: Load-slip response for specimens with different beam-to-column connection shapes.

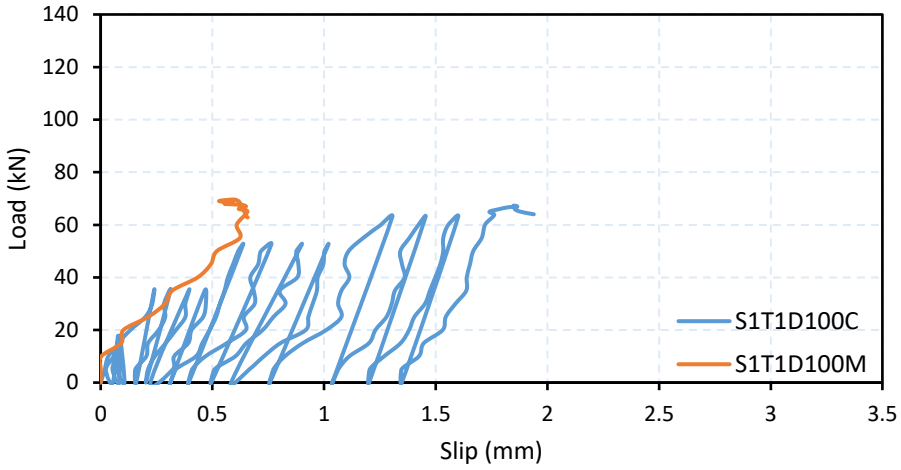

(a) Specimens $S_1T_1D_{100}M$ and $S_1T_1D_{100}C$.

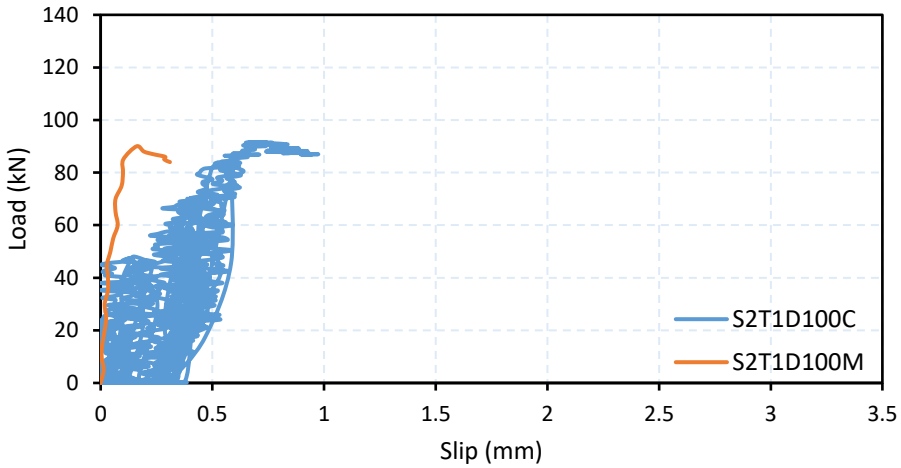

(b) Specimens $S_2T_1D_{100}M$ and $S_2T_1D_{100}C$.

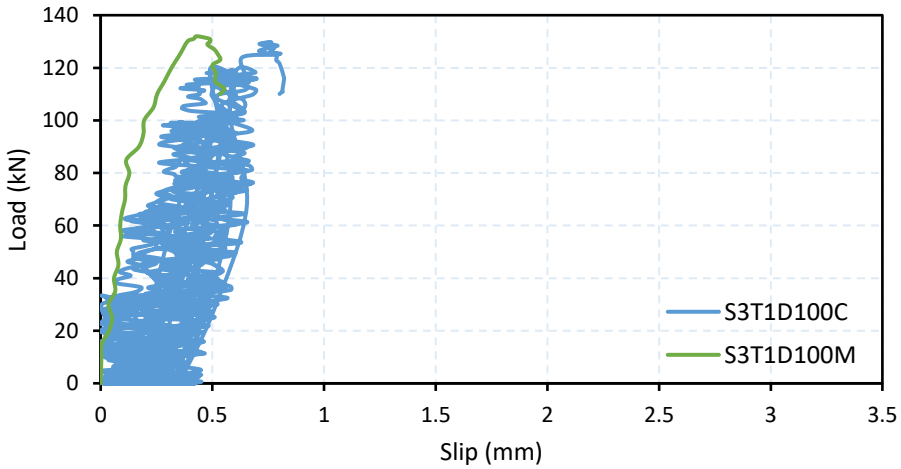

(c) Specimens $S_3T_1D_{100}M$ and $S_3T_1D_{100}C$.

Figure 4.45: Effect of cyclic load on the slip response.

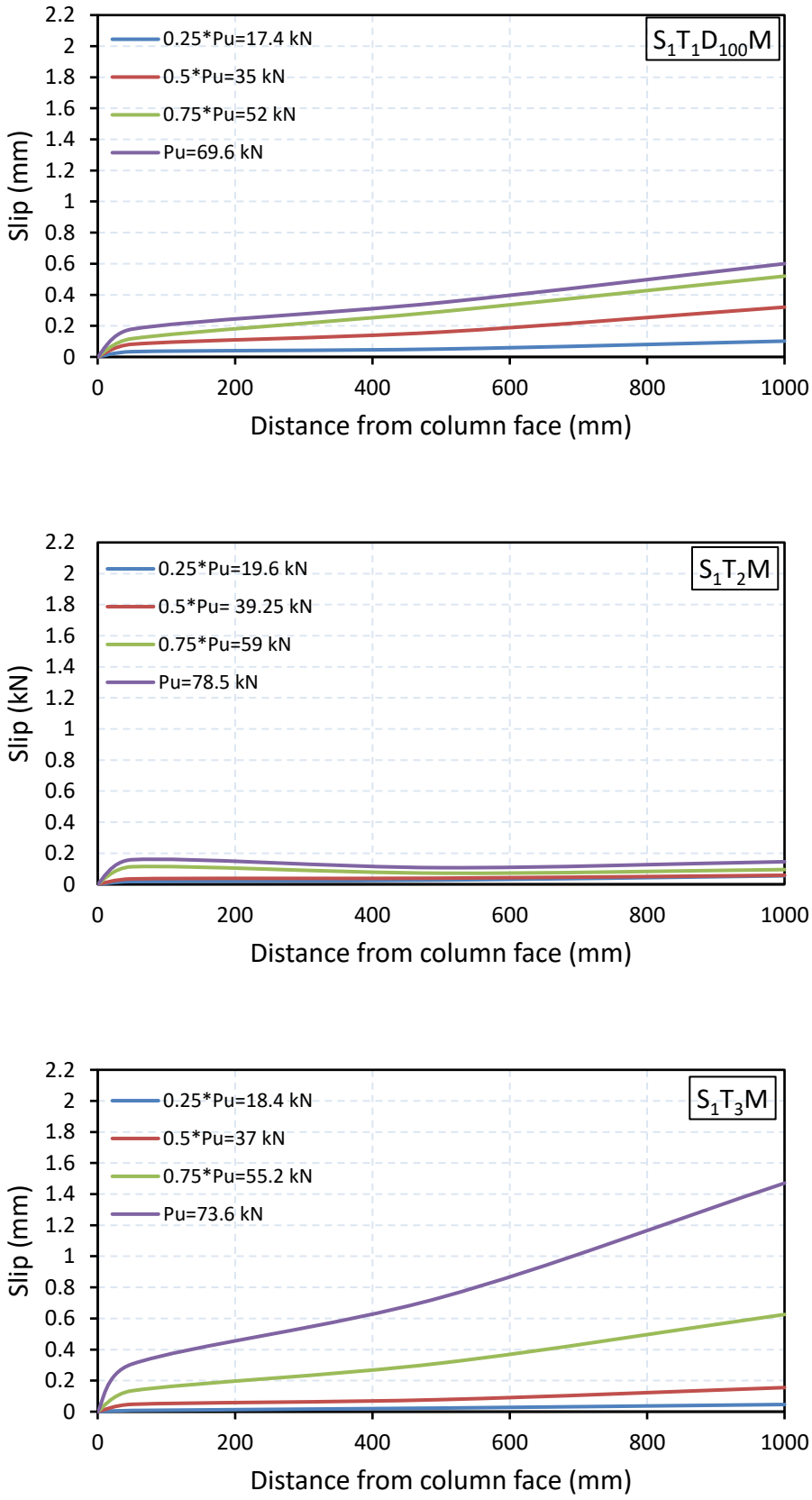

Figure 4.46: The slip response along beam span for specimens tested under monotonic load (continue).

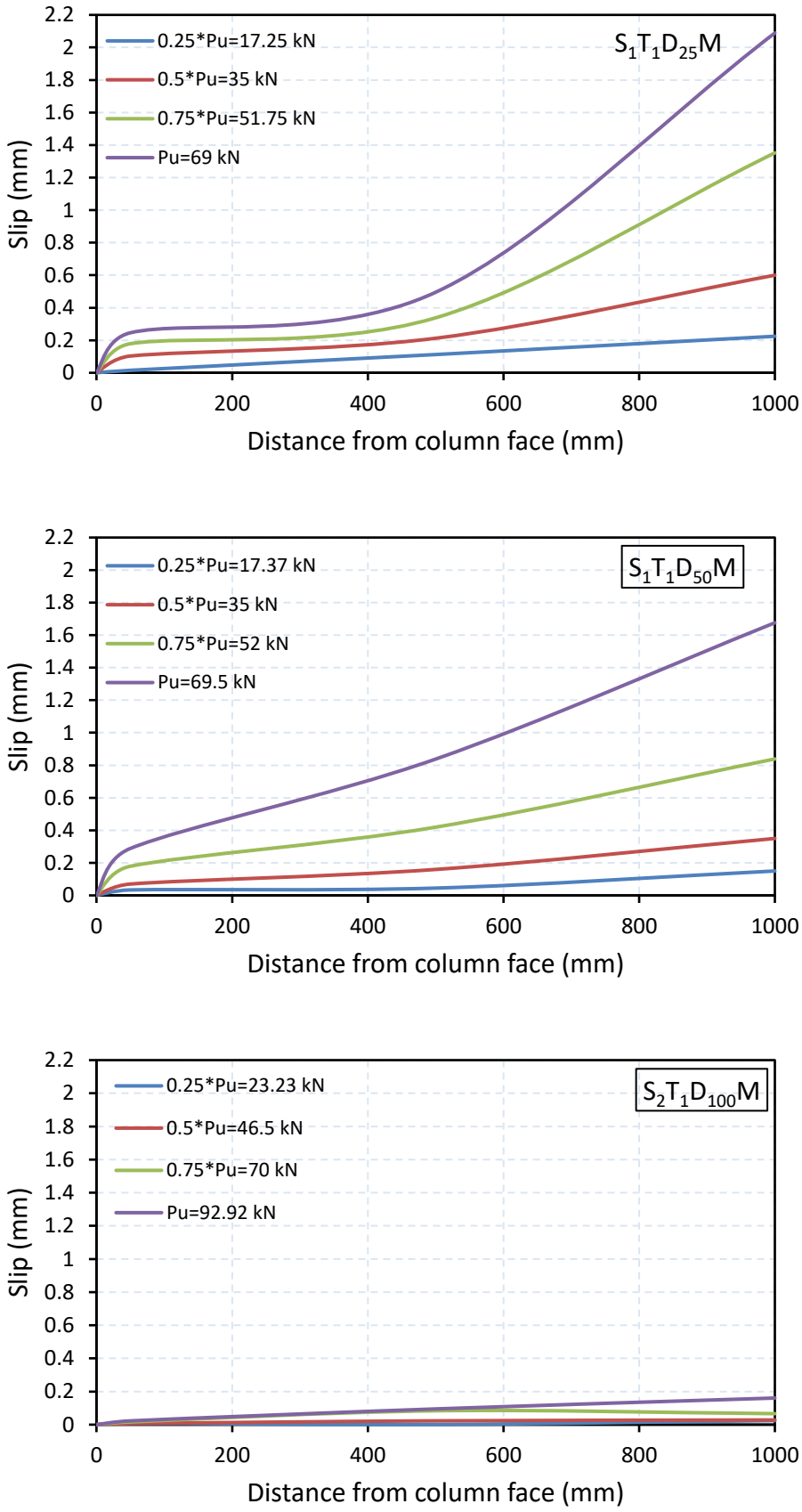

Figure 4.46: The slip response along beam span for specimens tested under monotonic load (continue).

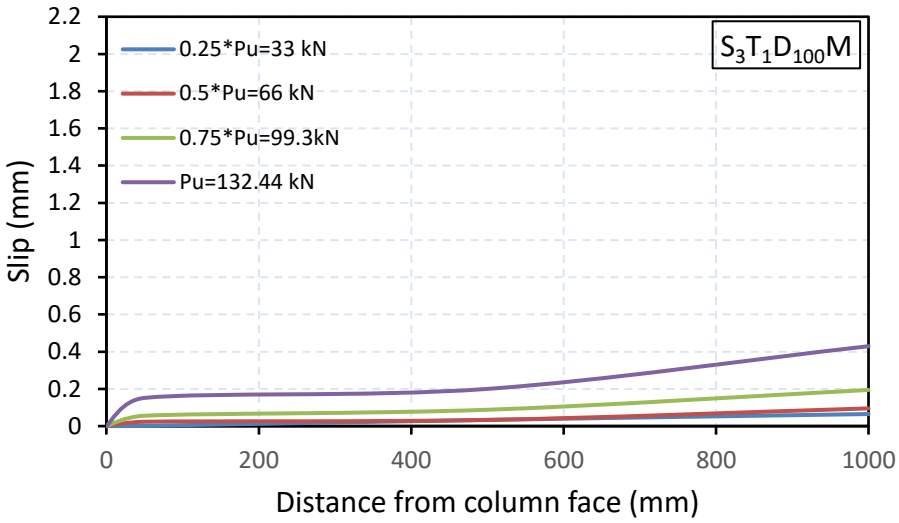

Figure 4.46: The slip response along beam span for specimens tested under monotonic load.

4.12 COMPOSITE JOINT DUCTILITY

Ductility, defined as the ability to undergo inelastic deformation before failure, not only warns of impending failure. The ratio of ultimate displacement to yielding displacement was defined as the ductility index. The displacement corresponding to the ultimate load represents the ultimate displacement (Δu). On the other hand, (Δy) was calculated depending on Park [115], as illustrated in Figure 4.47. The ductility index of all the tested specimens is listed in Table 4.5. The values of the ductility index ranged from 2.2 to 2.5 for the specimens connected by top and seat angles between the column and the beam, which had a semi-rigid behavior. While the specimens connected directly through the web, the ductility values ranged from 1.5 to 1.9, which had an almost rigid behavior. From the results shown in Figure 4.48, it is noticed that the semi-rigid joint appeared to increase the ductility because it allows for rotation, thus increasing the susceptibility to inelastic deformation before failure.

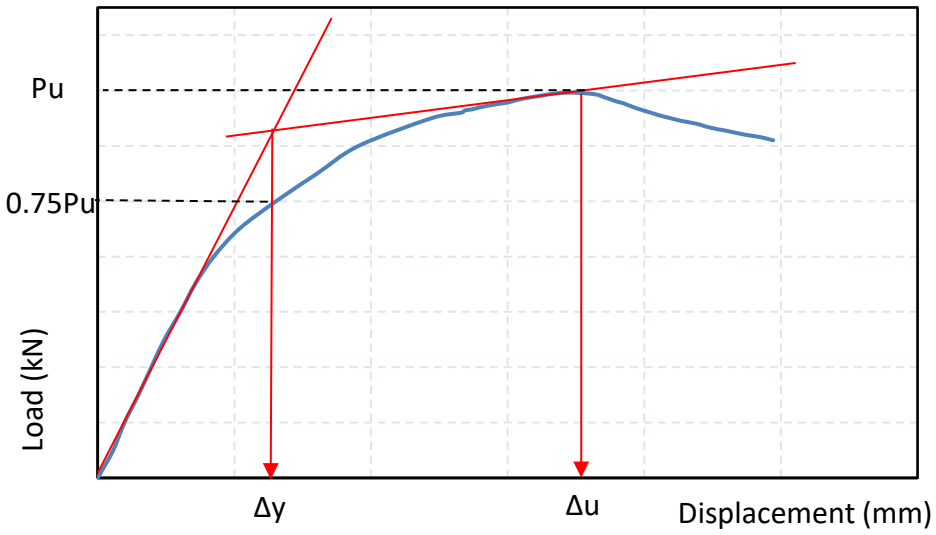

Figure 4.47: Procedures for determining the ductility component.

On the other hand, cyclic loading reduced ductility due to an increase in yield displacement due to a repeated loading, especially for specimen $S_1T_1D_{100}C$, where the plasticity decreased by about 12 percent compared with specimen $S_1T_1D_{100}M$.

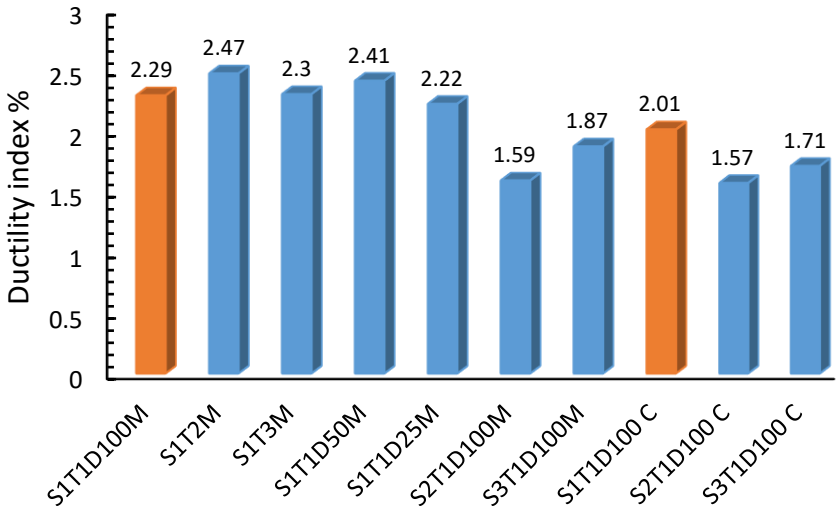

Figure 4.48: Ductility index values.

Table 4.5: Ductility index results.

Specimen symbol	Ultimate load (kN)	Yield deflection (mm)	Ultimate deflection (mm)	Ductility index	Energy absorption (kN.mm)
$S_1T_1D_{100}M$	69.81	28.95	66.22	2.29	3731.35
S_1T_2M	78.50	22.50	55.65	2.47	3401.97
S_1T_3M	73.68	25.11	57.69	2.30	3045.17
$S_1T_1D_{50}M$	69.50	30.80	74.35	2.41	3664.59
$S_1T_1D_{25}M$	69.00	28.62	63.56	2.22	3287.84
$S_2T_1D_{100}M$	92.92	10.33	16.38	1.59	887.04
$S_3T_1D_{100}M$	132.44	10.33	19.34	1.87	1667.13
$S_1T_1D_{100}C$	67.38	39.90	80.17	2.01	3814.68
$S_2T_1D_{100}C$	91.54	11.49	18.06	1.57	969.41
$S_3T_1D_{100}C$	129.81	11.03	18.89	1.71	1520.45

4.13 ENERGY ABSORPTION

The energy absorption capacity is defined as the area enclosed by the load-deflection curve until the maximum load reached, representing the composite joint energy absorption capacity before it exhibits a significant drop in load-carrying capacity. Previous research found that energy absorption capacity is the best index of structural response to earthquake motion and resistance to fire and impact loads [116]. The calculations of the area under the load-deflection curves until the maximum load for the $S_1T_1D_{100}M$, $S_2T_1D_{100}M$, and $S_3T_1D_{100}M$ composite joints were represented in Figure 4.49.

The energy absorption results of all the tested specimens are listed in Table 4.5. The shear connector type affected the energy absorption capacity

of specimens S_1T_2M and S_1T_3M by reduced the energy absorption by about 8.8 and 18.4 %, respectively, compared with specimen $S_1T_1D_{100}M$.

On the other hand, the beam-to-column joint connection shape clearly affected the energy absorption capacity, as shown in Figure 4.50. The energy absorption capacity of specimen $S_1T_1D_{100}M$ increased by 76.2 and 55.3% compared with specimens $S_2T_1D_{100}M$ and $S_3T_1D_{100}M$, respectively. This is due to the semi-rigid behavior of the joint in specimen $S_1T_1D_{100}M$, which is more capable of absorbing energy in contrast to specimens $S_2T_1D_{100}M$ and $S_3T_1D_{100}M$, in which the joint behavior was closer to that of a rigid joint.

The energy absorption increased for specimens tested under cyclic load $S_1T_1D_{100}C$ and $S_2T_1D_{100}C$ compared with corresponding specimens under monotonic load due to a repeated load effect that increased the ultimate deflection. Except for specimen $S_3T_1D_{100}C$, the absorption energy decreased because the box beam gave a high stiffness, so it was the same behavior as the sample $S_3T_1D_{100}M$, except that it failed with less load and less ultimate deflection.

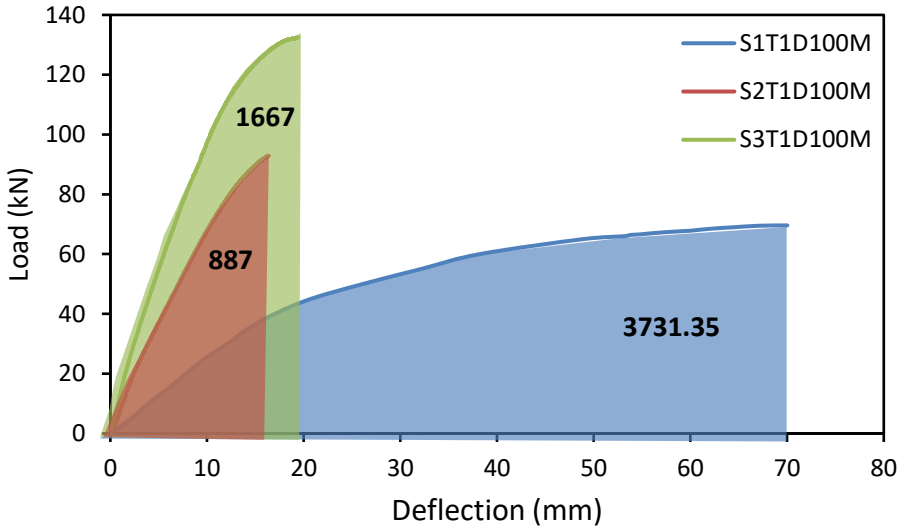

Figure 4.49: Diagram for calculating the area under the load-deflection curve.

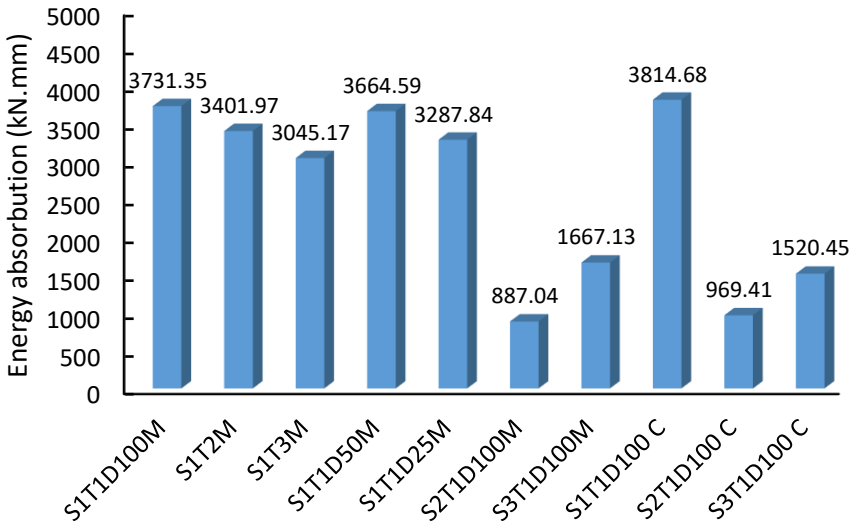

Figure 4.50: The results of energy absorption capacity for all tested specimens.

4.14 COMPOSITE CFS BEAM STRAINS WITH DEPTH

The strain profile through the depth of the composite CFS beam at the column face is measured using the DIC technique at ultimate load, as shown in Figures 4.51 and 4.52. It demonstrated that the steel beams in partial shear connection joints $S_1T_1D_{50}M$ and $S_1T_1D_{25}M$ were more strained than $S_1T_1D_{100}M$.

It is also worth noting the more pronounced change in the neutral axis position for specimens S_1T_2M and S_1T_3M compared to specimen $S_1T_1D_{100}M$, which can be attributed to the reinforcement and steel beam more extensive inelastic yielding in specimen $S_1T_1D_{100}M$. While specimen S_1T_2M, which has a CFS plate angle shear connector, reduced the strains generated in the concrete slab and CFS beam. The strain profile for specimens with different beam-to-column connection shapes is shown in Figure 4.53.

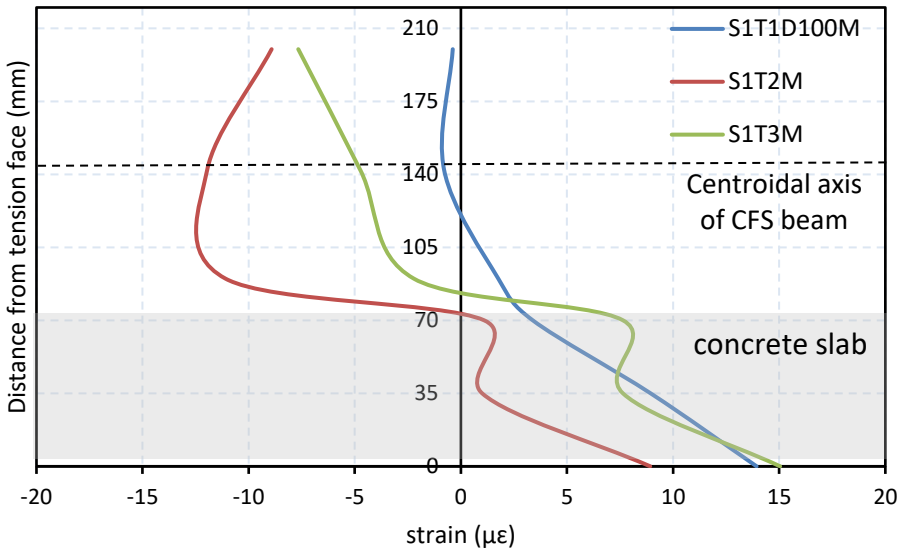

Figure 4.51: $S_1T_1D_{100}M$, S_1T_2M and S_1T_3M strain distribution at various cross-sections as measured from the column face.

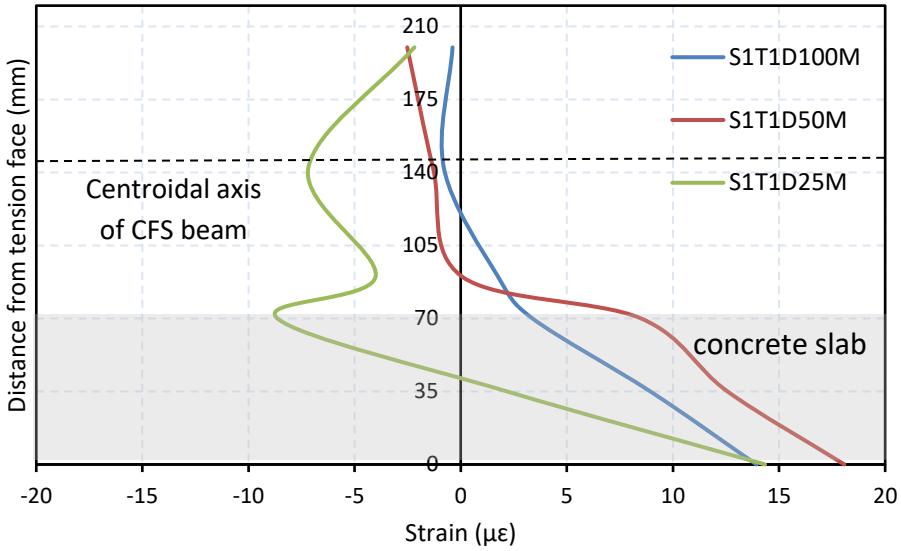

Figure 4.52: $S_1T_1D_{100}M$, $S_1T_1D_{50}M$ and $S_1T_1D_{25}M$ strain distribution at various cross-sections as measured from the column face.

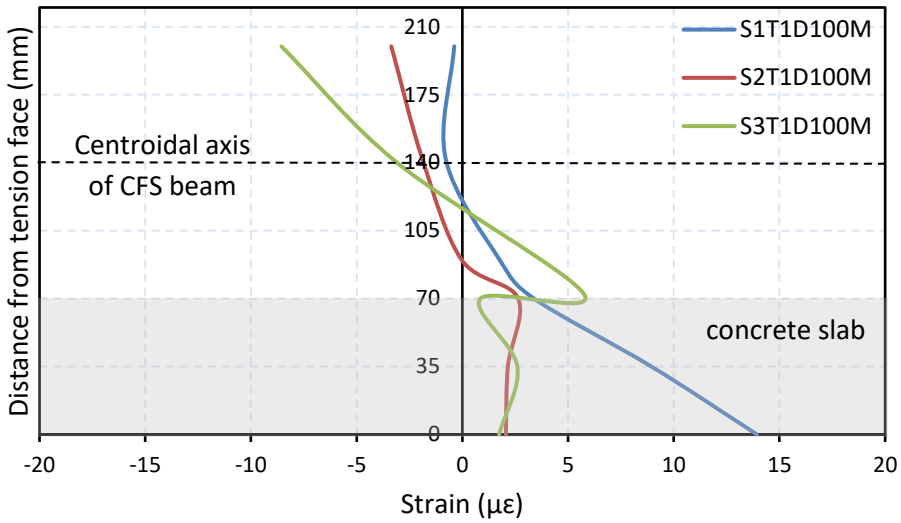

Figure 4.53: $S_1T_1D_{100}M$, $S_2T_1D_{100}M$ and $S_3T_1D_{100}M$ strain distribution at various cross-sections as measured from the column face.

CHAPTER FIVE

NUMERICAL ANALYSIS BY FINITE ELEMENT

5.1 INTRODUCTION

The primary goal of this chapter is to validate the current nonlinear finite element model used to investigate the behavior and ultimate load capacity of composite CFS beam-to-column joints with various connection shapes and shear connector types. Numerical analyses are performed using the ABAQUS Standard/Explicit 2017 finite element model to establish the validity and degree of accuracy of the adopted analytical finite element model and to compare the results with the experimental results shown in Chapter 4.

5.2 FINITE ELEMENT MODELING

The specimens were modelled to investigate the composite joints' strength, rotation capacity, and behavior. In modelling the concrete slab, CFS beam and column, connection and shear connector bolts and plates under loading, an 8-node linear brick, reduced integration, hourglass control (C3D8R) were used. For reinforcement, a three-dimensional two-node truss element T3D2 was used. Modelling the adopted composite joint specimens with different connection shapes presents some challenges. The presence of numerous and diverse parts with varying material properties, such as concrete, cold-formed steel, reinforcement, shear connectors, bearing plates, connection plates, and the connection bolt, necessitates some modelling accuracy. Furthermore, the method and type of interaction between these parts must

be carefully chosen to achieve a simulation as close to the real response as possible.

5.3 MATERIAL PROPERTIES

In three-dimensional finite element analysis, the performance of any structure under load was determined by the behavior of the material used to construct the member (modulus of elasticity, Poisson's ratio, and material stress-strain relationship). Composite joints were constructed from various materials (concrete, cold-formed steel, bolt, steel plate, and reinforcing steel) that joined together to form a composite system.

Appendix **B** shows the behavior and properties of the materials used in this study.

5.4 MODELING OF SPECIMENS

This section discusses the composite joint's parts and assembly, the interactions between the elements and the load and boundary conditions used in this study.

5.4.1 Parts and Assembly

The specimens consisted of many parts: a concrete deck, CFS beam and column, bearing plate at support and load, reinforcing bar, angle plate, connection bolt, and bolted shear connector, as shown in Figure 5.1. Each component is drawn separately, assembled, and merged with the other elements to form the composite joint. The assembly of parts used in modelling specimens is shown in Figure 5.2.

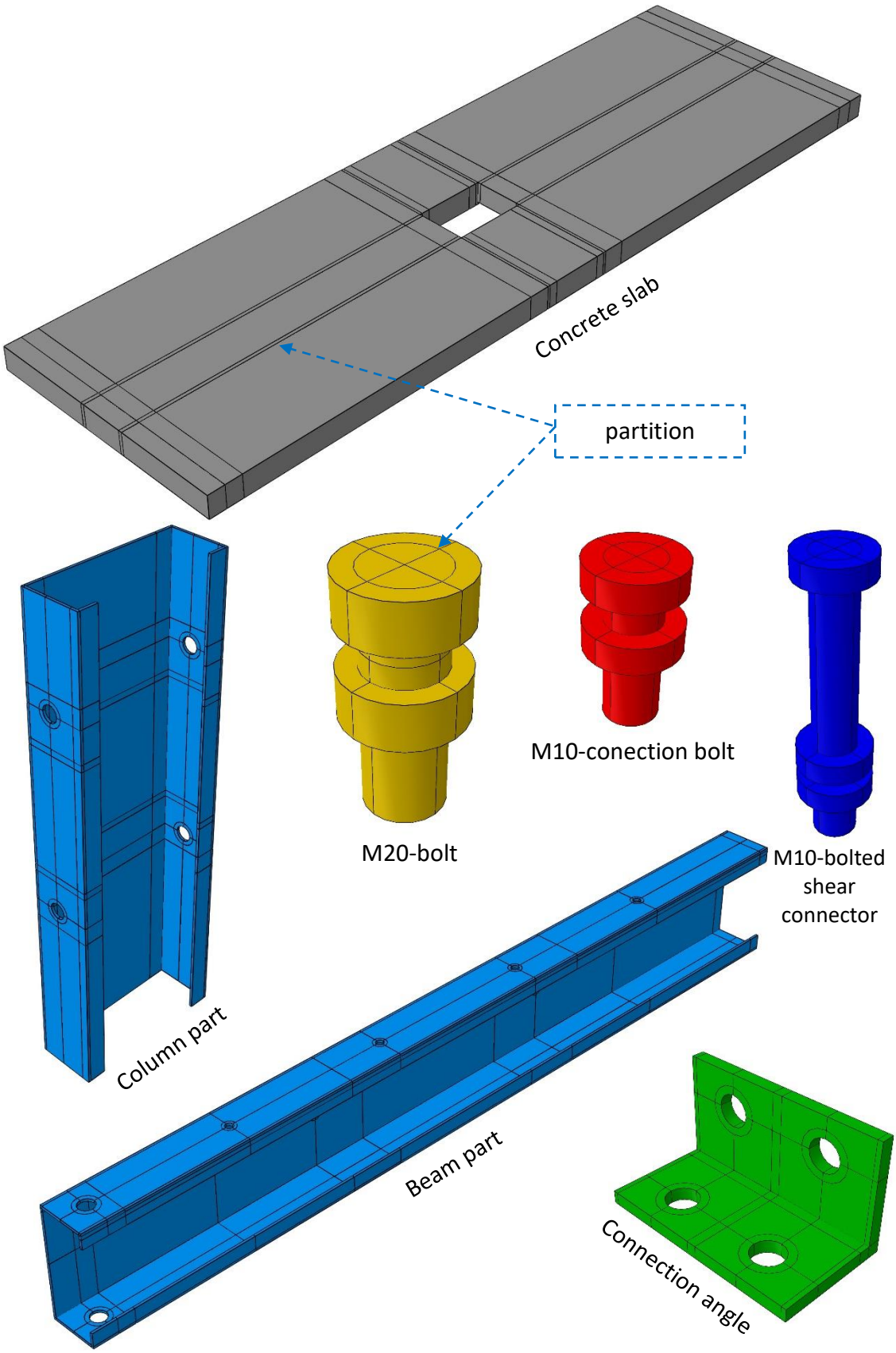

Figure 5.1: Parts used in the modeling of specimens.

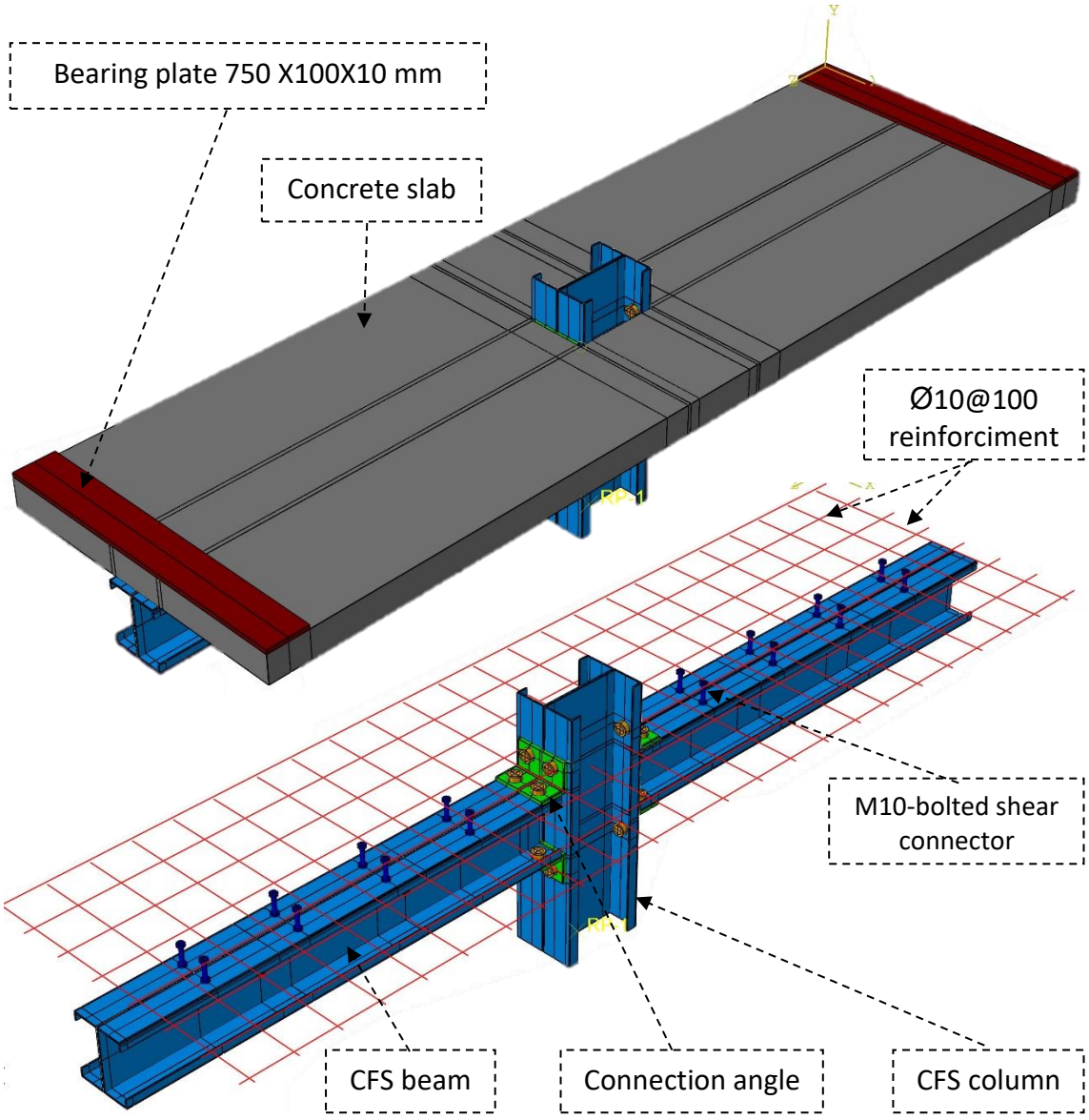

Figure 5.2: The Assembled Parts of Composite beam-to-column joint.

5.4.2 Finite Element Modeling Interaction

After assembling the parts, which must be connected together to operate a composite system, the surface-to-surface contact (Standard) provided by ABAQUS was used at all interfaces between the bolts, the concrete slab, and the CFS beam and column. The "hard contact" algorithm was used to depict the contacted behavior in the normal direction, allowing interaction forces to be transferred without interfering with the interaction. To describe the tangential responses, the "penalty" algorithm was used, which could simulate the effect of friction by introducing a friction coefficient. For the

CFS angle-to-CFS beam and column interfaces, the friction coefficient was set to 0.1, and for the CFS beam-to-concrete interfaces, it was set to 0.3. In addition, the embedded region constraint used for linked the reinforcing bars and the bolted shear connector with concrete slab, with the interface slip being neglected.

5.4.3 Loading and Boundary Conditions

The finite element model was loaded at the same locations in the experimental work for all composite joints, and the load was represented as a concentrated load applied on the column head. The supports were modeled similarly to the experimental work, in which a single line of nodes constrained the displacement in the directions x, y, and z for hinge support cases, and a single line of nodes constrained the displacement in the directions x and y-axis and free displacement was assumed in the direction z for case roller support. In addition, to avoid model coupling, the rotation in the direction of x-axis was constrained in both supports. Figure 5.3 shows the applied load and boundary conditions of the modeled composite joints.

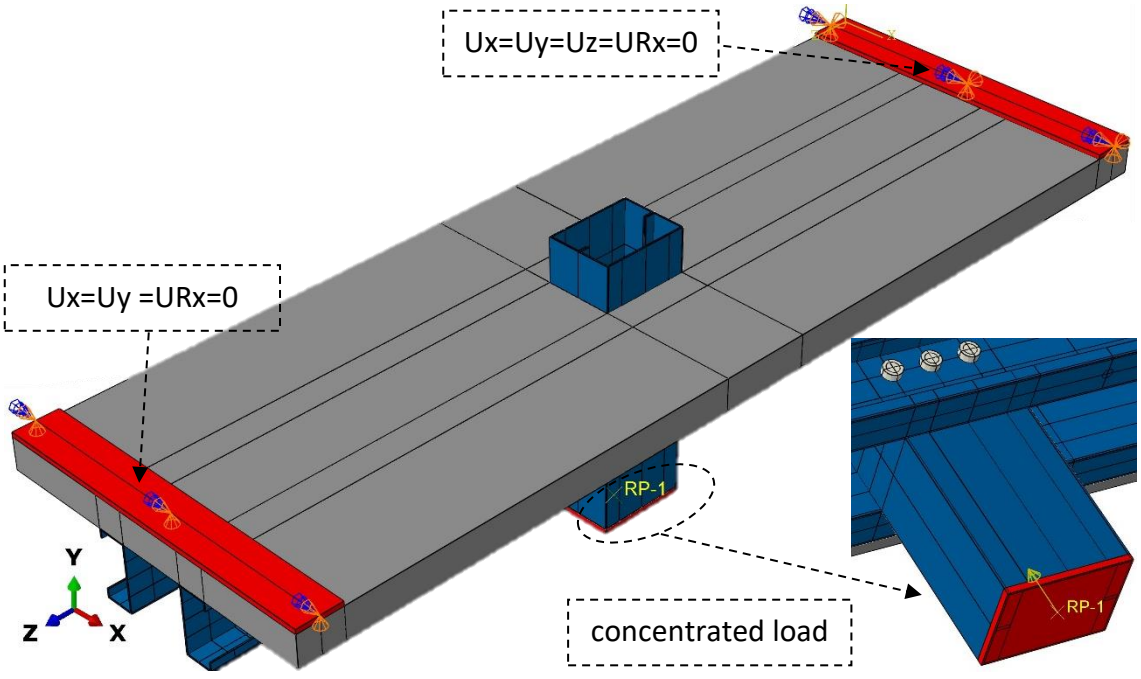

Figure 5.3: Boundary conditions of modeled composite joints.

5.5 CONVERGENCE STUDY

The main aim of the convergence study is to select the proper mesh size of the model with a minimum number of elements and maximum convergence with the results of the experimental test. This is practically achieved when the decrease in the mesh size has a negligible effect on the results. A control specimen $S_1T_1D_{100}M$ with the same material properties was modeled with a decrease in the element sides of 40, 30, 25, 20, and 15 mm.

The deflection under the column for specimens with different mesh sizes was observed at the same applied load level of 65 kN. A convergence study showed that the difference could be ignored when the mesh size decreased from 30 mm to 20 mm; therefore, the 30 mm model for CFS beams, columns, and angles was adopted for all tested specimens (see Figure 5.4). Due to the lack of effect of changing the mesh size from 20 to 30 mm, a size of 30 mm was chosen for the concrete slab to reduce the analysis time. The mesh details of the composite joint model are shown in Figure 5.5. On the other hand, all of the bolts in this model have a mesh size of 5.0 mm.

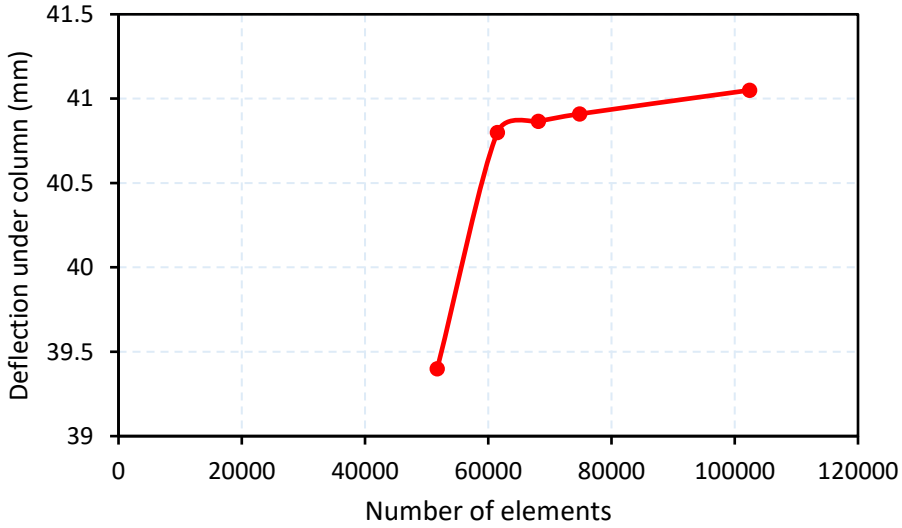

Figure 5.4: The convergence study results.

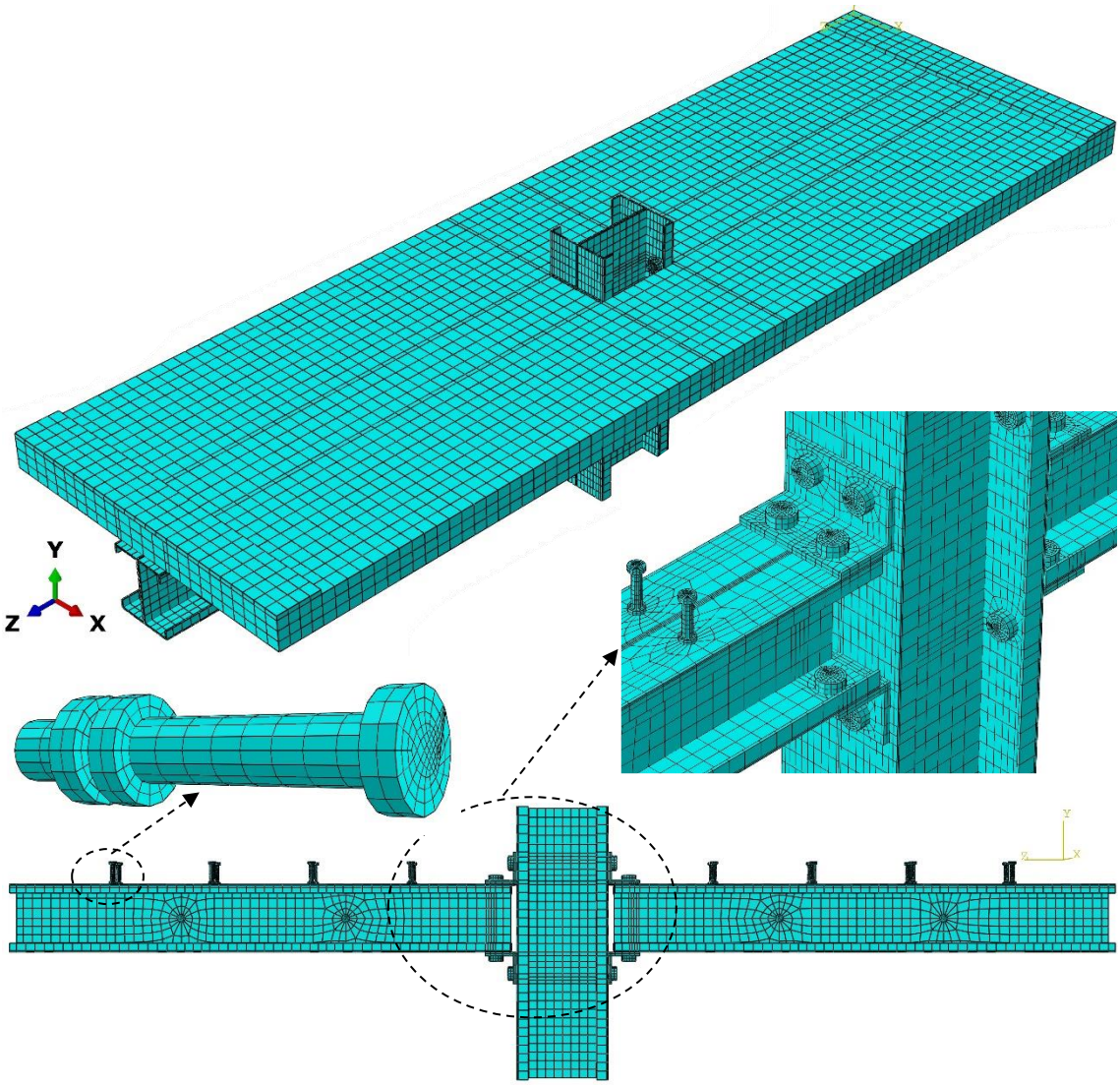

Figure 5.5: Finite Element Mesh.

5.6 RESULTS OF FINITE ELEMENT ANALYSIS

The experimental results for composite joint specimens with different connection shapes between the beam and column are compared to the results of finite element analysis using the ABAQUS program, 2017. ABAQUS results, including the ultimate moment and rotational capacity were compared with the practical results and showed good convergence. As a result, and after determining the validity of these models, expanding the experimental program by studying a large number of numerical cases that affected the composite joint behavior.

The comparison between the ultimate moment and ultimate rotation from the experimental tests and numerical models from finite element analysis of the analyzed composite joints is listed in Table 5.1. The greatest difference in results ranged from 2% to 5.2% increase in ultimate moment. As a reduction, the difference in rotation capacity for specimen $S_1T_1D_{100}M$ equal 9.65%, while for the specimens $S_2T_1D_{100}M$ and $S_3T_1D_{100}M$, where the rotation capacity increased about 10.7% and 15.7 % from the experimental result, respectively.

Table 5.1: Comparison of experimental and numerical results.

Specimens	Ultimate moments (kN.m)		$\frac{M_{u)\ Num.} - M_{u)\ EXP.}}{M_{u)\ EXP.}}$ %	Rotation capacity (mrad)		$\frac{\emptyset_{u)\ Num.} - \emptyset_{u)\ EXP.}}{\emptyset\Delta_{u)\ EXP.}}$ %
	$M_{u)\ EXP.}$	$M_{u)\ Num.}$		$\emptyset_{u)\ EXP.}$	$\emptyset_{u)\ Num.}$	
$S_1T_1D_{100}M$	38.28	39.05	2	50.04	45.207	- 9.65
$S_2T_1D_{100}M$	46.00	47.71	3.7	11.87	13.733	15.7
$S_3T_1D_{100}M$	66.00	69.45	5.2	11.11	12.3	10.7

5.6.1 Effect of connection shape under monolithic load

Figures 5.6 to 5.8 compare the moment rotation curves obtained from the experimental and numerical results. Also, the failure mode obtained by numerical analysis for all these specimens is approximately similar to the experimental failure mode, as shown in Figure 5.9.

Figure 5.10 depicts the mises-equivalent stress distribution at ultimate load for the specimens $S_1T_1D_{100}M$, $S_2T_1D_{100}M$, and $S_3T_1D_{100}M$. It is noted that the maximum stress in the column web is at the seat angle connection for specimens that used angle connections between beam and column, while the maximum stress in the beam is along the connection area for the other samples.

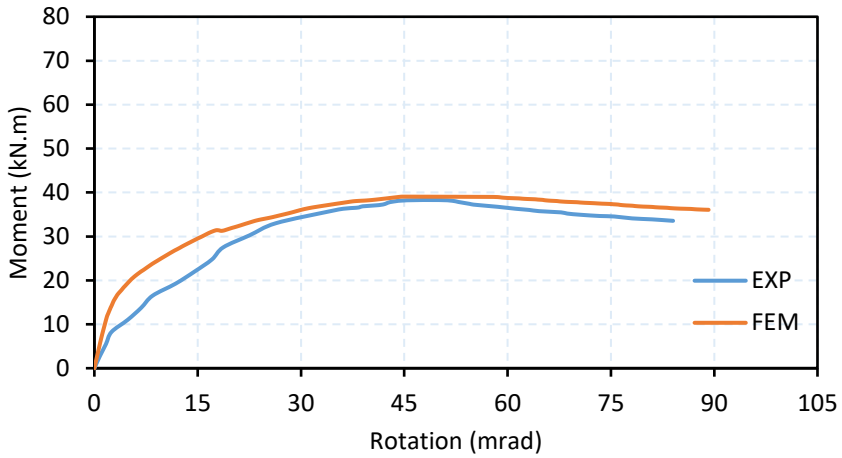

Figure 5.6: Moment-rotation curve for specimen $S_1T_1D_{100}M$.

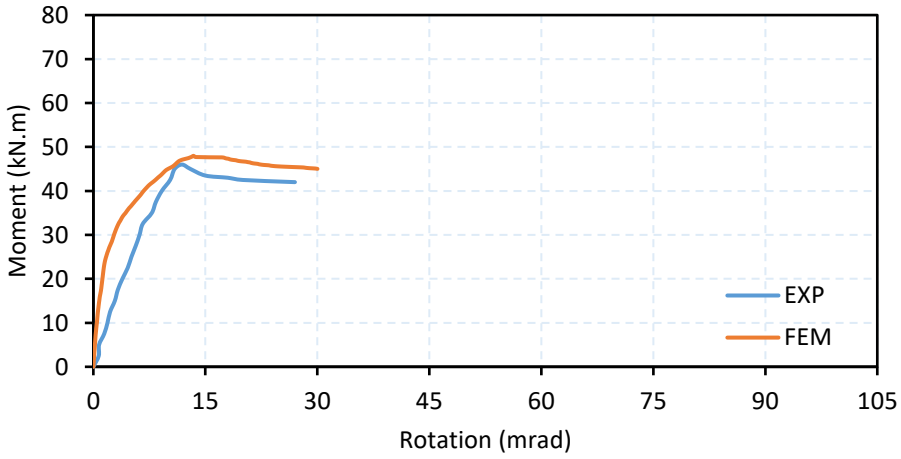

Figure 5.7: Moment-rotation curve for specimen $S_2T_1D_{100}M$.

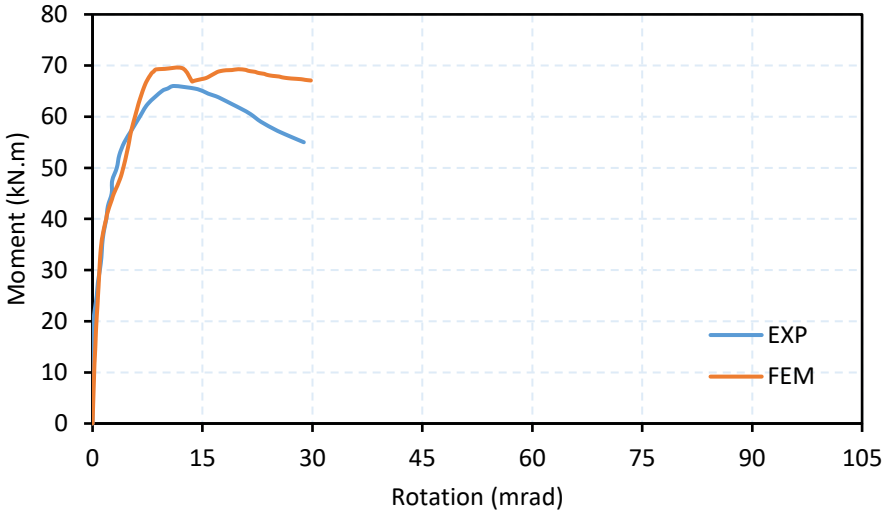

Figure 5.8: Moment-rotation curve for specimen $S_3T_1D_{100}M$.

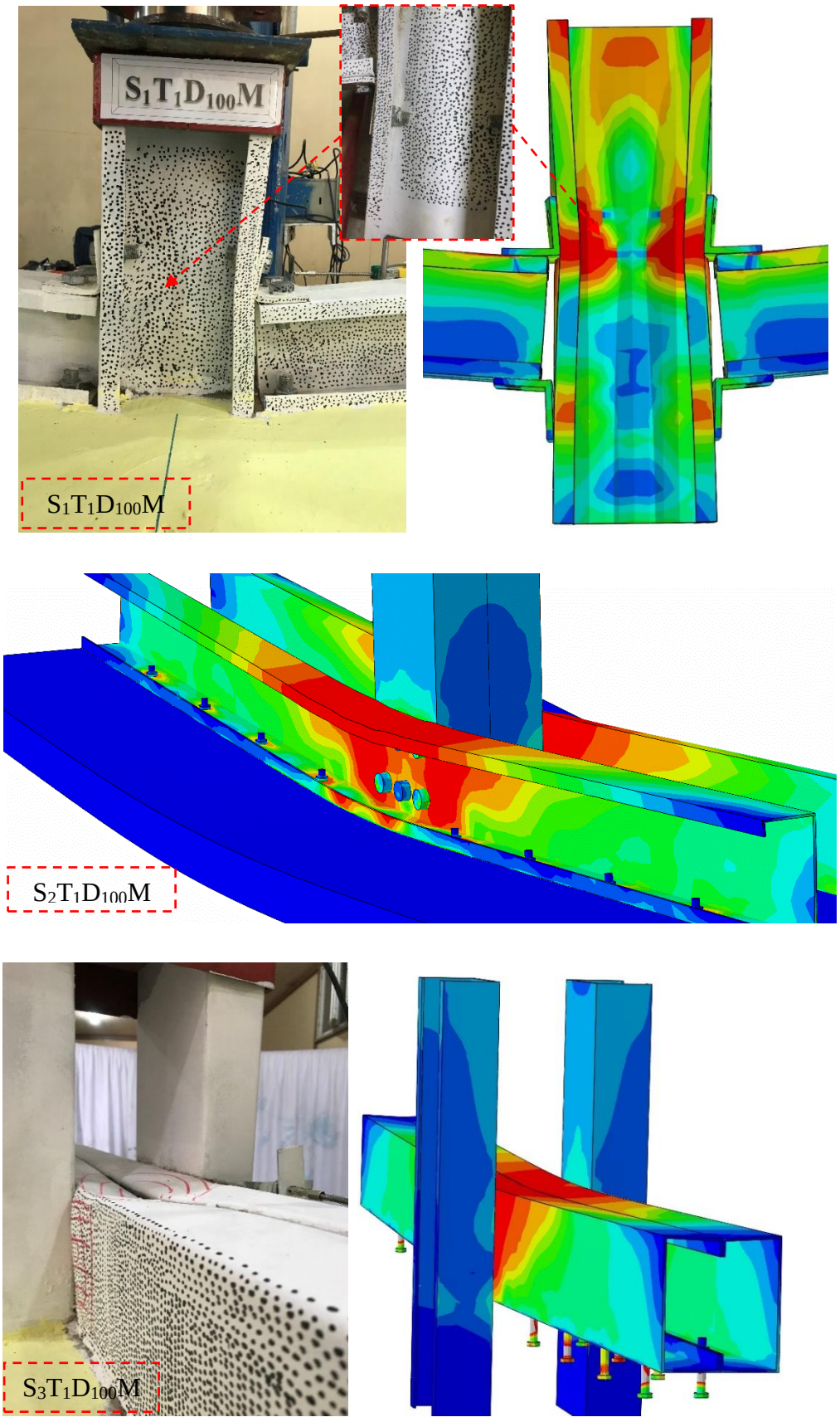

Figure 5.9: Numerical failure mode of specimen $S_1T_1D_{100}M$, $S_2T_1D_{100}M$ and $S_3T_1D_{100}M$.

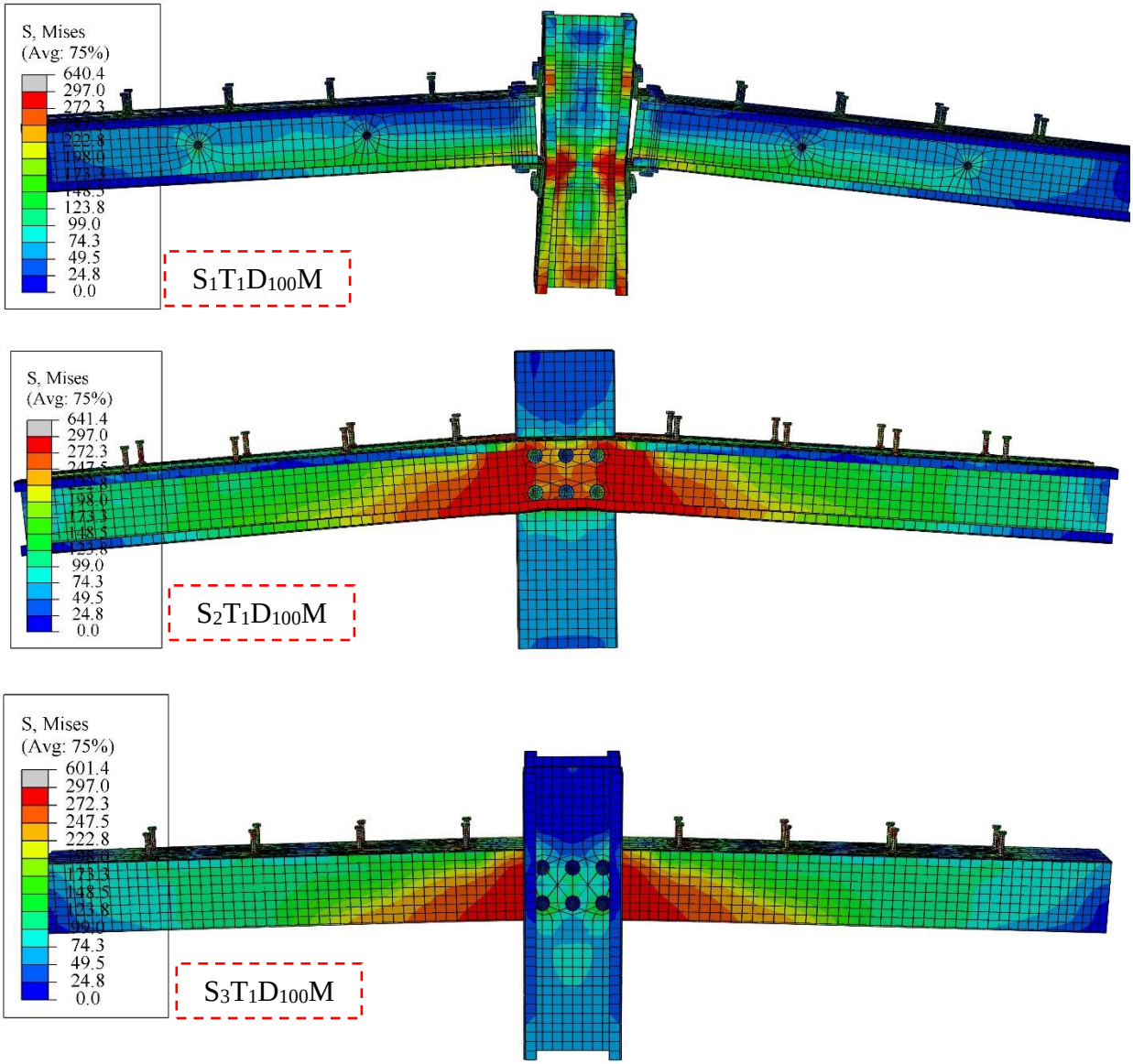

Figure 5.10: Von-Mises equivalent stress distribution.

5.7 PARAMETRIC STUDY

After studying the convergence of samples with different shapes of beam-to-column connection and obtaining a good convergence between the practical and numerical results, the experimental program was expanded by studying a set of variables and their impact on joint behavior. The variables studied include:

1- Effect of the column web confined by the concrete slab.

2- The thickness of the connection angle.

3- Reinforcement ratio effect.
4- The impact of the column web stiffener used.
5- Column shape effect.
6- The number of connection bolts.

The details and suggested names of the specimens studied in the parametric study are shown in Table 5.2. The control specimen S_1A-8 has the same details as the experimental specimen $S_1T_1D_{100}$M, which has the following information: the thickness of the connection angle of 8 mm, reinforcement ratio of 1.2, I-section column shape, and concrete slab thickness 70 mm. In addition, the results of the ultimate moment and rotation capacity of all these specimens are listed in Table 5.3.

Table 5.2: The details of the studied variables.

Specimen name	Symbol of variable	Variable	Value of variable
$S_1T_1D_{100}$MC	C	Confinement of the web of the column by concrete slab (connection angle thickness=8)	-
S_1A-8	control	Control specimen	8 mm
S_1A-10	A-10	Angle thickness	10 mm
S_1A-12	A-12		12 mm
S_1A-8R-0.9	R-0.9	Reinforcement ratio	0.9 %
S_1A-8R-0.6	R-0.6		0.6 %
S_1A-8S-2	S-2	Stiffener the column web	2 mm
S_1A-8S-4	S-4		4 mm
S_1A-8F-B	F-B	Column Form	Box shape
S_1A-8F-M	F-M		M shape
$S_2T_1D_{100}$M	N-6	Number of connection bolts	6
$S_2T_1D_{100}$MN-4	N-4		4
$S_3T_1D_{100}$M	N-6	Number of connection bolts	6
$S_3T_1D_{100}$MN-4	N-4		4

Table 5.3: Results of the parametric study.

Specimen name	Ultimate moment (kN.m)	Variation in moment %*	Rotation capacity (mrad)	Variation in rotation %*
$S_1T_1D_{100}MC$	39.055	3.3	45.207	-25.7
S_1A-8	37.797	-	60.855	-
S_1A-10	39.628	4.84	56.262	-7.54
S_1A-12	44.326	17.27	37.866	-37.77
S_1A-8R-0.9	39.51	4.53	68.62	12.76
S_1A-8R-0.6	37.69	- 0.269	22.64	- 62.8
S_1A-8S-2	48.615	28.62	72.18	18.62
S_1A-8S-4	53.907	42.62	130.83	115
S_1A-8F-B	37.30	-1.30	97.54	60.28
S_1A-8F-M	40.86	8.11	67.45	10.83
$S_2T_1D_{100}M$	47.71	26.22	13.7	-77.5
$S_2T_1D_{100}MN$-4	46.75	23.68	24.7	-59.41
$S_3T_1D_{100}M$	69.45	83.74	12.3	-80
$S_3T_1D_{100}MN$-4	62.88	66.36	32.57	-46.48

*All specimens were compared with specimen S_1A-8.

5.7.1 Effect of the column web confined by the concrete slab

This part studied the effect of the concrete confinement on the column web at the level of the top angle. It is noted that the presence of concrete increases the ultimate moment by 3.3 percent and reduces the capacity of the rotation by about 25.7 percent, see Figure 5.11. It also reduces the buckling of the column web, where the buckling is at the seat angle level, while the buckling is much more significant and extends to the whole column web without concrete, as shown in Figure 5.13.

Figure 5.12 shows the deformation of the column flange, where the displacement of the column flange for specimen S_1A-8 increases by 25% from the displacement of specimen $S_1T_1D_{100}MC$.

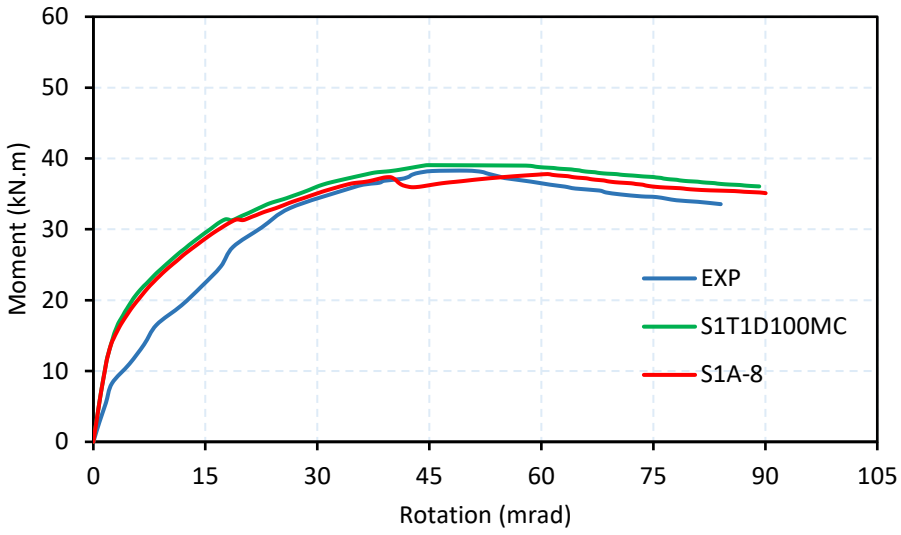

Figure 5.11: Moment-rotation curve for specimens $S_1T_1D_{100}MC$ and S_1A-8.

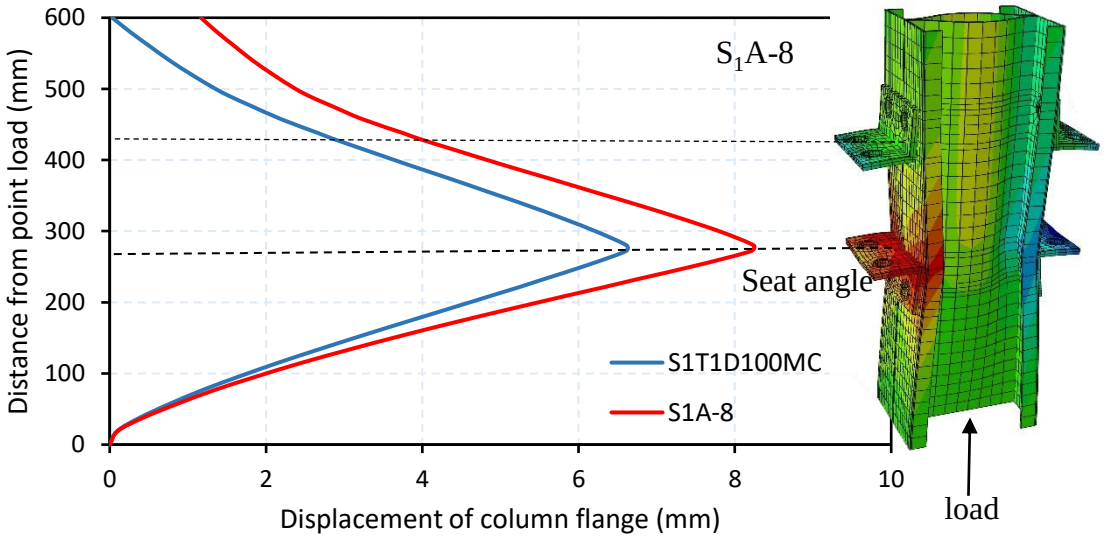

Figure 5.12: The deformation of the column flange in specimens $S_1T_1D_{100}MC$ and S_1A-8.

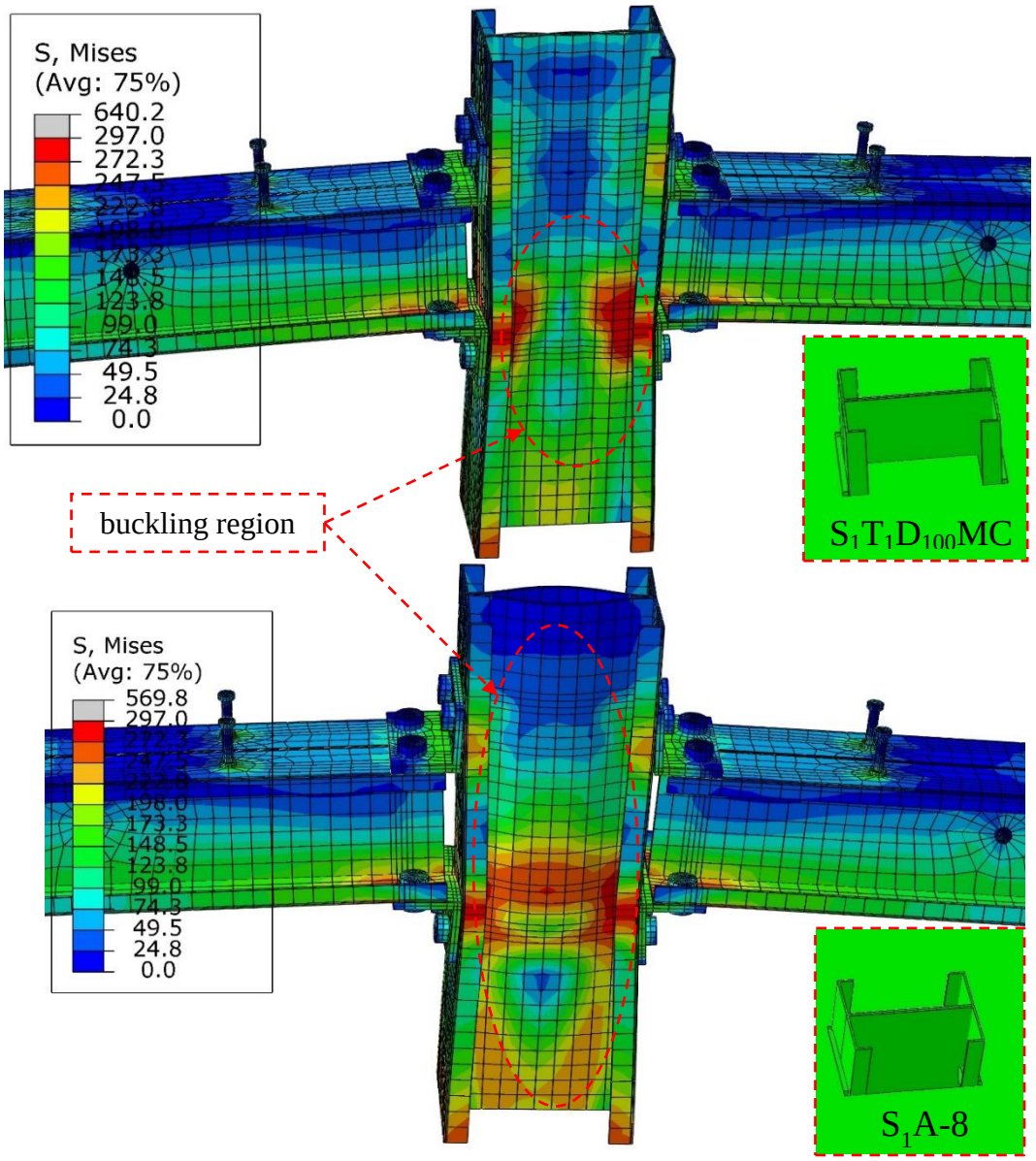

Figure 5.13: Von-Mises equivalent stress distribution for specimens $S_1T_1D_{100}MC$ and S_1A-8.

5.7.2 The thickness of the connection angle

The specimens S_1A-8, S_1A-10, and S_1A-12 studied in this part have the same details but differ in the connection angle thickness. The increase in angle thickness in specimens S_1A-10 and S_1A-12 to 10 mm and 12 mm increases about 4.84 and 17.27% of the ultimate moment and decreases the rotation capacity by 7.54 and 37.77% compared with specimen S_1A-8, which has an 8 mm angle thickness, respectively. However, in all specimens, the joint is still classified as semi-rigid, which means the

rotation capacity exceeds 30 mrad, as shown in Figure 5.14. In addition, the increased angle thickness reduces the seat angle deformation and the column web buckling. This is since increasing the thickness of the angle causes a reduction in the rotation and thus reduces the pressure of the angle on the column, which reduces the buckling of the web, as shown in Figures 5.15 to 5.17.

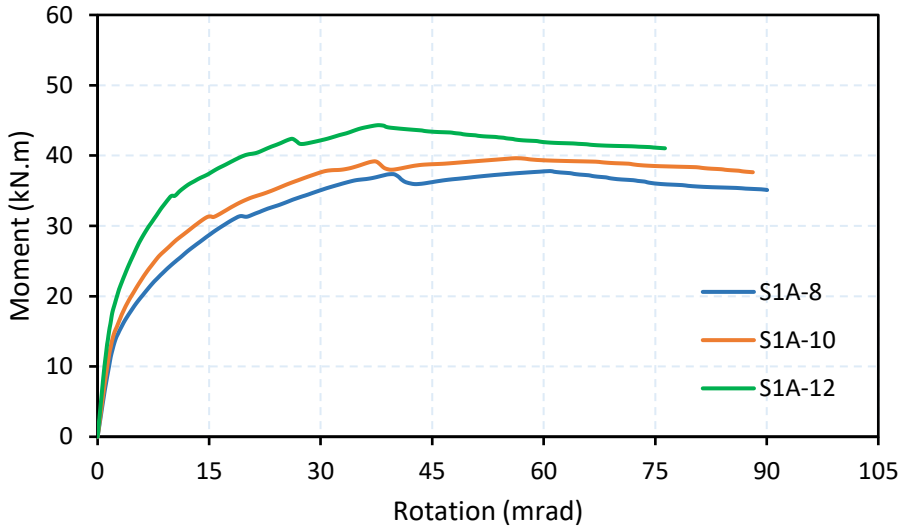

Figure 5.14: Moment-rotation curve for specimens with different connection angle thicknesses.

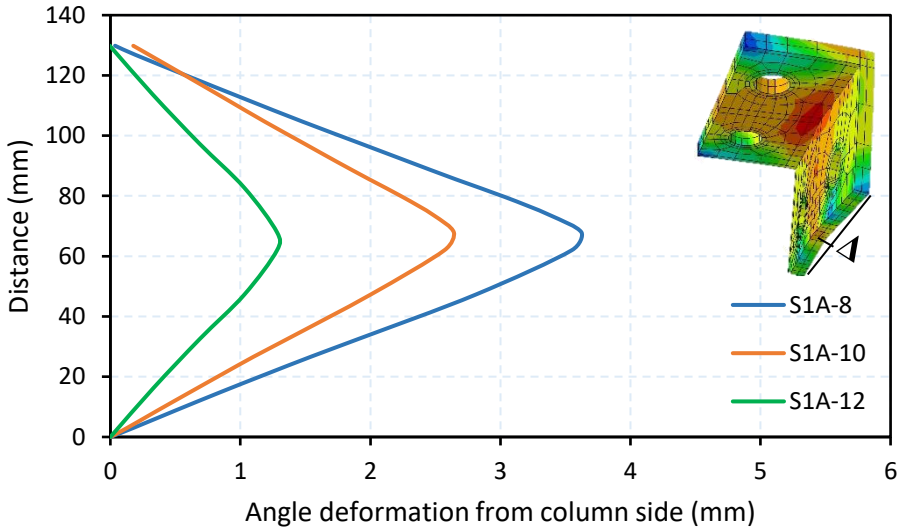

Figure 5.15: Seat angle deformation from the column flange at ultimate load.

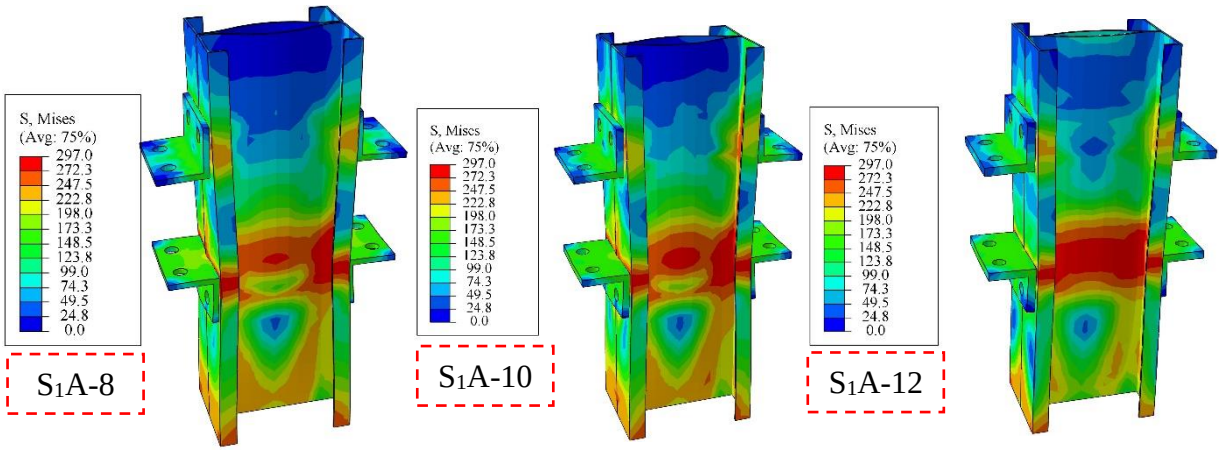

Figure 5.16: Von-Mises equivalent stress distribution for specimens S_1A-8, S_1A-10, and S_1A-12.

5.7.3 Reinforcement ratio effect

The reinforcement ratio effect on the composite joint behavior is studied in this part. The control specimen S_1A-8 has a reinforcing ratio of 1.2, with reinforcing distribution at each 100 mm in both directions, while the other specimens, S_1A-8R-0.9 and S_1A-8R-0.6, have a reinforcing ratio of 0.9 and 0.6 and distribution at each 140 and 233.3 mm in both directions, respectively.

The specimen S_1A-8R-0.9 gave an increase in the ultimate moment of 4.53% and an increase in rotation of 12.76% compared with specimen S_1A-8. Although the percentage of reinforcement is lower, the sample S1A-8 contains 8 bars; two are not continuous due to their intersection with the column, and therefore they did not bear the stresses, as shown in Figure 5.18. In addition to that, in sample S_1A-8R-0.9, the reinforcement is closer to the side of the column, i.e., close to the area of most significant stress. While in sample S_1A-8R-0.6, the reinforcement ratio is insufficient, and therefore the rotation of the joint is low due to exceeding the allowable stresses in the reinforcement and the lack of continuity of the moment and rotation curves, as shown in Figure 5.19.

The stress distribution at the ultimate moment in the first reinforcing bar from the side of the column is shown in Figure 5.20. The greatest stress is at the face of the column and gradually decreases toward the support, as expected, and the lower the reinforcement ratio, the greater the stresses.

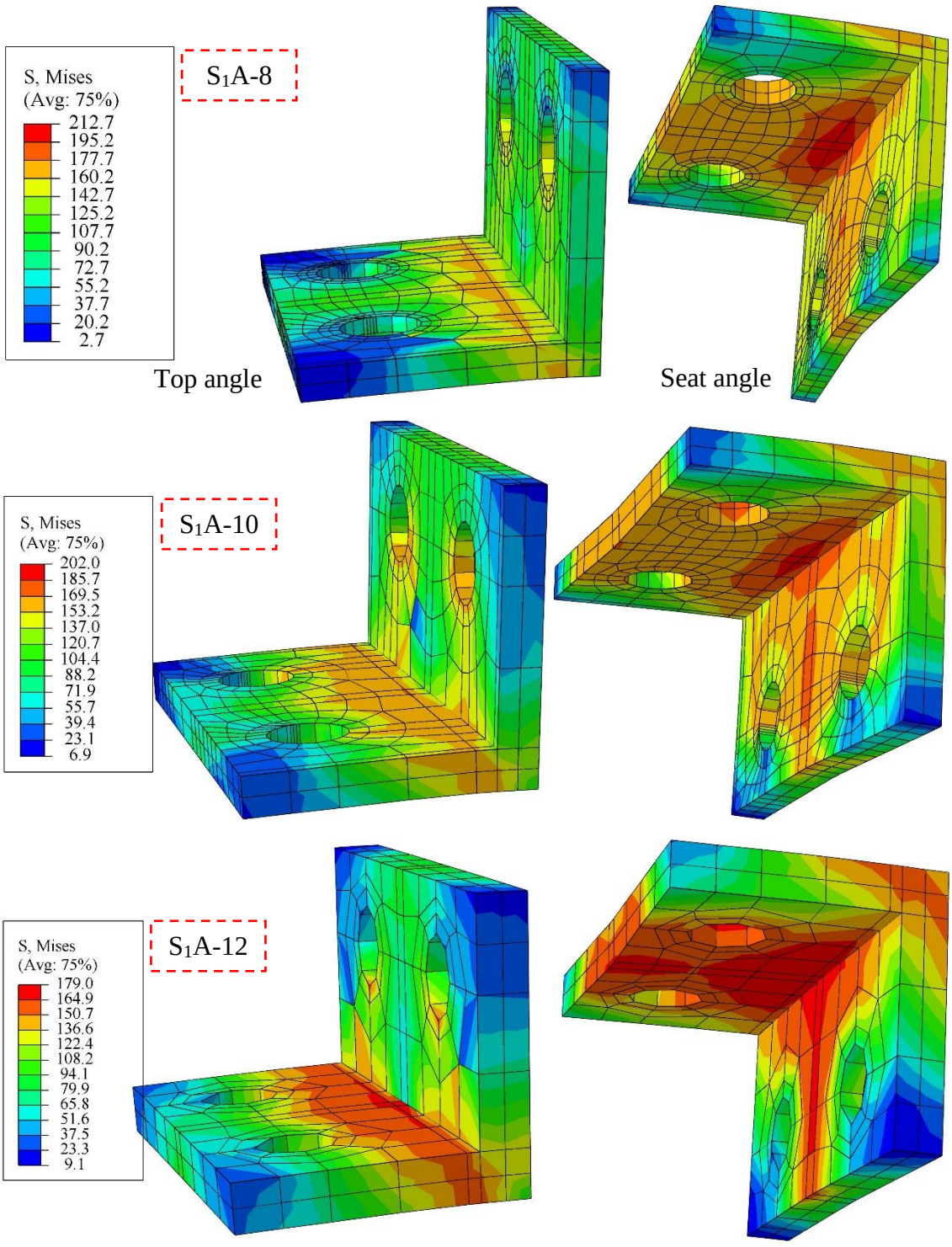

Figure 5.17: The deformation of top and seat angles with different thicknesses.

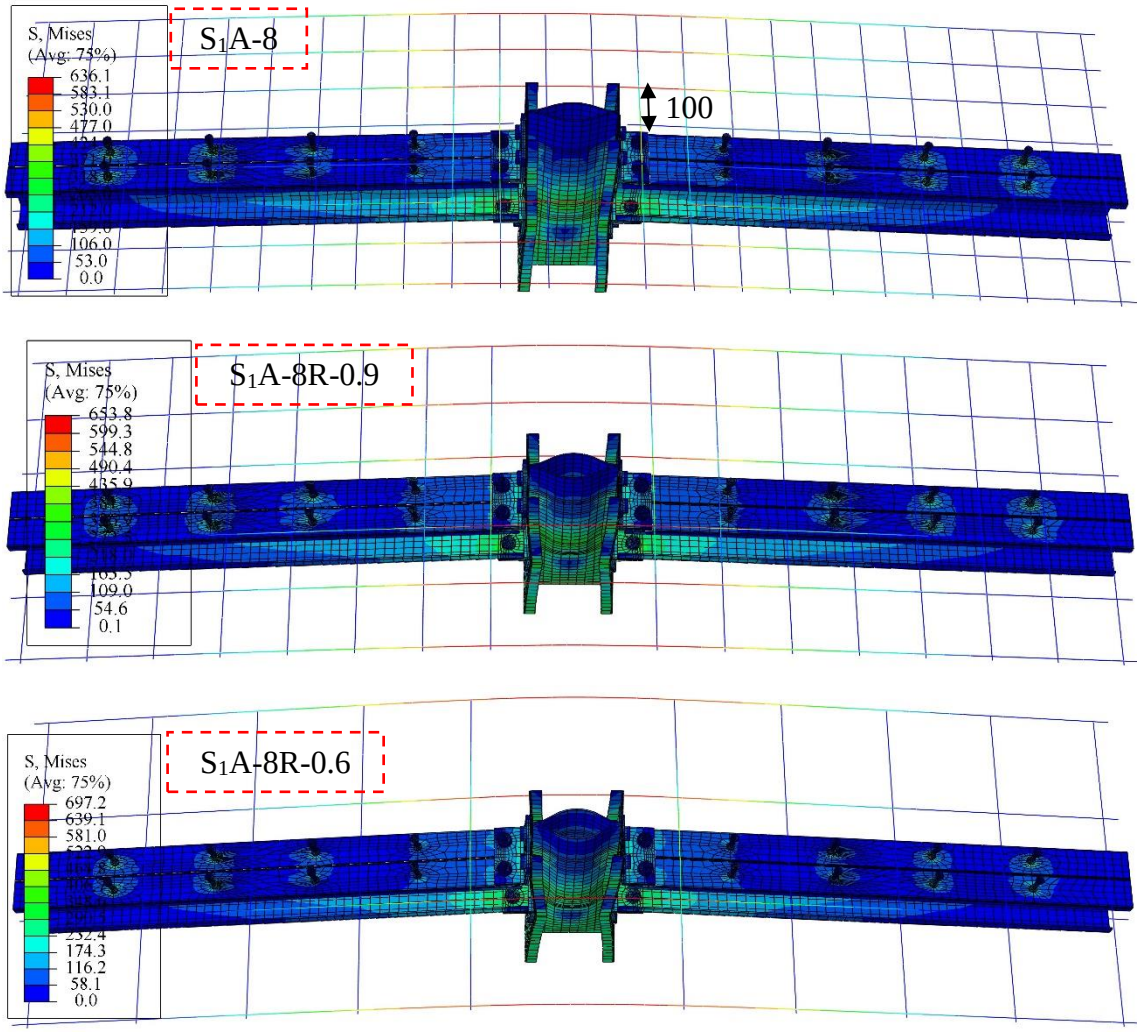

Figure 5.18: Von-Mises equivalent stress distribution for specimens with different reinforcing ratios.

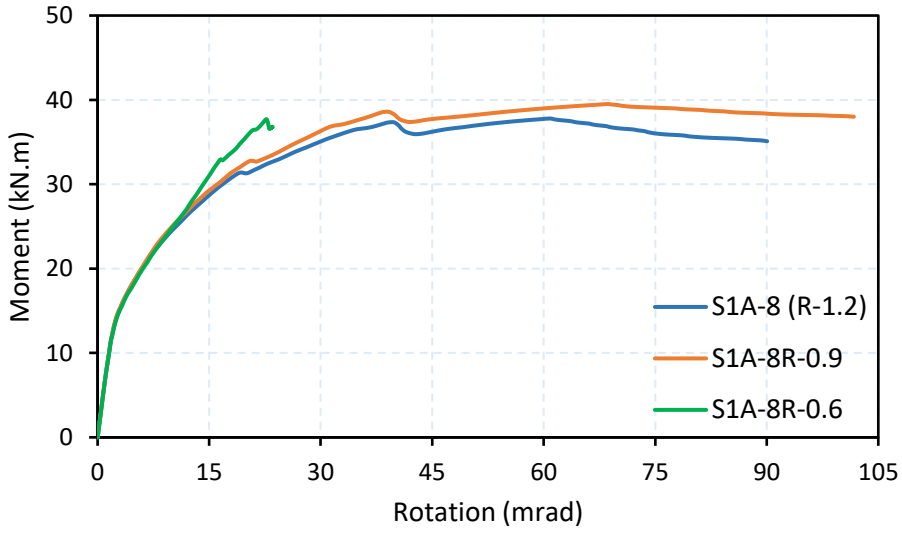

Figure 5.19: Moment-rotation curve for specimens with different reinforcing ratios.

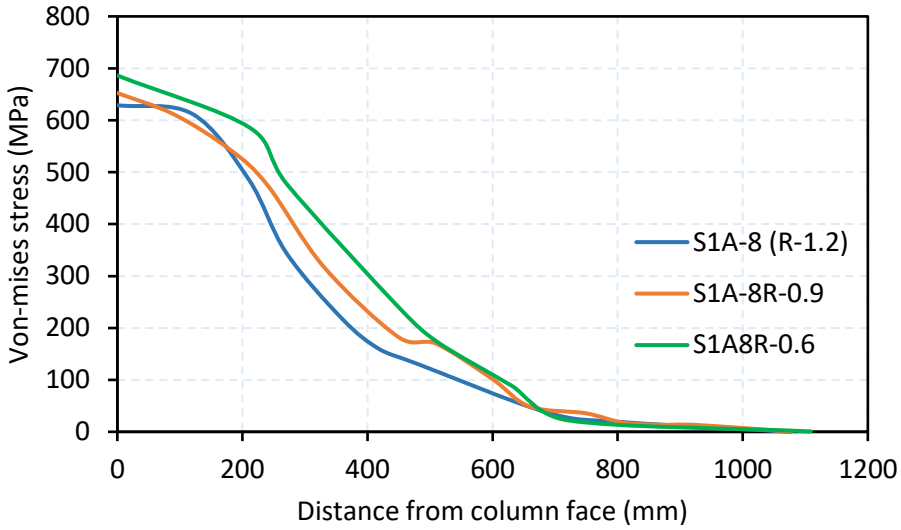

Figure 5.20: Distribution of reinforcement stress at the ultimate moment.

5.7.4 Impact of using the column web stiffener

The effect of adding stiffeners of different thicknesses to the column web at the seat angle level is studied in this part. Because the column web buckles in the above specimens are due to seat angle bending, adding a stiffener connected to the column web with a 10 mm bolt diameter prevents buckling and improves joint performance.

Compared to specimens $S_1T_1D_{100}MC$ and S_1A-8, the specimen S_1A-8S-2, with a stiffener thickness of 2 mm added from both sides of the column, increased strength by 24.5 and 28.6% and rotation capacity by about 59.6 and 18.6%, respectively. While the specimen S_1A-8S-4 with a stiffener thickness of 4 mm added from both sides of the column showed high ductility, the ultimate strength increased by 42.6%, and the rotational capacity increased by 115% compared with the specimen S_1A-8, as shown in Figure 5.21. Figures 5.22 and 5.23 show the mises-equivalent stress distribution and joint deformation for the specimens in this group. When stiffeners used, the maximum stresses being transferred to the beam and bent the beam at the end of the seat angle.

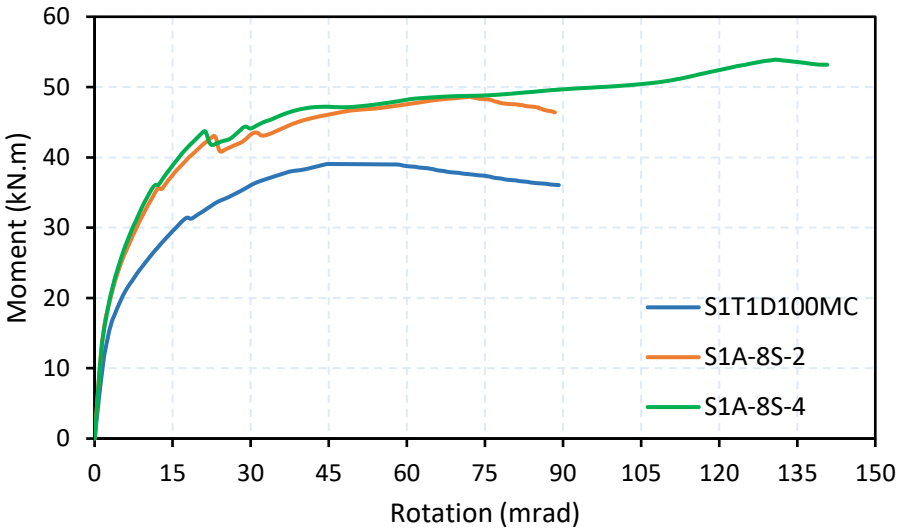

Figure 5.21: Moment-rotation curve for specimens with stiffener.

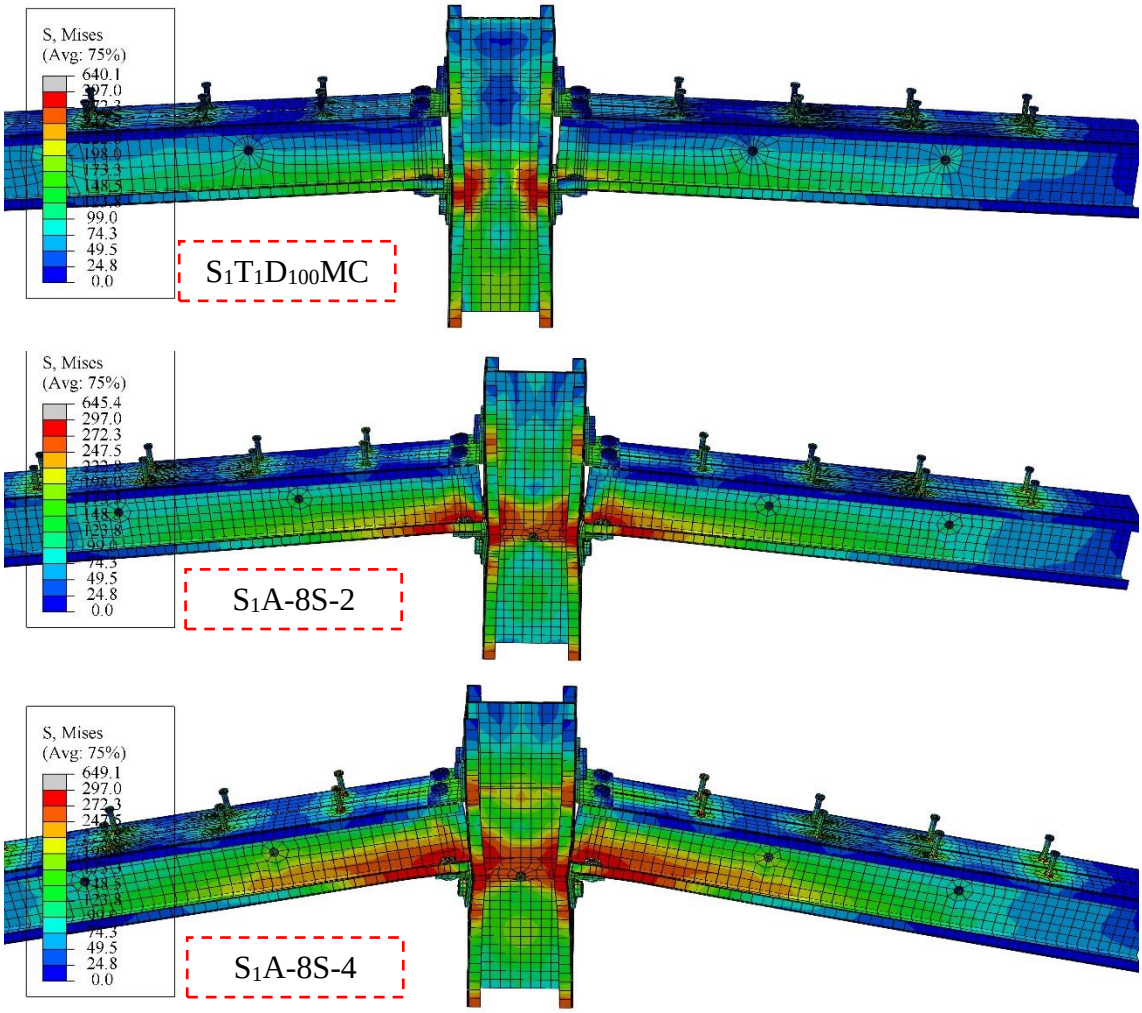

Figure 5.22: Von-Mises equivalent stress distribution in a column for specimens $S_1T_1D_{100}MC$, S_1A-8S-2 and S_1A-8S-4.

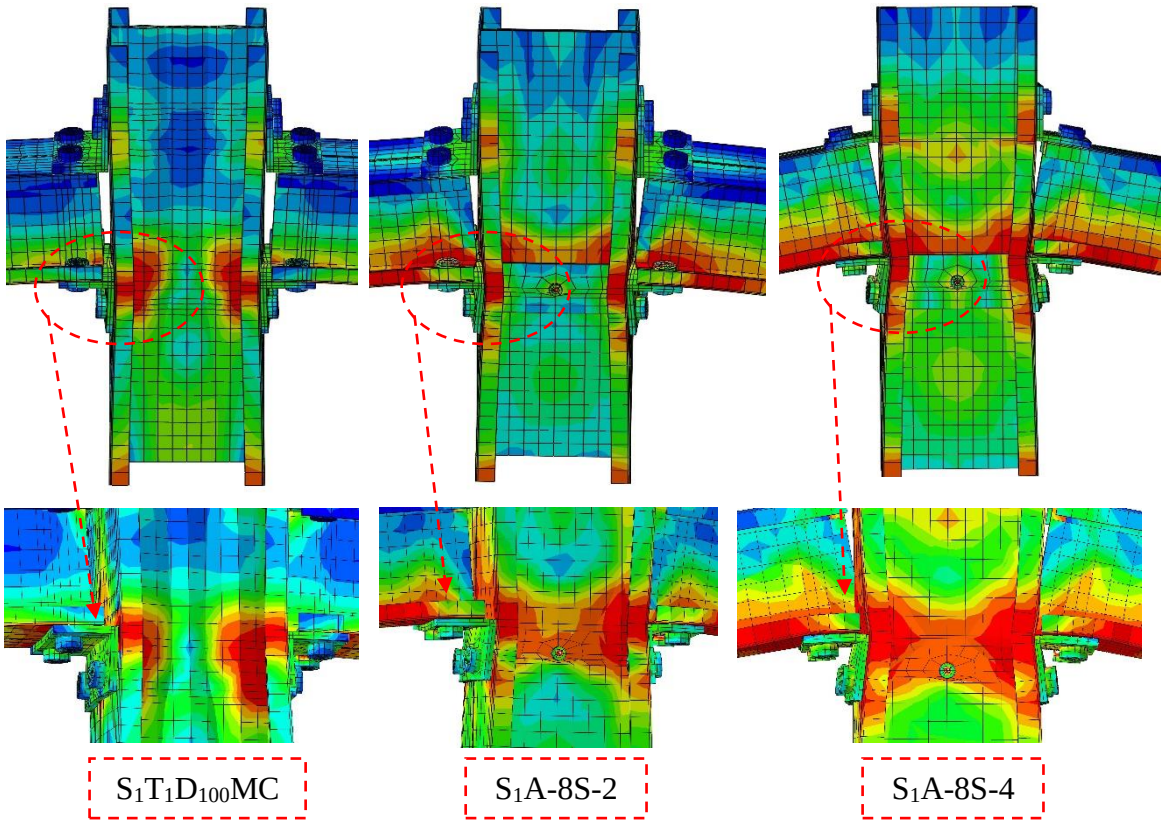

Figure 5.23: Von-Mises equivalent stress distribution in column and stiffener for specimens $S_1T_1D_{100}MC$, S_1A-8S-2 and S_1A-8S-4.

5.7.5 Column shape effect

Column shape is one of the factors affecting joint behavior. So, three specimens, S_1A-8, S_1A-8F-B, and S_1A-8F-M, with I-section, box-section, and M-section columns, respectively, are modelled in this study. The M-section column has a stiffer behavior than the other specimens, as shown in Figure 5.24, and increased the ultimate strength and rotation capacity by 8.11 and 10.8%, respectively, when compared with S_1A-8, without any buckling in the column web.

On the other hand, the box column section appeared to have a high rotational capacity, which increased by 60.3% compared with S_1A-8 due to a high buckling of the column flange and web, as shown in Figures 5.25 and 5.26.

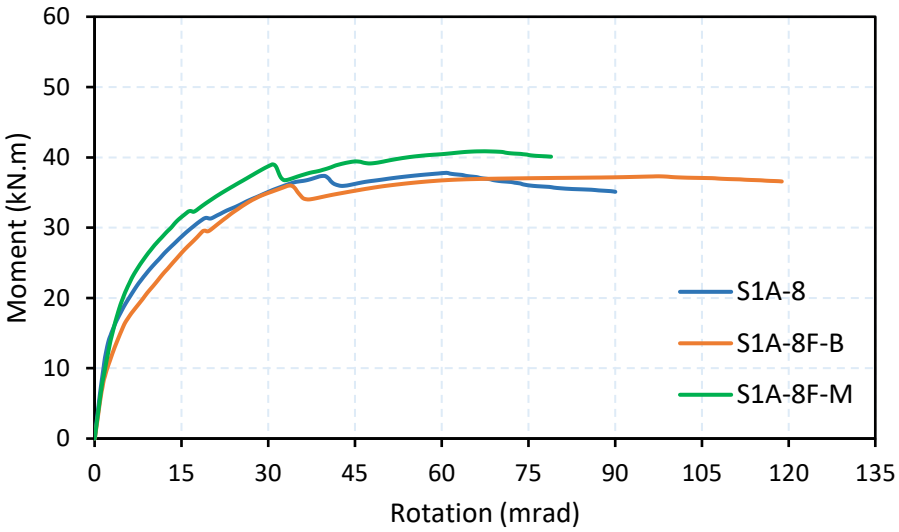

Figure 5.24: Moment-rotation curve for specimens with different column shapes.

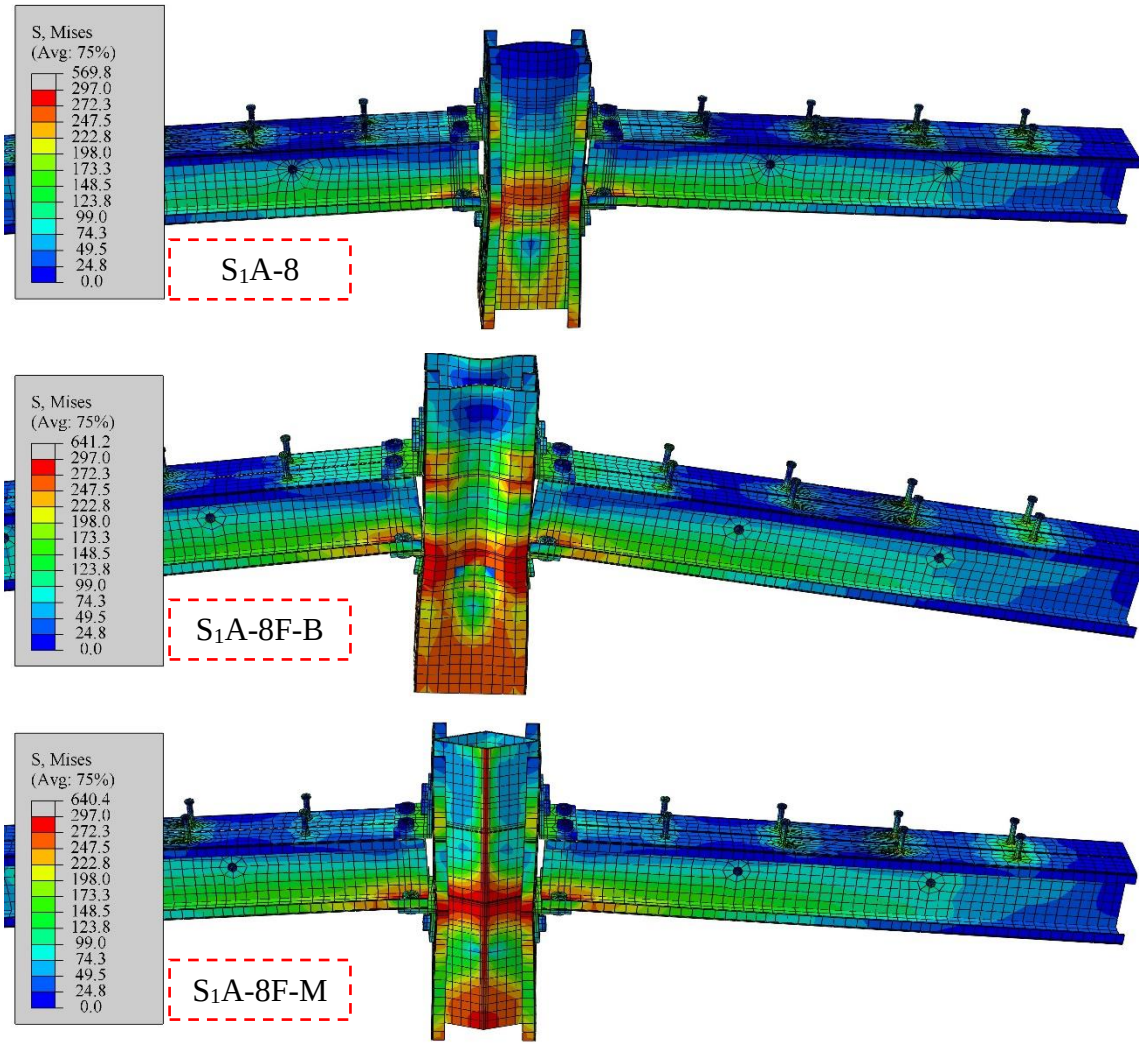

Figure 5.25: Von-Mises equivalent stress distribution for specimens S1A-8, S1A-8F-B and S1A-8F-M.

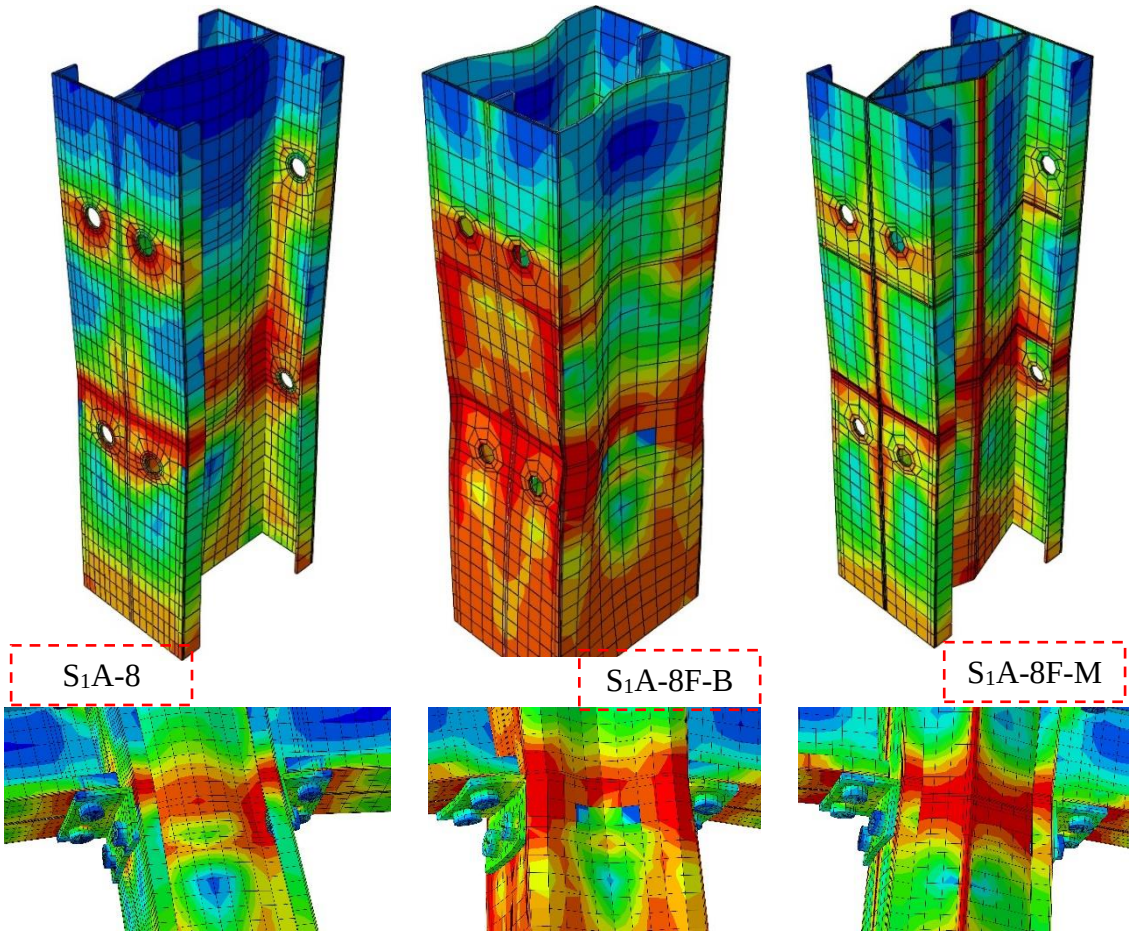

Figure 5.26: Von-Mises equivalent stress distribution in column and joint for specimens S1A-8, S1A-8F-B and S1A-8F-M.

5.6.6 The number of connection bolts

The effects of connection bolt numbers in specimens connected directly by back-to-back web connections on the composite joint behavior are studied in this part. The experimental work used six bolts on each side to connect the beam and column webs, giving a small rotational capacity. So, this part suggests using a 4-bolt to connect the webs of the beam and column on each side.

Using four bolts instead of six on each side to connect the beam and column and form a box column section improved the rotational capacity by 80.3%, as shown in Figure 5.27, where decreasing the number of bolts, increasing the freedom of rotation of the beam but causing a significant

buckling of the beam flange. The stress distribution at the ultimate moment for specimens $S_2T_1D_{100}M$ and $S_2T_1D_{100}MN$-4 is shown in Figure 5.28.

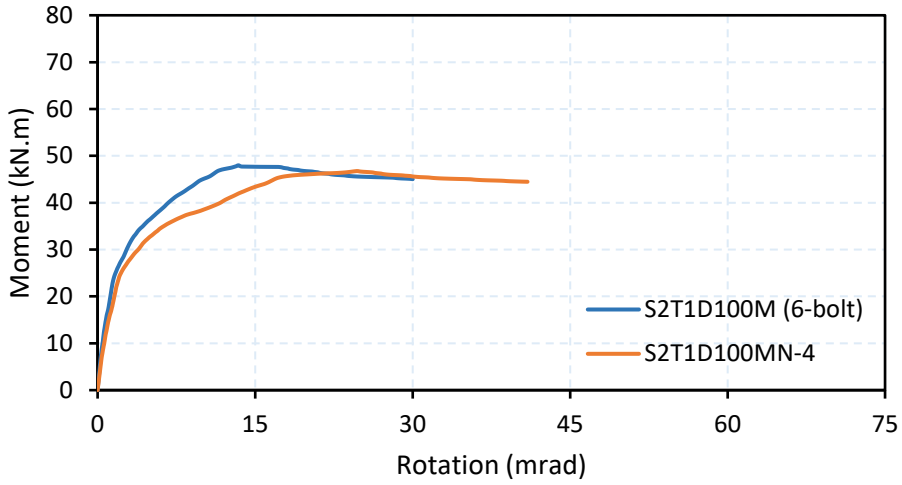

Figure 5.27: Moment-rotation curve for specimens $S_2T_1D_{100}M$ and $S_2T_1D_{100}MN$-4.

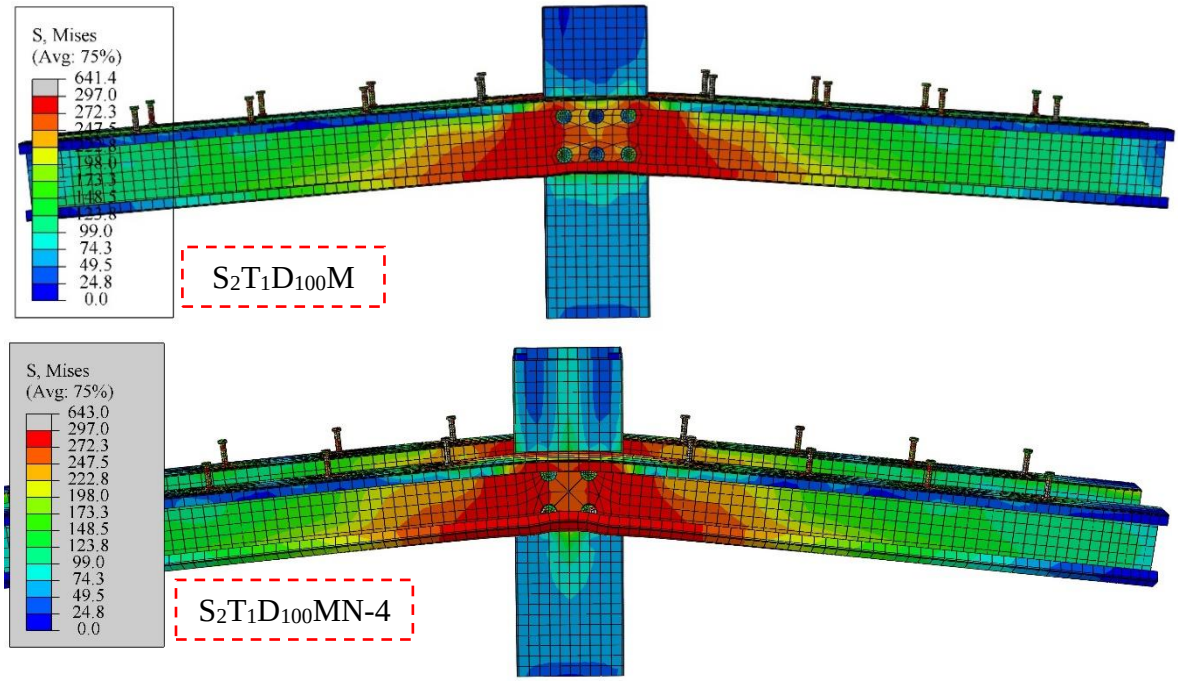

Figure 5.28: Von-Mises equivalent stress distribution for specimens $S_2T_1D_{100}M$ and $S_2T_1D_{100}MN$-4.

Also, using four bolts instead of six on each side to connect the beam and column and form a box beam section appears to result in a marked increase in the rotational capacity of the joint and shows a semi-rigid behavior. This is due to reduce the number of bolts and keep them away

from the flange of the column, which allows more freedom of rotation of the beam, as shown in Figure 5.29, and in contrast, the ultimate moment for specimen $S_3T_1D_{100}MN$-4 decreased by 9.5% compared with specimen $S_3T_1D_{100}M$. The stress distribution at the ultimate moment for specimens $S_3T_1D_{100}M$ and $S_3T_1D_{100}MN$-4 is shown in Figure 5.30.

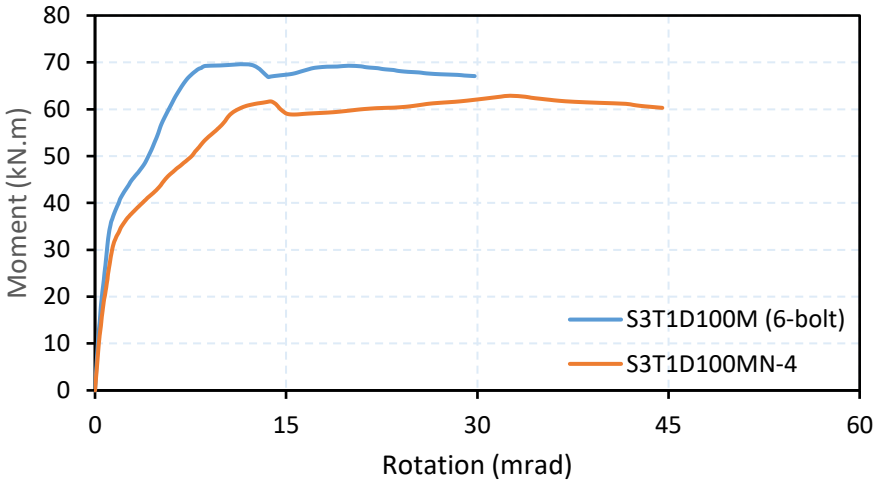

Figure 5.29: Moment-rotation curve for specimens $S_3T_1D_{100}M$ and $S_3T_1D_{100}MN$-4.

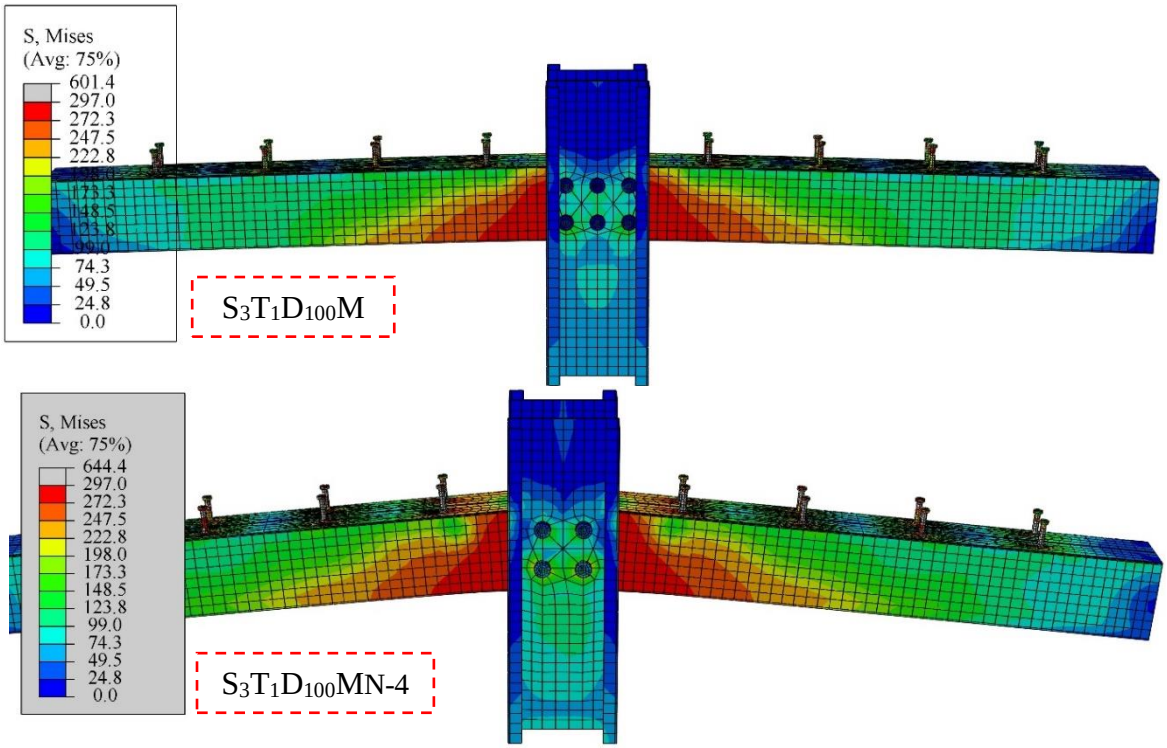

Figure 5.30: Von-Mises equivalent stress distribution for specimens $S_3T_1D_{100}M$ and $S_3T_1D_{100}MN$-4.

5.7 OPTIMUM CASE OF PARAMETRIC STUDY

From the parametric study in Section 5.6 above, the optimum case of each variable is chosen in this part to model a new sample. The suggested model has the same connection shape and details as specimen $S_1T_1D_{100}MC$ except the angle thickness is 12 mm, the reinforcement ratio is 0.9, and stiffeners are used at the column web with a 2 mm thickness.

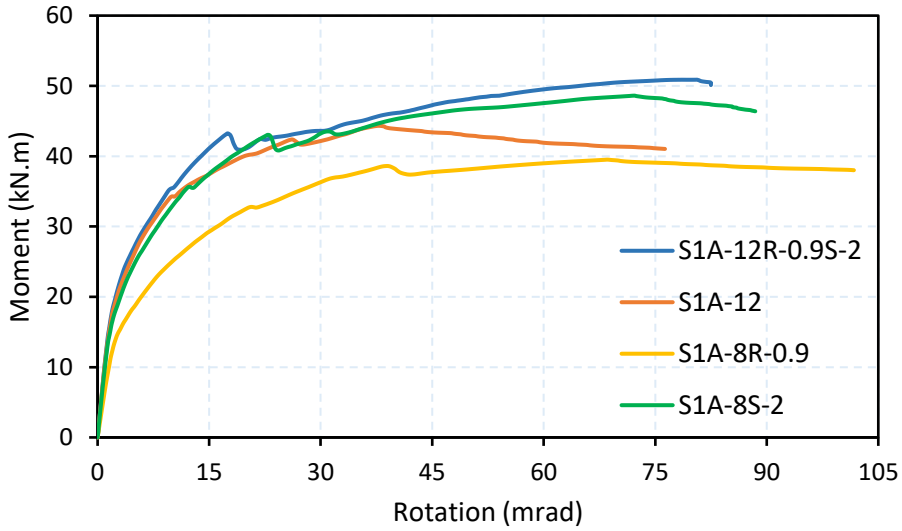

Figure 5.31: Moment-rotation curve for specimen S_1A-8R-0.9S-2.

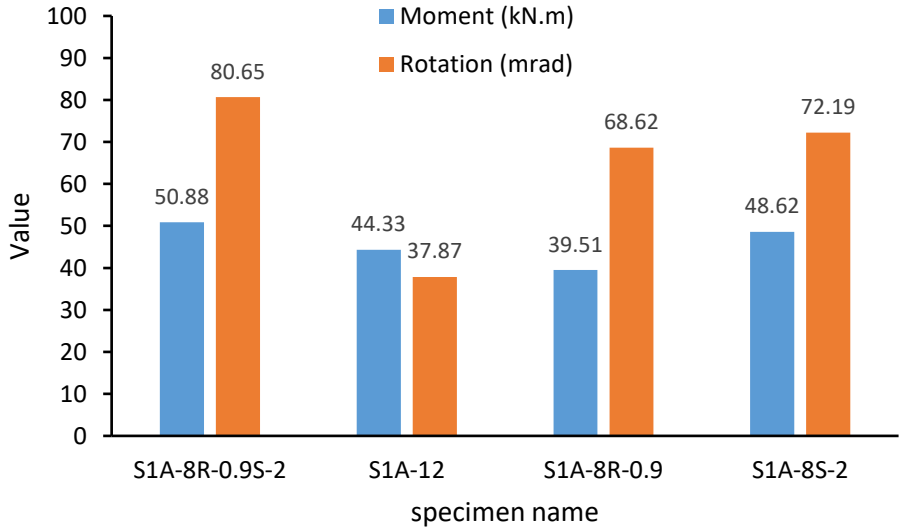

Figure 5.32: Moment and rotation value comparison.

The optimum specimen (S_1A-8R-0.9S-2) exhibits high ductility behavior and increases the moment capacity by about 14.8, 28.8, and 4.7 % compared with S_1A-8, S_1A-8R-0.9, and S_1A-8S-2, respectively, as shown in Figures 5.31 and 5.32. On the other hand, there is no buckling in the column web and a little bent of the column flange at the seat angle level compared with the other specimen, as shown in Figure 5.33.

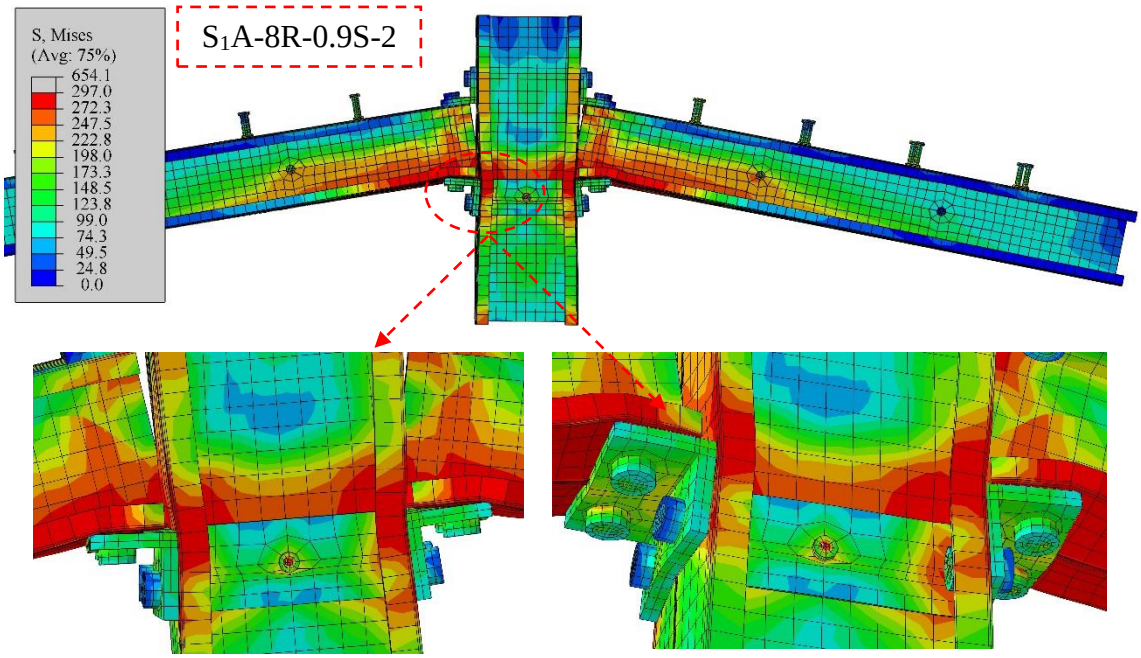

Figure 5.33: Von-Mises equivalent stress distribution for specimen S_1A-8R-0.9S-2.

5.8 SUMMARY

In this chapter, the primary samples were represented using the Abaqus 2017 program and compared with the experimental results. After reaching a good agreement, the study was expanded to study a set of variables and their impact on improving the behavior of the composite joint. The use of stiffener was one of the most important cases that led to an improvement in the strength and rotational capacity of the joint, especially when it was used with a thickness of 2 mm, as it increased the moment by 28% compared to the sample S_1A-8. Although 4 mm of stiffener thickness improves the moment capacity by 43% compared to the sample S_1A-8, it gives a very

high rotation. It, therefore, cannot be classified as a semi-rigid joint, so the optimum stiffener thickness was suggested at 2 mm. The variation (increase or decrease) in the ultimate moment or rotation capacity was compared with the sample S_1A-8, where these various percentages are presented in Figure 5.35.

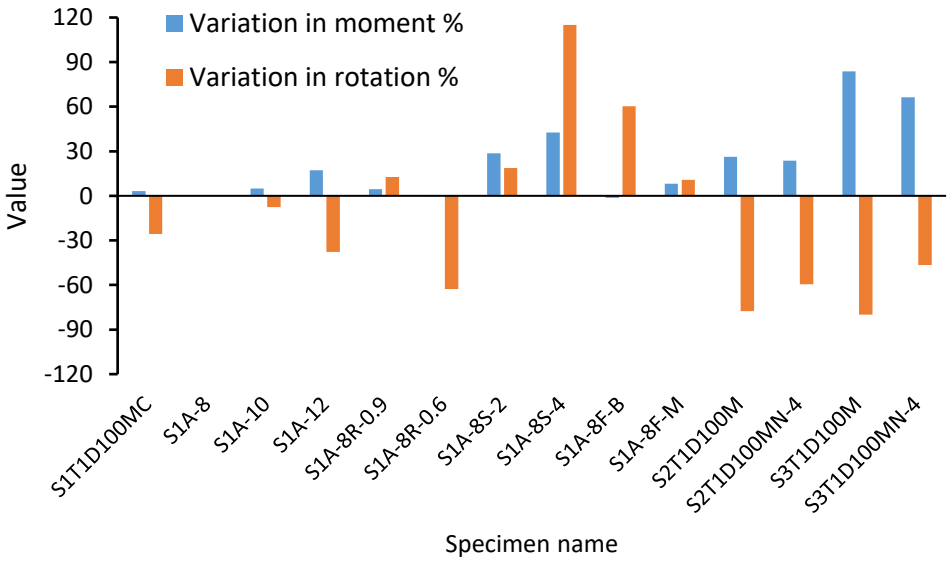

Figure 5.34: Summary of variation in the moment and rotation compared with specimen S_1A-8.

CHAPTER SIX

CONCLUSIONS AND RECOMMENDATIONS

6.1 INTRODUCTION

The primary goal of this study is to investigate the experimental and analytical analysis of composite cold-formed steel beam-to-column joints. The main conclusions derived from experimental and analytical results are presented in this chapter, along with some recommendations and suggestions for future work.

6.2 CONCLUSIONS

In this study, thirteen specimens with cruciform subassemblies of composite cold-formed steel beam-to-column joints with different connection shapes and shear connector degrees and types were prepared experimentally to investigate the structural performance, including the initial stiffness, moment and rotational capacities, and slip response. The ABAQUS program also prepared many parameter studies. In addition, nine pushout specimens were prepared to investigate the performance of different shear connector types with a cold-formed steel beam.

Based on the results obtained from experimental and analytical work, the main conclusions can be divided into three categories:

6.2.1 Conclusions of experimental composite joint specimens

1. The top and seat angle connections between the semi-rigid CFS beam-to-column joints exhibit high ductility where the rotational capacity

corresponding to the ultimate moment exceeds 30 mrad. As a result, they are adequate for plastic analysis and seismic design.

2. The CFS angle plate shear connector increases the moment capacity and initial stiffness by about 12% and 47%, respectively, compared with specimen has a bolted shear connector, which has a fully bonded shear connector.
3. Compared to specimen with fully bonded shear connector, the rotational capacities of specimens with 50% and 25% partial bonded shear connectors increased by 33.4% and 79.16%, respectively. This demonstrates that the partial shear connector improves ductility while decreasing initial rotational stiffness.
4. When the shear connector bond ratio is reduced, the initial rotational stiffness decreases by 20% and 47%, respectively, for specimens with 50% and 25% partial bonded shear connectors, compared to specimen with fully bonded shear connector, due to higher slip displacements for specimens with a lower degree of shear connection.
5. Compared to fully shear connected, using a partially bonded shear connector up to 50% of fully shear connected produced acceptable results and within the recommended limits for semi-rigid joints according to the European Code.
6. Based on the observations, the failure patterns are dominated by the yielding of connection angles since large deflections and rotations occur on the top and seat CFS angles. So, using an angle thickness equal three times of column thickness is recommended to obtain higher strength with rotational capacity, which also gives a semi-rigid behavior (ductility behavior).
7. The rotation capacity of specimens connected directly by back-to-back web is reduced by about 76-78% compared with specimens connected by

top-to-seat angles, indicating non-ductile behavior where the rotation capacity dose not exceed 30 mrad.

8. The cyclic load has a minor effect on the ultimate strength of the composite joints. On the other hand, it increases the rotation capacity of joints, especially for specimen connected by top-to-seat angles and specimen with box column section, which increases by 79 and 97%, respectively, compared with the corresponding specimen under monotonic load.
9. In terms of stiffness, all specimens appear to have a semi-rigid behavior according to EC4, in which the initial stiffness for unbraced frames is between 0.5 EI_b/L_b and 25 EI_b/L_b except for specimen connected by top-to-seat angles under monotonic load, which shows a pinned behavior because of the cyclic load effect. Also, for specimens tested under cyclic load, the initial rotational stiffness decreases due to fatigue of the connection becuase the effect of cyclic loading.
10. The energy absorption capacity of specimen connected by top-to-seat angles increases by 76.2 and 55.3% compared with specimens connected directly by back-to-back web and forming box column and box beam section , respectively. This is due to the semi-rigid behavior of the joint in specimen connected by top-to-seat angles.
11. The beam-to-column connection, formed by back-to-back bolted webs forming a box beam section or a box column section, showes high efficiency in terms of strength and rigidity, as well as avoiding failure in the column or connection area, which occurs in specimens connected by top-to-seat angle.

6.2.2 Conclusions of analytical composite joint specimens

1. The increase in angle thickness from 8 mm to 10 mm and 12 mm increases the ultimate moment by about 4.84 and 17.27%, respectively, and decreases the rotation capacity by about 7.54 and 37.77%. In

addition, the increased angle thickness reduces the seat angle deformation and the column web buckling, but the joint behavior is still classified as semi-rigid.

2. The reinforcement ratio of 0.9% is more suitable for composite joints than 1.2%, which may increase the ultimate moment by 4.53% and increase the rotation by 12.76% compared with a specimen with a 1.2% reinforcement ratio, in addition to the economic benefit.
3. The use of stiffeners in the column web at the seat angle level is one of the most important cases that improved the joint's strength and rotational capacity. The added stiffener thickness of 2 mm increases strength by 28.6% and rotation capacity by about 18.6% compared with the same specimen without a stiffener. While the added stiffener thickness of 4 mm showes high ductility, the ultimate strength increases by 42.6%, and the rotational capacity increases by 115%.
4. The M-section column shape has a stiffer behavior than the other shapes suggested in this study, which increases the ultimate strength and rotation capacity by 8.11 and 10.8%, respectively, when compared with the I-section column, without any buckling in the column web.
5. Using four bolts instead of six in the specimens connected directly by back-to-back web connections, forming a box column or box beam section, improved the rotational capacity by 80.3% and 165%, respectively. Thus, the behavior of the joint is semi-rigid, especially for the sample with a box section of the beam, as it exceeds the rotational capacity of 30 mrad.

6.2.3 Conclusions of pushout specimens

1. Compared to specimens with an I-section CFS beam for a bolted shear connector with 10 and 14 mm diameter, the box section of the cold-formed steel beam reduced the ultimate load capacity by about 13% and 16.7%, respectively.

2. An improvement in the strength capacity of up to 60% for the I-section beam and 54% for the box-section of the cold-formed steel beam was obtained by increasing the diameter of the single-embedded bolt shear connector from 10 mm to 14 mm.
3. According to EC4, bolted shear connectors with a 14 mm diameter can be assumed ductile and thus is used in partial shear connections.
4. Using a box section for the beam increases the shear connector stiffness by about 23% and 46% for specimens with 10 mm and 14 mm bolt diameters, respectively, compared with specimens with I-section beams.
5. The bolt fracture is the failure mode observed for specimens with a diameter of 10 mm of a single embedded bolted shear connector for both I and box sections of the CFS beam. At the same time, the concrete slab failed due to a crack around the bolted shear connector region, which occurr for specimens with a bolt diameter equal to 14 mm.
6. The cross-section of the cold-formed steel beam does not affect the failure mode of the specimens with the same bolted shear connector diameter.
7. The specimen with a corrugated cold-formed steel plate shear connector is as efficient as the angle-shaped shear connector. However, the conductor immerses in the concrete slab is about half the length of the angled connector.
8. The specimen with a double angle plate shear connector differed from the other specimens with plate shear connector, which has a ductile behavior with characteristic slip equal to 7 mm more than the required value in Eurocode 4 (6 mm).

6.3 RECOMMENDATIONS FOR FUTURE WORK

Some points are suggested to involve the recommended future work for composite CFS beam-to-column joints as follows:

1- The behavior of beam-to-column connections under seismic load. More testing is needed to demonstrate the benefits of using semi-rigid joints in this situation.
2- Because the cracks are concentrated around the column area, suggest using ultra-high-performance fibres reinforced concrete (UHPFRC) around the joint area to reduce these cracks and obtain high plasticity.
3- Data are very deficient on the behavior of beam-to-column joints exposure to fire effect. More testing should be undertaken to develop the joints in this situation.

REFERENCES

[1] Website, " collapse of composite steel structure". [Accessed October 12, 2019]. Available from: https://www.firstcoastnews.com/article/news/local/hard-rock-hotel-collapses-on-canal-street.

[2] Al-Jabri, K. S. (2007). Behavior of Steel-framed Buildings in a Fire. Steel Structures, 7, 227-237.

[3] Chen, W.F., & Liew, J.Y.R. (Eds.). (2002). *The Civil Engineering Handbook* (2nd ed.). CRC Press. https://doi.org/10.1201/9781420041217.

[4] Tizani, W., Wang, Z. Y., & Hajirasouliha, I. (2013). Hysteretic performance of a new blind bolted connection to concrete filled columns under cyclic loading: An experimental investigation. *Engineering structures*, 46, 535-546.

[5] Li, J. T., Li, G. Q., Lou, G. B., & Chen, L. Z. (2012). Experimental investigation on flush end-plate bolted composite connection in fire. *Journal of Constructional Steel Research*, 76, 121-132.

[6] Song, T. Y., Tao, Z., Razzazzadeh, A., Han, L. H., & Zhou, K. (2017). Fire performance of blind bolted composite beam to column joints. *Journal of Constructional Steel Research*, 132, 29-42.

[7] Han, L. H., Wang, W. D., & Zhao, X. L. (2008). Behaviour of steel beam to concrete-filled SHS column frames: Finite element model and verifications. *Engineering Structures*, 30(6), 1647-1658.

[8] Feng, R., & Young, B. (2015). Theoretical analysis of cold-formed stainless steel tubular joints. *Engineering Structures*, 83, 99-115.

[9] Yang, J., Sheehan, T., Dai, X. H., & Lam, D. (2015). Experimental study of beam to concrete-filled elliptical steel tubular column connections. *Thin-Walled Structures*, 95, 16-23.

[10] Díaz, C., Victoria, M., Martí, P., & Querin, O. M. (2011). FE model of beam-to-column extended end-plate joints. *Journal of Constructional Steel Research*, 67(10), 1578-1590.

[11] Tsavdaridis, K. D., & Papadopoulos, T. (2016). A FE parametric study of RWS beam-to-column bolted connections with cellular beams. *Journal of Constructional Steel Research*, 116, 92-113.

[12] Da Silva, L. S., Simoes, R. D., & Cruz, P. J. (2001). Experimental behaviour of end-plate beam-to-column composite joints under monotonical loading. *Engineering Structures*, 23(11), 1383-1409.

[13] Liew, J. R., Teo, T. H., Shanmugam, N. E., & Yu, C. H. (2000). Testing of steel–concrete composite connections and appraisal of results. *Journal of Constructional Steel Research*, 56(2), 117-150.

[14] Wang, J., & Guo, S. (2012). Structural performance of blind bolted end plate joints to concrete-filled thin-walled steel tubular columns. *Thin-Walled Structures*, 60, 54-68.

[15] Zhao, H., Kunnath, S. K., & Yuan, Y. (2010). Simplified nonlinear response simulation of composite steel–concrete beams and CFST columns. *Engineering Structures*, 32(9), 2825-2831.

[16] Gil, B., Goñi, R., & Bayo, E. (2013). Experimental and numerical validation of a new design for three-dimensional semi-rigid composite joints. *Engineering Structures*, 48, 55-69.

[17] Tao, Z., Hassan, M. K., Song, T. Y., & Han, L. H. (2017). Experimental study on blind bolted connections to concrete-filled stainless steel columns. *Journal of Constructional Steel Research*, 128, 825-838.

[18] Wang, A. J. (2010). A study on composite end-plate connections with flexible tensile reinforcements and shear connectors. *Canadian Journal of Civil Engineering*, 37(11), 1437-1450.

[19] Wang, A. J. (2010). Numerical studies on the structural behaviour of composite end-plate connections. *Canadian Journal of Civil Engineering*, 37(6), 907-921.

[20] Kataoka, M. N., & El Debs, A. L. H. (2014). Parametric study of composite beam-column connections using 3D finite element modelling. *Journal of Constructional Steel Research*, 102, 136-149.

[21] website, "history of cold-formed steel". https://www.ispansystems.com/news/why-cold-formed-steel-framing-is-growing-in-popularity-as-a-preferred-building-method/

[22] American Iron and Steel Institute (May 1970). Use of Steel Cuts Costs of Home Building. Steel Facts, Washington, DC.

[23] American Iron and Steel Institute. The Design and Fabrication of Cold-Formed Steel Structures. Washington, DC.

[24] Website," Reunion Rehabilitation Hospital Phoenix". [Accessed March 18, 2021]. Available from: https://mcdmag.com/2021/03/reunion-rehabilitation-hospital-phoenix-tops-out/

[25] Website," The Elan Westside building in Atlanta ". [Accessed March 10, 2017]. Available from: https://www.constructionspecifier.com/specifying-cold-formed-steel-to-meet-project-goals/

[26] Fu, F., Lam, D., & Ye, J. (2008). Modelling semi-rigid composite joints with precast hollowcore slabs in hogging moment region. *Journal of Constructional Steel Research*, 64(12), 1408-1419.

[27] Hayalioglu, M. S., & Degertekin, S. O. (2004). Design of non-linear steel frames for stress and displacement constraints with semi-rigid connections via genetic optimization. Structural and Multidisciplinary Optimization, 27, 259-271.

[28] Allen, D. (2006). Mid-rise construction detailing issues with cold-formed steel and compatible construction materials. In Structures Congress 2006: *Structural Engineering and Public Safety* (pp. 1-10).

[29] Irwan, J. M., Hanizah, A. H., Azmi, I., & Koh, H. B. (2011). Large-scale test of symmetric cold-formed steel (CFS)–concrete composite beams with BTTST enhancement. *Journal of Constructional Steel Research*, 67(4), 720-726.

[30] Schafer, B. W. (2011). Cold-formed steel structures around the world: A review of recent advances in applications, analysis and design. *Steel Construction*, 4(3), 141-149.

[31] Santos, H. A., & Silberschmidt, V. V. (2014). Hybrid equilibrium finite element formulation for composite beams with partial interaction. *Composite Structures*, 108, 646-656.

[32] Johnson, R. P. (2018). Composite Structures of Steel and Concrete: beams, slabs, columns and frames for buildings. John Wiley & Sons.

[33] Tadros, M. K., & Baishya, M. C. (1998). Rapid replacement of bridge decks (Vol. 407). *Transportation Research Board*.

[34] Tzouka, E., Karavasilis, T., Kashani, M. M., & Afshan, S. (2021, October). Finite element modelling of push-out tests for novel locking nut shear connectors. In *Structures* (Vol. 33, pp. 1020-1032). Elsevier.

[35] Hosseinpour, M., Zeynalian, M., Ataei, A., & Daei, M. (2021). Push-out tests on bolted shear connectors in composite cold-formed steel beams. *Thin-Walled Structures*, 164, 107831.

[36] Pavlović, M., Marković, Z., Veljković, M., & Buđevac, D. (2013). Bolted shear connectors vs. headed studs behaviour in push-out tests. *Journal of Constructional Steel Research*, 88, 134-149.

[37] Yang, T., Liu, S., Qin, B., & Liu, Y. (2020). Experimental study on multi-bolt shear connectors of prefabricated steel-concrete composite beams. *Journal of Constructional Steel Research*, 173, 106260.

[38] Ataei, A., Bradford, M. A., & Liu, X. (2016, August). Experimental study of flush end plate beam-to-column composite joints with precast slabs and deconstructable bolted shear connectors. In *Structures* (Vol. 7, pp. 43-58). Elsevier.

[39] Mirza, O., & Uy, B. (2009). Behaviour of headed stud shear connectors for composite steel–concrete beams at elevated temperatures. *Journal of Constructional Steel Research*, 65(3), 662-674.

[40] Ilveskoski, O (2005). Lecture 10.1: Composite Construction-General. Arranged by Erkan SAMHÂL from SSEDTA (European Steel Computer Aided Learning).

[41] Chen, W. F. (2011). *Semi-rigid connections handbook*. J. Ross Publishing.

[42] Bjorhovde, R., Colson, A., & Brozzetti, J. (1990). Classification system for beam-to-column connections. *Journal of Structural Engineering*, 116(11), 3059-3076.

[43] Goto, Y., & Miyashita, S. (1998). Classification system for rigid and semirigid connections. *Journal of Structural Engineering*, 124(7), 750-757.

[44] Nethercot, D. A., Li, T. Q., & Ahmed, B. (1998). Unified classification system for beam-to-column connections. *Journal of Constructional Steel Research*, 45(1), 39-65.

[45] Standard, B. (2006). Eurocode 3—Design of steel structures—. BS EN 1993-1, 1, 2005.

[46] AISC Committee. (2010). Specification for structural steel buildings (ANSI/AISC 360-10). American Institute of Steel Construction, Chicago-Illinois.

[47] Anonymous (2003). Parametric Bay Studies 4.1. Excel Spreadsheet updated 03/06/2003 at www.aisc.org, AISC, Chicago, Ill.

[48] Vinnakota, S. (2006). Steel Structures: Behaviour and LRFD. McGraw-Hill, Inc.

[49] Ghindea, M., Cătărig, A., & Ballok, R. (2015). Behavior of beam-to-column connections with angles. Part 1-experimental investigations. *Journal of Applied Engineering Sciences*, 5(2), 21-28.

[50] Hazlan, A., Tahir, M., Sulaiman, A., & Mahendran, M. (2011). Bolted beam-column moment connections between cold-formed steel members. Incorporating Sustainable Practice in Mechanics and Structures of Materials, 655-660.

[51] Chung, K. F., & Lawson, R. M. (2000). Structural performance of shear resisting connections between cold-formed steel sections using web cleats of cold-formed steel strip. *Engineering structures*, 22(10), 1350-1366.

[52] Uang, C. M., Hong, J. K., Sato, A., & Wood, K. (2008). Cold-formed Steel Special Bolted Moment Frames Cyclic Testing and Numerical Modeling of Moment Connections.

[53] Wong, M. F., & Chung, K. F. (2002). Structural behaviour of bolted moment connections in cold-formed steel beam-column sub-frames. *Journal of constructional steel research*, 58(2), 253-274.

[54] Bučmys, Ž., & Šaučiuvėnas, G. (2013). The behavior of cold formed steel structure connections. *Engineering structures and technologies*, 5(3), 113-122.

[55] Aminuddin, K. M., Saggaff, A., & Tahir, M. M. (2017, November). Experimental behaviour of beam-column connection using cold-formed steel sections with rectangular gusset-plate. In AIP Conference Proceedings (Vol. 1903, No. 1, p. 020006). AIP Publishing LLC.

[56] Siang, T. C., Tahir, M. M., Shek, P. N., & Kueh, A. B. H. (2011). Experimental investigation on slip-in connection for cold-formed steel

double channel Sections. In *Advanced Materials Research* (Vol. 250, pp. 1038-1041). Trans Tech Publications Ltd.

[57] Tan, S. H., Seah, L. K., & Fok, S. C. (1996). Connections in cold-formed *thin-walled structures*. Computers & *structures*, 60(1), 169-172.

[58] El-Abidi, K. M. A., & Zacoeb, A. Experimental Study of Semi-Rigid Beam-To-Column Connections Using Fasteners Due To Monotonic Loading.

[59] El-Abidi, K. M. A., & Suswanto, B. (2013). Experimental Study, Stiffness of Semi-Rigid Beam-to-Column Connections Using Bolts and Angles. Researchgate. Net,[S. l.], n, 60-64.

[60] Huang, Y., & Young, B. (2014). Experimental investigation of cold-formed lean duplex stainless steel beam-columns. *Thin-Walled Structures*, 76, 105-117.

[61] Torabian, S., Zheng, B., & Schafer, B. W. (2015). Experimental response of cold-formed steel lipped channel beam-columns. *Thin-walled structures*, 89, 152-168.

[62] Bajoria, K. M., & Talikoti, R. S. (2006). Determination of flexibility of beam-to-column connectors used in thin walled cold-formed steel pallet racking systems. *Thin-Walled Structures*, 44(3), 372-380.

[63] Prabha, P., Marimuthu, V., Saravanan, M., & Jayachandran, S. A. (2010). Evaluation of connection flexibility in cold formed steel racks. *Journal of Constructional Steel Research*, 66(7), 863-872.

[64] Xiao, Y., Choo, B. S., & Nethercot, D. A. (1994). Composite connections in steel and concrete. I. Experimental behaviour of composite beam—Column connections. *Journal of Constructional Steel Research*, 31(1), 3-30.

[65] Fu, F., & Lam, D. (2006). Experimental study on semi-rigid composite joints with steel beams and precast hollowcore slabs. *Journal of Constructional Steel Research*, 62(8), 771-782.

[66] Loh, H. Y., Uy, B., & Bradford, M. A. (2006). The effects of partial shear connection in composite flush end plate joints Part I—experimental study. *Journal of Constructional Steel Research*, 62(4), 378-390.

[67] Fu, F., Lam, D., & Ye, J. (2010). Moment resistance and rotation capacity of semi-rigid composite connections with precast hollowcore slabs. *Journal of Constructional Steel Research*, 66(3), 452-461.

[68] Ataei, A., Bradford, M. A., & Valipour, H. R. (2015). Experimental study of flush end plate beam-to-CFST column composite joints with deconstructable bolted shear connectors. *Engineering structures*, 99, 616-630.

[69] Ataei, A., Bradford, M. A., & Liu, X. (2016, August). Experimental study of flush end plate beam-to-column composite joints with precast slabs and deconstructable bolted shear connectors. In *Structures* (Vol. 7, pp. 43-58). Elsevier.

[70] Wang, J., Uy, B., Thai, H. T., & Li, D. (2018). Behaviour and design of demountable beam-to-column composite bolted joints with extended end-plates. *Journal of Constructional Steel Research*, 144, 221-235.

[71] Mairal, R., & Malite, M. (2010). COLD-FORMED STEEL AND CONCRETE COMPOSITE BEAMS: STUDY OF BEAM-TO-COLUMN CONNECTION AND REGION OF HOGGING BENDING. In *International Colloquium Stability and Ductility of Steel Structures*, Rio de Janeiro.

[72] EN1994-1-1, Eurocode 4 (2004). Design of Composite Steel and Concrete Structures. Part 1-1: General Rules and Rules for Buildings. Brussels, Belgium: European Committee for Standardization.

[73] Firdaus, M., Saggaff, A., Tahir, M. M., Ngian, S. P., Siang, T. C., Aminuddin, K. M., & Salih, M. N. A. (2020, May). Experimental study on composite connection with double lipped C-Sections. In IOP

Conference Series: *Materials Science and Engineering* (Vol. 849, No. 1, p. 012067). IOP Publishing.

[74] Firdaus, M., Saggaff, A., Tahir, M. M., Ngian, S. P., Aminuddin, K. M., & Saloma, S. (2019). Experimental Study of Composite Connections for Cold-Formed Steel Using Isolated Joint Test. In Journal of Physics: Conference Series (Vol. 8, No. 12). IOP Publishing.

[75] Da Silva, L. S., Simoes, R. D., & Cruz, P. J. (2001). Experimental behaviour of end-plate beam-to-column composite joints under monotonical loading. *Engineering Structures*, 23(11), 1383-1409.

[76] Li, T. Q., Nethercot, D. A., & Choo, B. S. (1996). Behaviour of flush end-plate composite connections with unbalanced moment and variable shear/moment ratios—I. Experimental behaviour. *Journal of Constructional Steel Research*, 38(2), 125-164.

[77] Liew, J. R., Teo, T. H., & Shanmugam, N. E. (2004). Composite joints subject to reversal of loading—Part 1: experimental study. *Journal of Constructional Steel Research*, 60(2), 221-246.

[78] Shi, G., Shi, Y., & Wang, Y. (2007). Behaviour of end-plate moment connections under earthquake loading. *Engineering structures*, 29(5), 703-716.

[79] Popov, E. P., & Takhirov, S. M. (2002). Bolted large seismic steel beam-to-column connections Part 1: experimental study. *Engineering structures*, 24(12), 1523-1534.

[80] Takhirov, S. M., & Popov, E. P. (2002). Bolted large seismic steel beam-to-column connections Part 2: numerical nonlinear analysis. *Engineering Structures*, 24(12), 1535-1545.

[81] Loh, H. Y., Uy, B., & Bradford, M. A. (2006). The effects of partial shear connection in composite flush end plate joints Part II—Analytical study and design appraisal. *Journal of Constructional Steel Research*, 62(4), 391-412.

[82] Wang, W. D., Han, L. H., & Uy, B. (2008). Experimental behaviour of steel reduced beam section to concrete-filled circular hollow section column connections. *Journal of Constructional Steel Research*, 64(5), 493-504.

[83] Mirza, O., & Uy, B. (2011). Behaviour of composite beam–column flush end-plate connections subjected to low-probability, high-consequence loading. *Engineering Structures*, 33(2), 647-662.

[84] Faridmehr, I., Tahir, M. M., & Lahmer, T. (2016). Classification system for semi-rigid beam-to-column connections. *Latin American Journal of Solids and Structures*, 13, 2152-2175.

[85] Guo, L., Gao, S., & Fu, F. (2015). Structural performance of semi-rigid composite frame under column loss. *Engineering structures*, 95, 112-126.

[86] Odrobiňák, J., Idunk, R., & Bačinský, T. (2014). Study on stiffness of composite beam-to-column joints. *Procedia Engineering*, 91, 268-273.

[87] Firdaus, M., Saggaff, A., Tahir, M. M., Aghlara, R., Sulaiman, A., Aminuddin, K., ... & Salih, M. N. A. (2020). Influence of seat angles on the behaviour of cold-formed steel concrete composite joints. *Journal of Constructional Steel Research*, 173, 106246.

[88] Kishi, N., & Chen, W. F. (1990). Moment-rotation relations of semi-rigid connections with angles. *Journal of Structural Engineering*, 116(7), 1813-1834.

[89] Kong, Z., & Kim, S. E. (2017). Moment-rotation behavior of top-and seat-angle connections with double web angles. *Journal of Constructional Steel Research*, 128, 428-439.

[90] Park, H. G., Hwang, H. J., Lee, C. H., Park, C. H., & Lee, C. N. (2012). Cyclic loading test for concrete-filled U-shaped steel beam–RC column connections. *Engineering structures*, 36, 325-336.

[91] Xu, X., Cheng, R., Yang, P., & Liu, R. (2020). Cyclic loading test for concrete-filled U-shaped steel beam to concrete-filled steel tube column connections. International Journal of Steel Structures, 20(6), 1859-1870.

[92] Chen, W. F., & Kishi, N. (1989). Semi-rigid steel beam-to-column connections: Data base and modeling. *Journal of Structural Engineering*, 115(1), 105-119.

[93] Krishnamurthy N. Modelling and prediction of steel bolted connection behaviour. *Computers and Structures* 1979;11:75–82.

[94] Krishnamurthy, N., & Graddy, D. E. (1976). Correlation between 2-and 3-dimensional finite element analysis of steel bolted end-plate connections. *Computers & Structures*, 6(4-5), 381-389.

[95] Bursi, O. S., & Jaspart, J. P. (1998). Basic issues in the finite element simulation of extended end plate connections. *Computers & structures*, 69(3), 361-382.

[96] Hibbitt, K. S. (2010). Abaqus User's Manual. Pawtucket, Ed. 6th, 2010.

[97] Choi, C. K., Chung, G. T., & Song, M. K. (1996). Refined three-dimensional finite element model for end-plate connections. In *Advances in Steel Structures* (ICASS'96) (pp. 365-370). Pergamon.

[98] Ayoub, A., & Filippou, F. C. (2000). Mixed formulation of nonlinear steel-concrete composite beam element. *Journal of Structural Engineering*, 126(3), 371-381.

[99] Sebastian, W. M., & McConnel, R. E. (2000). Nonlinear FE analysis of steel-concrete composite structures. *Journal of Structural Engineering*, 126(6), 662-674.

[100] Fabbrocino, G., Manfredi, G., & Cosenza, E. D. O. A. R. D. O. (2000). Analysis of continuous composite beams including partial interaction and bond. *Journal of Structural Engineering*, 126(11), 1288-1294.

[101] Ahmed, B. (1996). Numerical modelling of connections in composite frames (Doctoral dissertation, University of Nottingham).

[102] Baskar, K., Shanmugam, N. E., & Thevendran, V. (2002). Finite-element analysis of steel–concrete composite plate girder. *Journal of Structural Engineering*, 128(9), 1158-1168.

[103] El-Lobody, E., & Lam, D. (2002). Modelling of headed stud in steel-precast composite beams. Steel and Composite Structures, An *International Journal*, 2(5), 355-378.

[104] Ju, S. H., Fan, C. Y., & Wu, G. H. (2004). Three-dimensional finite elements of steel bolted connections. *Engineering Structures*, 26(3), 403-413.

[105] Hasan, M. J., Al-Deen, S., & Ashraf, M. (2019). Behaviour of top-seat double web angle connection produced from austenitic stainless steel. *Journal of Constructional Steel Research*, 155, 460-479.

[106] Iraqi specification No. 45 (1984), Natural Sources for Gravel that is Used in Concrete and Construction.

[107] ASTM, C. (1986). C 33-86; Standard Specification for Concrete Aggregates, Annual Book of ASTM Standards. ASTM: West Conshohocken, PA, USA.

[108] ASTM Designation A615 (2005). Standard specification for testing method and definitions for mechanical testing of steel products. Annual Book of ASTM Standards, American Society for Testing and Material, Philadelphia, Pennsylvania, Section 1, Vol. 1.01, pp. 248-287.

[109] Iraqi specification No. 5 (1984), Portland Cement.

[110] ASTM, A. (2005). 370-05," Standard Test Method and Definition for Mechanical Testing of Steel Products", Annual Book of ASTM Standard, Vol. 01.01. ASTM, Philadelphia, PA.

[111] ASTM International Committee C09 on Concrete and Concrete Aggregates. (2014). Standard test method for compressive strength of cylindrical concrete specimens. ASTM international.

[112] BS 1881, Part 116. (1989). Method for determination of compressive strength of concrete cubes. British Standards Institution, 3.

[113] ASTM C78-02; "Standard Test Method for Flexural Strength of Concret (Using Simple Beam with Third-Point Loading)." Annual Book of ASTM Standards, American Society for Testing and Materials.

[114] Takemura, H. (1997). Effect of hysteresis on ductility capacity of reinforced concrete bridge piers. *Structural Engineering Journal*, JSCE, A, 43, 849-848.

[115] Park, R. (1989). Evaluation of ductility of structures and structural assemblages from laboratory testing. Bulletin of the new Zealand society for earthquake engineering, 22(3), 155-166.

[116] Yu, R., Spiesz, P., & Brouwers, H. J. H. (2016). Energy absorption capacity of a sustainable Ultra-High Performance Fibre Reinforced Concrete (UHPFRC) in quasi-static mode and under high velocity projectile impact. *Cement and Concrete Composites*, 68, 109-122.

[117] ACI Committee. (2015). Building code requirements for structural concrete (ACI 318M-14) and commentary. American Concrete Institute.

[118] Swartz, B. D., Scanlon, A., & Schokker, A. J. (2012). AASHTO LRFD Bridge Design Specifications provisions for loss of prestress. *PCI journal*, 57(4).

[119] Chen, W. F. (2007). Plasticity in reinforced concrete. J. Ross Publishing.

[120] Neville, A. M., & Brooks, J. J. (1987). Concrete technology (Vol. 438). England: Longman Scientific & Technical.

[121] Metha, R. P. (1986.). 'Concrete Structure: Purposes and Material. Prentice-Hill, Inc., New Jersey.

[122] Bangash, M. Y. (1989). Concrete and concrete structures: Numerical modelling and applications.

[123] Kupfer, H., Hilsdorf, H. K., & Rusch, H. (1969, August). Behavior of concrete under biaxial stresses. In *Journal proceedings* (Vol. 66, No. 8, pp. 656-666).

[124] Eriksson, D., & Gasch, T. (2010). FEM-modeling of reinforced concrete and verification of the concrete material models available in ABAQUS. Royal Institute of Technology, Stockholm, SWEDEN.

[125] ASTM, C. (1996). 496-96. Standard test method for splitting tensile strength of cylindrical concrete specimens.

[126] Chaudhari, S. V., & Chakrabarti, M. A. (2012). Modeling of concrete for nonlinear analysis using finite element code ABAQUS. *International Journal of Computer Applications*, 44(7), 14-18.

[127] Malm, R. (2006). Shear cracks in concrete structures subjected to in-plane stresses (Doctoral dissertation, KTH).

[128] Lubliner, J., Oliver, J., Oller, S., & Oñate, E. (1989). A plastic-damage model for concrete. *International Journal of solids and structures*, 25(3), 299-326.

[129] Lee, J., & Fenves, G. L. (1998). Plastic-damage model for cyclic loading of concrete structures. *Journal of engineering mechanics*, 124(8), 892-900.

[130] Thorenfeldt, E. (1987). Mechanical properties of high-strength concrete and applications in design. In Symposium Proceedings, Utilization of High-Strength Concrete, Norway, 1987.

[131] CEB-FIP Model Code 90, (1993). 'Concrete Structures. Thomas Telford Publishing, 1993.

[132] Cornelissen, H., Hordijk, D., & Reinhardt, H. (1986). Experimental determination of crack softening characteristics of normalweight and lightweight. Heron, 31(2), 45-46.

[133] Hillerborg, A. (1985). The theoretical basis of a method to determine the fracture energy GF of concrete. *Materials and structures*, 18, 291-296.

APPENDIX-A

DESIGN EXAMPLE OF THE TESTED COMPOSITE BEAM TO COLUMN SIME-RIGD CONNECTIONS

Design procedure of the composite cold-formed steel beam-to-column connection specimen is produced in the present appendix. The cross-section of the selected composite joint specimen explained in Figure A.1.

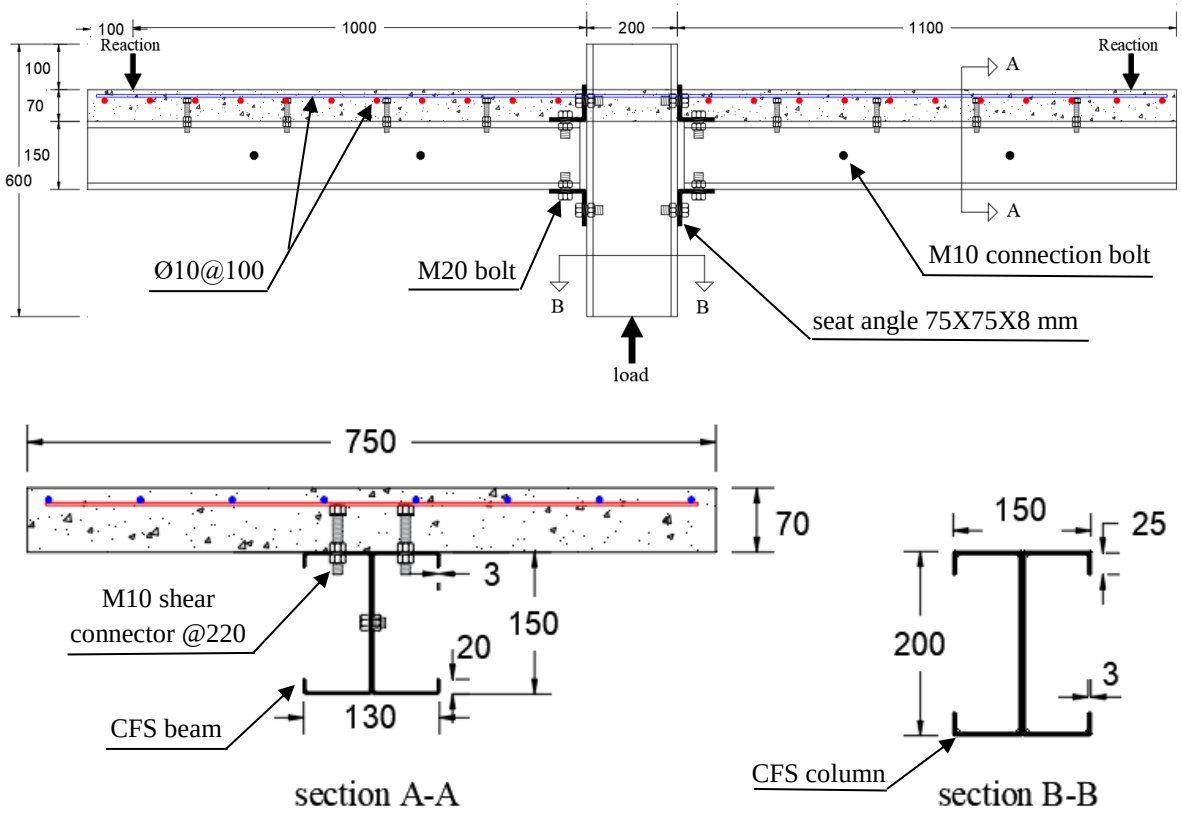

Figure A.1: Typical Cross-Section of the Specimen with shape I connection.

DESIGN STEPS

1. Calculating effective slab width:

Effective width of concrete slab is smaller of:

- ❖ 1/4 span length of the beam. (2200/4=550 mm)
- ❖ C/C distance between beams: Neglected, because of existing one beam.

Hence, the width of slab used in this study =750 mm

2. Using cold formed steel section (double C-section) with the properties shown in Table A.1.

Table A.1: Properties of CFS section used.

properties	symbol	value
Slab thickness (mm)	t_c	70
Slab width (mm)	b_c	750
Thickness of beam (mm)	t_{sb}	3
Flange width of beam (mm)	b_{fb}	65
Depth of beam (mm)	h_b	150
Thickness of column (mm)	t_{sc}	3
Flange width of column (mm)	b_{fc}	75
Depth of column (mm)	h_c	200
Depth of lip (mm)	h_{lip}	20
Yielding stress (MPa)	Fy	244
Ultimate strength (MPa)	Fu	297
Modulus of elasticity (MPa)	Es	200000

3. Properties of cold formed steel beam and column.

In this study, three types of connection shapes between the steel sections of the column and the beam were studied. For each one of these shapes, Ag, Ix, and Iy are as shown in Figure A.2. The calculation of cross section area and moment of inertia for each shape listed in Table A.2.

Table A.2: Calculation cross section area and moment of inertia.

Properties of section	Connection shape	Column	Beam
Ag	all shape	$2t_c[2b_{fc} + h_c + 2l_{lip}]$	$2t_b[2b_{fb} + h_b + 2l_{lip}]$
Ix	All shape	$= 2 * \left[\left(\frac{b_f * t^3}{12} + b_f * t\left(\frac{h}{2} - \frac{t}{2}\right)^2\right) * 2 + \frac{th^3}{12}\right]$	
Iy	shape 1(Figure A.2-a)	$= 2\left[\left(\frac{t * b_f^3}{12} + b_f * t\left(\frac{b_f}{2}\right)^2\right) * 2 + \frac{h * t^3}{12}\right]$	
	shape 2(Figure A.2-b)	Equation (A-1)	Equation (A-2)
	shape 3(Figure A.2-c)	Equation (A-2) *	Equation (A-1) *

* Replace the sub letter c by b when calculating Iy for the beam and vice versa.

$$I_y = 2 * \left[\left(\frac{t_c b_{fc}^3}{12} + b_{fc} t_c \left(b_{fb} + \frac{b_{fc}}{2}\right)^2\right) * 2 + \frac{h_c t_c^3}{12} + h_c t_c \left(b_{fb} + \frac{t_c}{2}\right)^2\right] \ldots\ldots\ldots (A-1)$$

$$I_y = 2 * \left[\left(\frac{t_b b_{fb}^3}{12} + b_{fb} t_b \left(\frac{b_{fb}}{2}\right)^2\right) * 2 + \frac{h_b t_b^3}{12} + h_b t_b \left(b_{fb} - \frac{t_2}{2}\right)^2\right] \ldots\ldots\ldots\ldots\ldots (A-2)$$

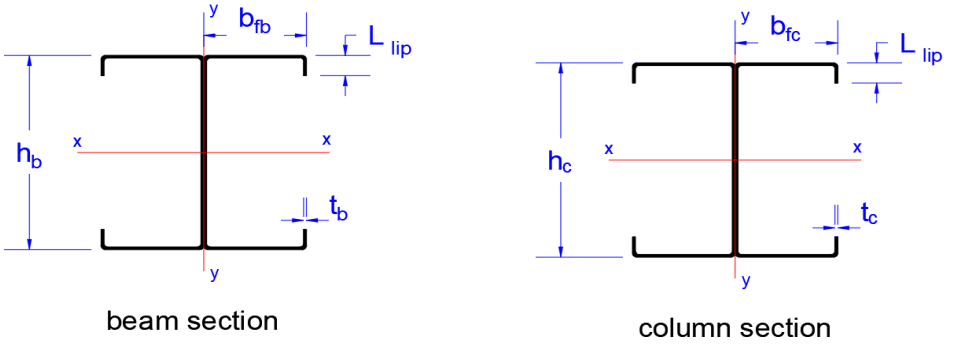

(a)

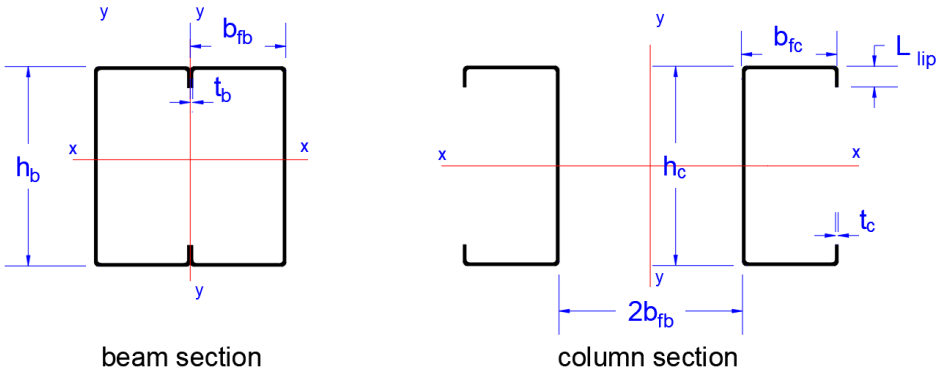

(b)

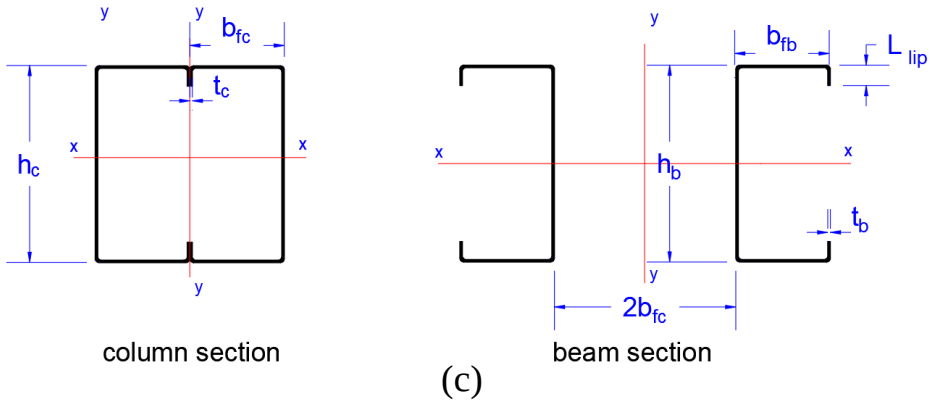

(c)

Figure A.2: Shown the shapes of connection used in this study which (a) shape 1 connection, (b) shape 2 connection and (c) shape 3 connection.

4. Used specimen with shape I connection for example design and with dimension shown in Figure A.3.

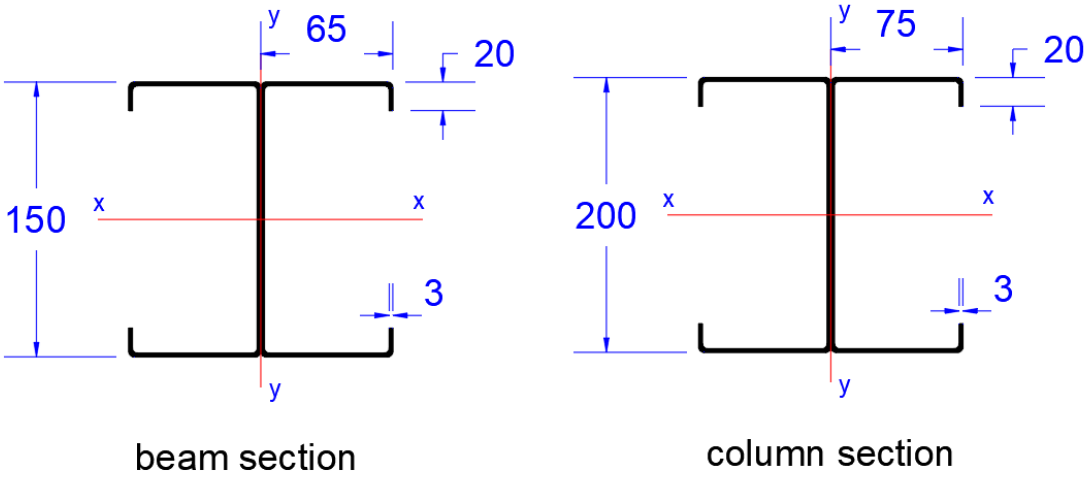

Figure A.3: Section dimensions for beam and column.

4-1 Properties of column

- $A_{gc} = 2t_c[2b_{fc} + h_c + 2l_{lip}] = 2 * 3 * [2 * 75 + 200 + 2 * 20] = 2340\ mm^2$
- $I_{xc} = 2 * \left[\left(\frac{b_{fc} * t_c^3}{12} + b_{fc} * t_c \left(\frac{h_c}{2} - \frac{t_c}{2}\right)^2\right) * 2 + \frac{t_c h_c^3}{12}\right] = 2 * \left[\left(\frac{75 * 3^3}{12} + 75 * 3 * \left(\frac{200}{2} - \frac{3}{2}\right)^2\right) * 2 + \frac{3 * 200^3}{12}\right] = 12.73 * 10^6 mm^4$

- $I_{yc} = 2\left[\left(\frac{\mathrm{tc}*\mathrm{b_{fc}^3}}{12} + \mathrm{b_{fc}} * \mathrm{tc}\left(\frac{\mathrm{b_{fc}}}{2}\right)^2\right) * 2 + \frac{\mathrm{hc}*\mathrm{tc}^3}{12}\right] = 2 * \left[\left(\frac{3*75^3}{12} + 75 * 3 * \left(\frac{75}{2}\right)^2\right) * 2 + \frac{200*3^3}{12}\right] = 1.69 * 10^6 mm^2$

4-2 Properties of beam

- $\mathrm{A_{gb}} = 2\mathrm{t_b}\left[2\mathrm{b_{fb}} + \mathrm{h_b} + 2\mathrm{l_{lip}}\right] = 2 * 3 * [2 * 65 + 150 + 2 * 20] = 1920\ \mathrm{mm^2}$
- $I_{xb} = 2 * \left[\left(\frac{\mathrm{b_{fb}}*t_b^3}{12} + \mathrm{b_{fb}} * t_b\left(\frac{h_b}{2} - \frac{t_b}{2}\right)^2\right) * 2 + \frac{t_b h_b^3}{12}\right] = 2 * \left[\left(\frac{65*3^3}{12} + 65 * 3 * \left(\frac{150}{2} - \frac{3}{2}\right)^2\right) * 2 + \frac{3*150^3}{12}\right] = 2.95 * 10^6 mm^4$
- $I_{yb} = 2\left[\left(\frac{\mathrm{tb}*\mathrm{b_{fb}^3}}{12} + \mathrm{b_{fb}} * t_b\left(\frac{\mathrm{b_{fb}}}{2}\right)^2\right) * 2 + \frac{h_b t_b^3}{12}\right] = 2 * \left[\left(\frac{3*65^3}{12} + 65 * 3 * \left(\frac{65}{2}\right)^2\right) * 2 + \frac{150*3^3}{12}\right] = 0.55 * 10^6 mm^4$

5. Design of column

$A_{gc} = 2340\ mm^2, I_{xc} = 12.73 * 10^6 mm^4, I_{yc} = 1.69 * 10^6 mm^2\ and\ L_c = 400mm$

K=0.8 (where K is the effective length factor as defined by AISC in Table C-C2.2)

$$r_x = \sqrt{\frac{I_x}{Ag}} = 73.75\ mm \quad , \quad r_y = \sqrt{\frac{I_y}{Ag}} = 26.87\ mm \quad control$$

$$\frac{k\ L}{r} = \frac{0.8 * 280}{26.87} = 8.33$$

$$F_e = \frac{\pi^2 E}{\left(\frac{k\ L}{r}\right)^2} = 28403.3\ MPa$$

$$\frac{k\ L}{r} = 8.33 < 4.71 * \sqrt{\frac{E}{Fy}} = 133 \rightarrow F_{cr} = \left[0.658^{\frac{Fy}{Fe}}\right] fy = 243.12\ MPa$$

$$P = Fy * Ag = 580.62\ kN$$

$$\lambda_r = 1.49 * \sqrt{\frac{E}{Fy}} = 42.14 \qquad ,\lambda = \frac{h}{tw} = \frac{200 - 2 * 3}{3} = 64.67$$

- For unstiffened elements

$$\lambda_r = 0.56 * \sqrt{\frac{E}{Fy}} = 15.84 \qquad ,\lambda = \frac{b_f}{t_f} = \frac{75}{3} = 25$$

$\lambda > \lambda_r \rightarrow slender\ section$

- Stiffened elements

$$\lambda_r = 1.49 * \sqrt{\frac{E}{Fy}} = 42.14 \qquad ,\lambda = \frac{h}{tw} = \frac{200 - 2 * 3}{3} = 64.67$$

$\lambda > \lambda_r \rightarrow local\ buckling\ occouring\ in\ web$

- Calculate $Q = Qs * Qa$

$Qs = 1 \quad (no\ local\ buckling\ occouring\ in\ flange)$

Calculate $Qa = \frac{Aeff.}{A}$

$$h_e = 1.92 * t * \sqrt{\frac{E}{Fy}}\left[1 - \frac{0.34}{(\lambda)}\sqrt{\frac{E}{Fy}}\right] = 138.7\ mm \leq h$$

$$Aeff. = Ag - (h - h_e) * 2t = 2340 - (200 - 138.7) * 2 * 3 = 1972.2\ mm^2$$

$$Qa = \frac{Aeff.}{A} = \frac{1972.2}{2340} = 0.843 \rightarrow Q = 1 * 0.843 = 0.843$$

$$\therefore F_{cr} = \left[0.658^{\frac{Qfy}{Fe}}\right] QFy = 205.07MPa$$

$$\therefore P = 205.07 * 2340 = 479.86\ kN$$

6. Slab thickness equal 70 mm and the design strength of the concrete used in the deck slab was 30 MPa.

7. Calculation of ultimate load for composite beam:

a- Elastic stage:

The modulus of elasticity and modular ratio are:

$$E_c = 4700\sqrt{fc'} = 25742.96\ MPa \qquad \text{(ACI-Code [117])}$$

$$\mathrm{n} = \frac{\mathrm{E_s}}{\mathrm{E_c}} = \frac{200000}{25742.96} = 7.769 \cong 8$$

- Depth to the elastic neutral axis (y):

$$\mathrm{y} = \frac{\frac{\mathrm{A_c}}{\mathrm{n}} \times 0.5 \times \mathrm{t_c} + \mathrm{A_{gb}} \times (0.5\mathrm{h}_b + \mathrm{t_c})}{\frac{\mathrm{A_c}}{\mathrm{n}} + \mathrm{A_{gb}}}$$

$$= \frac{\frac{52500}{8} \times 0.5 \times 70 + 1920(0.5 \times 150 + 70)}{\frac{52500}{8} + 1920} = 59.9\ mm$$

$$\mathrm{I_{tr}} = \mathrm{I_{xb}} + \frac{\mathrm{bc} \times \mathrm{t_c^3}}{\mathrm{n} * 12} + \frac{\mathrm{A_c}}{\mathrm{n}}(\mathrm{y} - 35)^2 + \mathrm{A_{gb}}(0.5\mathrm{h_b} + \mathrm{t_c} - \mathrm{y})^2$$

$$= 2.95 * 10^6 + \frac{750 \times 70^3}{8 \times 12} + \frac{52500}{8} \times (59.9 - 35)^2 + 1920$$

$$\times (0.5 \times 150 + 70 - 59.9)^2 = 23.6 \times 10^6 \mathrm{mm}^4$$

- Section modulus for the concrete and steel:

$$\mathrm{S_{xc}} = \mathrm{n} \times \frac{\mathrm{I_{tr}}}{\mathrm{y}} = 3152 \times 10^3 \mathrm{mm}^3$$

$$\mathrm{S_{xs}} = \frac{\mathrm{I_{tr}}}{(\mathrm{h_b} + \mathrm{t_c} - \mathrm{y})} = 147.4 \times 10^3 \mathrm{mm}^3$$

- Calculating maximum elastic moment:

$$\mathrm{M} = \mathrm{f_c'} \times \mathrm{S_{xc}} = 94.56\ \mathrm{kN.m}$$

$$\mathrm{M} = \mathrm{F_y} \times \mathrm{S_{xs}} = 36\ \mathrm{kN.m}\ \ \text{(control)}$$

The total applied load ($\mathrm{P_n}$) for the beam loaded by concentrated load ($\frac{\mathrm{P_n}}{2}$) applied at 10 mm from the end points of span from each side;

$$p_n = \frac{4M}{L} = 65.45 \text{ kN}$$

b- Plastic stage:

Table A.3 define the symbols used in plastic stage to calculate plastic moment of composite beam

Table A.3: Define the symbols in plastic stage.

Symbol	Define	Value	Unit
A_s	total cold formed steel area	1920	mm^2
A_{st}	cold formed steel area in tension (above plastic neutral axis)	432.21	mm^2
A_{sf}	the flange area of cold formed steel beam in tension	390	mm^2
A_{sc}	cold formed steel area in compassion	1466.4	mm^2
A_{rb}	reinforcement area	628.32	mm^2
y_p	Plastic neutral axis location	89.5	mm
T1	$A_{rb} * fy_b$	-	-
T2	$A_{sf} * fy_{steel}$	-	-
T3	$(A_{st} - A_{sf}) * fy_{steel}$	-	-
C	$A_{sc} * fy_{steel}$	-	-

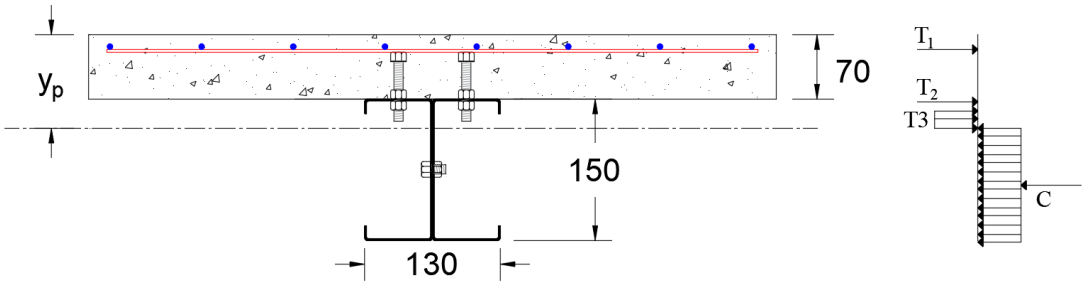

$$A_{sc} = A_{st} \Longrightarrow (A_s - A_{st}) * fy_{steel} = A_{rb} * fy_{bar} + A_{st} * fy_{steel}$$

$$(1920 - A_{st}) * 250 = 628.32 * 420 + A_{st} * 250 \Longrightarrow A_{st} = 433.21 \text{ mm}^2$$

$$A_{sf} = 65 * 3 * 2 = 390 \text{ mm}^2$$

$$A_{st} - A_{sf} = 433.21 - 390 = 42.21 \text{ mm}^2$$

$$\sum \text{M about N.A} = 0$$

$$A_{rb} * fy_{bar}(y_p - 20) + A_{sf} * fy_{steel} * (y_p - 70) + (A_{st} - A_{sf}) * fy_{steel} * \left(\frac{y_p - 70}{2}\right) = A_{sc} * fy_{steel} * (220 - \frac{150}{2} - y_p)$$

$$628.32 * 420 * (y_p - 20) + 390 * 244 * (y_p - 70) + 42.21 * 244 * \left(\frac{y_p - 70}{2}\right) = 1466.4 * 244 * (220 - 75 - y_p)$$

$$\Rightarrow y_p = 88.89 \text{ mm}$$

$$M_p = T_1 * (y_p - 20) - T_2 * (y_p - 70) - T_3 * \left(\frac{y_p - 70}{2}\right) + C * \left(\frac{150 + 70 - y_p}{2}\right)$$

$$Mp = 628.32 * 420 * (88.89 - 20) - 390 * 244 * (88.89 - 70) - 42.21 * \left(\frac{88.89 - 70}{2}\right) * 244 + 1466.4 * 244 * \left(\frac{150 + 70 - 88.89}{2}\right) = 39.74 \text{ kN} \cdot \text{m}$$

$$p_n = \frac{4M}{L} = 72.3 \text{ kN} \quad \text{(control)}$$

8. Ultimate vertical shear:

$V_c = 0.17\sqrt{f'_c} \times b_c t_c = 48.88$ kN

$V_s = 0.6F_y \times h_b \times t_w = 67.5$ kN

$Vn = Vs + Vc = 116.38\ kN \rightarrow \therefore Pn = 2 \text{ x } Vn = 232.76\ kN$

9. Shear connectors:

Shear resistance (Q_n) of a shear connector is lesser of:

- Resistance of Concrete; $Q_n = 0.5 * A_{scc}\sqrt{fc' * E_c} = 35\ kN$
- Resistance of Shear connector; $Q_n = A_{scc}F_u = 61\ kN$

Where: A_{scc}= cross sectional area of shear connector.

F_u= ultimate tensile strength of shear connector.

In the present study the diameter of the shear connector is (10 mm) and the ultimate tensile strength is (780 MPa), thus $Qn = 35\ kN$

- Calculating upper required number of shear connectors:

  Longitudinal shear force; $V' = \min(F_{s\,max}; F_{c\,max}) = 298\ kN$

  $$\therefore No.\ of\ S\text{hear Connector} = 2 * \frac{V'}{Qn} \cong 17$$

- Calculating lower required number of shear connectors:

  Longitudinal shear flow; $q = \frac{Vx\ Q}{I} = 283.63\ N/mm$

  $$No.\ of\ \text{Shear Connector} = 2 * \frac{L/2}{Q_n/q} \cong 15$$

- Calculating Degree of Composite Action:

  $$D.C.A = \frac{\text{Provided connectors}}{\text{No. ofconnectors for full composite action}}$$

  $$D.C.A = \frac{16}{17} = 94\% \geq 25\%$$

10. Geometry Provisions for Shear Connectors

- H/D ≥ 4 [117,118]
- Longitudinal spacing (c. to c.) ≤ 600mm (24") [118], ≥ 6D [117,118]
- Transverse spacing (c. to c.) ≥ 4D [117,118]
- Clear distance between edge of the top flange and the edge of the nearest shear connector shall not be less than 25mm (1.0") [117,118]
- Cover ≥ 50mm (2") and Penetration ≥ 50mm (2") [118]
- D ≤ 2.5 flange thickness (unless located over the web) [117]
- Maximum spacing ≤ 8 slab thickness [117]

  ≤ 36" [117]

11. Reinforcement

$$As_{min.} = \max\begin{cases} 0.0018\,A_c = 94.5\ mm^2 \\ \frac{0.0018*420}{fy} = 13.8\ mm^2 \end{cases}$$ (ACI-Code [117])

$$S_{max.} = \min.\begin{cases} 5t_c = 350\ mm \\ 450\ mm \end{cases} \rightarrow \text{For secondary reinforcement}$$

$$S_{max.} = \min.\begin{cases} 3t_c = 210\ mm \\ 500\ mm \end{cases} \rightarrow \text{For main reinforcement}$$

As for ∅10mm = 78.539 mm^2

- Long direction (main reinforcement)

  $As_{min.} = 0.0018 \times 750 \times 70 = 94.5\ mm^2$

  in this study used 8∅10 @100mm

  $$S_{c.to.c} = \frac{750 - 2 \times 20 - 8 \times \frac{10}{2}}{8 - 1} = 95.7\ \ mm$$

- Short direction (secondary reinforcement)

  $As = 0.0018 \times 2000 \times 70 = 252\ mm^2$

  in this study used ∅10 @100mm

APPENDIX B

MODELING OF MATERIAL PROPERTIES

B.1 INTRODUCTION

The behavior of any structure under loading depends upon the stress-strain relationship of the material from which it is made. Composite joints consist of different materials (concrete, steel, shear connectors, bolt, and reinforcing steel) which are connected in a certain form to work as a composite system. This system is designed to exploit the material relationship for each one according to its designated position to form a composite relationship describing the behavior of the whole configuration under a loading condition.

When considering the performance or behavior of the composite joint materials independently, it will be clear that each of the concrete slab and I-steel beam has different properties. Where the steel can been considered as a homogeneous material that exhibits a similar stress-strain relationship in tension and compression. However, concrete is a heterogeneous nonlinear material, dependent upon the properties of its components; cement mortar, aggregates, additives and air voids.

B.2 MECHANICAL BEHAVIOR OF CONCRETE

Concrete is a heterogeneous nonlinear material. The hardened concrete contains a large number of micro-cracks at interface between aggregate and mortar, even before any loads have been applied [119]. The gradual growth of these micro-cracks under additional load contributes to the nonlinear behavior of concrete. Since the aggregate-mortar interface has a significantly lower tensile strength than the mortar (because of the presence

of these micro-cracks). This interface forms the weakest link in the structure of concrete [120]. Many experimental studies of the concrete behavior under uniaxial and multi-axial loading conditions have been performed. The behavior of concrete under these states of stress is described in the following sections.

B.2.1 Uniaxial Stress Behavior of Concrete

B.2.1.1 Compression behavior

Figure B.1 shows a typical stress-strain relationship curve for normal weight concrete in compression and tension. The main characteristics in this curve can be summarized, as follows [117, 119]:

1. The axial stress-strain curve, Figure B.1, has a nearly linear elastic behavior up to about 30 % of its maximum compressive strength (f_c'). Above this point 0.30 f_c', concrete begins to soften and the curve shows a gradual increase in curvature up to about ($0.75f_c' - 0.90\ f_c'$), after which the curve bends more sharply until it approaches the peak point at f_c', after it reaches the maximum compressive strength f_c' (σ_{cu}), the curve descends into a softening region, and eventually crushing failure occurs at an ultimate strain εu (ε_{cu}).
2. The modulus of elasticity of conventional-strength concrete generally increases proportionally to the square root of the compressive strength.

$$Ec = 4700 * \sqrt{f'c} \qquad \text{(B-1)}$$

3. Poisson's ratio (v) of concrete has been approximately observed constant and ranged from about 0.15 to 0.22 up to a stress level equal to 0.8 fc'. Beyond this level, Poisson's ratio increases rapidly and becomes equal to1.0 at plastic stage. In the present study was taken equal to 0.18.

B.2.1.2 Tensile behavior

The stress-strain curve for concrete under uniaxial tension is shown in Figure B.1. It is nearly linear up to about 0.6 f_t (0.6 σ_{cu}). This is because

the creation of new micro cracks is negligible. Hence, this stress level corresponds to a limit of elasticity. Then, the bond micro cracks start to grow and nonlinearity of the curve to increase as the stress level increases until peak stress is reached. The ratio between uniaxial tensile strength (f_t) and compressive strength (fc') may vary considerably but usually ranges between 0.05 and 0.1[119]. The modulus of elasticity under uniaxial tension is somewhat higher and Poisson ratio somewhat lower than in compression [121]. The direct tensile strength of concrete is difficult to measure and is normally taken as approximately [119].

$$f_t = 0.33\sqrt{fc'} \quad \text{MPa} \tag{B-2}$$

The split-cylinder tensile strength is usually lower, and it is approximately:

$$f_t = 0.45\sqrt{fc'} \quad \text{MPa} \tag{B-3}$$

The modulus of rupture fr is often used to approximate the tensile strength of concrete. The value of the modulus of rupture varies widely but is normally taken as [121].

$$f_t = 0.62\sqrt{fc'} \quad \text{MPa} \tag{B-4}$$

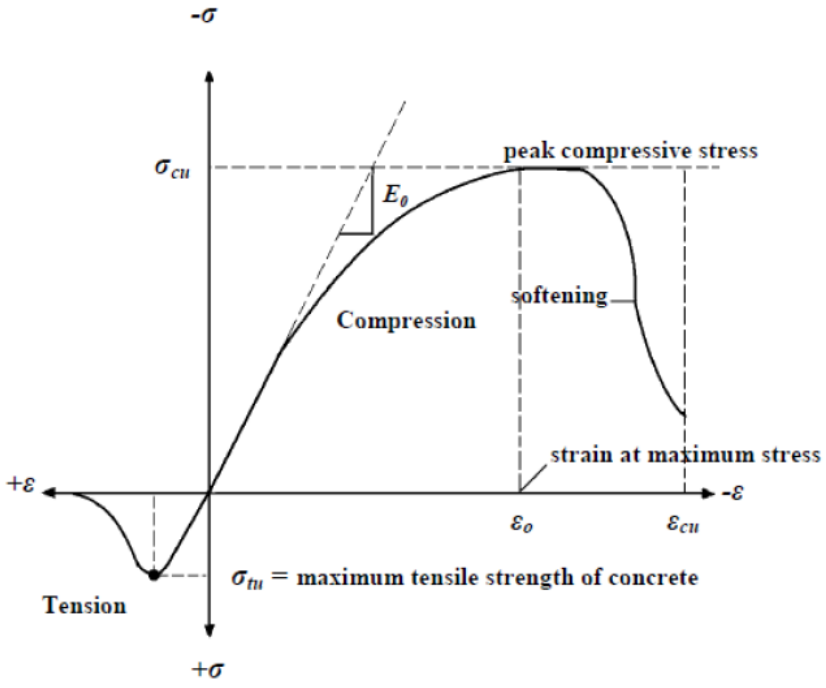

Figure B.1: Typical Uniaxial Compressive and Tensile Stress-Strain Curve for Concrete [122].

C.2.2 Biaxial Stress Behavior of Concrete

Knowledge of the concrete behavior subjected to multi-axial states of stress is essential to a better understanding of the failure mechanism of concrete. The test results of Kupfer [123] show that the ultimate strength of concrete in biaxial compression is greater than in uniaxial compression, and it is dependent on the principal stress ratio. Figure B.2 shows a typical biaxial strength envelope. It is clear that the maximum compressive strength increased for a biaxial compression state at about 25% at a stress ratio equal to (σ_2/σ_1= 0.5) but, when the stress ratio is equal to (σ_2/σ_1= 1), the maximum compressive strength increased at about 16%. Under biaxial compression-tension state, the compressive strength decreases almost linearly as the applied tensile stress is increased [119]. While under biaxial tension, the strength is almost the same as that of the uniaxial tensile strength.

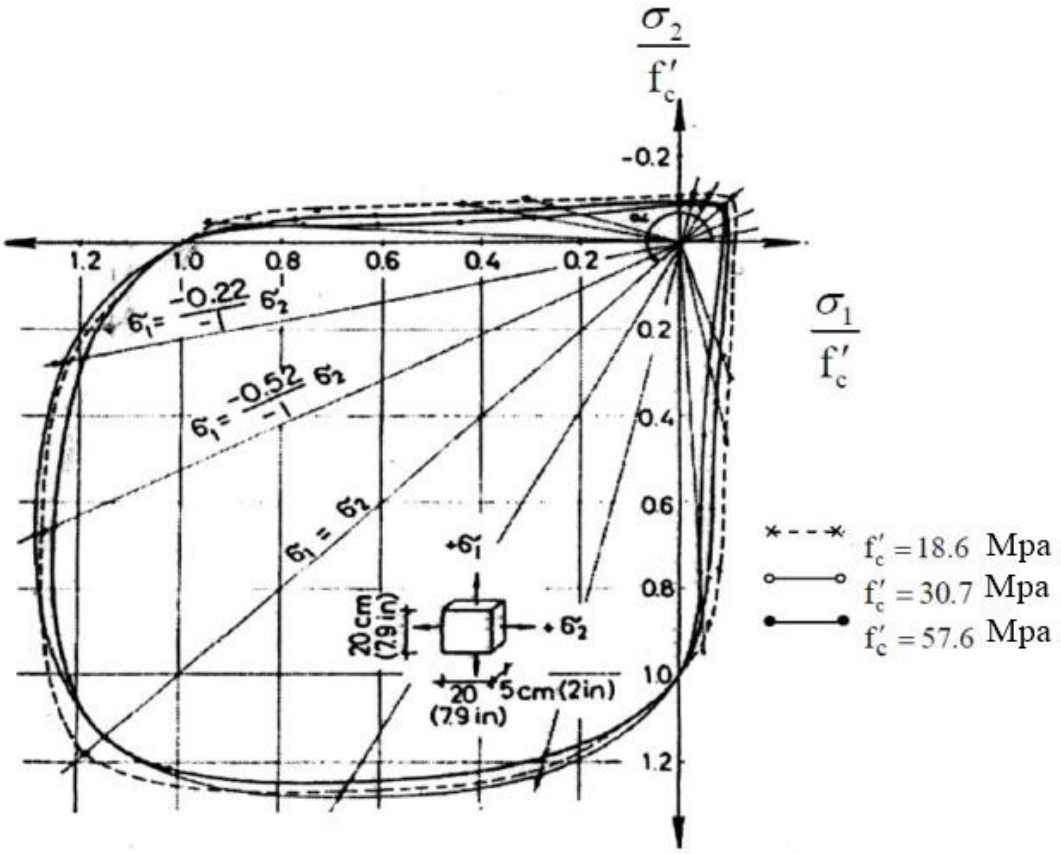

Figure B.2: Biaxial Strength of Concrete [123].

B.2.3 Tri-axial Stress Behavior of Concrete

Experimental studies indicate that the three dimensional failure envelope is a function of the three principal stresses. Figure B.3 shows a diagram failure surface of concrete in three dimensional stress space. The failure envelope is smooth, convex and its deviatoric sections (planes perpendicular to the hydrostatic axis, line of $\sigma_1 = \sigma_2 = \sigma_3$) become more circular in shape for increasing hydrostatic pressures. For smaller hydrostatics pressures, these cross sections are convex and non-circular. The limiting tensile stress required to define the onset of cracking can be calculated for states of tri-axial tensile stress and for combinations of tension and compression principal stresses. Both the function of stress and the failure surface are expressed in terms of principal stresses denoted asσ_1, σ_2 and σ_3 where, σ_1= max ($\sigma_x; \sigma_y; \sigma_z$) and σ3 = min ($\sigma_x; \sigma_y; \sigma_z$) and if $\sigma_1 \geq \sigma_2 \geq \sigma_3$, the failure of concrete is categorized into four domains:

- $0 \geq \sigma1 \geq \sigma2 \geq \sigma3$ (compression- compression- compression).
- $\sigma1 \geq 0 \geq \sigma2 \geq \sigma3$ (tension- compression- compression).
- $\sigma1 \geq \sigma2 \geq 0 \geq \sigma3$ (tension- tension- compression).
- $\sigma1 \geq \sigma2 \geq \sigma3 \geq 0$ (tension- tension- tension).

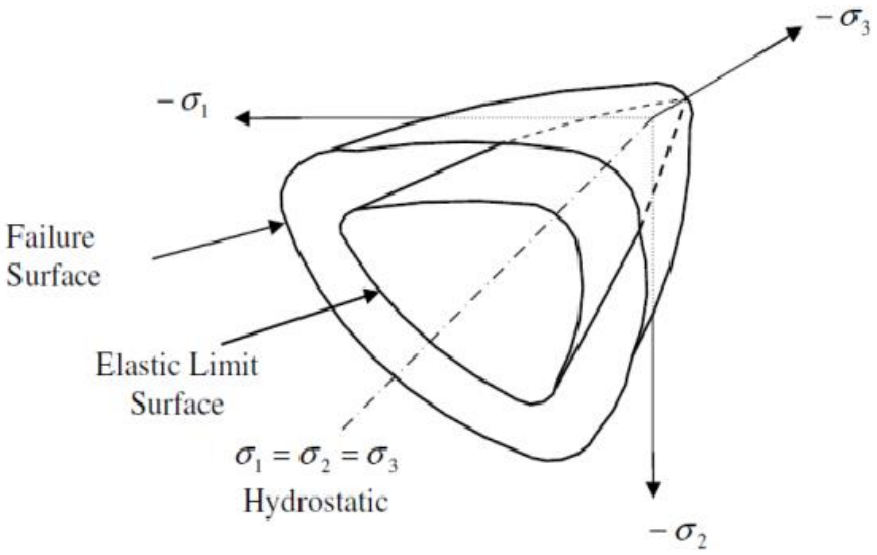

Figure B.3: Tri-axial Strength Envelope of Concrete [119].

B.3 ABAQUS

B.3.1 Introduction to ABAQUS

The most reliable method to evaluate accurate behavior of concrete structural elements is to experimentally study on actual structures, but because of being expensive and time consuming, usually experiments are not always possible to perform. Therefore, other methods, which take into account the anisotropic behavior of concrete including the effect from tensile cracks, are required. One method is Finite Element Modeling (FEM), which needs less cost and time to be implemented. Different commercial FEM software has been developed during years and one of them is ABAQUS**,** which was used in this study [124].

ABAQUS is a finite element program to evaluate the behavior of structures and solids under external loads. This program can analyze both static and dynamic problems and it is capable of modeling a wide range of 2D and 3D shapes and contacts between solids. It has an advanced and extensive library for elements and materials.

B.3.2 Constitutive Concrete Material Model

There are three material models for analyzing concrete at low confining pressures in ABAQUS; Concrete smeared cracking model in ABAQUS/Standard, Brittle cracking model in ABAQUS/Explicit and Concrete damaged plasticity model in both ABAQUS/Standard and ABAQUS/Explicit. Each model is designed to provide a general capability for modeling plain and reinforced concrete (as well as other similar quasi-brittle materials) in all types of structures: beams, trusses, shells, and solids.

The smeared crack concrete is intended for applications in which the concrete is subjected to essentially monotonic straining and a

material point exhibits either tensile cracking or compressive crushing. Plastic straining in compression is controlled by a “compression” yield surface. Cracking is assumed to be the most important aspect of the behavior and the representation of cracking and post cracking anisotropic behavior dominates the modeling.

The brittle cracking is intended for applications in which the concrete behavior is dominated by tensile cracking and compressive failure is not important. The model includes consideration of the anisotropy induced by cracking. In compression, the model assumes elastic behavior. A simple brittle failure criterion is available to allow the removal of elements from a mesh.

The concrete damaged plasticity is based on the assumption of scalar (isotropic) damage and is designed for applications in which the concrete is subjected to arbitrary loading conditions, including cyclic loading. The model takes into consideration the degradation of the elastic stiffness induced by plastic straining both in tension and compression. It also accounts for stiffness recovery effects under cyclic loading [124].

The concrete damage plasticity (CDP) model was selected in this study due to the following reasons [96,125, and126]:

- It has higher potential for convergence compared to the smeared crack model;
- It can consider different yield strength in tension and compression;
- It counts true post yield (plastic) response like softening behavior in tension as opposed to initial hardening followed by softening in compression;
- Different degradation of the elastic stiffness in tension and compression can be considered in this model.

B.3.3 Concrete Damage Plasticity

Concrete damaged plasticity is capable of modeling all structural types of reinforced or unreinforced concrete or other quasi-brittle materials subjected to monotonic, cyclic or dynamic loads. This model is based on a coupled damage plasticity theory and the multi-axial behavior of concrete in damaged plasticity model governs by a yield surface which proposed by Lubliner et al. and was modified later by Lee and Fenves [127-129]. Tensile cracking and compressive crushing of concrete are two assumed main failure mechanisms in this model. Furthermore, the degradation of material for both tension and compression behavior have been considered in this model.

B.3.4 Uniaxial and Multi-axial Behavior

Under uniaxial tension, as can be seen in Figure B.4, the stress increases with a linear elastic relationship with strain up to the ultimate tensile strength, f_t and then micro-cracks form microscopically with a tension softening response. There are three different methods to define tension softening response in ABAQUS: stress-strain, stress-displacement or by use of fracture energy [124].

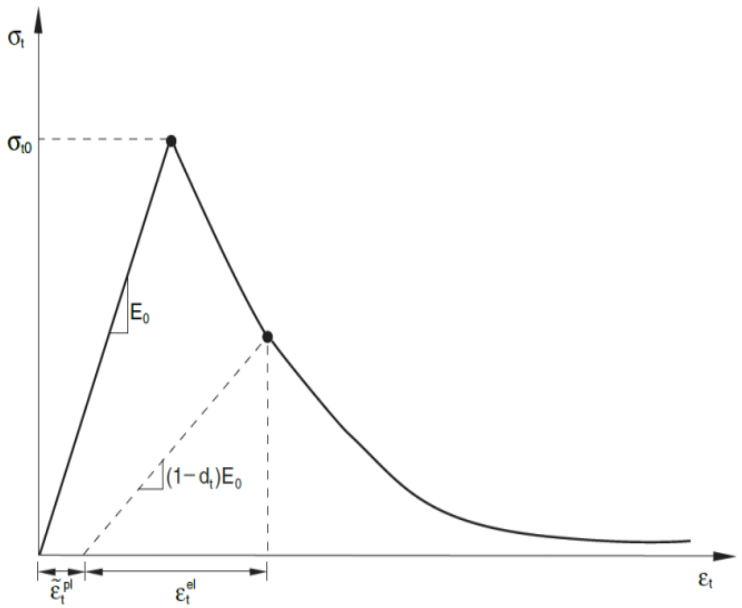

Figure B.4: Uniaxial Tensile Behavior of Concrete [124].

In addition, under uniaxial compression, there is a linear elastic relationship between stress-strain until initial yield, f_{co}. After losing stiffness due to bond failure between the aggregates and the cement paste, the behavior becomes nonlinear. In stresses greater than ultimate strength, plastic response is defined by stress hardening and strain softening. In other words, compressive stress decreases while the corresponding strain increases [57]. The uniaxial compressive behavior of concrete is depicted in Figure B.5.

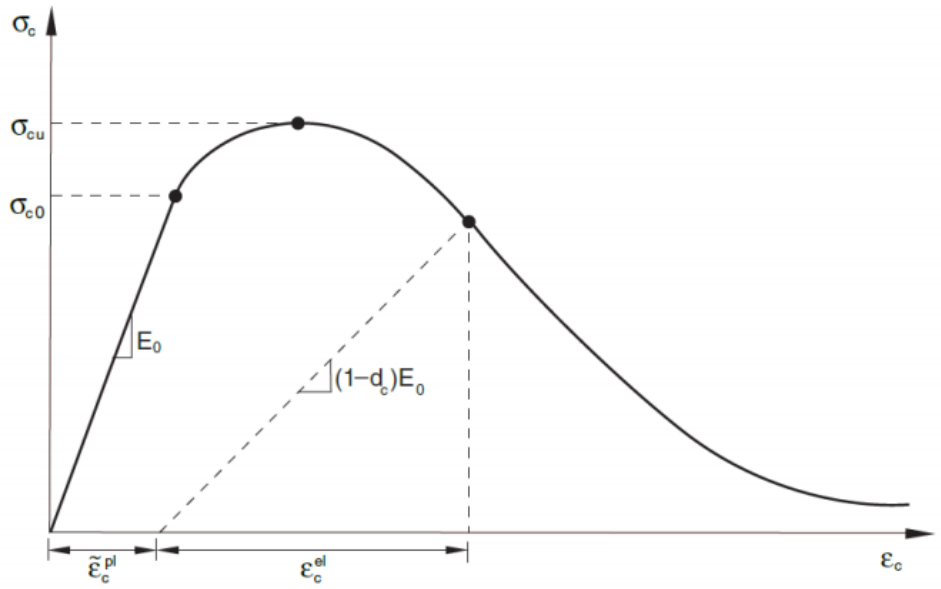

Figure B.5: Uniaxial Compressive Behavior of Concrete [124].

B.3.5 Concrete Damaged Plasticity Definition

Different input data, which should be defined in concrete damaged plasticity, are:

1- **ψ** is the dilation angle, measured in p -q plane and should be defined to calculate the inclination of the plastic flow potential in high confining pressures, Figure B.6. The dilation angle is equal to the friction angle in low stresses. In higher level of confinement stress and plastic strain, dilation angle is decreased. Maximum value of is ψ_{max} = 56.3° and minimum value is close to 0°. Upper values represent a more

ductile behavior and lower values show a more brittle behavior. According to Malm the effect of the dilation angle in values between $30^o \leq \psi \leq 40^o$ in some cases can be neglected and for normal concrete $\psi = 30^o$is acceptable.

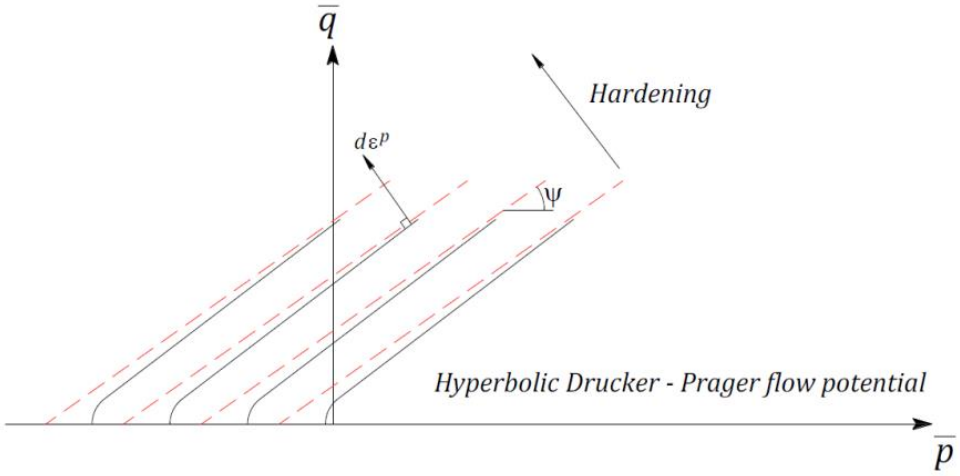

Figure B.6: Hyperbolic Plastic Flow Rule [124].

2- $\boldsymbol{\epsilon}$: is the flow potential eccentricity. It is a small positive number, which defines the range that the plastic potential function closes to the asymptote as shown in Figure B.6. The default value in ABAQUS is 0.1 and indicates that the dilation angle is almost constant in a wide range of confining pressure. In higher value of ϵ, with reduction of confining pressure, the dilation angle increases more rapidly. Very small values of ϵ in comparison with the default value make cause convergence problems in cases with low confining pressure, due to very tight flow-potential curvature at the point of intersection with the p-axis.

3- f_{b0}/f_{c0} : is the ratio of initial equiaxial compressive yield stress to initial uniaxial compressive yield stress. The default value is 1.16.

4- K_c : is the ratio of the second stress invariant on the tensile meridian to that on the compressive meridian at initial yield for any given value of the pressure invariant, such that the maximum principal stress is negative it must satisfy the condition $0.5 < Kc \leq 1$. The default value is 2/3.

5- Viscosity parameter (μ): used for the visco-plastic regularization of the concrete constitutive equations in ABAQUS/Standard analyses. This parameter is ignored in ABAQUS/Explicit. The default value is 0.0. According to Malm μ = $10^{-7}$is recommended because in comparison with characteristic time increment it should be small [127]**.**

6- The compressive behavior of concrete can be simulated accurately using an elasto-plastic and strain-hardening model. Compressive stress data can be provided as a function of plastic strain. The stress–strain curve can be defined beyond the ultimate stress, into the strain-softening regime. In order to simulate concrete with high compressive strength, the stress –strain relationship as proposed by Thorenfeldt et al. [130], Figure B.7, combined with the Hognestad's assumption on the elastic modulus of concrete was adopted. This applied a factor to increase the post-peak decay, which closely related to the real behavior of high strength concrete. This relationship was based on the concrete cylinder strength, as described in Equation (B-5).

$$\frac{fc}{fc'} = \frac{n\,(\frac{\varepsilon_c}{\varepsilon_o})}{n-1+(\frac{\varepsilon_c}{\varepsilon_o})^{nk}} \qquad \text{(B-5)}$$

$$n = 0.8 + \frac{fc'}{17}$$

$$k = 0.67 + \frac{fc'}{62}$$

$$\varepsilon_o = \frac{fc'}{E_c(\frac{n}{n-1})}$$

Where:

fc'= peak stress obtained from a cylinder test (MPa).

ε_o= strain when fc reaches fc'.

n = a curve-fitting factor.

Ec= modulus of elasticity (MPa).

k = factor to control the slopes of the ascending and descending branches of the stress–strain curve, taken equal to 1.0 for $\frac{\varepsilon_c}{\varepsilon_o}$ less than 1.0 and taken greater than 1.0 for $\frac{\varepsilon_c}{\varepsilon_o}$ greater than 1.0.

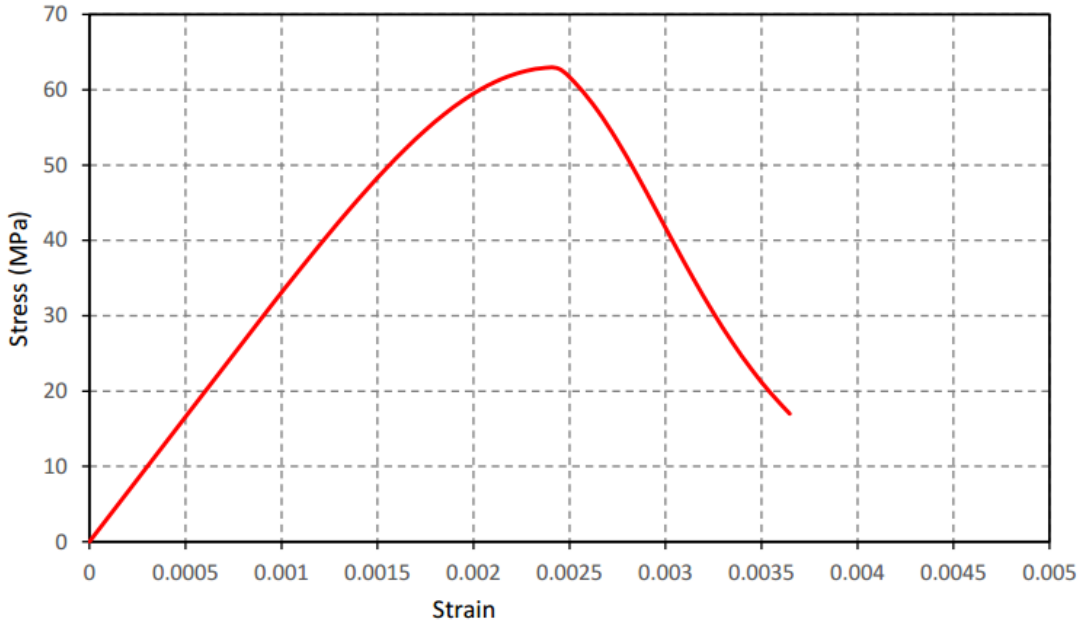

Figure B.7: Stress–strain Relationship for Concrete under Uniaxial Compression [124].

7- Tension stiffening is defined in the present study using the fracture energy (G_f) show in Figure B.8. The fracture energy depends on the concrete quality and aggregate size can be obtained from Table B.1.

Table B.1: G_f for Different Concrete Qualities and Aggregate Size [131].

$D_{max.}$ (mm)	G_f (N/m)							
	C12	C20	C30	C40	C50	C60	C70	C8
8	40	50	65	70	85	95	105	115
16	50	60	75	90	105	115	125	135
32	60	80	95	115	130	145	160	175

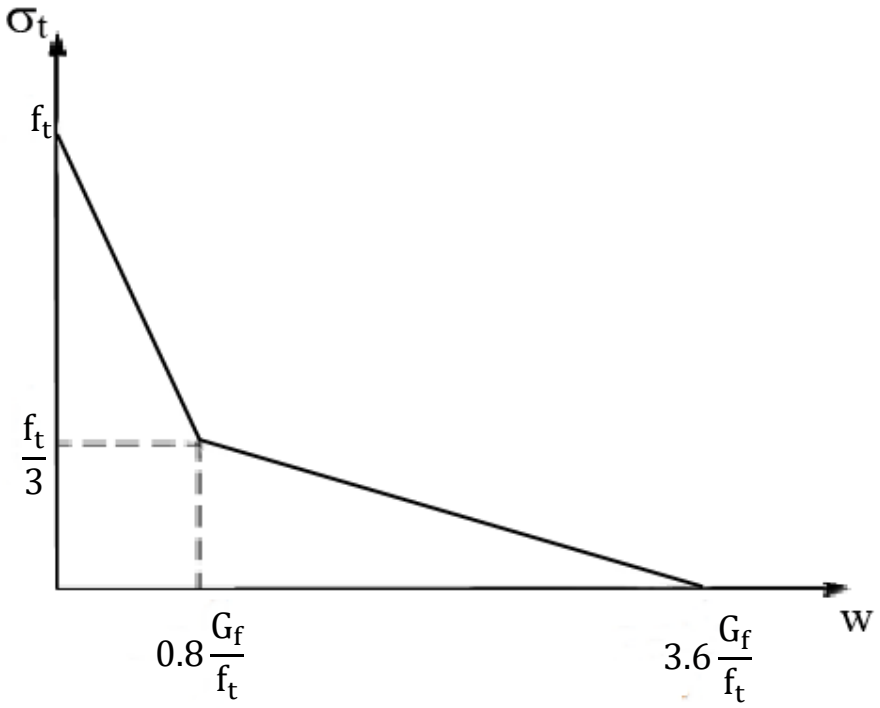

Figure B.8: Bilinear tension softening [132, 133].

B.3.6 Reinforcement

In ABAQUS reinforcement can be modeled with different methods including smeared reinforcement in the concrete, cohesive element method, discrete truss or beam elements with the embedded region constraint or built-in rebar layers [96]. Rebar defines the uniaxial reinforcement levels in membrane, shell and surface elements. One or multiple layers of reinforcements can be defined and for each layer the rebar layer name, the cross-sectional area of each reinforcement layer and the rebar spacing in the plane of definition should be determined [96]. In this part, just truss element with embedded region modeling, which is used for reinforcement modeling in this study, will be explained. Truss element is a common way of reinforcement modeling of which the only required input is the cross sectional area of bars. Beam element modeling is another common way, which takes into account the dowel effect and increases slightly the load bearing capacity of structures but its use is not recommended because it

require a large number of input parameters to be defined and consequently a high computational effort [124, 96, and 127]. According to Hibbit et al. the effect of bond slip is not considered in the embedded region modeling method but this effect is considered somewhat by definition of the tension stiffening behavior of concrete [127].

B.4 MATERIAL PROPERTIES INPUT IN THIS STUDY

B.4.1 Concrete Material

The properties of concrete with compressive strength 30 MPa used in this study are listed in Tables B.2 to B.6.

Table B.2: Elastic Properties of Concrete.

Elastic	Young's Modulus (Mpa)	Poisson's Ratio
fc'= 30 MPa	25742.96	0.2

Table B.3: Plastic Properties of Concrete.

Dilation angle	Eccentricity	Fb0/fc0	k	Viscosity parameter
31	0.1	1.16	0.667	0.001

Table B.4: Stress-Strain Relationship (Tensile behavior).

Yield stress	Cracking strain
3.083676	0
2.276673	8.13E-05
1.764493	0.000151
1.403172	0.000215
1.132869	0.000276
0.923344	0.000334
0.757201	0.00039

Table B.5: Stress-Strain Relationship (Concrete tensile damage).

Damage Parameter	Cracking Strain
0	0
0.355628	8.13E-05
0.569697	0.000151
0.703242	0.000215
0.789918	0.000276
0.848159	0.000334
0.888431	0.00039

Table B.6: Stress-Strain Relationship (Compressive Behavior).

Yield Stress	Inelastic Strain
10.89494	0
14.22907	6.34E-05
17.37647	9.11E-05
20.2684	0.0001288
22.84123	0.0001789
25.04338	0.0002433
26.84075	0.0003235
28.21951	0.0004199
29.18606	0.0005324
29.61273	0.0006158
30	0.0008346
29.24954	0.0010138
28.18468	0.0012052
26.89608	0.0014052
23.45777	0.0018888
19.98228	0.0023738
16.84746	0.0028456
14.17534	0.0032994
11.9592	0.0037354

10.14244	0.004156
8.65726	0.0045637
7.440646	0.004961
6.439317	0.0053499
5.610149	0.0057321
4.918928	0.0061089
4.118641	0.00664

B.4.2 Steel Material

The elastic and plastic properties of cold-formed steel sections are shown in Tables B.7 and B.8.

Table B.7: Elastic and Plastic Properties of CFS beam and column.

Elastic properties	**Young's modulus (MPa)**	**Passion's ratio**
	200000	0.3
Plastic properties	**Yield stress (MPa)**	**Plastic strain**
	244	0
	297	0.01

Table B.8: Elastic and Plastic Properties of CFS angle.

Elastic properties	**Young's modulus (MPa)**	**Passion's ratio**
	200000	0.3
Plastic properties	**Yield stress (MPa)**	**Plastic strain**
	158	0
	221	0.115

B.4.3 Properties of Reinforcement Bar.

The elastic and plastic properties for steel reinforcement and stiffeners are shown in Tables B.9**.**

Table B.9: Properties of Steel Reinforcement bars.

Elastic properties	**Young's modulus (MPa)**	**Passion's ratio**
	210826.39	0.3
Plastic properties	**Yield stress (MPa)**	**Plastic strain**
	623.4476	0
	652.8728	0.014048
	683.0307	0.022428
	712.5646	0.032478
	731.2375	0.040705
	747.1825	0.050391
	759.5152	0.061675
	747.6122	0.072505
	664.9437	0.079285
	537.4946	0.082066
	350.9884	0.082096

مدمجة لتكوين ربط جزئي بين البلاطة والعتب في هذه الدراسة، والذي يصل إلى حد ٥٠٪ مقارنة مع الربط الكامل، إلى نتائج مقبولة وكان ضمن الحدود الموصى بها للوصلات شبه الجاسئة وفقًا للمدونة الأوروبية.

الجزء الأخير من الدراسة هو دراسة تحليلية باستخدام طريقة العناصر المنتهية، والتي تبحث في السلوك غير الخطي للروابط المركبة. تم تمثيل العينات باستخدام برنامج ABAQUS Standard / Explicit 2017. حيث تتضمن نتائج نماذج العناصر المنتهية شكل الفشل عند التحميل الاقصى ومنحنيات العزم- الدوران.

أظهرت النتائج التحليلية توافق جيد مع النتائج التجريبية مما يعطي انطباع عن قدرة البرنامج على توسيع الدراسة للحصول على المزيد من النتائج لفهم السلوك الفعلي للروابط المركبة. في هذه الدراسة، تم دراسة العديد من المتغيرات للتحقيق في مجموعة واسعة من المتغيرات الرئيسية (سمك الزاوية العليا والسفلى، نسبة حديد التسليح، واستخدام تقوية في شبكة العمود، وشكل العمود، وعدد البراغي). استنتج من دراسة هذه المتغيرات أن الزاوية المستخدمة بنسبة سمك الى عرض تساوي ٠,٠٩٢ تعمل على تحسين مقدار العزم للروابط المركبة بنسبة ١٧,٣%، كما أن استخدام التقوية في شبكة العمود يحسن من مقدار العزم بنسبة ٤٢,٦٥% ويمنع التواء شبكة العمود مع الحفاظ على سلوك شبه جاسئ للمفصل.

الخلاصة

أدرك المصممون فوائد تصميم الروابط شبه الجاسئة حيث انها تقلل من وزن وعمق العتب، ارتفاع المبنى الكلي ويزيد من امتصاص الطاقة. وبالإضافة إلى ذلك، فأن الحديد المشكل على البارد (CFS) أصبح أكثر شيوعًا في العديد من البلدان، مما يشير إلى إمكانية جيدة لاستخدام مواد خفيفة الوزن كبديل لمقاطع الحديد التقليدية. ومع ذلك، لا تزال هناك حاجة الى مزيد من البيانات المتعلقة بسلوك المفاصل المركبة، خاصة بالنسبة للروابط المركبة المكونة من CFS، مما يعطي المزيد من الحافز لدراسة هذا النوع من المفاصل المركبة. تقدم هذه الدراسة اختبارا تجريبيًّا لمفصل عتب الى عمود شبه جاسئ يتكون من بلاطة خرسانية مركبة ومقطعين من الفولاذ المُشكل على البارد على شكل C للعتب والعمود.

تم اختبار ثلاث عشرة نموذجاً ذو تجميعات فرعية صليبية من مفاصل الحديد المشكل على البارد لمقطع العتب إلى العمود بشكل تجريبي باستخدام نهج جديد لأشكال الربط المختلفة للعتب إلى العمود، وأنواع ودرجات مختلفة من روابط القص. بالإضافة إلى ذلك، تم إعداد تسع عينات للتحقيق في قوة القص والصلادة والمطيلية لروابط القص المثبت ببراغي مع صامولة واحدة مدمجة وروابط القص المكونة من الحديد المشكل على البارد، مثل صفيحة مفردة، زاوية مفردة، وصفيحة مموجة مفردة وصفيحة مزدوجة الزاوية، التي تستخدم في عينات المفصل المركب.

تنقسم الدراسة إلى أربعة أجزاء: الاختبار التجريبي لعينات فحص القص المباشر. الاختبار التجريبي لثلاثة مفاصل مركبة تجريبية مسلحة بأدنى نسبة لحديد التسليح وعرض البلاطة ٣٠٠ ملم؛ الاختبار التجريبي لعشرة مفاصل مركبة رئيسية مسلحة بحديد قطر١٠ ملم وبأبعاد ١٠٠ملم في كلا الاتجاهين وعرض البلاطة ٧٥٠ ملم وبأشكال روابط مختلفة من العتب إلى العمود تم اختبارها تحت حمل رتيب ودوري وأنواع ودرجات مختلفة من موصل القص؛ وطريقة العناصر المحدودة.

أظهرت النتائج أن العينات المختبرة ذات وصلات العتب إلى العمود المتصلة بزوايا في مجموعة المفاصل المركبة الرئيسية تمتلك خصائص مطيلية عالية حيث تجاوزت قدرة الدوران ٣٠ ميلي راديان. وبالتالي، فإن جميع هذه العينات المقترحة تصنف على أنها مفاصل شبه جاسئة وفقًا لمحددات المواصفات الاوربية وهي مناسبة للتحليل المرن والتصميم الزلزالي. في حين أن الاتصال المباشر بين العتب والعمود والذي يشكل مقطع صندوقي للعمود أدى إلى زيادة الحمل الاقصى بنسبة ٣٣٪ ونقصان في قدرة الدوران بنسبة ٧٦٪. في حين، فإن العينة ذات اتصال المباشر بين العتب والعمود وتشكل مقطعًا صندوقي للعتب زادت الحمل الاقصى بنسبة ٩٠٪ وقللت من قدرة الدوران بنسبة ٧٨٪ مقارنةً بالعينة ذات المقطع I للعتب والعمود المرتبطة من خلال استخدام الزوايا. من ناحية أخرى، فإن الحمل الدوري له تأثير ضئيل على التحمل الاقصى للمفاصل المركبة، ولكنه يزيد بشكل كبير من قيمة الدوران. تعتبر أشكال الروابط المركبة لمقطع العتب إلى العمود الفولاذي المشكل على البارد المقترحة فعالة من حيث الصلابة وسعة العزم النهائية.

أيضًا، باستخدام نهج جديد لروابط القص المكون من صفيحة على شكل زاويا مشكلة على البارد أظهرت تحسنًا كبيرًا في العزم والصلابة الأولية للمفصل. اظهر استخدام روابط القص المثبت ببراغي مع صامولة واحدة

جمهورية العراق

وزارة التعليم العالي والبحث العلمي

جامعة بابل

كلية الهندسة/قسم الهندسة المدنية

الاستجابة الإنشائية لبلاطات خرسانية مسلحة مركبة ذات مقطع عتب الى عمود من الحديد المشكل على البارد ذو مفاصل شبه جاسئة

أطروحة

مقدمة الى كلية الهندسة / جامعة بابل

كجزء من متطلبات نيل درجة الدكتوراه فلسفة في الهندسة /الهندسة المدنية/ إنشاءات

من قبل

مصطفى صلاح شاكر محمود

اشراف

الأستاذ الدكتور هيثم حسن متعب الدعمي

1444هـ 2023 م